



Developing new heterogeneous catalysts based on polyoxometalates and metal-organic frameworks for CO photoreduction

Youven Benseghir

► To cite this version:

Youven Benseghir. Developing new heterogeneous catalysts based on polyoxometalates and metal-organic frameworks for CO photoreduction. Catalysis. Sorbonne Université, 2021. English. NNT : 2021SORUS383 . tel-03637610

HAL Id: tel-03637610

<https://theses.hal.science/tel-03637610>

Submitted on 11 Apr 2022

HAL is a multi-disciplinary open access archive for the deposit and dissemination of scientific research documents, whether they are published or not. The documents may come from teaching and research institutions in France or abroad, or from public or private research centers.

L'archive ouverte pluridisciplinaire **HAL**, est destinée au dépôt et à la diffusion de documents scientifiques de niveau recherche, publiés ou non, émanant des établissements d'enseignement et de recherche français ou étrangers, des laboratoires publics ou privés.

Sorbonne Université

École doctorale de Chimie moléculaire de Paris-Centre (ED 406)

Laboratoire de Chimie des Processus Biologiques

CNRS UMR 8229 Collège de France, Paris

Developing new heterogeneous catalysts based on polyoxometalates and Metal-Organic Frameworks for CO₂ photoreduction

Par Youven Benseghir

Thèse de doctorat de Chimie

Dirigée par Dr. Caroline Mellot-Draznieks et Pr. Pierre Mialane

Présentée et soutenue publiquement le 16 Décembre 2021

Devant un jury composé de :

Dr. Julien Bonin, Maître de conférences à l'Université de Paris	Rapporteur
Dr. Thomas Devic, Directeur de recherche à l'Institut des Matériaux de Nantes	Rapporteur
Dr. Sébastien Blanchard, Maître de conférences à Sorbonne Université	Examineur
Pr. Laurence Rozes, Professeure à Sorbonne Université	Examinatrice
Pr. Norbert Stock, Professeur à l'Université de Kiel	Examineur
Dr. Caroline Mellot-Draznieks, Directrice de recherche au Collège de France	Directrice de thèse
Pr. Pierre Mialane, Professeur à l'Université Paris-Saclay	Directeur de thèse (Membre invité)
Dr. Anne Dolbecq, Directrice de recherche à l'Institut Lavoisier de Versailles	Co-encadrante (Membre invité)
Pr. Marc Fontecave, Professeur au Collège de France	Membre invité

Remerciements

J'aimerais dans un premier temps remercier mes directeurs, et encadrants, de thèse Caroline Mellot-Draznieks, Pierre Mialane et Anne Dolbecq. Je les remercie de m'avoir permis de mener ce projet durant près de 3 ans et demi. Merci aussi à Maria Gomez-Mingot pour son implication. Merci à tous les quatre pour la qualité de nos discussions scientifiques, pour votre patience (je suis conscient du problème que je rencontre parfois avec les deadlines), pour votre soutien tout au long de cette thèse. Je remercie également Marc Fontecave pour m'avoir accueilli au laboratoire, et pour ses conseils scientifiques.

Merci à Mathis pour ces 3 années, je suis persuadé qu'avoir un autre doctorant dans le même groupe avec qui échanger et me plaindre m'a beaucoup aidé. Merci à Alex pour le côté scientifique et humain, merci pour les super échanges et le travail qu'on a pu faire sur l'UiO, pour les sorties et soirées, ma seule déception étant de ne pas t'avoir vu sauter, 15 m ce n'est pas rien. Thanks to Albert (switching to English so you won't have to google translate it, even though seeing how you progress in French maybe it's not needed), thank you for your hard work on all the different projects we had in common, it hasn't always been easy to understand everything but it has been very enriching each time. Thank you for your support, in particular in this last step, which is by far the worse, the manuscript writing up, and thanks for the gossips it helped a lot! Un grand merci à Grégoire, pour m'avoir fait découvrir les MOFs lors d'un super stage, et aidé lors de ma première année de thèse, et pour le reste. J'aimerais par ailleurs remercier Lauren Dalecky et Khadija Talbi pour leur aide, respectivement sur les projets P₄Mo₆ et POM@MOF-545, sans qui je n'aurais probablement pas eu le temps de faire tout ça. Merci aussi pour votre bonne humeur en toutes circonstances.

Merci à Julien Bonin, Thomas Devic, Sébastien Blanchard, Laurence Rozes et Norbert Stock d'avoir accepté de juger mes travaux, ainsi qu'à Guillaume Izzet et Benoit Fleury de m'avoir suivi au cours de ma thèse lors des CST.

Merci JohnnyBOY et Jess pour les pauses café, les pauses déjeuner, les différents restaurants qu'on a pu tester, et tout ce temps qui m'a permis de décompresser, aussi bien au laboratoire qu'à l'extérieur, ainsi qu'à Maxime alias Flax lors de son court passage. Merci aux autres membres du labo, avec qui j'ai aimé passer du temps, Silvia, Charlie, Dilan, Alessandro, Phong, Ellie, Adèle, José, Paolo, Jingjing, Raphaël, Iulia, Tam, Yun, Huan, Bruno, Hamid et les gens qui nous ont quittés pour continuer leur aventure, Ceci, Cameron, Yifan, Hemlata, Tanya, ainsi que tous ceux que je peux oublier.

Merci à mon équipe de l'Institut Lavoisier de Versailles, à ceux qui ont pu rendre mon passage plus facile de par leur aide sur les différentes machines ou leur implication dans le projet, à commencer par Catherine pour les discussions scientifiques et les réunions, Jérôme Marrot pour les structures RX, Mohamed Haouas pour son aide sur la RMN solide, Carine Livage et Nathalie Leclerc pour l'ATG, Flavien Bourdeux, Muriel Bouttemy, Solène Bechu et Mathieu Fregnaux pour l'EDX et l'XPS, Clémence Sicard pour sa patience avec le micro-ondes, Eddy, Marc et Olivier pour leur bonne humeur dans le bureau, Clément Falaise et enfin Emmanuel Cadot pour m'avoir accueilli dans son équipe. Merci aussi à tous mes amis de l'ILV, à commencer par Professeur/Directeur/Secrétaire Raulin, John Bachinours, Marcence bébéchat, Ioanna (accompagné du monde qu'il y a dans sa tête), Mamour à partir de 10h, la mère à Glier, Titi et Manon, Ali, Subha et Sri pour tous les bars, les pauses, les rires et la non-productivité nécessaire à me ressourcer, ainsi que tous ceux que je n'ai pas cité.

Merci à mes amis en dehors du laboratoire et du monde scientifique, je pense notamment à mes ministres. Merci Adam et Val de nous accueillir aussi souvent, Victor « Otcho » Miremont pour ces vacances à Vienne, mes frères Reda et Yassin et tous ces appels fréquents qui m'auront toujours fait beaucoup rire, le copaing Thibault et Féfé pour ces WE à trainer, Victor G, Virgile et Romain toujours un plaisir de vous voir. Merci aussi à Somia pour les repas mensuels, et à Axel. Une pensée enfin aux amis que je n'ai pas eu la chance de voir aussi souvent, mais qui n'en sont pas moins importants : Quentin, Julien et Baptiste.

Le plus important pour la fin, j'aimerais remercier mes parents qui m'ont soutenu jusqu'ici et toujours poussé à aller plus loin. Mon frère, ma sœur, ma tante, mon oncle et ma grand-mère qui ont été présents quotidiennement, ainsi que le reste de ma très grande famille.

Table of content	
Abbreviation list.....	7
General introduction.....	11
Chapter 1: Molecular catalysts and polyoxometalates, immobilization in Metal-Organic Frameworks	16
1. Homogeneous molecular catalysts	16
1.1 Molecular catalysts for CO ₂ RR	18
1.2 Polyoxometalates, fully inorganic molecular catalysts	26
2. Metal-Organic Frameworks.....	32
2.1 MOF structural description.....	33
2.2 Zirconium-based MOF	35
3. Encapsulation strategies	39
3.1 Synthetic encapsulation	40
3.2 Impregnation	40
3.3 Ship-in-a bottle	42
3.4 Charge compensation	43
4. Characterizations of Cat@MOF composites	46
4.1 Determination of the composition (ICP, solution NMR, UV-vis, TGA, EDX)	46
4.2 IR and Raman spectroscopy	49
4.3 BET measurements.....	50
4.4 Solid-State NMR	51
4.5 X-ray diffraction.....	52
5. References	55
Chapter 2: Co-immobilization of a Keggin POM and a Rh- catalyst in UiO-67 MOF: in-depth characterization and CO ₂ photosensitized reduction.....	64
1. State of the art for Rhodium bipyridine complexes for CO ₂ reduction	64
2. Synthesis and Characterizations of the (PW ₁₂ ,Cp*Rh)@UiO-67 composite	74
3. In-depth Characterizations of the (PW ₁₂ ,Cp*Rh)@UiO-67 composite.....	82
3.1 2D Solid-state NMR	82
3.2 DFT calculations	83
3.3 Pair Distribution Functions analysis.....	85
4. Photocatalytic reduction of CO ₂	88
4.1 Photocatalytic activity	88
4.2 Post-catalysis characterization.....	91
4.3 Mechanistic investigation.....	93
5. Conclusions and perspectives.....	95
5.1 PMo ₁₂ @UiO-67	96

5.2	PW ₁₀ Ti ₂ @UiO-67	97
5.3	(PW ₁₂ ,Cp*Rh)@POP.....	99
6.	Experimental Section	101
7.	References	104
8.	Appendix	107
Chapter 3: Photocatalytic reduction of CO ₂ by Porphyrinic Metal-Organic Framework		114
1.	State of the art of Zr ₆ -TCPP MOFs for CO ₂ reduction.....	115
2.	Synthesis and characterizations of metalated and nanosized MOF-545	121
3.	Photocatalytic reduction of CO ₂	126
4.	Reaction mechanism for CO ₂ reduction to formate in MOF-545.....	130
4.1.	DFT Calculation	130
4.2.	Complementary photocatalytic tests.....	136
5.	Co-catalyst immobilization in MOF-545	138
5.1.	Synthesis, characterization and photocatalytic activity of the cat@MOF composites....	141
5.2.	Synthesis and characterization and photocatalytic activity of POM@MOF composites	145
6.	Conclusions	150
7.	Experimental section	152
8.	References	153
9.	Appendix	156
Chapter 4: P ₄ Mo ₆ -based polyoxometalates for CO ₂ heterogeneous photoreduction		160
1.	Polyoxometalates for CO ₂ photoreduction	160
2.	Synthesis and characterization	164
2.1	Synthesis.....	164
2.2	Structure description.....	166
2.3	Characterization.....	171
3.	Photocatalytic properties	174
4.	Mechanistic study.....	176
5.	Conclusion.....	181
6.	Experimental section	183
7.	References	189
8.	Appendix	192
General Conclusion		200

Abbreviation list

ACN	acetonitrile
AuNP	Gold Nanoparticles
BDC	Benzenedicarboxylate
BET	Brunauer-Emmett-Teller
bib	1,4-bis(1-H-imidazol-4-yl)benzene
BNAH	Benzyl-dihydronicotinamide
bpdc	biphenyldicarboxylate
bpet	1,2-bis((pyridin-2-ylmethyl)thio)ethane
bpy	Bipyridine
bpydc	Bipyridinedicarboxylate
BTC	Benzenetricarboxylate
Cat	catalyst
CO ₂ RR	CO ₂ reduction reactions
Co ₄	[Co ₄ (H ₂ O) ₂ (PW ₉ O ₃₄) ₂] ¹⁰⁻
CP MAS	Cross polarization magic angle spinning
Cp*	Cyclopentadiene
CTTS	Charge transfer to solvent
DED	Difference envelope density
DFT	Density functional theory
DMA	Dimethylacetamide
DMF	Dimethylformamide
d-PDF	Differential pair distribution function
EDX	Energy dispersive X-ray
EPR	Electron paramagnetic resonance
F ₂₀	tetrakis(pentafluorophenyl)porphyrin
Fe-Mn	Na ₇ Mn ^{II} ₂ Fe ^{II} ₄ Fe ^{III} ₄ [P ₄ Mo ₆ O ₂₆ (OH) ₅] ₄ (PO ₄)·52H ₂ O
FePcS	Iron tetrasulfophthalocyanine
HER	Hydrogen evolution reaction
HKUST	Hong Kong University of Science and Technology
HRTEM	High-resolution transmission electron microscopy
ICP	Inductively coupled plasma
ICP-OES	Inductively coupled plasma – Optical Emission Spectrometry
IR	Infrared
IRMOF	Isorecticular metal-organic framework
LCPB	Laboratoire de chimie des processus biologiques
LSCT	Ligand-to-solvent charge transfer
MAS	Magic angle spinning
MC	Metal-centered
MeCN	Acetonitrile
MIL	Matériaux de l'institut lavoisier
MLCT	Metal ligand charge transfer

Mn(bpy)	Mn(bpy)(CO) ₃ Br
Mn ₄	[Mn ₄ (H ₂ O) ₂ (VW ₉ O ₃₄) ₂] ¹⁰⁻
MOF	Metal organic Framework
NENU	Northeast normal university
Ni(cyclam)-Mn	Na ₂ [Ni(cyclam)] ₃ Mn ^{II} ₂ [P ₄ Mo ₆ O ₂₅ (OH) ₆] ₂ ·12H ₂ O
Ni ₁₆	[{Ni ₄ (OH) ₃ AsO ₄ } ₄ (B-α-PW ₉ O ₃₄) ₄] ²⁸⁻
Ni ₄	[Ni ₄ (H ₂ O) ₂ (PW ₉ O ₃₄) ₂] ¹⁰⁻
NMR	Nuclear magnetic resonance
NNU	Northwest Nazarene University
NU	Northwestern University
OER	Oxygen evolution reaction
Otf-	Trifluoromethanesulphonate
PCN	Porous coordination network
PCy ₃	tricyclohexylphosphine
PDF	Pair distribution function
Phen	Phenanthroline
POM	Polyoxometalate
POMOF	POM-based metal-organic framework
Ppy	Phenylpyridine
PS	Photosensitizer
PSM	Post synthetic modification
PW ₁₂	H ₃ [PW ₁₂ O ₄₀]
PXRD	Powder X-ray diffraction
RoW	Rest of the world
Ru(bpy)	[Ru(bpy) ₃]Cl ₂
Ru(bpy)-Co	[Ru(bpy) ₃] ₂ Co ^{II} ₅ [P ₄ Mo ₆ O ₂₆ (OH) ₅] ₂ ·22H ₂ O
Ru(bpy)-Mn	Na ₂ [Ru(bpy) ₃] ₂ Mn ^{II} ₃ [P ₄ Mo ₆ O ₂₅ (OH) ₆] ₂ ·20H ₂ O
Ru ₄	[Ru ₄ (μ-O) ₄ (μ-OH) ₂ (H ₂ O) ₄ (γ-SiW ₁₀ O ₃₆) ₂] ¹⁰⁻
SA	Simulated Annealing
SEM	Scanning electron microscopy
SET	Single Electron Transfer
ssNMR	Solid-state nuclear magnetic resonance
ST	Supertetrahedron
STEM-HAADF	High-angle annular dark field scanning transmission electron microscopy
TBA	Tetrabutylammonium
TCPP	Tetrakis(4-carboxyphenyl)porphyrin
TCPPOMe	Tetramethoxyphenylporphyrin
TEA	Triethylamine
TEOA	Triethanolamine
TGA	Thermogravimetric analysis
tib	1,3,5-tris(1-imidazolyl)benzene

TM	Transition metal
TMA	Tetramethylammonium
TOF	Turnover Frequency
TON	Turnover number
TPP	Tetrakis(phenyl)porphyrin
tpy	Terpyridine
TS	Transition state
UiO	University i Oslo
UV-Vis	Ultraviolet visible
XRD	X-ray diffraction
ZIF	Zeolitic Imidazolate Framework
ZJU	Zhejiang University

List of publications concerning this PhD thesis:

- (1) Benseghir, Y., Solé-Daura, A., Cairnie, D. R., Duguet, M., Mialane, P., Gairola, P., Gomez-Mingot, M., Fontecave, M., Iovan, D., Bonnett, B., Morris, A. J., Dolbecq, A. & Mellot-Draznieks, C. Origin of the Photocatalytic CO₂ Reduction Promoted by Optimized Metalloporphyrinic Metal-Organic Frameworks: the Key Role of Triethanolamine. Submitted.
- (2) Benseghir, Y.; Solé-Daura, A.; Mialane, P.; Marrot, J.; Dalecky, L.; Gomez-Mingot, M.; Fontecave, M.; Mellot-Draznieks, C.; Dolbecq, A. Understanding the Photocatalytic Reduction of CO₂ with Heterometallic Molybdenum(V)-Phosphate Polyoxometalates in Aqueous Media. Accepted. *ACS Catalysis*.
- (3) Mialane, P. *et al.* Heterogenisation of polyoxometalates and other metal-based complexes in metal–organic frameworks: from synthesis to characterisation and applications in catalysis. *Chem. Soc. Rev.* **50**, 6152–6220 (2021)
- (4) Benseghir, Y. *et al.* Co-immobilization of a Rh Catalyst and a Keggin Polyoxometalate in the UiO-67 Zr-Based Metal–Organic Framework: In Depth Structural Characterization and Photocatalytic Properties for CO₂ Reduction. *J. Am. Chem. Soc.* **142**, 9428-9438 (2020)

List of publications outside the scope of this PhD thesis:

- (1) Duguet, M. *et al.* Structure-directing role of immobilized polyoxometalates in the synthesis of porphyrinic Zr-based metal–organic framework. *Chem. Commun.* **56**, 10143-10146 (2020)
- (2) Paille, G. *et al.* Thin Films of Fully Noble Metal-Free POM@MOF for Photocatalytic Water Oxidation. *ACS Appl. Mater. Interfaces* **11**, 47837–47845 (2019).

General introduction

Facing the increasing demand for energy, growing from 59 000 to 171 000 TWh in the last fifty years, and the limitation of fossil fuels, developing new energy sources is of immediate need in order to assure the energetic transition (**Figure 1.1**).¹ Developing renewable energies (solar, wind turbines, hydrokinetic turbines etc.) is considered a very promising solution. However, the intermittent nature of most of these energies, including those derived from solar energy, makes it a challenging alternative for fossil fuels as our energy consumption is not intermittent. Indeed, storing the excess of energy produced over favorable weather periods is a key issue.

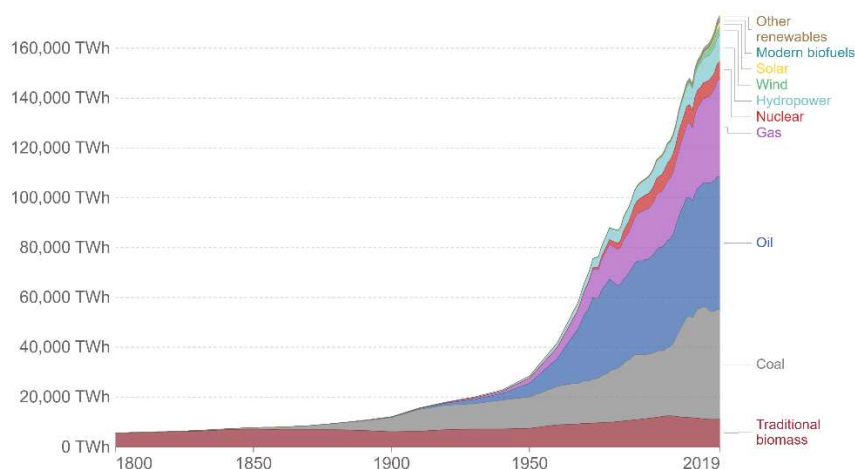


Figure 1.1: Evolution of the global annual energy consumption.¹

Storing this energy in the form of chemical bonds, which can be transformed later on to deliver this energy back, has been considered widely for the past few decades driving the ever-growing research effort in the chemical reduction of CO₂ (**Figure 1.2**, right). This process can be observed in nature where plants, algae and bacteria can harvest light and use water during the light phase of photosynthesis to stock energy and release O₂, then use the stored energy to transform CO₂ into sugars, cellulose or starch during the dark phase of photosynthesis. Using CO₂ as a C1 carbon feedstock to store energy in chemical bonds is thus an attractive strategy when working with intermittent renewable energies. In fact, carbon dioxide is largely produced from the combustion of fossil fuel. As shown in **Figure 1.2** (left) the annual CO₂ emissions coming from fossil sources exceeds 30 Gt per year, and is in most parts of the world still increasing.

The chemical transformation of CO₂ is thus beneficial in two points: i) climate change theories explain the global warming mainly through the increase carbon dioxide concentrations in the

General introduction

atmosphere and its greenhouse effect, ii) the gigantic amount of CO₂ available to be used as a substrate for chemical reaction, as only 150 Mt is used in the industry per year.

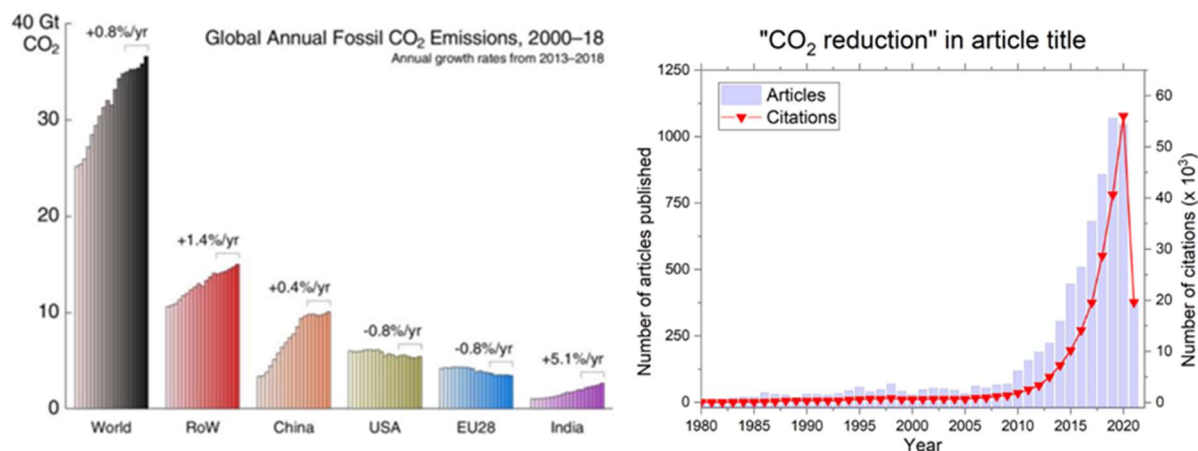


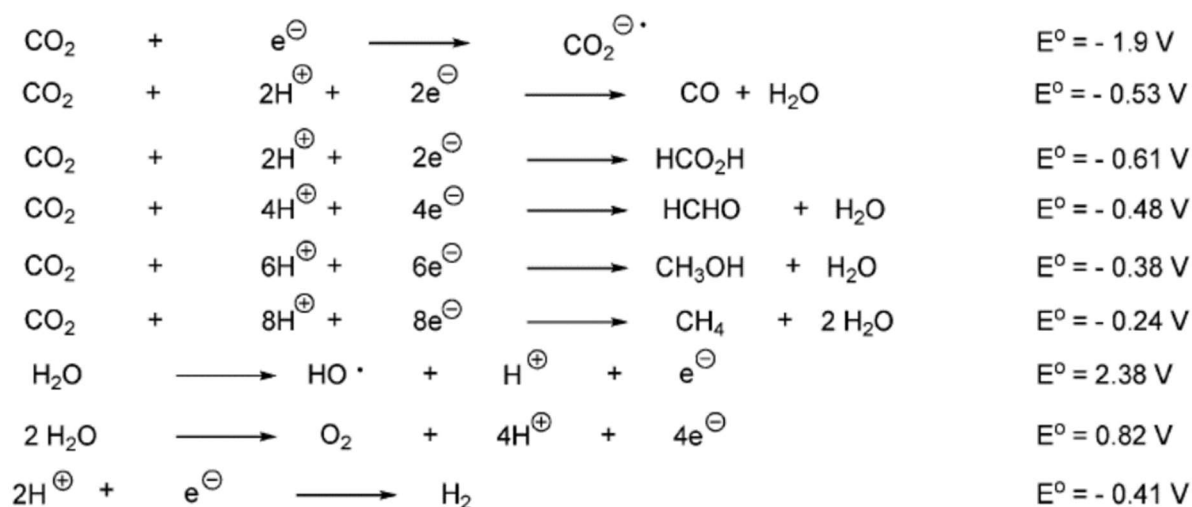
Figure 1.2: Global annual CO₂ emission, RoW = rest of the world (left) and CO₂ chemical valorization research reports (right).²

Chemical reduction of CO₂ on an industrial scale still faces two challenges, i) the difficulty to capture CO₂ due to its dilution in ambient air that makes it an expensive process and ii) the chemical reduction of carbon dioxide in energy-dense molecules (CH₄, ethanol, methanol, ethylene etc.) is a fascinating fundamental challenge because of the high thermodynamic stability of CO₂ and thus the endergonic nature of its reduction (**Table 1.1**).

Table 1.1: Equation, free enthalpy, Gibbs energy and potentials of CO₂ and proton reduction.

Equation	Reaction	ΔH^0 (kJ·mol ⁻¹)	ΔG^0 (kJ·mol ⁻¹)
1	$\text{CO}_{2(g)} \rightarrow \text{CO}_{(g)} + 1/2\text{O}_{2(g)}$	283	257
2	$\text{CO}_{2(g)} + \text{H}_2\text{O}_{(l)} \rightarrow \text{HCOOH}_{(l)} + 1/2\text{O}_{2(g)}$	270	286
3	$\text{CO}_{2(g)} + \text{H}_2\text{O}_{(l)} \rightarrow \text{HCHO}_{(l)} + \text{O}_{2(g)}$	563	522
4	$\text{CO}_{2(g)} + 2\text{H}_2\text{O}_{(l)} \rightarrow \text{CH}_3\text{OH}_{(l)} + 3/2\text{O}_{2(g)}$	727	703
5	$\text{CO}_{2(g)} + 2\text{H}_2\text{O}_{(l)} \rightarrow \text{CH}_4_{(g)} + 2\text{O}_{2(g)}$	890	818
6	$\text{H}_2\text{O}_{(l)} \rightarrow \text{H}_{2(g)} + 1/2\text{O}_{2(g)}$	286	237

Moreover, multiple electrons and protons are necessary to chemically reduce carbon dioxide inducing high energy barriers and kinetic limitations as more electrons and protons are needed (**Scheme 1.1**). Thus, the use of catalysts is needed to help the CO₂ chemical reduction process into C1 valuable chemicals.

Scheme 1.1: Equations and potentials of CO₂ reduction and water splitting (vs. NHE, at pH 7).

Focusing on CO₂ photocatalytic reduction, many parameters are to be taken into account when developing new catalysts: their efficiency, selectivity, stability, recyclability associated with the necessity to use a photosensitizer able to harvest visible light (often based on noble metals) and, of course, their cost when considering an economic point of view. As detailed below, the immobilization of molecular catalysts in porous materials is a valuable approach to increase both their stability and recyclability, while maintaining their catalytic activities when compared to those observed in homogeneous conditions. In this context, the main objective of my PhD thesis was to develop new heterogeneous photocatalytic systems for CO₂ reduction based on Metal-Organic Frameworks (MOFs) and polyoxometalates (POMs).

In this regard, the first chapter of this PhD thesis will describe in a non-exhaustive fashion current strategies of the literature making use of molecular catalysts and co-catalysts for CO₂ reduction and MOFs as immobilizing platforms. We will focus mainly on molecular complexes with polypyridyl groups, porphyrins and polyoxometalates. Concerning MOFs, we will shortly describe the mostly used ones for immobilizing catalysts before focusing on the subfamily of zirconium-based MOFs, which were specific MOF we used during this PhD. Finally, we will describe the various existing catalyst immobilization procedures and the main physicochemical methods used to characterize the resulting complex composites.

The three following chapters will be dedicated to the presentation of my results over the PhD. Three distinct families of photocatalytic systems for CO₂RR involving molecular catalysts, MOFs and POMs will be presented over the three following chapters.

General introduction

The second chapter will be dedicated to the co-immobilization of a Keggin polyoxometalate (PW_{12}) and a rhodium-based catalyst, $\text{Cp}^*\text{Rh}(\text{bpydc})\text{Cl}$, in the zirconium-based MOF UiO-67, leading to the $(\text{PW}_{12}, \text{Cp}^*\text{Rh})@\text{UiO}-67$ composite. We will describe its synthesis, characterization and photocatalytic properties for CO_2 reduction. A mechanism for carbon dioxide and proton reduction to formate and H_2 is proposed with a tentative interpretation of the role of the POM in that process.

In the third chapter, we will focus on an all-in-one platform for CO_2 reduction, making use of the porphyrinic zirconium-based MOF-545. This MOF can by itself reduce CO_2 , *i.e.* without the addition of any external photosensitizer or immobilized molecular catalyst. Similarly, we will describe the synthesis, characterization, photocatalytic properties and a proposed mechanism for carbon dioxide reduction to formate. In a second part, we will detail our attempts made in immobilizing three different molecular catalysts and various Keggin polyoxometalates in MOF-545.

Lastly, in the fourth chapter, we report three new polyoxometalate-based crystalline non-porous solids able to reduce carbon dioxide to methane and carbon monoxide in heterogeneous conditions. We will describe the hydrothermal synthesis, the structure of these novel POM-based materials, their photocatalytic properties and propose a plausible mechanism supported by DFT calculations.

Chapter 1: Molecular catalysts and polyoxometalates, immobilization in Metal-Organic Frameworks

We mentioned previously the need of a catalyst in order to reduce CO₂ photochemically. The nature of these catalysts can vary a lot from oxides, metal nanoparticles to organometallic complexes. Organometallic complexes have been widely studied as photocatalysts, or photocatalytic complexes, for CO₂ reduction reactions (CO₂RR) due to their tunable structures.³⁻⁵ The possibility to tune these catalysts at a molecular level can indeed allow a better control on the different CO₂RR key points such as the efficiency, the selectivity or stability of the catalyst. Polyoxometalates represent another family of molecular catalysts, recently identified as potentially interesting for CO₂RR, amongst others (see below). They can be functionalized with a wide variety of metals proven to be active for CO₂RR, including Mn, Fe, Cu, Co. Moreover, organometallic complexes can be linked covalently to polyoxometalates and bring additional properties to the hybrid species, such as electron relay.⁶ Nonetheless, these homogeneous catalysts suffer from two main drawbacks, i) their stability is often limited, with the catalyst deactivating after few hours and ii) the complexes being dissolved in solution cannot be easily recovered. Immobilizing these molecular catalysts in porous materials, namely metal-organic frameworks, is a commonly used approach in order to circumvent the above drawbacks. Indeed, MOF porosity and versatility regarding their organic building units enable the incorporation of molecular catalysts via covalent grafting or supramolecular interactions, thus increasing the stability of the catalyst as a result of its heterogenization. In this chapter we will first describe, in a non-exhaustive way, the commonly used organometallic complexes for CO₂RR and POMs. We will then present the main metal-organic frameworks used to heterogenize these molecular species. Finally, we will discuss the different synthetic methods used to immobilize catalysts in MOFs and go through the usual characterization methods for such composite materials.

1. Homogeneous molecular catalysts

Before introducing molecular catalysts, we will briefly present the different components needed for photocatalytic reduction: a solvent, a sacrificial electron donor for reduction reactions, a photosensitizer, light and lastly, a catalyst.

- Choosing the solvent is the first important step as gas concentration differs depending on the solvent and pH. For example, CO₂ concentration in acetonitrile is almost ten times higher

than in water at pH 7 (0.28 M vs. 0.033 M respectively).⁷ Moreover, the molecular catalyst as well as the sacrificial agent have to be soluble and stable in the chosen solvent.

- For light driven CO₂ reduction, the photosensitizer should be able to be excited by photons preferably in the visible region. It must possess properties such as light-harvesting ability, long excited-state lifetime and strong oxidizing/reducing power in its excited state in order to receive an electron from the sacrificial electron donor or reduce the substrate. Two possible quenching routes of the excited state of the photosensitizer are possible: oxidative quenching or reductive quenching as illustrated in **Figure 1.3**.⁸ In the case of oxidative quenching, the excited state of the photosensitizer reduces the substrate before being reduced by the sacrificial electron donor. In the reductive quenching mechanism, the excited state of the photosensitizer is first reduced by the electron donor before being oxidized by the substrate.

- The electron-donor will react with the photosensitizer (PS* or PS⁺ form). A list of usual electron donors (triethylamine, triethanolamine, benzyl-dihydronicotinamide, dimethylphenylbenzimidazoline) as well as their reaction mechanism has been reported recently by Odobel and Pellegrin.⁸

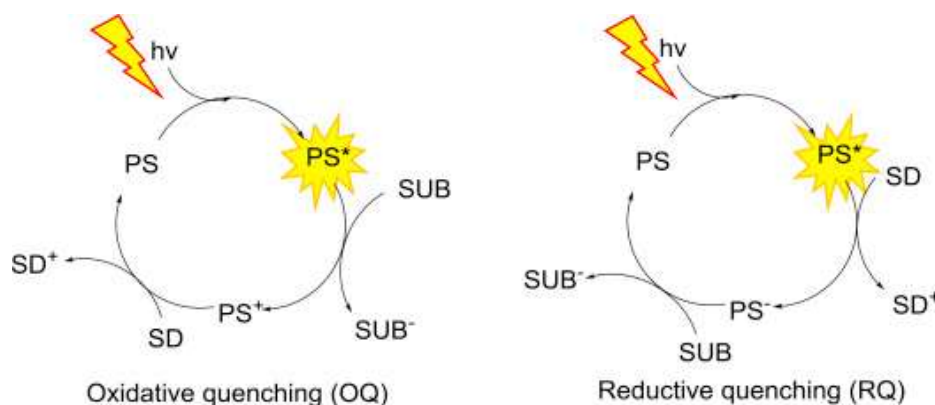


Figure 1.3: Oxidative and reductive quenching mechanisms. SD: Sacrificial Donor, PS: Photosensitizer, SUB: Substrate.⁸

- The last key component is the catalyst. The catalyst performances can be evaluated by four main factors: the catalyst's selectivity, turnover number, turnover frequency and quantum yield. The highest the catalyst's selectivity, the better as it avoids having a mixture of products. Turnover numbers (TONs) can be calculated as follows and correspond to the number of reductions occurring per catalytic site:

$$TON = \frac{\Sigma[product]}{[catalyst]}$$

Turnover frequencies (TOFs) are generally measured at the initial stage of the reaction when the product formation is still linear. It can be calculated with the following formula and is usually expressed in s⁻¹, min⁻¹ or h⁻¹:

$$TOF = \frac{TON}{time}$$

Apparent quantum yield (Φ) is the amount of product in respect to the number of induced photons used for the reaction. The number of induced photons can be calculated with the Plank-Einstein relation where E_{tot} is measured beforehand with a photodiode power sensor.

$$E_{photo} = \frac{hc}{\lambda_{max}}$$

$$[Incident\ photons] = \frac{E_{tot}}{E_{photo}}$$

$$\Phi = \frac{[product] * n_{electrons}}{[Incident\ photons]}$$

The nature of the catalyst, including both its metal center and organic ligands, will impact greatly its performances. In the following subsection, we will present briefly several families of catalysts for CO₂ photoreduction. The catalyst performances will not be detailed as they can be found in recent reviews.^{4,9}

1.1 Molecular catalysts for CO₂RR

In this subsection we separate the molecular complexes in two categories, where the first one gathers noble metal polypyridyl molecular catalysts for carbon dioxide reduction, and the second one, noble-metal-free polypyridyl catalysts. Noble metal catalysts described in this paragraph contain ruthenium and iridium. We will also consider rhenium complexes, even if rhenium is not usually reported as noble metal. Rhodium cyclopentadiene based photocatalytic systems will be treated in chapter 2.

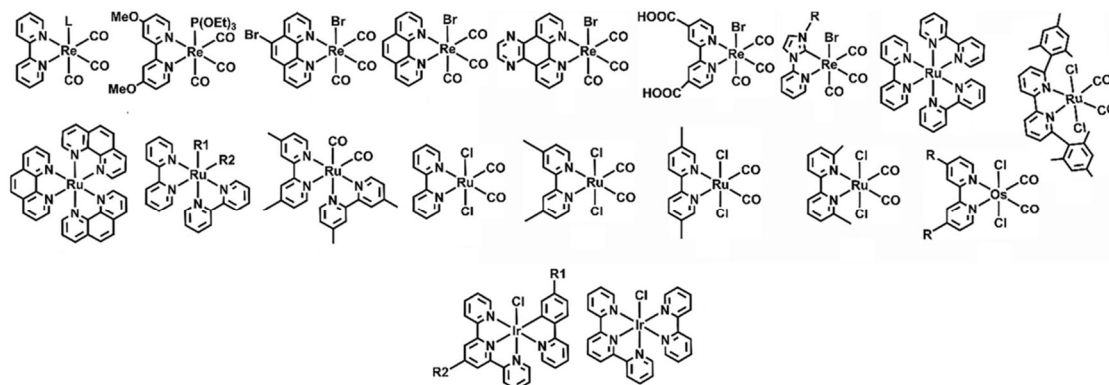
Noble metal-based CO₂ reduction catalysts

Figure 1.4: Examples of noble metal-based photocatalysts for CO₂RR.⁴

Rhenium polypyridyl catalysts were first reported in 1993 by Hawecker *et al.*¹⁰ working on $\text{Re}(\text{CO})_3(\text{bpy})\text{X}$ ($\text{X} = \text{Cl}$) (**Figure 1.4**). The catalyst could reduce CO₂ in CO as the sole product, in DMF with TEOA as an electron donor and could reach a TON of 48 after 4h. The solution was irradiated with visible light ($\lambda > 400 \text{ nm}$) without the use of external photosensitizer. The same catalyst with other X groups ($\text{X} = \text{CN}, \text{SCN}, \text{Br}$) was studied by different groups.^{11–14} It was demonstrated that with $\text{X} = \text{SCN}$, the rhenium catalyst exhibits the best CO₂RR properties, due to the easy dissociation of the SCN^- group after the first one-electron reduction of the complex.¹³ Indeed, to reduce CO₂ the rhenium is first excited, then quenched by TEOA leading to the reduced state of the complex. At this step, the X linker is lost and CO₂ can bind to the rhenium atom (**Figure 1.5**). Besides, Kurz *et al.*¹⁵ showed that the modification on the aromatic group (bipyridine-4,4'-dicarboxylic acid, phenanthroline, azopyridine, etc.) induced a decrease of their fluorescence lifetime, thus of their catalytic activity.

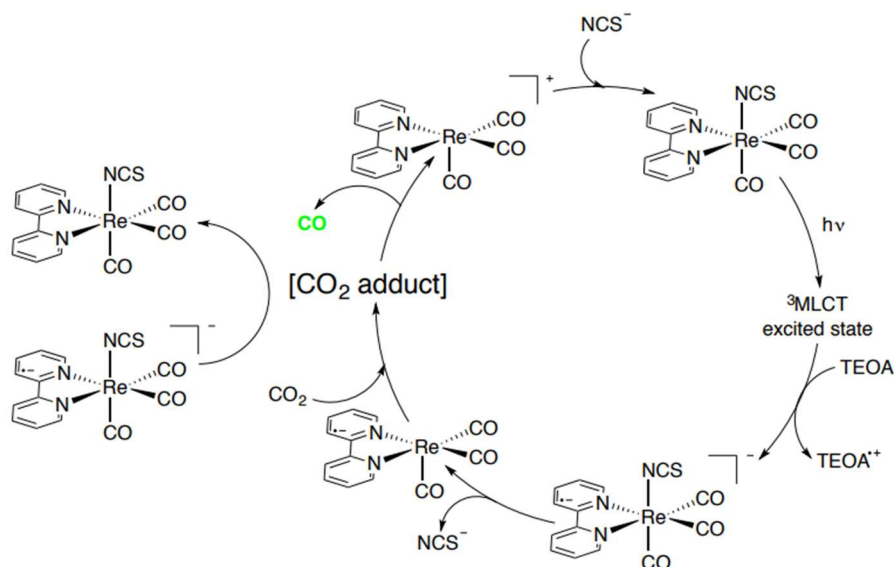


Figure 1.5: Proposed mechanism for CO₂ photoreduction with Re(bpy)(CO)₃NCS.¹³

The efficiency and catalytic conditions of the different catalysts presented in this subsection are summarized in **Table 1.2**.

Table 1.2: Comparison of CO₂ photoreduction experiments with noble-metal based polypyridyl catalysts.

Catalyst	Photosensitizer	Conditions	TON (Time) / Product
Re(CO) ₃ (bpy)Cl ¹⁰ 87 μM	-	DMF:TEOA (5:1)	16 (2h) CO
Re(CO) ₃ (bpy)Br ¹⁰ 79 μM	-	DMF:TEOA (5:1)	14 (2h) CO
Re(CO) ₃ (bpy)CNS ¹³ 0.5 mM	-	DMF:TEOA (5:1)	30 (25h) CO
Ru(bpy) ₃ ¹⁶ 11 mM	-	DMF:TEOA (4:1)	27 (24h) HCOOH
Ru(bpy) ₂ Cl ₂ ¹⁷ 3.3 μM	[Ru(bpy) ₃] ²⁺ 3.3 μM	DMF:TEOA (4:1), 15% water	51 (2h) HCOOH
Ru(bpy) ₂ (CO)Cl ¹⁷ 3.3 μM	[Ru(bpy) ₃] ²⁺ 3.3 μM	DMF:TEOA (4:1), 15% water	326 (2h) HCOOH
Ir(tpy)(ppy)Cl ²² 0.5 mM	-	CH ₃ CN:TEOA (5:1)	38 (5h) CO
Ir(R-tpy)(ppy) ²³ 0.5 mM	-	CH ₃ CN:TEOA (5:1)	310 (5h) CO

The first report of CO₂ photoreduction with a ruthenium polypyridyl catalyst was published in 1985 by Hawecker *et al.*¹⁶ where they studied [Ru(bpy)₃]²⁺. The ruthenium catalyst, now widely used as a photosensitizer, is able to reduce CO₂ to CO and formate in a dimethylacetamide/water mixture with benzyl-dihydronicotinamide (BNAH) as an electron donor. During the process, [Ru(bpy)₃]²⁺ loses a bipyridine ligand which is replaced by two solvent molecules leading to

$[\text{Ru}(\text{bpy})_2(\text{solvent})_2]^{2+}$ which is the actual catalyst for CO_2 reduction. To facilitate the formation of the active form of ruthenium polypyridyl complexes, $[\text{Ru}(\text{bpy})_2\text{R}_1\text{R}_2]$ complexes (**Figure 1.4**) were investigated (where $\text{R} = \text{H}, \text{Cl}, \text{CO}, \text{MeCN}, \text{DMF}$). No clear trend on which R substituent was the most efficient for CO_2 reduction, but the difference between the catalysts is outstanding. When $\text{R}_1 = \text{R}_2 = \text{Cl}$ a TON of 51 could be achieved, when substituting a Cl for a CO , the TON was increased to 326 after 2h.¹⁷ Besides, the selectivity of $\text{Ru}(\text{bpy})_2$ complexes towards CO and formate production is highly dependent on the pH. For example, in presence of TEOA (pH ~ 10) the only product observed was HCOOH . In contrast, when using BNAH, the formation of both HCOOH and CO could be obtained at a neutral or acidic pH. The main issue with $\text{Ru}(\text{bpy})_2$ -type catalysts is their poor stability. Indeed, after a few hours a black precipitate could be observed inducing a slowdown in the catalyst performances.^{18,19} Finally, ruthenium catalysts bearing only one bipyridine and two CO ligands were studied with different bipyridine functionalizations (**Figure 1.4**).^{20,21} The various catalysts have shown similar properties as the previously described ones, with a mixture of CO and HCOOH as reduction products.

Iridium complexes have been barely studied as photocatalysts for CO_2 reduction. Two complexes are presented in **Figure 1.4**: $[\text{Ir}(\text{R}_2\text{-tpy})(\text{R}_1\text{-ppy})\text{Cl}]$ and $[\text{Ir}(\text{tpy})(\text{bpy})]$ (tpy = terpyridine and ppy = phenylpyridine). These complexes can reduce CO_2 selectively in CO in acetonitrile with TEOA as an electron donor. When $\text{R}_1 = \text{R}_2 = \text{H}$, the catalyst could exhibit TONs up to 38,²² functionalization on the aromatic rings with methyl groups could slightly increase the catalyst's efficiency with turnover numbers up to 50. Genoni *et al.*²³ have shown that functionalizing the tpy linker with an electron donating group, an anthryl, could drastically increase the TONs that can reach 310.

Another emerging strategy is the covalent grafting of photosensitizer on molecular catalyst to form a diade. This strategy allows an easier electron transfer from the photosensitizer to the catalyst thus increasing impressively the system efficiency, often reaching TONs of several thousands.⁴

As we have seen, noble metal-based molecular catalysts present many advantages: their high selectivity, efficiency and light adsorbing properties. They generally do not need the addition of external photosensitizer. The main critical issue is their rare nature and thus the high price of the metal needed to design these catalysts. When considering a large-scale production, the metal prices would be a huge drawback with prices ranging from ~ 20 k€/kg for ruthenium to almost

500 k€/kg for rhodium. Developing noble-metal-free catalysts is thus a necessity for considering sustainable photocatalytic systems. For comparison, the price of nickel is ~20 €/kg and that of cobalt ~50 €/kg which makes these more abundant metals a thousand times less expensive.

Metalloporphyrins.

Metalloporphyrins are well known for their electron transfer roles in a myriad of redox systems in nature (chlorophyll, heme, vitamin B12, cytochrome P450, etc.) as well as highly effective photocatalysts thanks to their strong absorption in the 400-450 nm region (Soret band) and weak absorption in the 500-700 nm region (Q-bands). Metalloporphyrins and related derivatives are strong light absorbers with extremely large extinction coefficients in the visible spectral region. However, yields of active catalysts formed after light absorption are very low, mainly due to the short (picosecond) lifetimes of their excited states. Metalloporphyrins and related derivatives studied for CO₂ reduction include metallocorrins, metallophthalocyanines and metallocorroles. These different systems have been largely studied by Savéant and his group in the 1990s. Among the metalloporphyrins, they have shown that iron porphyrins are highly selective for CO in protic solvents in presence of a weak Brønsted acid (phenol, trifluoroethanol) or a Lewis acid. In early stages of the development of the field, the porphyrin efficiency was low and photodecomposition of the catalyst could be observed.²⁴ Addition of external photosensitizer can, sometimes, be beneficial for the reduction reaction. Dhanasekaran *et al*²⁵ have shown that the addition of *p*-terphenyl in solution with iron tetrakis(phenyl)porphyrin (FeTPP) could promote the reduction of Fe^{II} to Fe^I and Fe^I to Fe⁰. The presence of *p*-terphenyl could thus multiply by ten the CO production. The same study was performed with CoTPP and also showed a higher CO production, both photo and electrochemically.²⁶ Conditions and TONs are detailed in **Table 1.3**.

Some metalloporphyrins bear functional groups with negative or positive charges at the meso substituents, designed to enhance efficiency of their catalytic properties. Bonin *et al.*²⁷ reported in 2014 the functionalization of FeTPP phenyl groups with alcohol (CAT) or fluorine (FCAT) (**Figure 1.6**). The introduction of OH groups on the phenyl rings allows stabilizing the CO₂ adduct owing to the internal hydrogen bonding between –OH groups and the CO₂ molecule bound to the metal center. FeTPP could reach TONs of 5.5 for H₂ and less than 0.5 for CO after 1h irradiation but was poorly selective, with only 8% selectivity for CO. In contrast, CAT and FCAT were highly selective for CO, with a product selectivity reaching 93% for CAT and 85% for FCAT. All the catalytic tests were conducted in acetonitrile with TEA as an electron donor,

with or without trifluoroethanol and without external photosensitizer. The production rate of CO is linear for a few hours before decaying, showing the limited stability of the molecular catalyst.

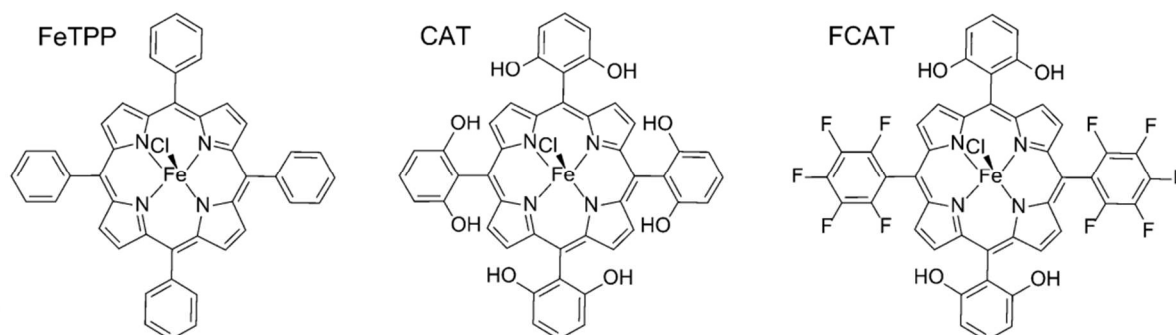


Figure 1.6: Iron porphyrins used as molecular catalysts.²⁷

The same group reported a few years later the catalytic activity of CAT with the addition of $[\text{Ir}(\text{ppy})_3]^+$ or 9-cyanoanthracene as photosensitizer.²⁸ The addition of a photosensitizer not only increases the TONs of the system but also its stability, with no decaying production even after 50h.

A last example of porphyrin design was reported by the same group in 2017. Rao *et al.*²⁹ reported the catalytic activity for CO_2 reduction of a trimethylammonium substituted FeTPP on the *p*-position in water with purpurin as a photosensitizer. The catalyst is 95% selective for CO and reaches TONs of 120 after 47h. Interestingly, when working with $[\text{Ir}(\text{ppy})_3]^+$ as a photosensitizer the catalyst is highly selective for CH_4 (82%). They propose that the high reduction property of $[\text{Ir}(\text{ppy})_3]^+$ might be necessary to reduce the carbonyl from the Fe^{II} -CO adduct.³⁰

Table 1.3: Comparison of catalytic CO₂ reduction with different porphyrin-based catalysts.

Catalyst	Photosensitizer	Conditions	TON (Time) / Product
FeTPP ²⁵ 100 μ M	p-terphenyl (TP) 3 mM	CH ₃ CN, 5% TEA	20 (6h) CO 25 (6h) HCOOH
CoTPP ²⁶ 10 μ M	-	CH ₃ CN, 5% TEA	80 (200h) CO 320 (200h) HCOOH
FeTPP ²⁷ 10-50 μ M	-	CH ₃ CN, 0.36 M TEA, 50 mM trifluoroethanol	7 (10h) CO 23 (10h) H ₂
CAT ²⁷ 10-50 μ M	-	CH ₃ CN, 0.36 M TEA, 50 mM trifluoroethanol	30 (10h) CO 10 (10h) H ₂
FCAT ²⁷ 10-50 μ M	-	CH ₃ CN, 0.36 M TEA, 50 mM trifluoroethanol	23 (10h) CO 12 (10h) H ₂
CAT ²⁸ 2 μ M	[Ir(ppy) ₃] ⁺ 0.2 mM	CH ₃ CN, 0.36 M TEA	140 (60h) CO 10 (60h) H ₂
CAT ²⁸ 2 μ M	9-cyanoanthracene 0.2 mM	CH ₃ CN, 0.36 M TEA	40 (45h) CO
FeTPP(TMA) ²⁹ 2 μ M	Purpurin 0.2 mM	CH ₃ CH:H ₂ O (1:9), 50 mM TEA	60 (47h) CO 3 (47h) H ₂
FeTPP(TMA) ³⁰ 2 μ M	[Ir(ppy) ₃] ⁺ 0.2 mM	CH ₃ CN, 50 mM TEA	140 (102h) CH ₄ 28 (102h) H ₂

Manganese pyridyl complexes

The CO₂ reduction catalytic activity of manganese analogues to [Re(bpy)(CO)₃]⁺ complexes was first reported in 2011 by Chardon-Noblat, Deronzier and co-workers.³¹ They performed the electrocatalytic reduction of CO₂ to CO using the catalysts Mn(bpy)(CO)₃Br and Mn(4,4'-Me-bpy)(CO)₃Br at the potential of -1.70 V vs. Ag/Ag⁺. When used in photocatalytic conditions with [Ru(4,4'-Me-bpy)₃]²⁺ as a photosensitizer, Mn(bpy)(CO)₃Br would be expected to yield CO as the only product as observed electrocatalytically.³² It was shown instead to lead to the formation of a mixture of CO and formate in DMF/TEOA solution (4:1, v/v) with BNAH as an electron donor. This observation was independently confirmed in two reports of Kubiak and co-workers,^{33,34} in which Mn(bpy)(CO)₃Br and Mn(bpy)(CO)₃CN (**Figure 1.7**) were assessed for CO₂RR in the same photocatalytic conditions. The selectivity towards CO or formate in the photosensitized system with Mn(bpy)(CO)₃CN was shown to be dependent on the nature of the solvent, with formate production favored in DMF and CO production in MeCN. In DMF it could reach TON of 130 for formate after 15h, whereas the TONs for CO were only of 8. Moreover, it must be noted that Mn(bpy) catalysts tend to dimerize irreversibly under catalytic condition leading to an inactive form of the catalyst.

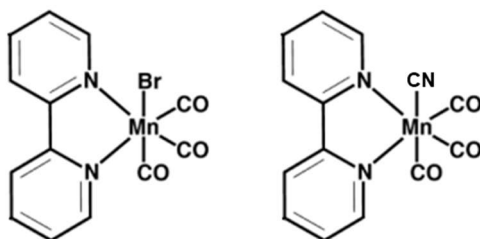


Figure 1.7: Manganese pyridyl complexes used for catalytic CO₂ reduction.

Nickel complexes.

Craig *et al.*³⁵ firstly reported the photocatalytic activity of [Ni(cyclam)]²⁺ for CO₂RR (**Figure 1.8 a**). CO was obtained as the major product (TON = 4.8) in aqueous solution with [Ru(bpy)₃]²⁺ as photosensitizer. Besides, when [Ni(cyclen)]²⁺ (which showed a structure similar to that of [Ni(cyclam)]²⁺ (**Figure 1.8 b**)) was used as the catalyst, CO₂ was reduced to both CO and HCOOH in aqueous solution.³⁶

The photocatalytic activities of various macrocyclic Ni-based dimeric complexes for CO₂RR were also studied.³⁷ When [Ni₂(6,6'-Bi(Me₂-cyclam))] ⁴⁺ (**Figure 1.8 c**) was used as a catalyst, the production of CO was 6.8 times higher than that of the corresponding mono-macrocyclic Ni complex. Later on, Chang *et al.* reported a series of Ni^{II} complexes based on distorted square-planar tetradentate ligands (**Figure 1.8 d**).³⁸ The catalyst could selectively reduce CO₂ to CO when irradiated in the presence of [Ir(ppy)₃]⁺ and afforded a TON as high as 98 000 within 7 h. Nonetheless, this TON was reached with a concentration of catalyst equal to 2 nM, which might be too low to have a proper quantification. With a more conventional concentration (0.2 μM), the TON at 7h for CO was equal to 1500.

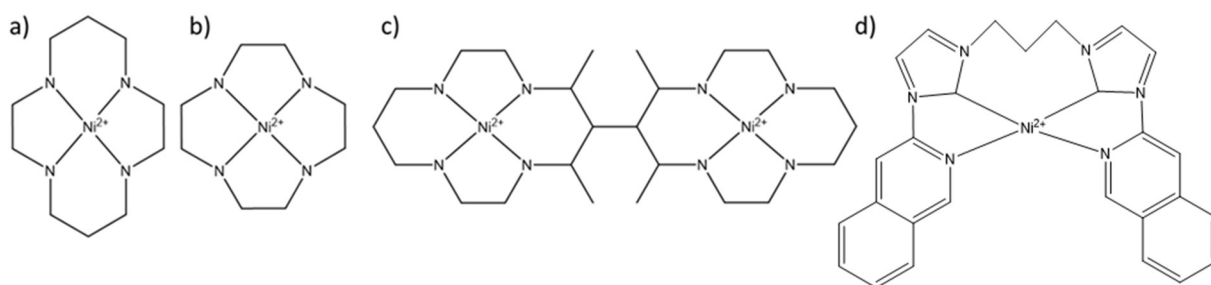


Figure 1.8: Nickel macrocyclic complexes for CO₂RR.

We presented a variety of molecular catalysts. As shown, the presence of organic linker allows an easy modification of the catalyst to improve its properties. Nonetheless, these complexes, in homogeneous conditions, tend to be rather fragile. Another kind of molecular catalyst that are worth of interest is polyoxometalates. Even though only few POMs have been reported for CO₂ reduction they display properties that can support molecular catalysts during CO₂ reduction processes, such as electron and proton relay properties.³⁹

1.2 Polyoxometalates, fully inorganic molecular catalysts

Polyoxometalates (POMs) are anionic molecular metal oxides of the early transition metals, which have been recognized for their remarkable redox activity and their ability to undergo reversible multi-electronic reduction processes. They have accordingly found numerous applications in electrocatalysis, energy storage, and photochemical processes, assorted with a wide variety of structures, as described in more detail below. POMs have been discovered in 1826 by Berzelius,⁴⁰ but structurally characterized only a century later by Keggin, in 1933.⁴¹

1.2.1 Polyoxometalate structures

POMs are constituted of MO_x polyhedra, mainly octahedra ($x = 6$), but polyhedra with $x = 4$ or 5 are also encountered, with M being mainly W(VI/V), Mo(VI/V) and V(V/IV). The polyhedra are linked by their vertices, edges or faces with bridging oxygen atoms noted (μ -O) for vertices, (μ -O)₂ for edges and (μ -O)₃ for faces (**Figure 1.9**). Polyoxometalates are exclusively anionic species, their charge is compensated either by protons for their acidic form, or by alkaline cations. These counterions can be exchanged by organic counter cations, for example tetrabutylammonium (TBA) in order to increase the POM's solubility in organic solvents,⁴² or to form ionic liquids.⁴³

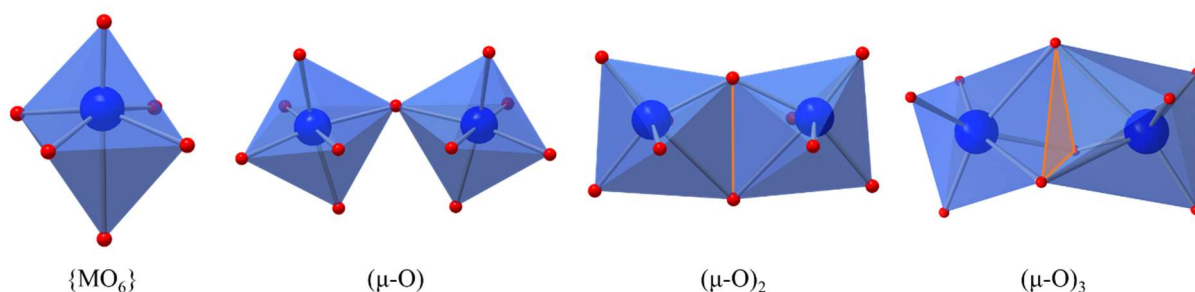


Figure 1.9: Polyoxometalates building bricks and connectivity by their vertices (μ -O), edges (μ -O)₂ or faces (μ -O)₃.

POMs can include heteroatoms from group *p*- or *d*-, such as phosphorus, silicon, boron for the *p*-group or cobalt for the *d*-group. This divides the POMs in two categories, isopolyoxometalates, on the one hand, with the general formula $[M_xO_y]^{n-}$, without heteroatoms at their center and, heteropolyoxometalates, on the other hand, with the general formula $[X_xM_yO_z]^{n-}$ with X being a heteroatom. The most studied POMs are represented in **Figure 1.10**: for the isopolyoxometalate family, the Lindqvist $[M_6O_{19}]^{n-}$, the decavanadate $[V_{10}O_{28}]^{6-}$ and the paratungstate $[H_2W_{12}O_{42}]^{10-}$ and for the heteropolyoxometalate family, the Keggin $[XM_{12}O_{40}]^{n-}$ and the Dawson $[X_2M_{18}O_{62}]^{n-}$.

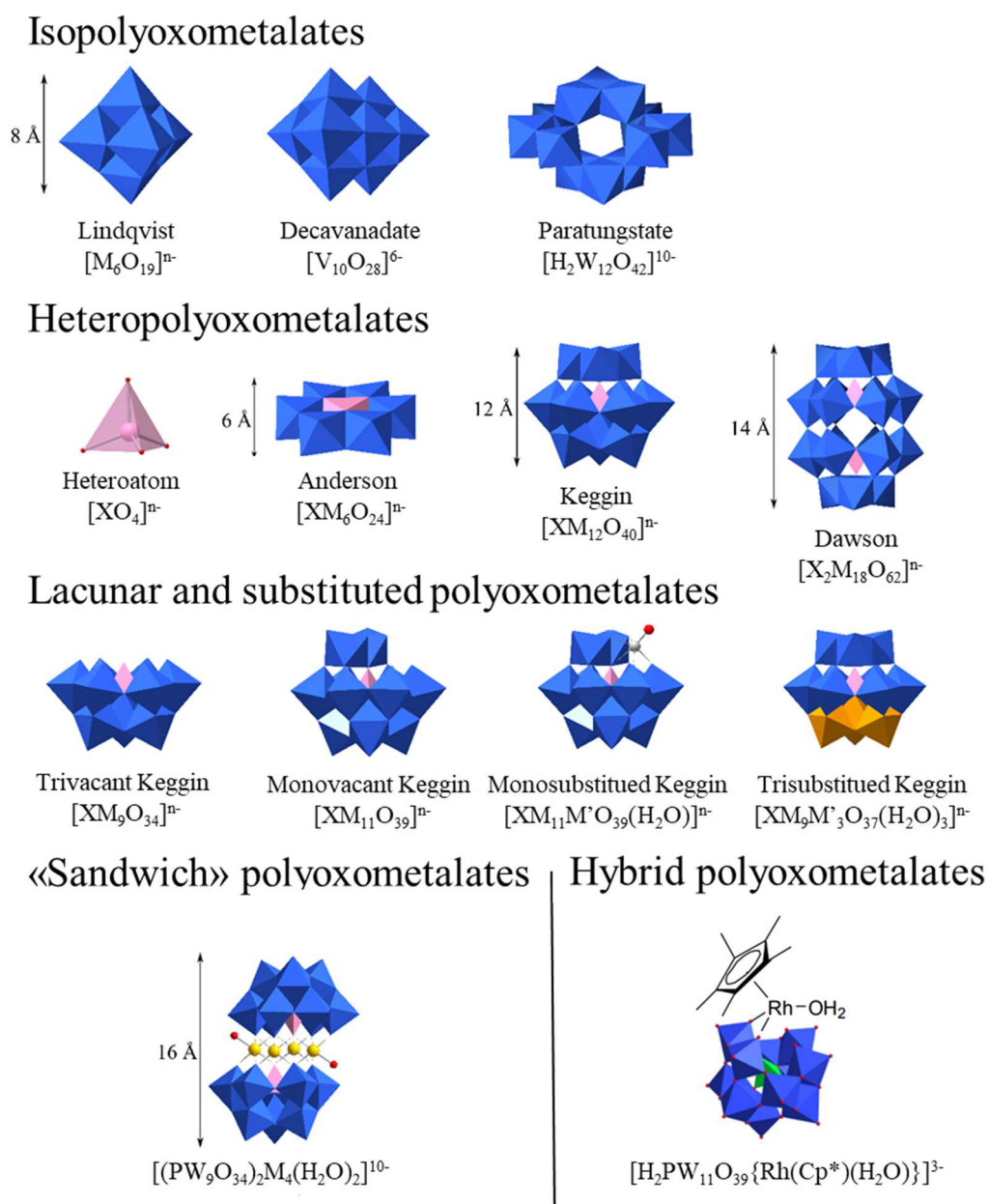


Figure 1.10: Structures and general formula of different types of polyoxometalates.

The structure of the Keggin POM XM_{12} is built from the assembly of four trimetallic subunits M_3O_{13} around a XO_4 tetrahedron. Each trimetallic subunit consists of three MO_6 octahedra connected by their edges. In the center, a $\mu_3\text{-O}$ atom connects the trimetallic group to the central heteroatom. The trimetallic subunits are connected to each other via vertices or edges.⁴⁴ Thus, four types of oxygen atoms are present in Keggin-type POMs: terminal $\text{M}=\text{O}$ oxygen atoms, bonding oxygen atoms $\mu\text{-O}$ between two MO_6 octahedra of a same trimetallic subunit, bonding oxygen atoms $\mu\text{-O}$ between different trimetallic subunits, and oxygen atoms connected to the central heteroatom. Keggin anions have five isomers, α , β , γ , δ , ϵ depending on how many trimetallic M_3O_{13} units are rotated (**Figure 1.11**). The most stable isomers (for M in oxidation state VI) are α and β .

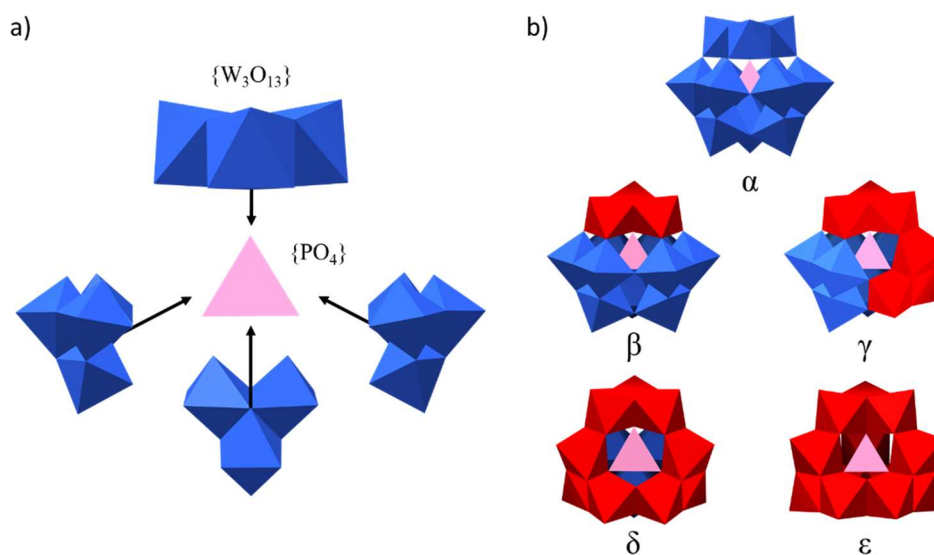


Figure 1.11: a) Detailed representation of $[\alpha\text{-PW}_{12}\text{O}_{40}]^{3-}$; b) Keggin POM 5 isomers, red trimetallic subunits have been rotated by 60° .

Several other structures of POMs derived from the Keggin structure can be synthesized by selective hydrolysis of one or more metal centers from a saturated species XM_{12} . These species are then called lacunary or vacant. They are obtained in a controlled manner in basic conditions. Their stability domains have been studied by ^{183}W NMR. Mono-vacant $[\text{XM}_{11}\text{O}_{39}]^{n-}$, di-vacant $[\text{XM}_{10}\text{O}_{36}]^{n-}$ or tri-vacant $[\text{XM}_9\text{O}_{34}]^{n-}$ derivatives can thus be formed.⁴⁵ Keggin-type POMs are thus highly sensitive to pH. Indeed, as mentioned above, a pH increase can lead to metal hydrolysis and formation of lacunary compounds. Dawson type POMs can be seen as two tri-vacant Keggin XM_9 linked together by their terminal oxygen atoms, leading to the formation of a $\text{X}_2\text{M}_{18}\text{O}_{62}$ polyoxometalate. Furthermore, the reaction of those lacunary Keggin ions with

transition metals M' can lead to the formation of substituted Keggin, as seen in **Figure 1.10** with $[\text{SiW}_9\text{Co}_3(\text{H}_2\text{O})_3\text{O}_{37}]^{10-}$ and $[\text{XW}_{11}M'\text{O}_{39}(\text{H}_2\text{O})]^{n-}$ ($M' = \text{Ti, Fe, Co, Cu, Zn}$). The sandwich-type POMs $[(\text{XW}_9\text{O}_{34})_2M'_4(\text{H}_2\text{O})_2]^{n-}$ ($M' = \text{Co, Ni}$) are formed by the reaction of two tri-vacant Keggin POMs XW_9 with transition metal ions⁴⁶ and Anderson POMs are constituted of a ring of six MO_6 octahedra connected by edges around a central XO_6 octahedron. Another way to achieve new POM structures is to functionalize POMs with organic molecules. This can be done either by direct synthesis or by post functionalization. The addition of organic or organometallic moieties can add new properties to POMs. For example, the addition of $[(\text{cyclopentadiene})\text{Rh}(\text{H}_2\text{O})]^+$ to a $[\text{PW}_{11}\text{O}_{39}]^{7-}$ POM leads to the $[\text{H}_2\text{PW}_{11}\text{O}_{39}(\text{cyclopentadiene})\text{Rh}(\text{H}_2\text{O})]^{3-}$ complex which is active for CO_2RR , nonetheless favoring H_2 production when compared to the parent rhodium bipyridine complex.⁴⁷

1.2.2 Polyoxometalates in catalysis

Polyoxometalates have shown applications in various fields including biology,^{48,49} magnetism, energy^{50,51} and mostly catalysis.^{50,52–54} POMs are constituted of a wide range of metals in high oxidation states. They can be reduced several times and used as an electron and proton reservoirs.^{39,55} This reduction process is reversible for most POMs, and can be beneficial for redox reactions. This is the case for “sandwich” type POMs which have been used for several catalytic reactions such as water oxidation or reduction.^{56,57}

In 2008, Sartorel *et al.*⁵⁸ reported the synthesis of a ruthenium sandwich POM $[\text{Ru}_4(\mu\text{-O})_4(\mu\text{-OH})_2(\text{H}_2\text{O})_4(\gamma\text{-SiW}_{10}\text{O}_{36})_2]^{10-}$ (Ru_4). Ru_4 , in water, with $(\text{NH}_4)_2\text{Ce}(\text{NO}_3)_6$ as sacrificial agent, is able to oxidize H_2O in O_2 with an impressive TON of 488 and TOF of 450 h^{-1} . At the same moment, the same POM with different counterions was reported by Hill and co-workers⁵⁹ for the same reaction. In their conditions, without sacrificial cerium acceptor the TONs were of 18.

However, as mentioned previously, in regard of noble metal prices, building noble-metal-free catalysts is a necessity. In 2011, Hill and co-workers⁶⁰ reported the synthesis of a cobalt sandwich POM $[\text{Co}_4(\text{H}_2\text{O})_2(\text{PW}_9\text{O}_{34})_2]^{10-}$ (Co_4) able to oxidize H_2O into O_2 with $[\text{Ru}(\text{bpy})_3]\text{Cl}_2$ as a photosensitizer under visible light irradiation. At this time, the catalyst's stability was not studied and the longest reported time for catalysis was only 15 min. Nonetheless, the catalyst reaches impressive TOF $> 1000 \text{ h}^{-1}$.

Concerning reduction reactions, the same group reported proton reduction with two related POMs $[\text{Mn}_4(\text{H}_2\text{O})_2(\text{VW}_9\text{O}_{34})_2]^{10-}$ (Mn_4) and $[\text{Ni}_4(\text{H}_2\text{O})_2(\text{PW}_9\text{O}_{34})_2]^{10-}$ (Ni_4). The two system

have shown an impressive stability with photoreduction of protons for a week without substantial activity loss. Concerning their activity, Mn_4 has shown poor efficiency with TONs of 41 after 7 days, in contrary Ni_4 could efficiently reduce H^+ with TONs of 6500 after the same period.^{61,62} Other nickel-based POMs have also been reported for the same reaction, the dimeric nickel POM $[\text{Ni}_3(\text{OH})_3(\text{H}_2\text{O})_3\text{P}_2\text{W}_{16}\text{O}_{59}]^{9-}$ described by Guo *et al.*⁶³ and the $[\{\text{Ni}_4(\text{OH})_3\text{AsO}_4\}_4(\text{B}-\alpha\text{-PW}_9\text{O}_{34})_4]^{28-}$ tetrameric one (Ni_{16}) described by Lv *et al.*⁶⁴ The latter POM is able to reduce protons in a $\text{CH}_3\text{CN}:\text{DMF}$ mixture, with TEA as an electron donor and with an iridium photosensitizer, with a TON of 580 after 5h (**Figure 1.12**).

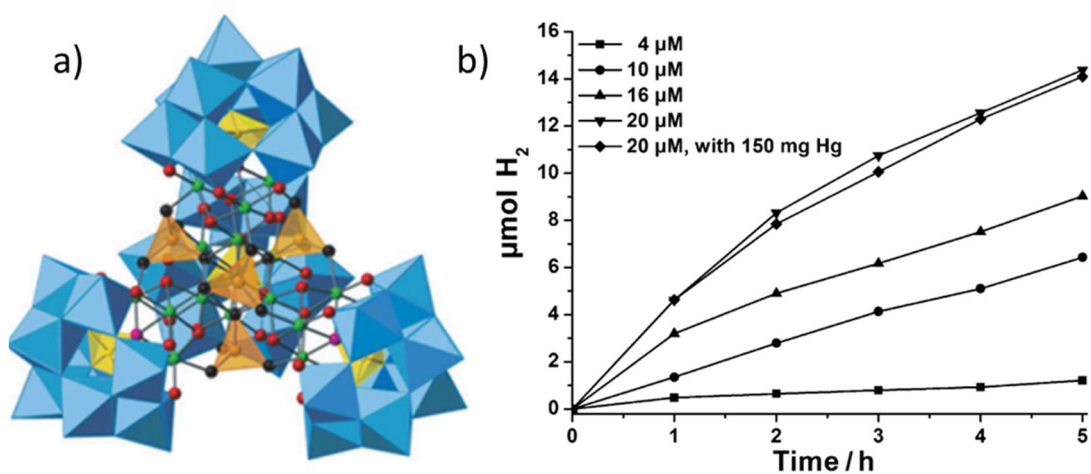


Figure 1.12: a) Ni_{16} POM, WO_6 light blue octahedra, AsO_4 orange tetrahedra, PO_4 yellow tetrahedra, Ni green balls, O red balls and b) Photochemical H_2 evolution at different catalyst concentrations under otherwise identical conditions: LED light (20 mW, 455 nm), $[\text{Ir}(\text{ppy})_2(\text{dtbbpy})]^+$ (0.2 mM), TEOA (0.25 M), H_2O (1.4 mM), catalyst (20 μM or 320 μM as noted), $\text{CH}_3\text{CN}/\text{DMF}$ (1:3 v/v, 2 mL) degassed with Ar.⁶⁴

To our knowledge, the number of reports about POMs for CO_2 reduction is very limited.^{52,54} This can probably be explained by the unfavorable electrostatic interaction between CO_2 and POMs⁶⁵ and because POM redox potentials are too low to reduce CO_2 .⁶⁶ Szczepankiewicz *et al.* proposed in 1998 the use of Keggin POM functionalized with transition metals coordinated to a water molecule, as this water molecule could easily be replaced by CO_2 .⁶⁷ Nonetheless, a decade before Szczepankiewicz suggestion, Yamase *et al.* have reported the eight electrons CO_2 photoreduction to CH_4 with a disubstituted Keggin POM $[\text{PW}_{10}\text{Ti}_2\text{O}_{40}]^{7-}$ showing that even with unfavorable interactions between POM and CO_2 , the reduction might still be possible.

As most of the POM are not active for CO_2 reduction, the grafting of catalytic organometallic complexes able to reduce CO_2 has been considered. This has been reported previously by

Ettehadgui *et al.*⁶⁸ who grafted a rhenium-based catalyst $[\text{Re}(\text{L})\text{CO}_3(\text{MeCN})]^+$ with L being a sodium 15-crown-5 crown ether covalently linked to a Keggin POM (**Figure 1.13 a**). The hybrid POM is able to reduce CO_2 to CO under UV light. DFT investigations of the role of each component of this system was reported a few years later in a computational chemistry paper. Cie *et al.*⁶ proposed that the rhenium metal center is the catalytic site, whereas the Keggin POM is the photosensitizer (with UV light) and acts as an electron and proton donor (**Figure 1.13 b**). More recently, Proust and co-workers⁴⁷ studied the grafting of a rhodium-based catalyst $[\text{Rh}(\text{Cp}^*)]^{2+}$ on a $[\alpha\text{-H}_2\text{PW}_{11}\text{O}_{39}]^{5-}$ POM. They reported the electroreduction of CO_2 to formate and of protons to H_2 . Compared to $[\text{Rh}(\text{Cp}^*)(\text{bpy})\text{Cl}]\text{Cl}$, the hybrid POM favored the reduction of protons.

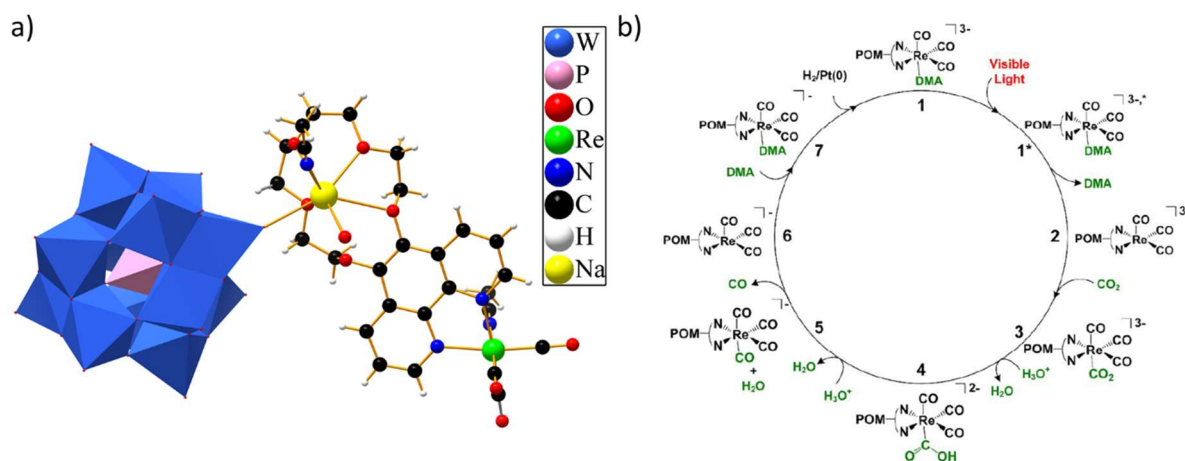


Figure 1.13: a) Hybrid POM $[\text{Re}^{\text{I}}(\text{L})-(\text{CO})_3(\text{MeCN})][\text{MHPW}_{12}]^{68}$ and b) Proposed mechanism for CO_2 photoreduction with the hybrid POM.⁶

We have seen in this subsection a wide variety of catalysts, going from organometallic complexes to functionalized polyanions. These catalysts often show a good selectivity and efficiency for CO_2 reduction but also often lack stability. Supporting these catalysts on a solid could improve their performances, especially with respect to stability. Metal-organic frameworks represent an immobilization platform of choice. Also, with their chemical versatility, they can provide what molecular catalysts are lacking. For example, by considering a photosensitive MOF, one can avoid using an external photosensitizer which is often noble metal-based. Besides, their high porosity allows different encapsulation procedures. We will in the next subsection describe the most used MOFs for catalysts and POM encapsulation before focusing on Zr-based MOF more specially used over the period of my PhD research work

2. Metal-Organic Frameworks

Metal-organic frameworks, also called porous coordination networks (PCN), are crystalline and porous solids. MOFs are hybrid materials composed of organic linkers coordinated to metal ions or metal oxoclusters. The diversity of possible metal precursors and organic linkers leads to a huge variety of MOFs in terms of structure and chemical composition. Moreover, the same {metal ion, organic linker} combination can give several different metal-organic frameworks, making their phase diagram particularly complex and sensitive to synthetic conditions.⁶⁹ In order to differentiate these unique structures, they are labeled with a prefix (usually MOF, PCN or the university where the MOF has been discovered) and a number. Nonetheless, the same structure can sometimes be discovered by two different teams at the same moment resulting in two different names for the same MOF. To date, more than a hundred thousand MOFs have been synthesized and more than half a million predicted.⁷⁰

MOFs present several advantages such as thermal and chemical stability, high surface area and the possibility to accommodate the molecular catalytic guest into their cavities, with, however, some variations from one MOF to the other. Looking at a recent review we published,⁷¹ it can be concluded that the Cr-based MIL-101 MOF has been by far the most studied one for molecular catalyst's immobilization. We can propose several reasons: MOF-101 can be synthesized in water with high yields, and its Cr-based version is very stable while possessing large cavities and windows capable of accommodating a large range of bulky species (see below). However, its main drawback is that it contains chromium ions which are considered as one of the most toxic heavy metal ions. MIL-100(Fe) and NH₂-MIL-101(Al) have thus also been largely investigated as alternative platforms. Zr-based MOFs also appear more eco-friendly and among them, UiO-66 and UiO-67 are the most commonly used but the porphyrinic Zr-based MOF-545 has also been encountered. Finally, among the other MOFs, HKUST-1 and ZIF-8, copper- and zinc-based MOF respectively, seem to be the most popular. A representation of the main MOF hosts with their formulas and the dimensions of their cavities is given in **Figure 1.14** and a short description of their structure as well as their stability is given below. Both the structure and stability of the MOF are obviously important parameters to take into account when choosing a MOF as a platform to immobilize a catalytic species.

Acronym	Metal (M)	Linker (L)	Empirical Formula	Structure
MIL-101	Cr ^{III}		$M_3OL_3(H_2O)_2X$ M = Cr, Al X = F, Cl, NO ₃ , CH ₃ COO ⁻ , C ₆ F ₅ COO ⁻	29 Å 34 Å
NH ₂ -MIL-101	Al ^{III} Cr ^{III}			
MIL-100	Fe ^{III} Al ^{III} Cr ^{III}		$M_3OL_2(H_2O)_3X$ M = Cr, Al, Fe X = F, Cl, SO ₄	25 Å 29 Å
HKUST-1	Cu ^{II}		Cu_3L_2	13 Å
ZIF-8	Zn ^{II}		ZnL_2	12 Å

Figure 1.14: Schematic representation of the structures of the main MOF guests with the dimensions of their cavities, the formula of the linker and of the MOFs.

2.1 MOF structural description

In this subsection, we will introduce the main metal-organic frameworks used as immobilization platforms for catalysts. Then we will emphasize on zirconium-based MOFs, which are the main focus of this PhD thesis.

HKUST-1, also called Cu-BTC, is one of the oldest MOF, first synthesized in 1999 by Chui *et al.*⁷² HKUST-1 is composed of dimeric cupric tetra-carboxylate units. Each copper dimer is linked to four different benzenetricarboxylate through 8 oxygen, Cu ions complete its coordination with aqua ligands. Each BTC linker is connected to three Cu dimers leading to a paddle-wheeled framework. Cu-BTC has 18.6 Å diameter hexagonal cages and 13 Å diameter square pore windows.⁷² This MOF exhibits a relatively low surface area of 690 m²·g⁻¹. Cu-BTC is known to be unstable to water and steam leading to a partial transformation after a short period of time but is stable to air and oxidative conditions (5% H₂O₂) for a few days.⁷³

ZIF-8⁷⁴ is a zeolitic imidazolate framework where two zinc tetrahedra are bridged with an imidazole forming a sodalite-type network. ZIF-8 has a unique pore type of 12 Å diameter and

a window made of six zinc clusters with an aperture diameter of 3.4 Å. The empty ZIF-8 BET surface area is equal to 1630 m²·g⁻¹. ZIF-8 has been claimed to be highly stable to air, water, steam showing no degradation over a few days in those conditions. It can withstand acid and basic condition (from ~ pH 4 to pH 12) for several days and oxidative conditions for the same duration.⁷³

MIL-101(M) (M = Cr^{III}, Fe^{III}, Al^{III})⁷⁵ is built on M^{III} octahedra trimers connected with benzenedicarboxylate (BDC) linkers giving the general formula M₃O(BDC)₃(H₂O)₂X (X = F, Cl, NO₃, CH₃COO⁻, C₆F₅COO⁻).⁷⁶ The structure displays two types of mesoporous cages, the first one with a free diameter of 29 Å and pentagonal windows of 12 Å, and the second and larger cage with a free diameter of 34 Å and both pentagonal windows of 14x14 Å and hexagonal windows of 16x16 Å².⁷⁵ MIL-101(M) displays a gigantic cell volume of 702 000 Å³ and a huge BET surface area of around 4500 m²·g⁻¹ allowing the hosting of large molecules. Moreover, MIL-101(M) is easily functionalized via post synthetic modification or via direct pre-synthetic modification of the BDC linker (adding NH₂, NO₂, SO₃ or other functions)⁷⁷ which allows great control and uniformity of the MOF. MIL-101(M) stability is highly linked to the nature of the metal and the BDC functionalization. MIL-101(Cr) is highly stable to water (as solvent, moisture or even steam) and can last several days in boiling water without any structural degradation. The MIL-101 Fe and Al homologues show much lower stability toward hydrolysis, with for example NH₂-MIL-101(Al) transforming into the more thermodynamically stable NH₂-MIL-53(Al) after only 5 min exposure to water.⁷⁸ MIL-101(Cr) is stable to both acidic and basic conditions for several weeks, and stable to oxidative conditions (5% H₂O₂) for a few days. Again, Al and Fe homologues show poor stability toward acidic or basic condition with partial transformation into MIL-53 and high loss of porosity.⁷⁹

MIL-100⁸⁰ is built on metal octahedra trimers connected by their summit and interconnected by BTC linkers giving the general formula M₃O(BTC)₂(H₂O)₂X (X = F, Cl, SO₄).⁸¹ Four metal trimers are linked together by BTC forming a supertetrahedron (ST), the STs being linked to each other by BTC forming a pentagonal mesoporous cage (20 STs) or a hexagonal mesoporous cage (28 STs). The smallest cage has a diameter of 25 Å and pentagonal windows of 4.8x5.8 Å. The largest cage displays a diameter of 29 Å and has hexagonal windows with an aperture of 8.6x8.6 Å². Those two cages lead to a huge surface area of 3100 m²·g⁻¹. MIL-100 MOFs display high water stability and no degradation after 24h at 323K⁸² and are stable in most solvents. However, again, the thermal stability is highly linked to the nature of the metal node, being stable up to 270, 325 and 370°C for MIL-100(Fe), MIL-100(Cr) and MIL-100(Al)

respectively.⁸³ MIL-100 MOFs are mainly stable in acidic pH and start degrading at pH 7 as shown for MIL-100(Fe) by Bezverkhyy *et al.*⁸⁴

2.2 Zirconium-based MOF

Zirconium-based MOFs are made of zirconium oxoclusters. The zirconium building bricks can either be consisted of 6 or 8 Zr(IV) ions.⁸⁵ The MOFs studied in this PhD thesis are solely composed of Zr_6 oxoclusters with formula $Zr_6O_4(OH)_4$. The Zr_6 cluster can be coordinated to either 6, 8 or 12 ligands, being fully coordinated with 12 ligands (**Figure 1.15**). When the Zr_6 cluster is unsaturated (coordination less than 12), the free sites are occupied by OH or H_2O groups. In this thesis, we will focus on two MOFs, namely UiO-67 (12 coordinated Zr_6) and MOF-545 (8 coordinated Zr_6). We will thus describe the UiO MOF family and the Zr_6 -porphyrin MOF family in more detail.

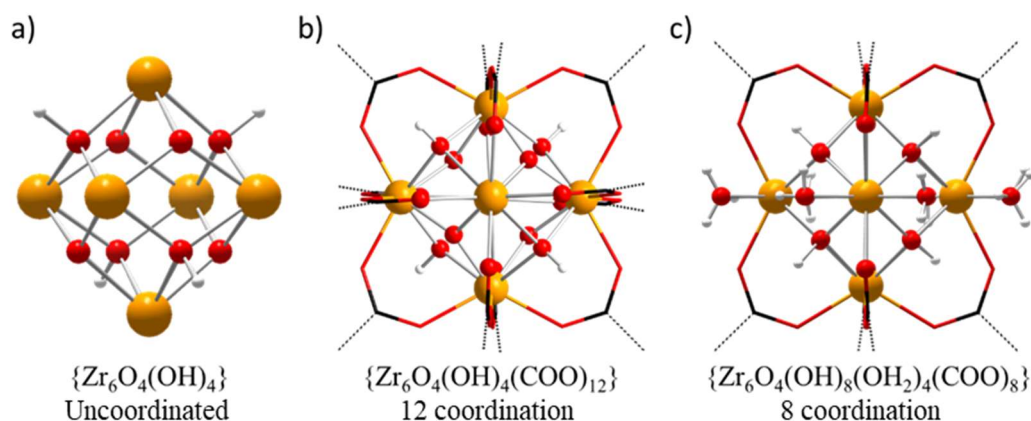


Figure 1.15: a) Zr_6 building brick; b) 12 coordinated Zr_6 oxocluster and c) 8 coordinated Zr_6 oxocluster.

UiO isorecticular series of MOF includes UiO-67, UiO-68 and UiO-69, these MOFs are differentiated by the number of benzene ring of their linkers going from one for UiO-66 to four for UiO-69. UiO-66 with the formula $Zr_6O_4(OH)_4(BDC)_6$ is one of the most studied Zr-based MOF. First synthesized in 2008,⁸⁶ it consists of Zr_6 clusters linked together with BDC linkers forming octahedral mesoporous cages with a diameter of 11 Å and tetrahedral cages of 8 Å diameter. The accessible space inside the framework amounts to 1200 m²·g⁻¹. As with MIL-101, the functionalization of the BDC ligand leads to a variety of UiO-66 derivatives. The high connectivity (12 linkers per Zr_6 unit) allows maintaining high crystallinity even with up to 25%

linker defect.⁸⁷ UiO-66 is stable to water and organic solvents for several weeks and can withstand long exposure to acidic or basic pH ranging from 4 to 12. It also does not show any XRD change after several weeks in oxidative conditions (5% H₂O₂) but lacks stability toward air and moisture, leading to its partial destruction after only 3 days.⁷³ Stability tests on UiO-66-NH₂ have shown that using functionalized linkers not only doesn't reduce its stability to water but increase its stability to air.

UiO-67⁸⁶ with the formula Zr₆O₄(OH)₄(bpdc)₂ is an analogue to UiO-66, replacing the BDC linker with 4,4'-biphenyldicarboxylic acid (bpdc), and thus increasing the distances between each Zr₆ node, the pore sizes and the pore windows (**Figure 1.16**). UiO-67 is composed of octahedral cages of 18 Å of diameter and tetrahedral cages of 11.5 Å⁸⁸ diameter and displays a 3000 m²·g⁻¹ BET surface area.⁸⁶ UiO-67 is less stable than UiO-66: it exhibits a total loss of porosity after 3 days in air/moisture, partial loss of porosity at pH 4 and 12 after 3 days, loss of crystallinity at pH 4 after several weeks, and a total destruction after 3 days in 5% H₂O₂.⁷³ The lack of stability to water has been attributed to the linker hydrolysis.

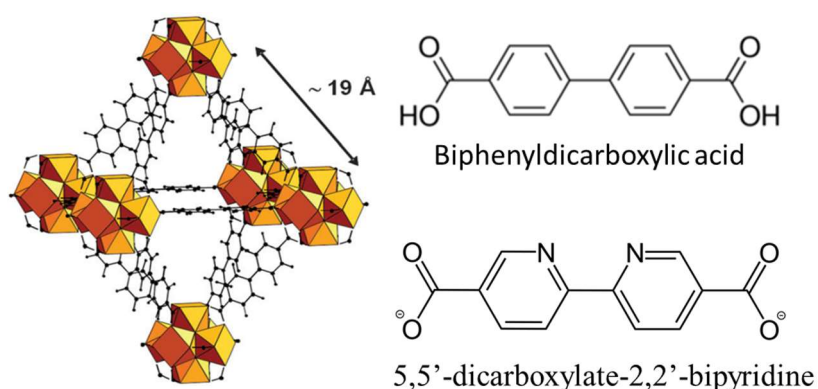
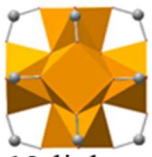
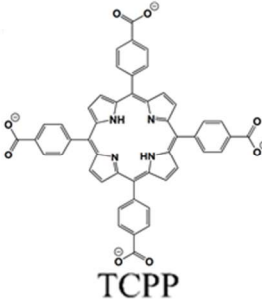
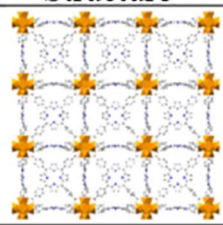

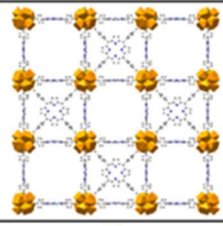
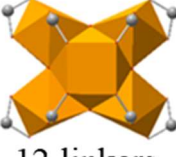
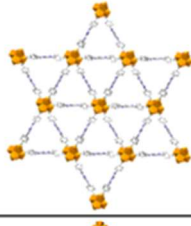

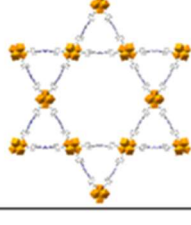

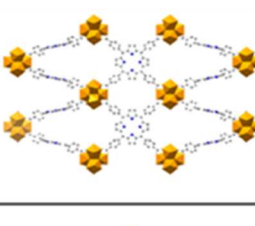

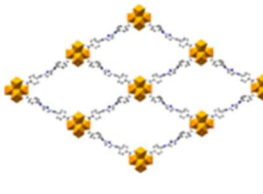


Figure 1.16: Structure of the UiO-67.

UiO-67 allows the grafting of several catalysts seen in the first subsection. Indeed, UiO-67 can be built with biphenyldicarboxylate linkers partially substituted with bipyridinedicarboxylate ones, thus allowing the covalent binding of pyridyl and polypyridyl-type catalysts. The main drawbacks for this MOF are its relative water sensitivity but also its non-photosensitive linkers, thus requiring the addition of an external PS, often noble-metal based, for photocatalytic purposes. Immobilizing catalysts inside a photosensitive MOF could thus avoid the use of external PS and allow the design of three-in-one noble-metal-free platforms: catalytic, porous and photosensitive. This strategy was been adopted by a former PhD student of our group, Grégoire Paille,⁸⁹ whereby he immobilized Co₄ sandwiches POMs in MOF-545, a Zr₆ porphyrin

MOF for the purpose of water oxidation. We will now describe the Zr_6 porphyrin MOF family (Figure 1.17).

Name	Metallic Node	Linker	Structure
MOF-525 PCN-221	 12 linkers	 TCPP	
PCN-224	 6 linkers		
PCN-223	 12 linkers		
MOF-545 PCN-222 MMPF-6	 8 linkers		
PCN-225	 8 linkers		
NU-902	 8 linkers		

TCPP = Tetrakis(4-carboxyphenyl)porphyrin

Figure 1.17: Structures of Zr_6 -TCPP MOFs.

The rotational freedom of the porphyrin carboxylate groups allows the formation of six different Zr₆-TCPP MOFs: MOF-525,^{90,91} PCN-224,⁹² PCN-223,⁹³ MOF-545,^{90,94,95} PCN-225⁹⁶ and NU-902.⁹⁷ MOF-525 and PCN-224 exhibit cubic phases, with PCN-224 being the Zr-unsaturated version of MOF-525 (one out of two TCPP missing). The coordination of only 6 ligands to the Zr-oxoclusters in PCN-224 leads to the formation of big channels. This is also the case for PCN-223 and MOF-545, with MOF-545 being the Zr-unsaturated version of PCN-223. Both MOFs crystallize in hexagonal phases, with PCN-223 having only one channel size. In contrast MOF-545 has two types of channels, a small triangular one and a bigger hexagonal one of 12 and 36 Å respectively. PCN-225 and NU-902 have both been less studied than these MOFs.

Controlling accurately the synthesis media is thus extremely important, as any of these six MOFs can be synthesized with the same reactants. In this thesis, we will focus on MOF-545, of formula Zr₆O₈(H₂O)₈(TCPP)₂.⁹⁸ Each TCPP linker is bound to four distinct Zr₆ subunits on two different layers, creating two long porous tunnels, one triangular of 12 Å diameter and a bigger hexagonal one of 36 Å diameter with a total BET surface area of 2200 m².g⁻¹. The huge tunnel size allows easy post-synthetic impregnation of various bulky molecules or species. Moreover, the photosensitivity of TCPP and its easy metalation render the composite promising for catalytic reactions such as CO₂ photoreduction or water splitting.^{99,100} MOF-545 is stable in organic solvents as well as in water even in strong acidic conditions (concentrated HCl solution), but decomposes at pH above 10.¹⁰¹

MOF-545 with its gigantic pore of 3.6 nm diameter, and UiO-67 with its biphenyldicarboxylate linkers that can be substituted for bipyridinedicarboxylate ones, are both ideal candidates for catalyst immobilization. Moreover, as formerly detailed, the photosensitive and catalytic nature of porphyrins is ideal for building noble metal-free catalysts. In the following subsection, we will discuss the immobilization protocols, their advantages and limitations.

3. Encapsulation strategies

The synthesis of the Cat@MOF composites (Cat being a molecular catalyst immobilized in the MOF) can be performed using various strategies according to i) the chemical nature of the catalyst, ii) its size compared to that of the pores or windows and iii) its stability (**Figure 1.18**). It can be deduced from a recent review we published on catalyst encapsulation in MOFs⁷¹ that PW_{12} represents around 35 % of the POMs immobilized in MOFs, for the possible following reasons: i) it is a well-known catalyst for several catalytic reactions,¹⁰² ii) it is stable in the conditions used for the most common MOFs synthesis and also in impregnation conditions, iii) its charge and size are among the smallest for a POM which allows to obtain a high POM loading, allowing minimal linkers defects for charge compensation, iv) it is commercially available at low cost and v) it possesses characteristic IR and ^{31}P NMR signatures useful to check the stability of the POM after immobilization, before and after catalysis.

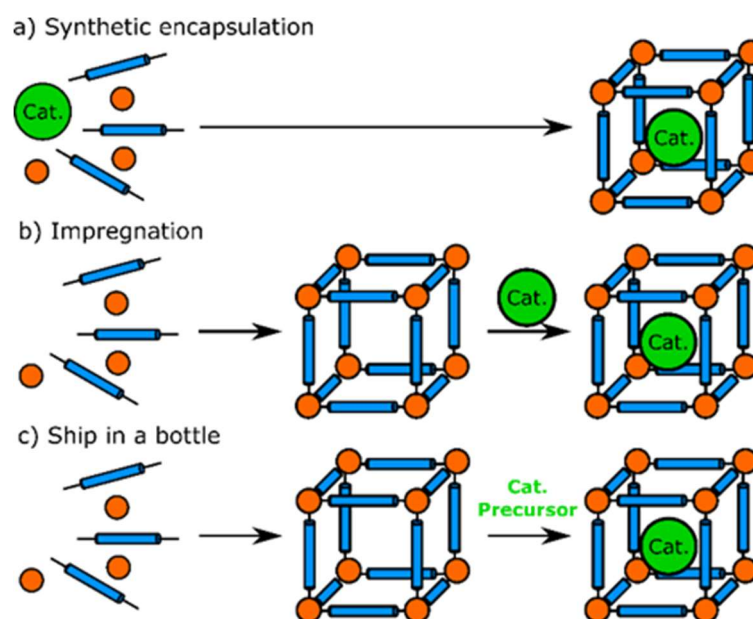


Figure 1.18: Schematic representation of the various synthetic pathways used for the synthesis of pore-functionalized Cat@MOFs.

3.1 Synthetic encapsulation

Molecular catalysts can be encapsulated within the cavities of MOFs by direct synthesis also called “bottle-around-the-ship” or “synthetic encapsulation” method. The catalysts are added as reactants during the MOF synthesis. This method thus requires that the catalysts are soluble and stable in the conditions of the MOF’s synthesis. For example, hydrothermal conditions, with temperatures of 180°C (during 72 h) or 220°C (during 8h) are usually described for the synthesis of MIL-101(Cr) composites. Note that microwave conditions have also been reported for the synthesis of $\text{PW}_{12}@\text{MIL-101}(\text{Cr})$,¹⁰³ $\text{PW}_{11}\text{Zn}@\text{NH}_2\text{-MIL-101}(\text{Al})$ ¹⁰⁴ and $\text{PW}_{12}@\text{NH}_2\text{-MIL-53}(\text{Al})$ ¹⁰⁵ composites. Zr-based MOFs composites are usually synthesized under solvothermal conditions in DMF at 120°C for 6 to 24 h while HKUST derivatives are isolated by heating the reactants in water at 180°C for 6 to 72 h or in mixed $\text{H}_2\text{O}/\text{EtOH}$ solvents, at lower temperatures (even at RT). An original method which attracts a growing interest, the mechanochemical synthesis,^{106,107} has been described for $\text{PMo}_{10}\text{V}_2@\text{HKUST-1}$,¹⁰⁸ $\text{PW}_{12}@\text{HKUST-1}$,¹⁰⁹ $\text{XM}_{12}@\text{ZIF-8}$ ($\text{X} = \text{P}$, $\text{M} = \text{W}$, Mo ; $\text{X} = \text{Si}$, $\text{M} = \text{W}$)¹¹⁰ and $\text{PMo}_{12-x}\text{V}_x@rho\text{-ZIF}$ ($x = 0\text{-}3$).¹¹¹ This method which consists in grinding the solid precursors in an agate mortar or using a ball-milling grinder, is very fast and easy, does not consume any solvent and does not require any heating.

The synthetic encapsulation method is mostly applied to Cats having dimensions greater than the sizes of the MOF windows. In this case, the advantage is that catalyst leaching is then impossible. The major drawback is that the pores can be blocked and that the diffusion of reactants through the framework can thus be hindered.

3.2 Impregnation

Some catalysts are not stable in the conditions used for the MOF synthesis (acidic medium, high temperature, etc.) and thus can only be immobilized by impregnation, provided they are small enough to diffuse through the MOF windows. In this milder synthetic method, the catalyst is dissolved in a solvent in which it is stable, usually water or CH_3CN for POM catalysts with respectively protons and alkaline or TBA counter-cations and various organic solvents (acetone, CH_2Cl_2 , CHCl_3 , MeOH , toluene, DMF) for coordination complexes. The crystallites of MOFs are then added and the suspension is stirred for a determined amount of time which can go from 2 hours to 4 days, usually at room temperature. Note that the condition that the catalyst is stable in the impregnation solution is not sufficient to ensure its integrity after its immobilization

inside the MOF. Indeed, for example, ^{31}P NMR as well as IR spectroscopy have shown that the hybrid sandwich-type POM $[(\text{PW}_9\text{O}_{34})_2\text{Co}_7(\text{OH})_2(\text{H}_2\text{O})_4(\text{O}_3\text{PC}(\text{O})(\text{C}_3\text{H}_6\text{NH}_3)\text{PO}_3)_2]^{14-}$ (noted $\text{P}_2\text{W}_{18}\text{Co}_7(\text{Ale})_2$) evolves into $\text{P}_2\text{W}_{18}\text{Co}_4$ inside the cavities of the mesoporous MIL-101(Cr) material.¹¹² Two explanations have been proposed to account for the instability of the hybrid Co-containing POM under the impregnation conditions. The first one is the presence of Brønsted acid sites inside the MOF. The second one relies on the observation that the stability of the POM depends on the nature of the counter-cation. These observations might explain why there are so far no examples of hybrid organic-inorganic POMs immobilized in MOFs, these species being less stable than the fully inorganic POMs. The drawbacks of the impregnation method are i) a limited amount of catalyst loading for MOFs in which the immobilization of POMs is based on an ionic exchange, ii) possible leaching and iii) lower homogeneity than for the synthetic encapsulation.

A few strategies have been reported to prevent leaching in composites synthesized by impregnation. For example, carboxylated functionalized Rh and Ru complexes were co-immobilized in NH_2 -MIL-101(Cr).¹¹³ The authors show that the interactions between the carboxylate groups of the complexes and the MOF framework prevent their leaching. In the same way, Chen *et al.* described the post-synthetic modification (PSM) of the linker after the encapsulation in order to block the apertures of the MOF cavities and avoid leaching.¹¹⁴ A chiral Co(III)-salen catalyst was first immobilized in the cavities of the Zn-MOF IRMOF-3. In a second step, the free-amino groups of the BDC- NH_2 linker were acylated by reaction with acetic anhydride, the acylamide groups blocking the windows as a fence. ICP analyses indicate that catalyst leaching was important in the sample before PSM treatment after soaking in CHCl_3 , which was not the case after PSM treatment.

Finally, it can also be noticed that dissociative linker exchange reactions can allow to encapsulate molecular guests larger than the aperture size of a MOF host. For example, Li *et al.* have described the encapsulation of the Ru catalyst $(^t\text{BuPNP})\text{Ru}(\text{CO})\text{HCl}$ ($^t\text{BuPNP}$ = 2,6-bis((di-tert-butyl-phosphino)methyl)pyridine) in the pores of UiO-66 by exposing MOF crystallites to a solution of the catalyst in MeOH for 5 days (**Figure 1.19**).¹¹⁵ The authors thus show that this aperture-opening process exists even in a robust MOF and is highly dependent on the identity of the solvent used. Protic solvents such as MeOH are perfectly adapted to this process. On the contrary aprotic solvents do not favor dissociative linker exchange reactions and are thus required for the catalysis reaction, preventing linker dissociation and leaching.

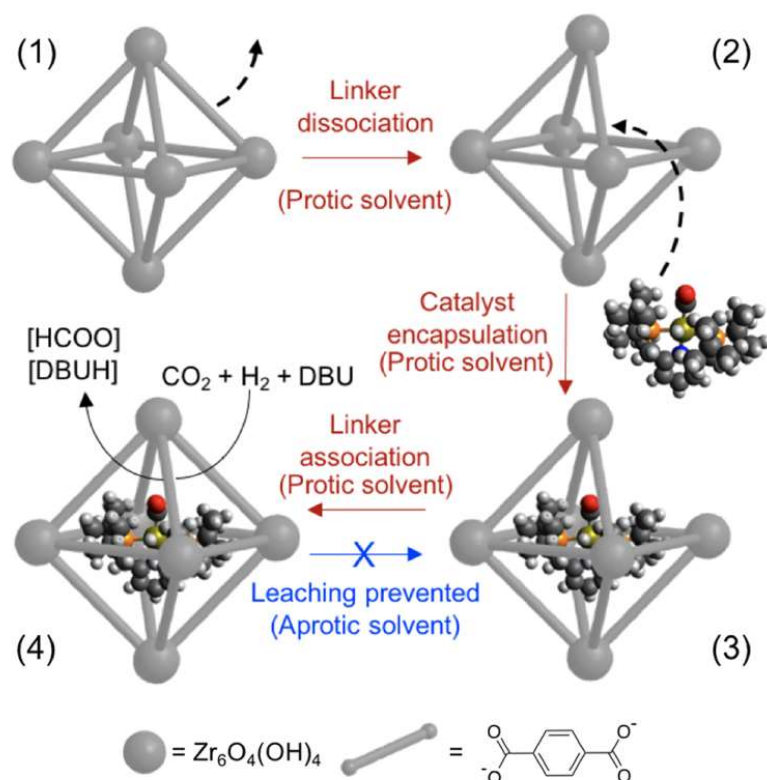


Figure 1.19: Schematic representation of the aperture-opening process used for the encapsulation of a Ru complex in the cavities of UiO-66.¹¹⁵

3.3 Ship-in-a bottle

This method consists in adding the catalyst precursors in a suspension of the MOF before performing its synthesis within the cavities of the MOF and is used in particular for catalysts with large dimensions and/or low solubility, which thus prevents their immobilization by the impregnation and synthetic encapsulation methods. It has almost never been used for POM@MOF composites, POMs having rarely solubility problems and the synthetic conditions of POMs being often not compatible with the stability of MOFs.

On the contrary, there have been several examples of Complex@MOF composites synthesized by the ship-in-a-bottle strategy. This is the case for $[\text{Ni}(\text{bpet})(\text{H}_2\text{O})_2]@\text{Ru-UiO-67}$ (bpet = 1,2-bis((pyridin-2-ylmethyl)thio)ethane, Ru-UiO-67 = UiO-67 MOF with Ru ions coordinated to 5% of the 4,4'-biphenyldicarboxylic linkers).¹¹⁶ This composite is obtained by adding first bpet ligands in a suspension of the MOF in CH_3CN , and after washing and drying, $\text{Ni}(\text{ClO}_4)_2$ is added to a suspension of the MOF in an acetone/ H_2O (20/1) mixture (**Figure 1.20**). Similarly, Co complexes have been *in situ* synthesized by adding first the flexible ligands and then the Co

ions in the cages of the visible-light photoactive $\text{NH}_2\text{-MIL-125(Ti)}$ MOF.^{117,118} After synthesis, the rigid complex is well-entrapped inside the MOF. Phthalocyanines metal complexes were also immobilized in MIL-101(Cr) ^{119,120} and MIL-100(Fe) ¹¹⁹ by “ship-in-a-bottle” synthetic methods.

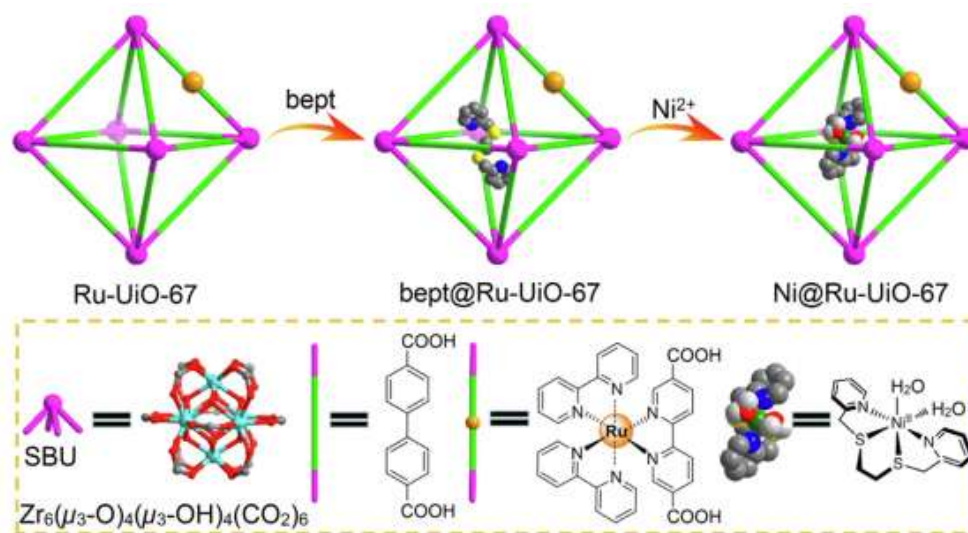


Figure 1.20: Schematic illustration for the “Ship-in-a-bottle” synthetic strategy to prepare $[\text{Ni}(\text{bpet})(\text{H}_2\text{O})_2]@\text{Ru-Uio-67}$.¹¹⁶

3.4 Charge compensation

In most of the cases, the molecular catalyst is charged, with a negative charge for POMs, and most often a positive charge for coordination complexes, and the question thus arises of the charge compensation of the catalysts after their immobilization. Discussions on this matter are quite rare in articles. For composites isolated by impregnation or *in situ*, the catalyst can be immobilized with the counterions present in the catalyst precursor, with thus no modification of the composition of the MOF. This is for example the case of POM@HKHUST-1 composites, where the Cu-based MOF framework is neutral and the negative charge of the encapsulated Keggin ions is compensated by TMA cations and/or protons.^{121–126} Interestingly, TMA cations can be exchanged by K^+ ions without loss of crystallinity¹²⁶ or be eliminated by thermal treatment (180°C under vacuum).¹²⁷ The cationic Zn(II) porphyrin complex $[\text{Zn}^{\text{II}}\text{NMeTPyP}]^{4+}$ was also immobilized in the Zr porphyrinic MOF PCN-224 with its iodide counterions as shown by EDS analysis.¹²⁸ In the $\text{CoW}_{12}@\text{ZIF-8}$ composite, isolated by synthetic encapsulation, the absence of K^+ counter-ions (present in the POM precursor) was evidenced by elemental analysis

and the authors propose that charge compensation of the $[\text{CoW}_{12}\text{O}_{40}]^{6-}$ POM comes from solution protons trapped by the composite.¹²⁹ The localization of the protons is however not discussed.

The immobilization of anionic catalysts by impregnation in MIL-101(Cr) has been described as based on ion exchange reactions. It must be noted that, if the solvent is water, the value of the pH determines the charge of the MOF. Zeta potential can be measured to determine surface charge characteristics of MOFs in aqueous solution as a function of pH. For example, zeta potential measurements showed that particles of MIL-101(Cr) are positively charged for pH below 7,¹³⁰ which favors the encapsulation of anionic species such as POMs. MIL-101(Cr) possesses negatively charged counterions (mostly F^- or NO_3^- counterions) which can be exchanged by negatively charged Cats. This implies a limitation in the catalyst loading in impregnation reactions, the total charge brought by the catalysts being equal, at the maximum, to the initial negative charge of the counter-ions.¹¹² The immobilization of the anionic $[\text{Co}(\text{CO})_4]^-$ complex in MIL-101(Cr) is also based on an ion-exchanged process and is performed in two steps: first the charge-balancing F^- anions, which are directly coordinated to the Cr(III) sites in the as-synthesized MIL-101(Cr), are exchanged by Cl^- anions (by reaction with AlCl_3) then in a second step the mobile Cl^- ions are exchanged by the negatively charged complex by reaction with $\text{Na}[\text{Co}(\text{CO})_4]$.¹³¹

In a similar way, the immobilization of the $\text{P}_2\text{W}_{18}\text{Co}_4$ sandwich-type POM by impregnation of MOF-545 in an aqueous solution of the POM is also based on an ionic exchange reaction. Indeed, the MOF-545 framework is positively charged due to the protonation of the Zr_6 clusters and possesses Cl^- counter-anions. These Cl^- counterions can be exchanged by POMs, leading to a composite with the following formula: $[\text{Zr}_6\text{O}_{16}\text{H}_{18}][\text{TCPPH}_2]_2[\text{P}_2\text{W}_{18}\text{Co}_4]_{0.2}$.⁹⁹ Likewise, in $\text{PW}_{12}@NU-1000$, the charge compensation of the POM results from protons which go on the hydroxyl groups on the Zr_6 nodes and the synthesis of the composite is thus performed in acidic pH (pH 2.5) in order to favor the protonation of the MOF.¹³²

In $\text{POM}@UiO-67$ composites, which are synthesized by in situ methods, it has been proposed that the negative charge of the POM guests is also compensated by the positively charged framework but this positive charge does not result from the protonation of the MOF but is rather due to linker defects.⁸⁸ For example, three $\text{POM}@UiO-67$ composites have been synthesized with the proposed following formulas: $[\text{Zr}_6\text{O}_4(\text{OH})_4][\text{C}_{14}\text{H}_8\text{O}_4]_{5.37}[\text{PW}_{12}\text{O}_{40}]_{0.42}$ ($\text{PW}_{12}@UiO-67$), $[\text{Zr}_6\text{O}_4(\text{OH})_4][\text{C}_{14}\text{H}_8\text{O}_4]_{5.73}[\text{PW}_{11}\text{O}_{39}\text{Zr}]_{0.18}$ ($\text{PW}_{11}\text{Zr}@UiO-67$), and

$[\text{Zr}_6\text{O}_4(\text{OH})_{4.30}][\text{C}_{14}\text{H}_8\text{O}_4]_{5.10}[\text{P}_2\text{W}_{18}\text{O}_{62}]_{0.25}$ ($\text{P}_2\text{W}_{18}@ \text{UiO-67}$) where the percentage of missing linkers is equal to 10.5, 4.5 and 15 respectively.

Encapsulation of cationic coordination complexes in anionic MOFs, while quite rarer, has also been reported. For example, the encapsulation of $[\text{Ru}(\text{bpy})_3]^{2+}$ has been performed in the In-based anionic PCN-99 MOF by impregnation.¹³³ The sulfonated MIL-101(Cr) is another example of an anionic MOF. It can be isolated as a Na^+ salt with sodium ions counter-balancing the negative charge of the deprotonated sulfonate groups on the linkers. The encapsulation of cationic Rh^{134} and Ir^{135} complexes has thus been described as a cation exchange between some of the sodium ions and the complexes. The heterogenization of the same Rh complex in the anionic In-MOF ZJU-28¹³⁶ and of cationic Fe and Co complexes in the related $[\text{R}_4\text{N}]_3[\text{In}_3(\text{BTC})_4]$ ($\text{R} = \text{Et}, n\text{Pr}, n\text{Bu}$) MOFs¹³⁷ has also been performed by partial exchange of the H_2NMe^+ and R_4N^+ cations respectively of the MOF with the cationic complexes. The exchange of R_4N^+ cations of the $[\text{R}_4\text{N}]_3[\text{In}_3(\text{BTC})_4]$ MOF with the cationic $[\text{Cp}_2\text{Co}]^+$ complexes has been thoroughly studied and the authors have shown that the percentage of cation exchange depends on i) the duration of the impregnation experiment, ii) the starting $[\text{Cp}_2\text{Co}]^+ / [\text{R}_4\text{N}]^+$ ratio, iii) the size of the organic cation.¹³⁷ The exchange is thus maximum and reaches 82% for impregnation experiments lasting 72 h, for a $[\text{Cp}_2\text{Co}]^+ / [\text{R}_4\text{N}]^+$ ratio 3/1 and for the smallest TEA cations.

The catalyst immobilization is the first step when developing new cat@MOF for catalytic purposes. A thorough characterization is needed, as one needs first to be sure of the stability of the MOF host as well as the integrity of the catalyst immobilized. Depending on the catalyst encapsulated on the MOF a wide range of characterization techniques, such as NMR, XRD, N_2 adsorption, TGA, etc., can be performed. Last but not least, the quantification of the amount of catalyst immobilized in the MOF guest is primordial. Indeed, to probe the catalytic performance of the cat@MOF, as most of the time only the catalyst immobilized is active, a miscalculated loading could lead to wrong conclusions. In the following part we will discuss the different characterization methods for host/guest materials.

4. Characterizations of Cat@MOF composites

4.1 Determination of the composition (ICP, solution NMR, UV-vis, TGA, EDX)

A combination of several techniques can be used to determine the composition of the Cat@MOF materials and give access to the Cat loading. The control of the loading is important in view of catalytic applications. A material with only a small amount of immobilized catalyst will have low performances. On the other hand, overloading can block the cages and windows and thus the accessibility of the reactants to the catalytic species. This has for example been described for $\text{PW}_{12}\text{@MOF-808X}$ ($X = \text{F}, \text{A}, \text{and P}$ where the coordinated monocarboxylate group is formic, acetic or propionic, respectively).¹³⁸ The precise knowing of the composition of the Cat@MOF is also essential for the determination of the turn over numbers (TONs) in catalytic studies. The most common and also the most precise technique of determination of the composition is the ICP analysis of digested solutions of Cat@MOFs. For example the Co/In ratio of a composite $[\text{Cp}_2\text{Co}]@[\text{R}_4\text{N}]_3[\text{In}_3(\text{BTC})_4]$ ($\text{R} = \text{Et}, n\text{Pr}, n\text{Bu}$) digested in diluted HNO_3 (1/10 v/v) was measured by ICP-OES and allowed to quantify the amount of immobilized complex.¹³⁷ Note that ICP is also a powerful technique to monitor uptake of catalysts during impregnation reactions by an analysis of the impregnation solutions and has for example been used for $\text{PW}_{12}\text{@NU-1000}$.¹³² This analytic method also allowed to follow POM leaching when the same material was dispersed in acidic aqueous solutions.

Several other techniques can also be used to apprehend the composite composition. UV-vis spectroscopy can thus allow monitoring the incorporation of the catalyst in the MOF during the impregnation and to estimate the amount of Cat immobilized in the MOF. For example, the decrease of the bands around 250 nm (assigned to the charge transfer from the bridging O-atoms to W-atoms) allowed to follow qualitatively the immobilization of PW_9 ,¹³⁹ PW_{11} ,¹⁴⁰ SiW_{11} ,¹⁴⁰ PW_{11}Ti ,¹⁴¹ and PW_{11}Co ¹⁴¹ in MIL-101(Cr). A detailed UV-vis study was also performed to measure the catalyst concentration in the supernatant after the impregnation experiment of various Ru catalysts in $\text{NH}_2\text{-MIL-101(Al)}$ and MIL-101(Cr) MOFs¹⁴² and of a Rh catalyst and a Ru photosensitizer in $\text{NH}_2\text{-MIL-101(Al)}$.¹¹³ This study allowed to determine the catalyst loading and to find the best solvent for their immobilization. The analysis of digested solutions of the composite instead of the supernatant solutions should allow a more accurate determination of the catalyst loading. Indeed, due to Cat species adsorbed at the surface

of the MOF crystallites that go out after careful washing, the amount of immobilized Cats is overestimated by an analysis of the supernatant solutions.⁹⁹

Thermogravimetric analysis (TGA) can also be used to confirm the composition of a Cat@MOF. A typical example is represented in **Figure 1.21** for a $\text{PW}_{11}\text{Zn@MIL-101}(\text{Cr})$ composite.¹⁴³ The first weight loss is attributed to the departure of solvent molecules, the second weight loss to the decomposition of the framework. The total weight loss for the POM@MOF is lower than for the parent MOF due to the presence of POM guests which decompose into oxides. Thus, the comparison of the weight loss calculated from the results of elemental analysis with the experimental weight loss allow confirming the formula of the composite and in particular the guest loading. TGA also allows studying the thermal stability of the composites. It can be noted that the temperature of decomposition of POM@MOF composites is usually very close to that of the MOF, which indicates that the insertion of POMs only slightly affects their thermal stability. This is also the case for the rare examples of TGA curves reported for Complex@MOFs. A few exceptions can be noticed. For example, the $\text{SiW}_{12}\text{@HKUST-1}$ (also named NENU-1) composite, after thermal treatment (180°C under vacuum) to remove TMA^+ cations and H_2O molecules (NENU-1a material), is stable up to 300°C while the POM-free MOF is stable only up to 240°C . The authors attributed this difference to physicochemical interactions between the POM and the MOF framework.

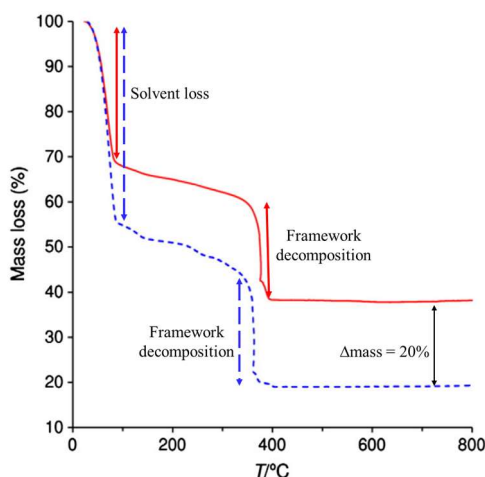


Figure 1.21: Typical TGA curve of a Cat@MOF composite: TGA curves under air of a $\text{PW}_{11}\text{Zn@MIL-101}(\text{Cr})$ composite (red curve) and of the parent MIL-101(Cr) (dashed blue line).¹⁴³

Scanning electron microscopy (SEM) and energy-dispersive X-ray spectroscopy (EDX) are largely used to characterize the morphology and composition of the composite materials, after

synthesis and sometimes also after the catalytic reaction. The SEM images allow showing that the composite is still crystalline and EDX analyses indicate the distribution of the elements of the catalyst within the MOF. It can be noted that in all the reported cases, SEM-EDX analyses suggest a uniform distribution of the elements. However, one has to be cautious for composites isolated by impregnation reactions because SEM-EDX mapping is not sufficient to prove the homogeneity of the distribution.^{99,144} For example, SEM experiments on $P_2W_{18}Co_4@MOF-545$ seem to indicate a homogeneous repartition of the Co, W and P elements of the POMs while HRTEM showed higher concentrations of these elements at both extremities of the crystal rods of the MOF (**Figure 1.22**).⁹⁹ This distribution is consistent with the alignment of the channels of the MOF along the c axis, that is, the longest dimension of the rods, and an accumulation of the POMs at the extremities of the channels during the impregnation reaction. EDX analysis can also be used to follow anion exchange reactions during impregnation reactions. For example, EDX showed the exchange of F^- anions by Cl^- anions (absence of the F $K\alpha$ peak, presence of the Cl $K\alpha$ peak) followed by the exchange of F^- by $[Co(CO)_4]^-$ anions (absence of the Cl $K\alpha$ peak and presence of the Co $K\alpha$ and L α peaks) in the two-step procedure leading to $[Co(CO)_4]@MIL-101(Cr)$.¹³¹

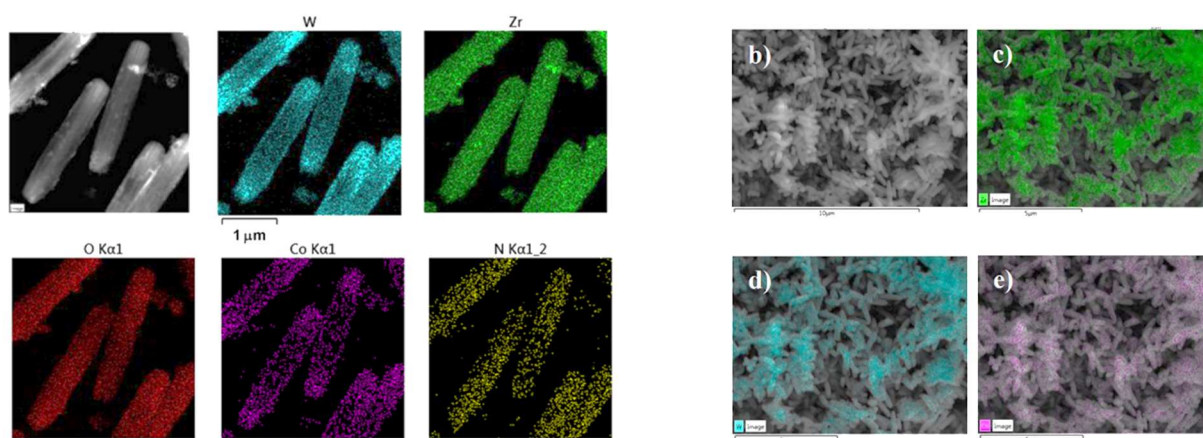


Figure 1.22: Comparison of a) STEM-HAADF images of $P_2W_{18}Co_4@MOF-545$ and EDS mapping of the various elements contained in the POM and the MOF and b)-e) SEM images and EDS elemental mapping.⁹⁹

Regarding the morphology of the composite crystallites, while in almost all cases, the crystals of the Cat@MOF composites have morphologies similar to that of the parent MOF, there are a few reports where the crystals have altered morphologies. For example, $PW_{12}@UiO-66$ crystallites obtained by synthetic encapsulation do not exhibit regular shapes but look like agglomerated small particles, with irregular inter-grown microcrystalline poly-octahedra

morphologies.¹⁴⁵ SEM images of (Fe-salen,SiW₁₂)@ZIF-8 also show the uneven surface of the nanocrystals of the composite, when compared with the smooth surface of the nanocrystals obtained in the absence of POM.¹⁴⁶ This provides strong evidence in support of the growth of POMs on ZIF-8, which was also suggested by the very large amount of POM determined by ICP-OES analysis.

4.2 IR and Raman spectroscopy

In all the reported Cat@MOF studies, IR spectra are recorded to check whether the catalyst and MOF structures are preserved. This technique is also routinely performed to study the stability of the composites after the catalytic experiments. For example, for the PW₁₂ catalyst, characteristic P-O, W=O and W-O-W bands are observed around 1000, 980 and between 800 and 900 cm⁻¹ respectively. Red shifts have sometimes been described between the POM precursor and the encapsulated POM. A red shift of about 30 cm⁻¹ was thus observed for the P-O and W=O bands of PW₁₂ immobilized in MOF-808X.¹³⁸ The P-O vibration was also shifted from 1030 to 1048 cm⁻¹ from P₂W₁₈Co₄ to P₂W₁₈Co₄@MIL-101(Cr) (Figure 1.23 a).¹¹² These shifts were attributed to strong interactions between the POM and the MOF. IR spectroscopy can also evidence the catalyst transformation after its immobilization in the MOF.

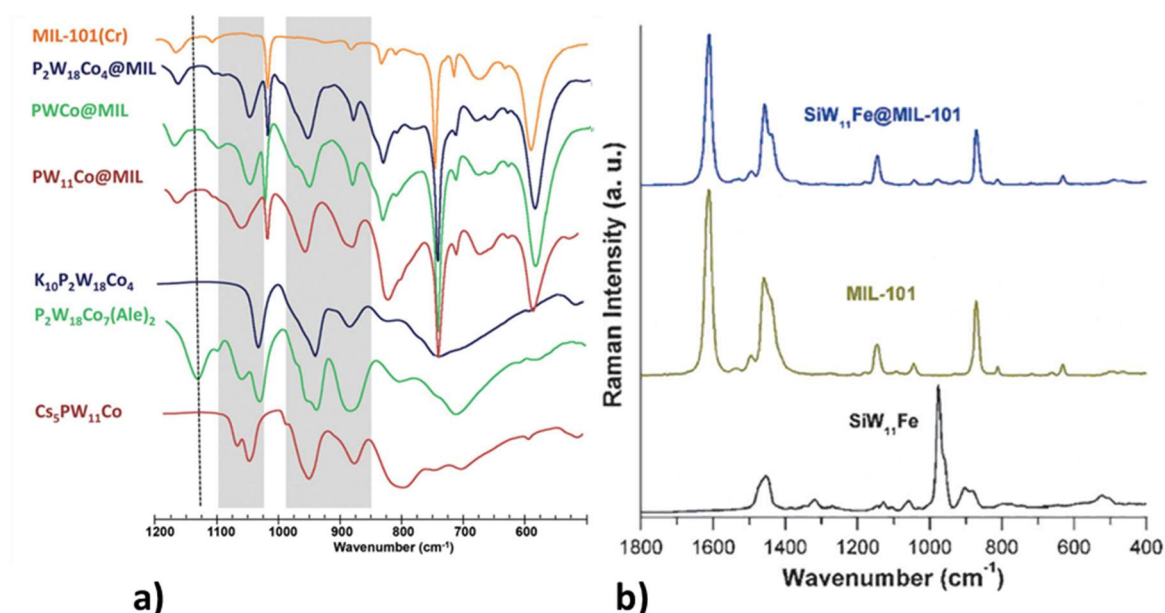


Figure 1.23: a) IR spectra of composites synthesized by immobilizing Co-substituted POMs in MIL-101(Cr); the composite named PWCo@MIL results from the immobilization of the hybrid P₂W₁₈Co₇(Ale)₂ POM. b) Raman spectra of SiW₁₁Fe, MIL-101(Cr) and SiW₁₁Fe@MIL-101(Cr).^{112,147}

Semi-quantitative analysis can also be performed on the IR spectra of Cat@MOFs. For example, the relative intensities of the bands at 1077 cm^{-1} attributed to the P-O vibration of the Keggin ion and at 1180 cm^{-1} attributed to C-C and C-N vibrations of the linker were followed in the IR spectra of $\text{PW}_{12}@Zr_6\text{-TCPP-Fe}$ (where $Zr_6\text{-TCPP-Fe}$ is a MOF built from the connection of Zr_6 clusters by Fe-metallated porphyrinetetracarboxylate linkers). The evolution of the ratio between both intensities reveals the maximum amount of POM that can be immobilized in the MOF by synthetic encapsulation experiments. In some cases, the IR bands of the guest cannot be observed, for example in $\text{P}_2\text{W}_{18}\text{Co}_4@\text{MOF-545}$,⁹⁹ $\text{PMo}_{12}@\text{UiO-67}$,¹⁴⁸ and $\text{CoW}_{12}@\text{ZIF-8}$,¹²⁹ probably because of low loading.

In addition to IR, or when the catalyst bands cannot be clearly identified, Raman spectroscopy is sometimes used to characterize the materials. However, in the case of POM@MOFs, the intensities of these bands are also often quite weak. For example, the Raman spectrum of $\text{SiW}_{11}@\text{MIL-101(Cr)}$ exhibits a small band at approximately 978 cm^{-1} assigned to a W=O stretching mode of SiW_{11} (**Figure 1.23 b**).¹⁴⁷ In $\text{P}_2\text{W}_{18}\text{Co}_4@\text{MIL-101(Cr)}$ the W=O band of the POM at 982 cm^{-1} is clearly visible in the Raman spectrum of the composite but also with a rather weak intensity.¹⁴⁹ In rare examples, the intensity of the characteristic bands of the catalyst is stronger.^{150,151}

Raman spectroscopy was also used to characterize Complex@MOFs. For example, the bands attributed to the iron tetrasulfophthalocyanine FePcS are clearly visible in the Raman spectrum of $\text{FePcS}@\text{MIL-101(Cr)}$ at the same position as in the bulk FePcS precursor.¹⁵² Furthermore, no new bands are observed. This indicates the integrity of the complex after its immobilization.

4.3 BET measurements

N_2 porosimetry is also a technique largely used to characterize MOF derivatives. The significant reduction of the N_2 amount adsorbed in Cat@MOF compared with the MOF is considered as a clear indication of the successful incorporation of the catalyst. The Brunauer-Emmett-Teller (BET) specific surface area and total pore volume of Cat@MOF composites are found to be lower compared to the guest-free MOF, as a result of both the mass increases due to the introduction of the catalyst and of the pore space occupied by the guests. For example, it was shown that the surface area of $\text{PW}_{12}@\text{MIL-100(Fe)}$ depends on the amount of POM incorporated. While even for high loadings (35 wt %) $\text{PW}_{12}@\text{MIL-100(Fe)}$ exhibits a high BET surface area of $1046\text{ m}^2\cdot\text{g}^{-1}$, this one is indeed significantly lower than that of the POM-free MOF ($2055\text{ m}^2\cdot\text{g}^{-1}$) (**Figure 1.24**).¹⁵³ It is also noticeable that the mesopores and microporous

windows are also retained, which ensures that substrates enter into the pores and come into contact with the POM.

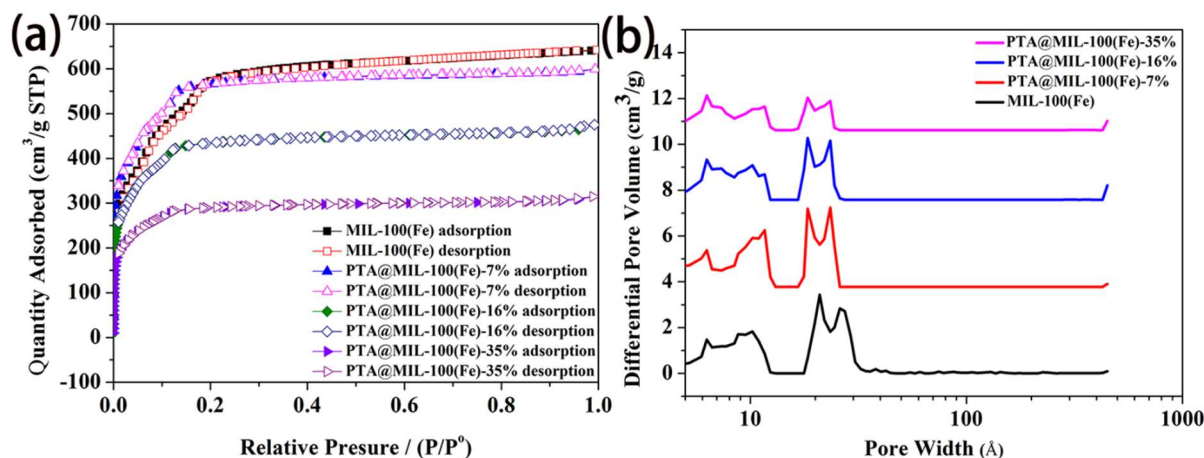


Figure 1.24: a) N₂ adsorption–desorption isotherms at 77 K and b) pore size distribution of MIL-100(Fe) and PW₁₂@MIL-100(Fe) with 7 wt % (PW₁₂@MIL-100(Fe)-7%), 16% (PW₁₂@MIL-100(Fe)-16%), and 35% (PW₁₂@MIL-100(Fe)-35%) loading in POM.¹⁵³

Besides, Juan-Alcañiz *et al.* deduced from the comparison of N₂ isotherms of various samples of PW₁₂@MIL-101(Cr) that in the sample isolated by direct synthesis the dispersion of the POMs in the MOF matrix was better than in the sample obtained by impregnation.¹⁴⁴ The encapsulated samples with high POM loadings show indeed an adsorption behavior similar to that of the POM-free MOF, with two steps corresponding to the filling of the two types of cages. This strongly suggests that the filling of the pores by the POM molecules is quite homogeneous, with no indication of blocking of the cavities. In contrast, for the impregnated samples, only the large cavities are occupied and most of these cavities are blocked. Besides, N₂ adsorption/desorption isotherms allowed to show that the bulky metal phthalocyanines (FePctBu₄)₂N are not incorporated into the mesoporous structure of MIL-101(Cr) but adsorbed at the surface of the crystallites. Indeed, the total pore volume of the composite decreases by only 5 %, which corresponds to the weight gain of 5.2 wt % after loading.¹⁵⁴

4.4 Solid-State NMR

For the POMs which contain P atoms, and in particular for the most studied POM, PW₁₂, ³¹P cross-polarization magic angle spinning (CP MAS) NMR has proved a valuable tool to study their stability after immobilization, before and after catalysis. In most cases, a single peak is observed after immobilization of the POM into the MOF. For example, a single peak at -12.2

ppm is observed for $\text{PW}_{11}@\text{MIL-101}(\text{Cr})$, confirming the integrity of the POM.⁷⁵ However, a few studies have reported the presence of several ^{31}P NMR peaks after the immobilization of PW_{12} . For example, Maksimchuk *et al.* showed the existence of three main peaks at -16.4, -14.8 and -11.8 ppm in $\text{PW}_{12}@\text{MIL-101}(\text{Cr})$.¹⁵⁵ They proposed that these peaks could correspond to different modes of interaction between the POM and the MOF surface, as IR spectra did not indicate any noticeable change and thus any degradation of the POM. In another composite with PW_{12} , namely $\text{PW}_{12}@\text{MOF-808A}$ with 42% POM loading, the ^{31}P MAS NMR spectrum exhibited three resonances at -15.1, -16.2, and -17.6 ppm, much broader in comparison with those for the pure POM. The existence of these three signals was attributed as either different protonation states of PW_{12} or POM distortion resulting from strong interactions with the host framework.¹³⁸

Solid-state NMR has also been used to characterize Complex@MOFs. For example, ^{13}C CP-MAS NMR of $\text{CuPhen}@\text{MIL-100}(\text{Al})$ presents signals assigned to the aromatic carbons and of the carboxylate groups of the MOF linkers as well as of the Phen ligand. Only one broad peak was observed at around 15 ppm in the $^{31}\text{P}\{^1\text{H}\}$ MAS NMR spectrum of $[\text{Ir}(\text{cod})(\text{PCy}_3)(\text{py})]@\text{NaSO}_3\text{-MIL-101}(\text{Cr})$ and was assigned to PCy_3 ligands. The absence of peaks characteristic of PF_6^- anions suggests a complete cation exchange.

Solution NMR is also useful to study the formation of composites. For example ^{31}P solution NMR was also used to study the interactions between Cu^{2+} and PMo_{12} ions during the synthetic process of $\text{PMo}_{12}@\text{HKHUST-1}$, with a shift from 3.72 ppm for the ^{31}P signal of a solution of PMo_{12} to 3.00 ppm after addition of Cu^{2+} and 3.09 ppm after subsequent addition of BTC.¹⁵⁷ Shifts in the ^{183}W NMR spectra of a solution of PW_{12} also support the existence of strong interactions between the copper ions and the POM during the synthesis of $\text{PMo}_{12}@\text{HKHUST-1}$ and confirmed the integrity of the POM.

4.5 X-ray diffraction

Powder X-ray diffraction is generally used to check the crystallinity and confirms the phase purity of the MOF host after the immobilization of a catalyst guest. In almost all cases of reported Cat@MOF, some redistribution of the intensities of the XRD peaks was observed for POM@MOF composites compared with the pristine MOF, but both the positions and width of the X-ray reflections usually remain unchanged, indicating that the MOF does not lose its crystallinity after the immobilization of the catalyst. A detailed study on the influence of the catalyst loading on the relative intensity of the peaks was made on $\text{CuPhen}@\text{MIL-100}(\text{Al})$.¹⁵⁶

The authors showed that the $2\theta = 4.0^\circ$ Bragg intensity peak gradually decreased with increasing CuPhen loadings. Such variation was not observed for a sample prepared by impregnation of the MOF with a solution of the CuPhen complex. In some rare examples of Cat@MOF obtained by synthetic encapsulation, it has been observed that the crystallinity of the MOF depends on the amount of encapsulated guests. For example, in $\text{PW}_{12}\text{@MOF-808X}$, the crystallinity was improved compared to the pristine MOF for POM loadings lower than 32%. The authors attributed this result to the modulator role of the POMs for low loading, while higher loadings induce the presence of defects (by inhibiting the coordination between the zirconium ions and ligands) and thus leads to a decrease in crystallinity.¹³⁸ Some authors have reported an increase of the intensity of some peaks; this is the case for the peaks around 5° in a $\text{P}_2\text{W}_{18}\text{Co}_4\text{@MIL-101(Cr)}$ composite.¹⁴⁹ Also, the apparition of new diffraction peaks in the powder X-ray diffraction patterns of such composites has been observed. This phenomenon has been observed in $\text{PW}_{12}\text{@MIL-101(Cr)}$ ¹⁵⁸ and $\text{PW}_{12}\text{@NH}_2\text{-MIL-101(Cr)}$.¹⁵⁹ The positions of the new peaks are consistent with the unit cell of MIL-101 but had a null intensity in the POM-free MOFs. The authors proposed that the electron density of the crystal structure of the MOF increases after the incorporation of the POM, thus creating the observed diffracted intensity at these peak positions. These various studies highlight the fact that the localization of the POMs in the cavities of the MOF can have a great influence on the PXRD patterns of the composites and that their analysis can thus allow making hypotheses on the structure of the POM@MOF. It is possible to go further in the structural characterization by using Pair Distribution Function (PDF) and Difference envelope density analysis (DED).

Once fully characterized, the MOF and cat@MOF materials can be probed for their catalytic performances. It is important to keep in mind that some MOFs can be active for CO_2 reduction without any need of immobilized catalyst. It is for example the case of various MIL-125(Ti)-NHX (with X = H, Me, Et, iPr, Bu, etc.)^{160,161} as well as UiO-66-NH₂¹⁶² which has been found to be selective for HCOOH production, BDC-NH₂ acting as a photosensitive linker and also helping CO_2 adsorption. Porphyrin-based MOFs have also been able to reduce by themselves CO_2 to formate or CO/CH₄. Their activity toward CO_2 reduction will be discussed in the introduction of the third chapter of this manuscript. Other examples of catalytic MOFs for CO_2 reduction can be found in a recent review from Luo *et al.*⁴ where they discuss molecular catalysts, MOFs, and immobilization of catalysts in MOFs. The review we recently published also discuss the rich catalytic properties of cat@MOF composites, highlighting that these

materials are able to perform a wide range of reactions going from small molecule activation for energy (OER, HER, CO₂RR) to desulfurization, alcohol oxidation etc.⁷¹

With all this developed knowledge, we propose in the present work the design of new heterogeneous and stable photocatalytic systems for CO₂ reduction. In the following chapter, we describe a first strategy whereby we co-immobilize a rhodium-based organometallic molecular catalyst and a POM in the Zr-UiO-67 for CO₂ and proton reduction to formate and H₂, assisted by the [Ru(bpy)₃]Cl₂ photosensitizer. In the third chapter, we managed to avoid the use of noble metal by using the active porphyrinic MOF-545 and optimized its efficiency towards CO₂ reduction by metalating the porphyrin. We also attempted to immobilize different molecular catalysts in its wide pores, which we will briefly describe. In the last fourth chapter, we present the CO₂ reduction properties of three new polyoxometalates in heterogeneous conditions.

5. References

1. Energy Transitions: Global and National Perspectives (Second expanded and updated edition) – Vaclav Smil. <http://vaclavsmil.com/2016/12/14/energy-transitions-global-and-national-perspectives-second-expanded-and-updated-edition/>.
2. Jackson, R. B. *et al.* Persistent fossil fuel growth threatens the Paris Agreement and planetary health. *Environ. Res. Lett.* **14**, 121001 (2019).
3. Perazio, A., Lowe, G., Gobetto, R., Bonin, J. & Robert, M. Light-driven catalytic conversion of CO₂ with heterogenized molecular catalysts based on fourth period transition metals. *Coord. Chem. Rev.* **443**, 214018 (2021).
4. Luo, Y.-H., Dong, L.-Z., Liu, J., Li, S.-L. & Lan, Y.-Q. From molecular metal complex to metal-organic framework: The CO₂ reduction photocatalysts with clear and tunable structure. *Coord. Chem. Rev.* **390**, 86–126 (2019).
5. Boutin, E. *et al.* Molecular catalysis of CO₂ reduction: recent advances and perspectives in electrochemical and light-driven processes with selected Fe, Ni and Co aza macrocyclic and polypyridine complexes. *Chem. Soc. Rev.* **49**, 5772–5809 (2020).
6. Ci, C., Carbó, J. J., Neumann, R., Graaf, C. D. & Poblet, J. M. Photoreduction Mechanism of CO₂ to CO Catalyzed by a Rhenium(I)-Polyoxometalate Hybrid Compound. *ACS Catal.* **6**, 6422–6428 (2016).
7. Volume 42, Iss. 4 (2007) | Journal of Chemical Technology and Metallurgy. <https://dl.uctm.edu/journal/j2007-4>.
8. Pellegrin, Y. & Odobel, F. Sacrificial electron donor reagents for solar fuel production. *Comptes Rendus Chim.* **20**, 283–295 (2017).
9. Takeda, H., Cometto, C., Ishitani, O. & Robert, M. Electrons, Photons, Protons and Earth-Abundant Metal Complexes for Molecular Catalysis of CO₂ Reduction. *ACS Catal.* **7**, 70–88 (2017).
10. Hawecker, J., Lehn, J.-M. & Ziessel, R. Efficient photochemical reduction of CO₂ to CO by visible light irradiation of systems containing Re(bipy)(CO)₃X or Ru(bipy)₃²⁺–Co²⁺ combinations as homogeneous catalysts. *J. Chem. Soc. Chem. Commun.* 536–538 (1983).
11. Stor, G. J., Hartl, F., van Outersterp, J. W. M. & Stufkens, D. J. Spectroelectrochemical (IR, UV/Vis) Determination of the Reduction Pathways for a Series of [Re(CO)₃(α -diimine)L']^{0/+} (L' = Halide, OTf-, THF, MeCN, n-PrCN, PPh₃, P(OMe)₃) Complexes. *Organometallics* **14**, 1115–1131 (1995).
12. Tsubaki, H. *et al.* Photocatalytic reduction of CO₂ using cis,trans-[Re(dmbpy)(CO)₂(PR₃)(PR'₃)]⁺ (dmbpy=4,4'-dimethyl-2,2'-bipyridine). *Res. Chem. Intermed.* **33**, 37–48 (2007).
13. Takeda, H., Koike, K., Inoue, H. & Ishitani, O. Development of an Efficient Photocatalytic System for CO₂ Reduction Using Rhenium(I) Complexes Based on Mechanistic Studies. *J. Am. Chem. Soc.* **130**, 2023–2031 (2008).
14. Huckaba, A. J., Sharpe, E. A. & Delcamp, J. H. Photocatalytic Reduction of CO₂ with Re-Pyridyl-NHCs. *Inorg. Chem.* **55**, 682–690 (2016).
15. Kurz, P., Probst, B., Spingler, B. & Alberto, R. Ligand Variations in [ReX(diimine)(CO)₃] Complexes: Effects on Photocatalytic CO₂ Reduction. *Eur. J. Inorg. Chem.* **2006**, 2966–2974 (2006).
16. Hawecker, J., Lehn, J.-M. & Ziessel, R. Photochemical reduction of carbon dioxide to formate mediated by ruthenium bipyridine complexes as homogeneous catalysts. *J. Chem. Soc. Chem. Commun.* 56–58 (1985).
17. Lehn, J.-M. & Ziessel, R. Photochemical reduction of carbon dioxide to formate catalyzed by 2,2'-bipyridine- or 1,10-phenanthroline-ruthenium(II) complexes. *J. Organomet. Chem.* **382**, 157–173 (1990).

18. Tamaki, Y., Morimoto, T., Koike, K. & Ishitani, O. Photocatalytic CO₂ reduction with high turnover frequency and selectivity of formic acid formation using Ru(II) multinuclear complexes. *Proc. Natl. Acad. Sci.* **109**, 15673–15678 (2012).
19. Ishida, H., Terada, T., Tanaka, K. & Tanaka, T. Photochemical carbon dioxide reduction catalyzed by bis(2,2'-bipyridine)dicarbonylruthenium⁽²⁺⁾ using triethanolamine and 1-benzyl-1,4-dihydronicotinamide as an electron donor. *Inorg. Chem.* **29**, 905–911 (1990).
20. Kuramochi, Y., Itabashi, J., Toyama, M. & Ishida, H. Photochemical CO₂ Reduction Catalyzed by Trans(Cl)-[Ru(2,2'-bipyridine)(CO)₂Cl₂] Bearing Two Methyl Groups at 4,4', 5,5'- or 6,6'-Positions in the Ligand. *ChemPhotoChem* **2**, 314–322 (2018).
21. Kuramochi, Y. *et al.* Unexpected effect of catalyst concentration on photochemical CO₂ reduction by trans(Cl)-Ru(bpy)(CO)₂Cl₂: new mechanistic insight into the CO/HCOO-selectivity. *Chem. Sci.* **6**, 3063–3074 (2015).
22. Sato, S., Morikawa, T., Kajino, T. & Ishitani, O. A Highly Efficient Mononuclear Iridium Complex Photocatalyst for CO₂ Reduction under Visible Light. *Angew. Chem. Int. Ed.* **52**, 988–992 (2013).
23. Genoni, A. *et al.* Tuning Iridium Photocatalysts and Light Irradiation for Enhanced CO₂ Reduction. *ACS Catal.* **7**, 154–160 (2017).
24. Grodkowski, J., Behar, D., Neta, P. & Hambright, P. Iron porphyrin-catalyzed reduction of CO₂. Photochemical and radiation chemical studies. *J. Phys. Chem. A* **101**, 248–254 (1997).
25. Dhanasekaran, T., Grodkowski, J., Neta, P., Hambright, P. & Fujita, E. p-Terphenyl-Sensitized Photoreduction of CO₂ with Cobalt and Iron Porphyrins. Interaction between CO and Reduced Metalloporphyrins. *J. Phys. Chem. A* **103**, 7742–7748 (1999).
26. Behar, D. *et al.* Cobalt Porphyrin Catalyzed Reduction of CO₂. Radiation Chemical, Photochemical, and Electrochemical Studies. *J. Phys. Chem. A* **102**, 2870–2877 (1998).
27. Bonin, J., Chaussemier, M., Robert, M. & Routier, M. Homogeneous Photocatalytic Reduction of CO₂ to CO Using Iron(0) Porphyrin Catalysts: Mechanism and Intrinsic Limitations. *ChemCatChem* **6**, 3200–3207 (2014).
28. Bonin, J., Robert, M. & Routier, M. Selective and Efficient Photocatalytic CO₂ Reduction to CO Using Visible Light and an Iron-Based Homogeneous Catalyst. *J. Am. Chem. Soc.* **136**, 16768–16771 (2014).
29. Rao, H., Bonin, J. & Robert, M. Visible-light Homogeneous Photocatalytic Conversion of CO₂ into CO in Aqueous Solutions with an Iron Catalyst. *ChemSusChem* **10**, 4447–4450 (2017).
30. Rao, H., Schmidt, L. C., Bonin, J. & Robert, M. Visible-light-driven methane formation from CO₂ with a molecular iron catalyst. *Nature* **548**, 74–77 (2017).
31. Bourrez, M., Molton, F., Chardon-Noblat, S. & Deronzier, A. [Mn(bipyridyl)(CO)₃Br]: An Abundant Metal Carbonyl Complex as Efficient Electrocatalyst for CO₂ Reduction. *Angew. Chem. Int. Ed.* **50**, 9903–9906 (2011).
32. Takeda, H., Koizumi, H., Okamoto, K. & Ishitani, O. Photocatalytic CO₂ reduction using a Mn complex as a catalyst. *Chem. Commun.* **50**, 1491–1493 (2014).
33. Smieja, J. M. *et al.* Manganese as a Substitute for Rhenium in CO₂ Reduction Catalysts: The Importance of Acids. *Inorg. Chem.* **52**, 2484–2491 (2013).
34. Cheung, P. L., Machan, C. W., Malkhasian, A. Y. S., Agarwal, J. & Kubiak, C. P. Photocatalytic Reduction of Carbon Dioxide to CO and HCO₂H Using fac-Mn(CN)(bpy)(CO)₃. *Inorg. Chem.* **55**, 3192–3198 (2016).
35. Grant, J. L., Goswami, K., Spreer, L. O., Otvos, J. W. & Calvin, M. Photochemical reduction of carbon dioxide to carbon monoxide in water using a nickel(II) tetra-azamacrocyclic complex as catalyst. *J. Chem. Soc. Dalton Trans.* 2105–2109 (1987).
36. Craig, C. A., Spreer, L. O., Otvos, J. W. & Calvin, Melvin. Photochemical reduction of carbon dioxide using nickel tetraazamacrocycles. *J. Phys. Chem.* **94**, 7957–7960 (1990).

37. Mochizuki, K., Manaka, S., Takeda, I. & Kondo, T. Synthesis and Structure of [6,6'-Bi(5,7-dimethyl-1,4,8,11-tetraazacyclotetradecane)]dinickel(II) Triflate and Its Catalytic Activity for Photochemical CO₂ Reduction. *Inorg. Chem.* **35**, 5132–5136 (1996).
38. Thoi, V. S., Kornienko, N., Margarit, C. G., Yang, P. & Chang, C. J. Visible-Light Photoredox Catalysis: Selective Reduction of Carbon Dioxide to Carbon Monoxide by a Nickel N-Heterocyclic Carbene–Isoquinoline Complex. *J. Am. Chem. Soc.* **135**, 14413–14424 (2013).
39. Liu, R. *et al.* Enhanced proton and electron reservoir abilities of polyoxometalate grafted on graphene for high-performance hydrogen evolution. *Energy Environ. Sci.* **9**, 1012–1023 (2016).
40. Berzelius, J. J. Beitrag zur näheren Kenntniss des Molybdäns. *Ann. Phys.* **82**, 369–392 (1826).
41. Keggin, J. F. The Structure and Formula of 12-Phosphotungstic Acid. *Proc. R. Soc. Math. Phys. Eng. Sci.* **144**, 75–100 (1934).
42. Misra, A., Kozma, K., Streb, C. & Nyman, M. Beyond Charge Balance: Counter-Cations in Polyoxometalate Chemistry. *Angew. Chem. Int. Ed.* **59**, 596–612 (2020).
43. Martinetto, Y., Pégot, B., Roch-Marchal, C., Cottyn-Boitte, B. & Floquet, S. Designing Functional Polyoxometalate-Based Ionic Liquid Crystals and Ionic Liquids. *Eur. J. Inorg. Chem.* **2020**, 228–247 (2020).
44. Keggin, J. F. Structure of the Molecule of 12-Phosphotungstic Acid. *Nature* **131**, 908–909 (1933).
45. Téazéa, A., Hervéa, G., Finke, R. G. & Lyon, D. K. α -, β -, and γ -Dodecatungstosilicic Acids: Isomers and Related Lacunary Compounds. in *Inorganic Syntheses* (ed. Ginsberg, A. P.) 85–96 (John Wiley & Sons, Inc., 2007).
46. Weakley, T. J. R., Evans, H. T., Showell, J. S., Tourné, G. F. & Tourné, C. M. 18-Tungstotetracobalto(II)diphosphate and related anions: a novel structural class of heteropolyanions. *J. Chem. Soc. Chem. Commun.* 139–140 (1973).
47. Girardi, M. *et al.* Assessing the Electrocatalytic Properties of the Cp*RhIII²⁺-Polyoxometalate Derivative [H₂PW₁₁O₃₉RhIIICp*(OH₂)]³⁻ towards CO₂ Reduction. *Eur. J. Inorg. Chem.* **2019**, 387–393 (2019).
48. Guedes, G., Wang, S., Santos, H. A. & Sousa, F. L. Polyoxometalate Composites in Cancer Therapy and Diagnostics. *Eur. J. Inorg. Chem.* **2020**, 2121–2132 (2020).
49. Hasenknopf, B. Polyoxometalates: introduction to a class of inorganic compounds and their biomedical applications. *Front. Biosci.* **10**, 275 (2005).
50. Zhang, Y., Liu, J., Li, S.-L., Su, Z.-M. & Lan, Y.-Q. Polyoxometalate-based materials for sustainable and clean energy conversion and storage. *EnergyChem* **1**, 100021 (2019).
51. Chen, L. *et al.* Polyoxometalates in dye-sensitized solar cells. *Chem. Soc. Rev.* **48**, 260–284 (2019).
52. Wang, S.-S. & Yang, G.-Y. Recent Advances in Polyoxometalate-Catalyzed Reactions. *Chem. Rev.* **115**, 4893–4962 (2015).
53. Wang, D., Liu, L., Jiang, J., Chen, L. & Zhao, J. Polyoxometalate-based composite materials in electrochemistry: state-of-the-art progress and future outlook. *Nanoscale* **12**, 5705–5718 (2020).
54. Cao, Y., Chen, Q., Shen, C. & He, L. Polyoxometalate-Based Catalysts for CO₂ Conversion. *Molecules* **24**, 2069 (2019).
55. Liu, S.-M. *et al.* Ti-Substituted Keggin-Type Polyoxotungstate as Proton and Electron Reservoir Encaged into Metal-Organic Framework for Carbon Dioxide Photoreduction. *Adv. Mater. Interfaces* **5**, 1801062 (2018).
56. Lv, H. *et al.* Polyoxometalate water oxidation catalysts and the production of green fuel. *Chem. Soc. Rev.* **41**, 7572–7589 (2012).

57. Geletii, Y. V. *et al.* Polyoxometalates in the Design of Effective and Tunable Water Oxidation Catalysts. *Isr. J. Chem.* **51**, 238–246 (2011).
58. Sartorel, A. *et al.* Polyoxometalate Embedding of a Tetraruthenium(IV)-oxo-core by Template-Directed Metalation of $[\gamma\text{-SiW}_{10}\text{O}_{36}]^{8-}$ A Totally Inorganic Oxygen-Evolving Catalyst. *J. Am. Chem. Soc.* **130**, 5006–5007 (2008).
59. Geletii, Y. V. *et al.* An All-Inorganic, Stable, and Highly Active Tetraruthenium Homogeneous Catalyst for Water Oxidation. *Angew. Chem. Int. Ed.* **47**, 3896–3899 (2008).
60. Huang, Z. *et al.* Efficient Light-Driven Carbon-Free Cobalt-Based Molecular Catalyst for Water Oxidation. *J. Am. Chem. Soc.* **133**, 2068–2071 (2011).
61. Lv, H. *et al.* Visible-light-driven hydrogen evolution from water using a noble-metal-free polyoxometalate catalyst. *J. Catal.* **307**, 48–54 (2013).
62. Lv, H. *et al.* A Noble-Metal-Free, Tetra-nickel Polyoxotungstate Catalyst for Efficient Photocatalytic Hydrogen Evolution. *J. Am. Chem. Soc.* **136**, 14015–14018 (2014).
63. Guo, W. *et al.* Syntheses, Structural Characterization, and Catalytic Properties of Di- and Trinickel Polyoxometalates. *Inorg. Chem.* **55**, 461–466 (2016).
64. Lv, H. *et al.* A Noble-Metal-Free, Tetra-nickel Polyoxotungstate Catalyst for Efficient Photocatalytic Hydrogen Evolution. *J. Am. Chem. Soc.* **136**, 14015–14018 (2014).
65. Streb, C. New trends in polyoxometalate photoredox chemistry: From photosensitisation to water oxidation catalysis. *Dalton Trans.* **41**, 1651–1659 (2012).
66. Hiskia, A., Mylonas, A. & Papaconstantinou, E. Comparison of the photoredox properties of polyoxometallates and semiconducting particles. *Chem. Soc. Rev.* **30**, 62–69 (2001).
67. Szczepankiewicz, S. H. *et al.* Interaction of Carbon Dioxide with Transition-Metal-Substituted Heteropolyanions in Nonpolar Solvents. Spectroscopic Evidence for Complex Formation. *Inorg. Chem.* **37**, 4344–4352 (1998).
68. Etteedgui, J., Diskin-Posner, Y., Weiner, L. & Neumann, R. Photoreduction of Carbon Dioxide to Carbon Monoxide with Hydrogen Catalyzed by a Rhenium(I) Phenanthroline–Polyoxometalate Hybrid Complex. *J. Am. Chem. Soc.* **133**, 188–190 (2011).
69. McKinstry, C., Cussen, E. J., Fletcher, A. J., Patwardhan, S. V. & Sefcik, J. Effect of Synthesis Conditions on Formation Pathways of Metal Organic Framework (MOF-5) Crystals. *Cryst. Growth Des.* **13**, 5481–5486 (2013).
70. Moosavi, S. M. *et al.* Understanding the diversity of the metal-organic framework ecosystem. *Nat. Commun.* **11**, 4068 (2020).
71. Mialane, P. *et al.* Heterogenisation of polyoxometalates and other metal-based complexes in metal–organic frameworks: from synthesis to characterisation and applications in catalysis. *Chem. Soc. Rev.* **50**, 6152–6220 (2021).
72. Chui, S. S.-Y., Lo, S. M.-F., Charmant, J. P. H., Orpen, A. G. & Williams, I. D. A Chemically Functionalizable Nanoporous Material $[\text{Cu}_3(\text{TMA})_2(\text{H}_2\text{O})_3]_n$. *Science* **283**, 1148–1150 (1999).
73. Leus, K. *et al.* Systematic study of the chemical and hydrothermal stability of selected “stable” Metal Organic Frameworks. *Microporous Mesoporous Mater.* **226**, 110–116 (2016).
74. Park, K. S. *et al.* Exceptional chemical and thermal stability of zeolitic imidazolate frameworks. *Proc. Natl. Acad. Sci.* **103**, 10186–10191 (2006).
75. Ferey, G. A Chromium Terephthalate-Based Solid with Unusually Large Pore Volumes and Surface Area. *Science* **309**, 2040–2042 (2005).
76. Rallapalli, P. B. S., Raj, M. C., Senthilkumar, S., Somani, R. S. & Bajaj, H. C. HF-free synthesis of MIL-101(Cr) and its hydrogen adsorption studies. *Environ. Prog. Sustain. Energy* **35**, 461–468 (2016).

77. Lammert, M., Bernt, S., Vermoortele, F., De Vos, D. E. & Stock, N. Single- and Mixed-Linker Cr-MIL-101 Derivatives: A High-Throughput Investigation. *Inorg. Chem.* **52**, 8521–8528 (2013).
78. Wittmann, T. *et al.* Enhancing the Water Stability of Al-MIL-101-NH₂ via Postsynthetic Modification. *Chem. – Eur. J.* **21**, 314–323 (2015).
79. Bhattacharjee, S., Chen, C. & Ahn, W.-S. Chromium terephthalate metal–organic framework MIL-101: synthesis, functionalization, and applications for adsorption and catalysis. *RSC Adv.* **4**, 52500–52525 (2014).
80. Férey, G. *et al.* A Hybrid Solid with Giant Pores Prepared by a Combination of Targeted Chemistry, Simulation, and Powder Diffraction. *Angew. Chem. Int. Ed.* **43**, 6296–6301 (2004).
81. Akiyama, G., Matsuda, R. & Kitagawa, S. Highly Porous and Stable Coordination Polymers as Water Sorption Materials. *Chem. Lett.* **39**, 360–361 (2010).
82. Küsgens, P. *et al.* Characterization of metal–organic frameworks by water adsorption. *Microporous Mesoporous Mater.* **120**, 325–330 (2009).
83. Haouas, M., Volkringer, C., Loiseau, T., Férey, G. & Taulelle, F. Monitoring the Activation Process of the Giant Pore MIL-100(Al) by Solid State NMR. *J. Phys. Chem. C* **115**, 17934–17944 (2011).
84. Bezverkhy, I., Weber, G. & Bellat, J.-P. Degradation of fluoride-free MIL-100(Fe) and MIL-53(Fe) in water: Effect of temperature and pH. *Microporous Mesoporous Mater.* **219**, 117–124 (2016).
85. Feng, L., Day, G. S., Wang, K.-Y., Yuan, S. & Zhou, H.-C. Strategies for Pore Engineering in Zirconium Metal–Organic Frameworks. *Chem* **6**, 2902–2923 (2020).
86. Cavka, J. H. *et al.* A New Zirconium Inorganic Building Brick Forming Metal Organic Frameworks with Exceptional Stability. *J. Am. Chem. Soc.* **130**, 13850–13851 (2008).
87. Wu, H. *et al.* Unusual and Highly Tunable Missing-Linker Defects in Zirconium Metal–Organic Framework UiO-66 and Their Important Effects on Gas Adsorption. *J. Am. Chem. Soc.* **135**, 10525–10532 (2013).
88. Salomon, W. *et al.* Immobilization of polyoxometalates in the Zr-based metal organic framework UiO-67. *Chem. Commun.* **51**, 2972–2975 (2015).
89. Paille, G. *et al.* A Fully Noble Metal-Free Photosystem Based on Cobalt-Polyoxometalates Immobilized in a Porphyrinic Metal–Organic Framework for Water Oxidation. *J. Am. Chem. Soc.* **140**, 3613–3618 (2018).
90. Morris, W. *et al.* Synthesis, structure, and metalation of two new highly porous zirconium metal–organic frameworks. *Inorg. Chem.* **51**, 6443–6445 (2012).
91. Liu, T.-F. *et al.* Topology-Guided Design and Syntheses of Highly Stable Mesoporous Porphyrinic Zirconium Metal–Organic Frameworks with High Surface Area. *J. Am. Chem. Soc.* **137**, 413–419 (2015).
92. Feng, D. *et al.* Construction of Ultrastable Porphyrin Zr Metal–Organic Frameworks through Linker Elimination. *J. Am. Chem. Soc.* **135**, 17105–17110 (2013).
93. Feng, D. *et al.* A Highly Stable Porphyrinic Zirconium Metal–Organic Framework with shp-a Topology. *J. Am. Chem. Soc.* **136**, 17714–17717 (2014).
94. Feng, D. *et al.* Zirconium-Metalloporphyrin PCN-222: Mesoporous Metal–Organic Frameworks with Ultrahigh Stability as Biomimetic Catalysts. *Angew. Chem. Int. Ed.* **51**, 10307–10310 (2012).
95. Chen, Y., Hoang, T. & Ma, S. Biomimetic Catalysis of a Porous Iron-Based Metal–Metalloporphyrin Framework. *Inorg. Chem.* **51**, 12600–12602 (2012).
96. Jiang, H.-L. *et al.* An Exceptionally Stable, Porphyrinic Zr Metal–Organic Framework Exhibiting pH-Dependent Fluorescence. *J. Am. Chem. Soc.* **135**, 13934–13938 (2013).

97. Deria, P., Yu, J., Balaraman, R. P., Mashni, J. & White, S. N. Topology-dependent emissive properties of zirconium-based porphyrin MOFs. *Chem. Commun.* **52**, 13031–13034 (2016).
98. Morris, W. *et al.* Synthesis, Structure, and Metalation of Two New Highly Porous Zirconium Metal–Organic Frameworks. *Inorg. Chem.* **51**, 6443–6445 (2012).
99. Paille, G. *et al.* A Fully Noble Metal-Free Photosystem Based on Cobalt-Polyoxometalates Immobilized in a Porphyrinic Metal–Organic Framework for Water Oxidation. *J. Am. Chem. Soc.* **140**, 3613–3618 (2018).
100. Xu, H.-Q. *et al.* Visible-Light Photoreduction of CO₂ in a Metal–Organic Framework: Boosting Electron–Hole Separation via Electron Trap States. *J. Am. Chem. Soc.* **137**, 13440–13443 (2015).
101. Feng, D. *et al.* Zirconium-Metalloporphyrin PCN-222: Mesoporous Metal-Organic Frameworks with Ultrahigh Stability as Biomimetic Catalysts. *Angew. Chem. Int. Ed.* **51**, 10307–10310 (2012).
102. Wang, S.-S. & Yang, G.-Y. Recent Advances in Polyoxometalate-Catalyzed Reactions. *Chem. Rev.* **115**, 4893–4962 (2015).
103. Taherimehr, M. *et al.* Strategies for Enhancing the Catalytic Performance of Metal-Organic Frameworks in the Fixation of CO₂ into Cyclic Carbonates. *ChemSusChem* **10**, 1283–1291 (2017).
104. Julião, D. *et al.* Zinc-Substituted Polyoxotungstate@amino-MIL-101(Al) - An Efficient Catalyst for the Sustainable Desulfurization of Model and Real Diesels: Zinc-Substituted Polyoxotungstate@amino-MIL-101(Al) - An Efficient Catalyst for the Sustainable Desulfurization of Model and Real Diesels. *Eur. J. Inorg. Chem.* **2016**, 5114–5122 (2016).
105. Bromberg, L., Su, X. & Hatton, T. A. Heteropolyacid-Functionalized Aluminum 2-Aminoterephthalate Metal-Organic Frameworks As Reactive Aldehyde Sorbents and Catalysts. *ACS Appl. Mater. Interfaces* **5**, 5468–5477 (2013).
106. James, S. L. *et al.* Mechanochemistry: opportunities for new and cleaner synthesis. *Chem Soc Rev* **41**, 413–447 (2012).
107. Szczeńsiak, B., Borysiuk, S., Choma, J. & Jaroniec, M. Mechanochemical synthesis of highly porous materials. *Mater. Horiz.* **7**, 1457–1473 (2020).
108. Liu, Y. *et al.* Facile Synthesis of a Nanocrystalline Metal-Organic Framework Impregnated with a Phosphovanadomolybdate and Its Remarkable Catalytic Performance in Ultradeep Oxidative Desulfurization. *ChemCatChem* **5**, 3086–3091 (2013).
109. Zhong, X. *et al.* A Nanocrystalline POM@MOFs Catalyst for the Degradation of Phenol: Effective Cooperative Catalysis by Metal Nodes and POM Guests. *Chem. - Eur. J.* **24**, 3045–3051 (2018).
110. Li, R. *et al.* Polyoxometallates trapped in a zeolitic imidazolate framework leading to high uptake and selectivity of bioactive molecules. *J Mater Chem A* **2**, 2168–2173 (2014).
111. Zhao, X. *et al.* Efficient Mechanochemical Synthesis of Polyoxometalate⊂ZIF Complexes as Reusable Catalysts for Highly Selective Oxidation. *Inorg. Chem.* **56**, 14506–14512 (2017).
112. Salomon, W. *et al.* Immobilization of Co-containing polyoxometalates in MIL-101(Cr): structural integrity versus chemical transformation. *Dalton Trans* **43**, 12698–12705 (2014).
113. Wang, X., Wisser, F. M., Canivet, J., Fontecave, M. & Mellot-Draznieks, C. Immobilization of a Full Photosystem in the Large-Pore MIL-101 Metal-Organic Framework for CO₂ reduction. *ChemSusChem* **11**, 3315–3322 (2018).
114. Chen, D. *et al.* Salen(Co(III)) imprisoned within pores of a metal–organic framework by post-synthetic modification and its asymmetric catalysis for CO₂ fixation at room temperature. *Chem. Commun.* **53**, 10930–10933 (2017).

115. Li, Z., Rayder, T. M., Luo, L., Byers, J. A. & Tsung, C.-K. Aperture-Opening Encapsulation of a Transition Metal Catalyst in a Metal–Organic Framework for CO₂ Hydrogenation. *J. Am. Chem. Soc.* **140**, 8082–8085 (2018).
116. Yan, Z.-H. *et al.* Encapsulating a Ni(II) molecular catalyst in photoactive metal–organic framework for highly efficient photoreduction of CO₂. *Sci. Bull.* **64**, 976–985 (2019).
117. Li, Z., Xiao, J.-D. & Jiang, H.-L. Encapsulating a Co(II) Molecular Photocatalyst in Metal–Organic Framework for Visible-Light-Driven H₂ Production: Boosting Catalytic Efficiency via Spatial Charge Separation. *ACS Catal.* **6**, 5359–5365 (2016).
118. Nasalevich, M. A. *et al.* Co@NH₂-MIL-125(Ti): cobaloxime-derived metal–organic framework-based composite for light-driven H₂ production. *Energy Environ. Sci.* **8**, 364–375 (2015).
119. Yeganeh, A. D., Amini, M. M. & Safari, N. *In situ* synthesis and encapsulation of copper phthalocyanine into MIL-101(Cr) and MIL-100(Fe) pores and investigation of their catalytic performance in the epoxidation of styrene. *J. Porphyr. Phthalocyanines* **23**, 1118–1131 (2019).
120. Boroujeni, M. B., Hashemzadeh, A., Shaabani, A. & Amini, M. M. *In situ* synthesis of metallophthalocyanines into pores of MIL-101: A novel and green strategy for preparation of host-guest catalysts. *Appl. Organomet. Chem.* **31**, e3715 (2017).
121. Yang, L., Naruke, H. & Yamase, T. A novel organic/inorganic hybrid nanoporous material incorporating Keggin-type polyoxometalates. *Inorg. Chem. Commun.* **6**, 1020–1024 (2003).
122. Sun, C.-Y. *et al.* Highly Stable Crystalline Catalysts Based on a Microporous Metal–Organic Framework and Polyoxometalates. *J. Am. Chem. Soc.* **131**, 1883–1888 (2009).
123. Liu, Y. *et al.* Crystal Facets Make a Profound Difference in Polyoxometalate-Containing Metal–Organic Frameworks as Catalysts for Biodiesel Production. *J. Am. Chem. Soc.* **137**, 12697–12703 (2015).
124. Song, J. *et al.* A Multiunit Catalyst with Synergistic Stability and Reactivity: A Polyoxometalate–Metal Organic Framework for Aerobic Decontamination. *J. Am. Chem. Soc.* **133**, 16839–16846 (2011).
125. Liu, S.-M. *et al.* Ti-Substituted Keggin-Type Polyoxotungstate as Proton and Electron Reservoir Encaged into Metal–Organic Framework for Carbon Dioxide Photoreduction. *Adv. Mater. Interfaces* **5**, 1801062 (2018).
126. Ma, F.-J. *et al.* Adsorption of volatile organic compounds in porous metal–organic frameworks functionalized by polyoxometalates. *J. Solid-State Chem.* **184**, 3034–3039 (2011).
127. Liang, D.-D., Liu, S.-X., Ma, F.-J., Wei, F. & Chen, Y.-G. A Crystalline Catalyst Based on a Porous Metal–Organic Framework and 12-Tungstosilicic Acid: Particle Size Control by Hydrothermal Synthesis for the Formation of Dimethyl Ether. *Adv. Synth. Catal.* **353**, 733–742 (2011).
128. Sharma, N., Dhankhar, S. S. & Nagaraja, C. M. Environment-friendly, co-catalyst- and solvent-free fixation of CO₂ using an ionic zinc(II)–porphyrin complex immobilized in porous metal–organic frameworks. *Sustain. Energy Fuels* **3**, 2977–2982 (2019).
129. Mukhopadhyay, S., Debgupta, J., Singh, C., Kar, A. & Das, S. K. A Keggin Polyoxometalate Shows Water Oxidation Activity at Neutral pH: POM@ZIF-8, an Efficient and Robust Electrocatalyst. *Angew. Chem. Int. Ed.* **57**, 1918–1923 (2018).
130. Gkaniatsou, E. *et al.* Enzyme Encapsulation in Mesoporous Metal–Organic Frameworks for Selective Biodegradation of Harmful Dye Molecules. *Angew. Chem. Int. Ed.* **57**, 16141–16146 (2018).
131. Park, H. D., Dincă, M. & Román-Leshkov, Y. Heterogeneous Epoxide Carbonylation by Cooperative Ion-Pair Catalysis in Co(CO)₄[−]-Incorporated Cr-MIL-101. *ACS Cent. Sci.* **3**, 444–448 (2017).

132. Buru, C. T. *et al.* Adsorption of a Catalytically Accessible Polyoxometalate in a Mesoporous Channel-type Metal–Organic Framework. *Chem. Mater.* **29**, 5174–5181 (2017).
133. Wang, X., Lu, W., Gu, Z.-Y., Wei, Z. & Zhou, H.-C. Topology-guided design of an anionic **bor**-network for photocatalytic $[\text{Ru}(\text{bpy})_3]^{2+}$ encapsulation. *Chem. Commun.* **52**, 1926–1929 (2016).
134. Genna, D. T. *et al.* Rhodium Hydrogenation Catalysts Supported in Metal Organic Frameworks: Influence of the Framework on Catalytic Activity and Selectivity. *ACS Catal.* **6**, 3569–3574 (2016).
135. Grigoropoulos, A. *et al.* Encapsulation of Crabtree’s Catalyst in Sulfonated MIL-101(Cr): Enhancement of Stability and Selectivity between Competing Reaction Pathways by the MOF Chemical Microenvironment. *Angew. Chem. Int. Ed.* **57**, 4532–4537 (2018).
136. Genna, D. T., Wong-Foy, A. G., Matzger, A. J. & Sanford, M. S. Heterogenization of Homogeneous Catalysts in Metal–Organic Frameworks via Cation Exchange. *J. Am. Chem. Soc.* **135**, 10586–10589 (2013).
137. Grigoropoulos, A. *et al.* Encapsulation of an organometallic cationic catalyst by direct exchange into an anionic MOF. *Chem. Sci.* **7**, 2037–2050 (2016).
138. Lin, Z.-J. *et al.* Encapsulation of Phosphotungstic Acid into Metal–Organic Frameworks with Tunable Window Sizes: Screening of PTA@MOF Catalysts for Efficient Oxidative Desulfurization. *Inorg. Chem.* **57**, 13009–13019 (2018).
139. Granadeiro, C. M. *et al.* Oxidative catalytic versatility of a trivacant polyoxotungstate incorporated into MIL-101(Cr). *Catal. Sci. Technol.* **4**, 1416 (2014).
140. Granadeiro, C. M. *et al.* Monovacant polyoxometalates incorporated into MIL-101(Cr): novel heterogeneous catalysts for liquid phase oxidation. *Appl. Catal. Gen.* **453**, 316–326 (2013).
141. Maksimchuk, N. *et al.* Heterogeneous selective oxidation catalysts based on coordination polymer MIL-101 and transition metal-substituted polyoxometalates. *J. Catal.* **257**, 315–323 (2008).
142. Chołuj, A., Zieliński, A., Grela, K. & Chmielewski, M. J. Metathesis@MOF: Simple and Robust Immobilization of Olefin Metathesis Catalysts inside (Al)MIL-101-NH₂. *ACS Catal.* **6**, 6343–6349 (2016).
143. Julião, D. *et al.* Desulfurization of model diesel by extraction/oxidation using a zinc-substituted polyoxometalate as catalyst under homogeneous and heterogeneous (MIL-101(Cr) encapsulated) conditions. *Fuel Process. Technol.* **131**, 78–86 (2015).
144. Juan-Alcañiz, J., Ramos-Fernandez, E. V., Lafont, U., Gascon, J. & Kapteijn, F. Building MOF bottles around phosphotungstic acid ships: One-pot synthesis of bi-functional polyoxometalate-MIL-101 catalysts. *J. Catal.* **269**, 229–241 (2010).
145. Yang, X.-L., Qiao, L.-M. & Dai, W.-L. Phosphotungstic acid encapsulated in metal-organic framework UiO-66: An effective catalyst for the selective oxidation of cyclopentene to glutaraldehyde. *Microporous Mesoporous Mater.* **211**, 73–81 (2015).
146. Mukhopadhyay, S., Basu, O., Kar, A. & Das, S. K. Efficient Electrocatalytic Water Oxidation by Fe(salen)–MOF Composite: Effect of Modified Microenvironment. *Inorg. Chem.* **59**, 472–483 (2020).
147. Fernandes, D. M. *et al.* SiW₁₁Fe@MIL-101(Cr) Composite: A Novel and Versatile Electrocatalyst. *ChemElectroChem* **1**, 1293–1300 (2014).
148. Song, X. *et al.* Polyoxomolybdic Cobalt Encapsulated within Zr-Based Metal–Organic Frameworks as Efficient Heterogeneous Catalysts for Olefins Epoxidation. *ACS Sustain. Chem. Eng.* **7**, 3624–3631 (2019).
149. Balula, S. S., Granadeiro, C. M., Barbosa, A. D. S., Santos, I. C. M. S. & Cunha-Silva, L. Multifunctional catalyst based on sandwich-type polyoxotungstate and MIL-101 for liquid phase oxidations. *Catal. Today* **210**, 142–148 (2013).

150. Granadeiro, C. M. *et al.* Novel heterogeneous catalysts based on lanthanopolyoxometalates supported on MIL-101(Cr). *Catal. Today* **218–219**, 35–42 (2013).
151. Jarrah, A. & Farhadi, S. $K_6P_2W_{18}O_{62}$ encapsulated into magnetic Fe_3O_4 /MIL-101 (Cr) metal–organic framework: a novel magnetically recoverable nanoporous adsorbent for ultrafast treatment of aqueous organic pollutants solutions. *RSC Adv.* **8**, 37976–37992 (2018).
152. Zalomaeva, O. V. *et al.* Iron tetrasulfophthalocyanine immobilized on metal-organic framework MIL-101: synthesis, characterization and catalytic properties. *Dalton Trans.* **40**, 1441 (2011).
153. Wang, X.-S., Li, L., Liang, J., Huang, Y.-B. & Cao, R. Boosting Oxidative Desulfurization of Model and Real Gasoline over Phosphotungstic Acid Encapsulated in Metal-Organic Frameworks: The Window Size Matters. *ChemCatChem* **9**, 971–979 (2017).
154. Kockrick, E., Lescouet, T., Kudrik, E. V., Sorokin, A. B. & Farrusseng, D. Synergistic effects of encapsulated phthalocyanine complexes in MIL-101 for the selective aerobic oxidation of tetralin. *Chem Commun* **47**, 1562–1564 (2011).
155. Maksimchuk, N. V. *et al.* Hybrid Polyoxotungstate/MIL-101 Materials: Synthesis, Characterization, and Catalysis of H_2O_2 -Based Alkene Epoxidation. *Inorg. Chem.* **49**, 2920–2930 (2010).
156. Chen, Y., Fan, B., Lu, N. & Li, R. Aluminum metal–organic framework as a new host for preparation of encapsulated metal complex catalysts. *Catal. Commun.* **64**, 91–95 (2015).
157. Bajpe, S. R. *et al.* Direct Observation of Molecular-Level Template Action Leading to Self-Assembly of a Porous Framework. *Chem. - Eur. J.* **16**, 3926–3932 (2010).
158. Bromberg, L., Diao, Y., Wu, H., Speakman, S. A. & Hatton, T. A. Chromium(III) Terephthalate Metal Organic Framework (MIL-101): HF-Free Synthesis, Structure, Polyoxometalate Composites, and Catalytic Properties. *Chem. Mater.* **24**, 1664–1675 (2012).
159. Wang, X.-S., Huang, Y.-B., Lin, Z.-J. & Cao, R. Phosphotungstic acid encapsulated in the mesocages of amine-functionalized metal–organic frameworks for catalytic oxidative desulfurization. *Dalton Trans* **43**, 11950–11958 (2014).
160. Fu, Y. *et al.* An Amine-Functionalized Titanium Metal–Organic Framework Photocatalyst with Visible-Light-Induced Activity for CO_2 Reduction. *Angew. Chem. Int. Ed.* **51**, 3364–3367 (2012).
161. Luo, T. *et al.* Metal–Organic Framework-Stabilized CO_2 /Water Interfacial Route for Photocatalytic CO_2 Conversion. *ACS Appl. Mater. Interfaces* **9**, 41594–41598 (2017).
162. Sun, D. *et al.* Studies on Photocatalytic CO_2 Reduction over NH_2 -Uio-66(Zr) and Its Derivatives: Towards a Better Understanding of Photocatalysis on Metal–Organic Frameworks. *Chem. – Eur. J.* **19**, 14279–14285 (2013)

Chapter 2: Co-immobilization of a Keggin POM and a Rh-catalyst in UiO-67 MOF: in-depth characterization and CO₂ photosensitized reduction

As mentioned in the first chapter, catalyst incorporation in porous materials increases in most cases its stability, eventually its efficiency while allowing the final composite to be collected back after the catalytic run, thus enhancing its recyclability. This chapter highlights the co-immobilization of a rhodium catalyst, namely Cp^{*}Rh^I and the Keggin type POM PW₁₂ in the UiO-67 MOF used as an heterogenization scaffold. Both the immobilization of Cp^{*}Rh and PW₁₂, in two separated studies, have been previously achieved by previous fellows from the laboratories. Cp^{*}Rh once in the UiO-67 is still able to reduce CO₂ in formate and H₂, while PW₁₂ can act as an electron and/or proton relay. The co-immobilization of the two moieties in the UiO-67 framework could show synergetic effects and enhance the overall composite efficiency for CO₂ photoreduction.

This work has been conducted in close collaboration with Mathis Duguet, Alex Lemarchand, and Mohamed Haouas, student, postdoctoral fellow and researcher respectively, at the time of the study. Mathis Duguet conducted DFT calculations to find where the POM could be positioned inside the MOF pores while Alex Lemarchand focused on the pair distribution analysis (PDF) of the POM@MOF and (POM,cat)@MOF materials, Mohamed Haouas performed the ssNMR. My involvement to this project is in two points: first, the synthesis of all POM@MOF, cat@MOF and (POM,cat)@MOF composites as well as most of their physicochemical characterization; second, the photochemical CO₂ reduction tests. In this chapter, I will emphasize on my contribution. Nevertheless, a subpart is dedicated to the work of my coworkers since without their efforts, this study would have been incomplete. Lastly, Dr. Albert Solé-Dora succeeded in computing a plausible mechanism for the CO₂ reduction with our system which I will briefly describe.

1. State of the art for Rhodium bipyridine complexes for CO₂ reduction

Rhodium bipyridine complexes were first used as catalysts for CO₂ electroreduction by Bolinger *et al.* in 1985² and 1988³. They have based their research on the cis-[Rh(bpy)₂X₂]⁺ complexes (X = Cl⁻ or trifluoromethanesulphonate OTf⁻). The catalysts were investigated by cyclic voltammetry which revealed an enhanced cathodic current density in presence of CO₂,

attributed to catalytic CO_2 reduction. These complexes were further studied by bulk electrolysis at -1.93 V vs. Fc^+/Fc in MeCN, and afforded the production of mixtures of H_2 and formate. The faradaic yields varied depending on the total charge passed, starting close to 100% and decreasing as more coulombs were passed. For example, the faradaic yield for formate dropped from 83% to 52% and 36% as the charge passed increased from 77 to 111 and about 150 C. By contrast, the faradaic yield for H_2 rose slightly, from 10% to 20% as the current increased. This change of selectivity is assigned by the authors to the irreversible reduction of Rh and bpy ligand.

Meanwhile, Kölle and Grützel published in 1987⁴ the synthesis of a new Rh-bipyridine based catalyst, namely $[\text{Cp}^*\text{Rh}(\text{ppy})\text{L}]^{n+}$ (with $n = 1$ or 2 depending on L charge, $\text{L} = \text{H}_2\text{O}$, OH^- , Cl^- and I^- and $\text{ppy} = 2,2'$ -bipyridine, $2,2'$ -bipyridine $4,4'$ -dicarboxylic acid, $4,4'$ -diacetyl- $2,2'$ -bipyridine or $1,10$ -phenanthroline) (**Figure 2.1**). The catalysts were built by the reaction of a solution of $\{\text{Cp}^*\text{RhCl}(\mu\text{-Cl})\}_2$ dimers and an oligopyridine ligand in methanol at ambient temperature for 30 min. The different catalysts were investigated for proton photoreduction and represent the first report of these rhodium bipyridine systems for photochemical catalysis. At $\text{pH} < 7$, irradiation of $5\text{ }\mu\text{mol}$ of $[\text{Cp}^*\text{Rh}(\text{bpy})\text{L}]^{n+}$ in 20 mL of a solution containing 25 mg of TiO_2 leads after 3h to the formation of 0.5 mL of H_2 which corresponds to a TON of 4.5.

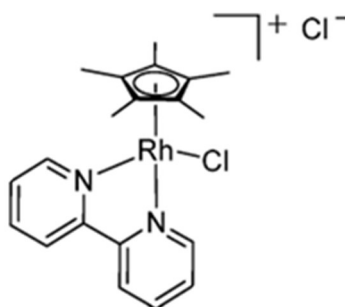


Figure 2.1: Scheme of $[\text{Cp}^*\text{Rh}(2,2'\text{-bipyridine})\text{Cl}]\text{Cl}$

Later, Deronzier⁵ and his team worked with the same molecular complex reporting for the first time the use of rhodium bipyridine systems for CO_2 electrocatalytic reduction. The main reaction products observed were formate and H_2 with a varying selectivity depending on reaction conditions. In acetonitrile, with tetrabutylammonium perchlorate as an electrolyte and at $E_{\text{app}} = -1.60\text{ V}$ vs. Ag/Ag^+ , no catalytic effect can be observed, requiring the addition of 3% of water to start the catalytic reaction. Further addition of water increases the faradaic yield for both formate and H_2 where at 5% water content the current efficiency of formate reaches 25%

while that of H_2 reaches about 10%. The best faradaic yield is reached at 20% water content where the formate current efficiency is at 36% and H_2 at 30%. The suggested mechanism involves a two electrons -one proton reduction of the rhodium center going from Rh(III) to Rh(I) , followed by a single electron transfer on the bipyridine ligand leading to the active species. The presence of water increases the proton concentration leading to higher faradaic yields.

The Cp^*Rh complex has been first studied for its ability to photoreduce CO_2 in 2015 by a previous postdoc of our laboratory at LCPB, Matthew Chambers,¹ and his co-workers. Surprisingly, no study of the Cp^*Rh for CO_2 photoreduction was indeed conducted so far, although this complex was first reported in 1988 for H_2 photoreduction and in 1997 for CO_2 electroreduction, as mentioned above. Moreover, at the time of Chambers *et al.* study only two reports of immobilized CO_2 reducing complexes in coordination polymers were published, being limited to a rhenium carbonyl and a ruthenium carbonyl complex immobilized in UiO-67 MOF by Wenbin Lin and collaborators⁶ and to an iridium complex immobilized in a non-porous coordination polymer based on ytterbium.⁷ Brief reminder, UiO-67 elemental formula is $\text{Zr}_6\text{O}_4(\text{OH})_4(\text{C}_{14}\text{O}_4\text{H}_8)_6$ and is constituted of Zr oxo-clusters linked by 4,4'-biphenyldicarboxylate (BPDC) linkers. UiO-67 is composed of octahedral and tetrahedral cages of 18 Å and 11.5 Å internal diameters, respectively (**Figure 2.2 a**). Its zirconium cluster is fully saturated with a coordination of 12. The pores are big enough to host a large variety of molecules.⁸

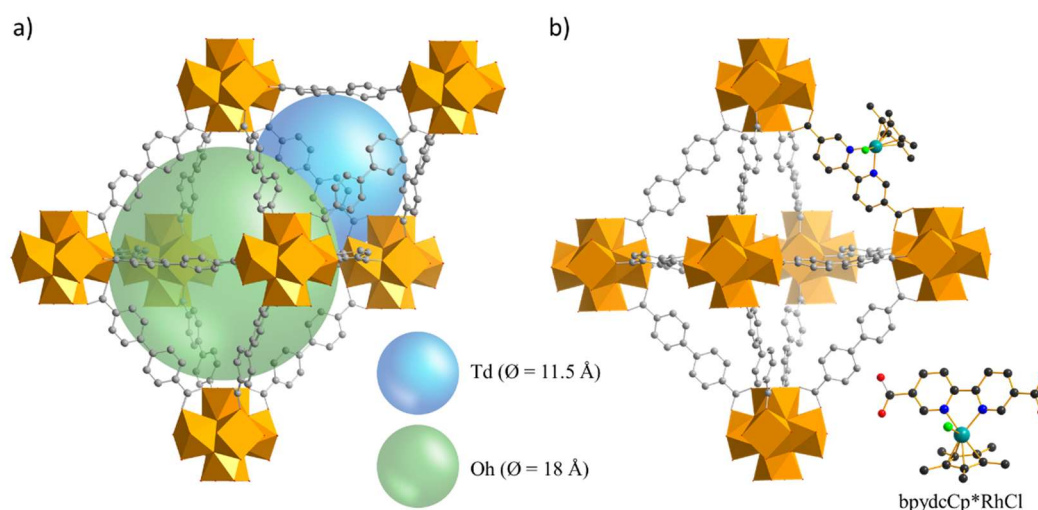


Figure 2.2: a) Representation of the UiO-67 framework and b) the $\text{Cp}^*\text{Rh}@ \text{UiO-67}$. $\text{Zr}_6\text{O}_4(\text{OH})_4$ clusters are represented in orange, C in grey, Rh in cyan, N in deep blue and Cl in green.

Research on catalyst immobilization in porous materials has been since then intensively developed, whereby a range of different works can be found in a recent review.⁹ The aim of the previous work¹ of our group at LCPB was two-fold: first, to successively immobilize this catalytic complex in a porous host, the UiO-67 MOF, as part of the framework (**Figure 2.2 b**), and second to demonstrate the ability of the Cp^*Rh complex to photoreduce CO_2 . The scope of the study was limited to two homologues of the Cp^*Rh catalyst, i.e. $[\text{Cp}^*\text{Rh}(\text{bpy})\text{Cl}]\text{Cl}$ and $[\text{Cp}^*\text{Rh}(\text{bpydc})\text{Cl}]\text{Cl}$, with bpydc being the 2,2'-bipyridine-5,5'-dicarboxylic acid version of the linker, so as to allow its incorporation into the MOF as a linker. The complexes were both studied in homogeneous conditions and $[\text{Cp}^*\text{Rh}(\text{bpydc})\text{Cl}]\text{Cl}$ has been immobilized in the UiO-67 MOF using a post-synthetic exchange (PSE) method developed by Pullen *et al.*¹⁰ (**Figure 2.3 a**). The MOF and the complex were reacted in deionized water leading to the formation of four UiO-67-based materials where 5%, 10%, 20% and 35% of the original biphenyl dicarboxylic acid linker were exchanged by the catalytic $[\text{Cp}^*\text{Rh}(\text{bpydc})\text{Cl}]^+$ linker. The photocatalytic reduction of CO_2 was conducted in ACN:TEOA (5:1) with 1 mM of $[\text{Ru}(\text{bpy})_3]\text{Cl}_2$ as an external photosensitizer. The authors reported for the homogeneous catalyst a good activity during the CO_2 photocatalytic reduction process with a selective production of formate (TON = 125 for $\text{Cp}^*\text{Rh}(\text{bpy})$ and 42 for $\text{Cp}^*\text{Rh}(\text{bpydc})$). The significant decrease with $\text{Cp}^*\text{Rh}(\text{bpydc})$ is attributed by the authors to the electron-withdrawing nature of COOH which decreases the efficiency for CO_2 reduction. No other carbon products were detected and H_2 was the only other product with TON = 55 and 38 for $\text{Cp}^*\text{Rh}(\text{bpy})$ and $\text{Cp}^*\text{Rh}(\text{bpydc})$, giving a similar selectivity than in electrochemical conditions.

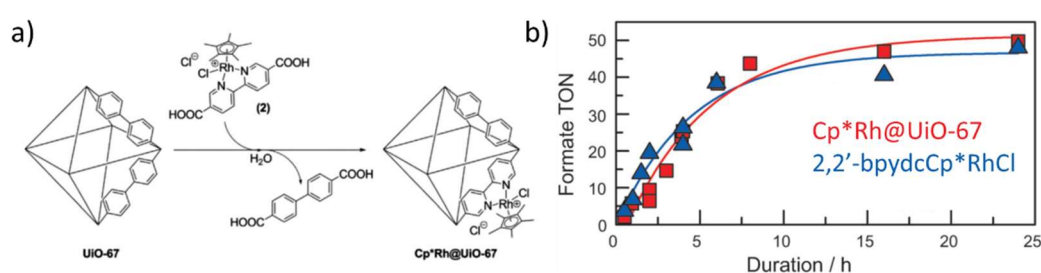


Figure 2.3: a) Scheme of the $\text{Cp}^*\text{Rh@UiO-67}$ composite preparation : Schematic PSE of biphenyl dicarboxylic acid by the $\text{Cp}^*\text{Rh}(\text{bpydc})$ catalyst and b) formate production over time by the homogeneous $\text{Cp}^*\text{Rh}(\text{bpydc})$ (blue) and heterogenous $\text{Cp}^*\text{Rh@UiO-67}$ (red) catalysts.¹

The investigation of heterogeneous complexes thus showed that the catalytic activity was retained and comparable to that found for the homogeneous $\text{Cp}^*\text{Rh}(\text{bpydc})$ catalyst (**Figure 2.3 b**), with TON = 47 vs 42 for formate and TON = 36 vs 38 for H_2 . The recyclability experiments

were taken with 4 mg of 10%-Cp*Rh@UiO-67 irradiated for six cycles of 16h. Between each cycle, the cat@MOF was collected by centrifugation and the formate was assessed by ionic chromatography, showing a retained activity even after six cycles. Lastly, different materials %Cp*Rh@UiO-67, differing by the amount of catalyst introduced in the MOF, have been tested (**Table 2.1**), the authors showing that the lesser Cp*Rh in the MOF, the better the activity, whereby the 5%-Cp*Rh@UiO-67 was found as the most active compound. Other examples of immobilized Cp*Rh in MOF have been later reported where, for example Cp*Rh has been co-immobilized with [Ru(bpy)₂(bpydc)]²⁺ in the MIL-101-NH₂(Al) MOF giving a photosensitive and photocatalytic composite.^{11,12}

Table 2.1: Catalytic CO₂ photoreduction with varying amount of substituted Cp*Rh linker in %Cp*Rh@UiO-67.¹

Entry	%Rh	$\mu\text{mol Rh}$	TOF /hr (formate)	TON (formate)	TOF /hr (H ₂)	TON (H ₂)	TOF Ratio	TON Ratio
1	0	0	0	0.22	0	0.1	-	-
2	5	0.04	8.4	85	4.2	54	2.0	1.6
3	10	0.09	7.4	47	5.4	36	1.4	1.3
4	20	0.16	3.0	37	3.6	45	0.83	0.82
5	35	0.23	0.2	6	2.4	14	0.08	0.41

In 2019, Todorova et al.¹³ highlighted the mechanism for CO₂ reduction with [Cp*Rh(bpy-R)Cl]Cl derivatives. Combining both experimental and theoretical results, they investigated the effect of the substituent of bipyridine (**Figure 2.4**) on the selectivity toward HCOOH and the overall efficiency. They focus the DFT calculations on the C3 and C8 derivatives (see **Figure 2.4**) corresponding to an electron-donating and -withdrawing group, respectively. In both cases, the first step is a two-electron reduction of the Rh(III) to Rh(I) accompanied by the loss of the Cl⁻ counterion. This step is followed by the protonation of the Rh then a first proton transfer from the Rh to the Cp* ring, which is strongly facilitated by the presence of electron-withdrawing groups, leading to an equilibrium between [RhH] and [Cp*H], with [Cp*H] being the more stable by 2 to 3 kcal·mol⁻¹. CO₂ reduction happens by a direct hydride transfer from [RhH] to CO₂ to form the [Rh···HCO₂⁻] adduct, a protonation then leads to the formation of HCOOH. A hydride transfer from the [Cp*H] to CO₂ is less likely to occur as the transition state is much higher in energy. The nature of the substituents plays a huge role on the selectivity as electron-donating ligands can facilitate the hydride transfer to formate by lowering the energy barrier thus increasing the HCOOH:H₂ ratio (**Figure 2.4**).

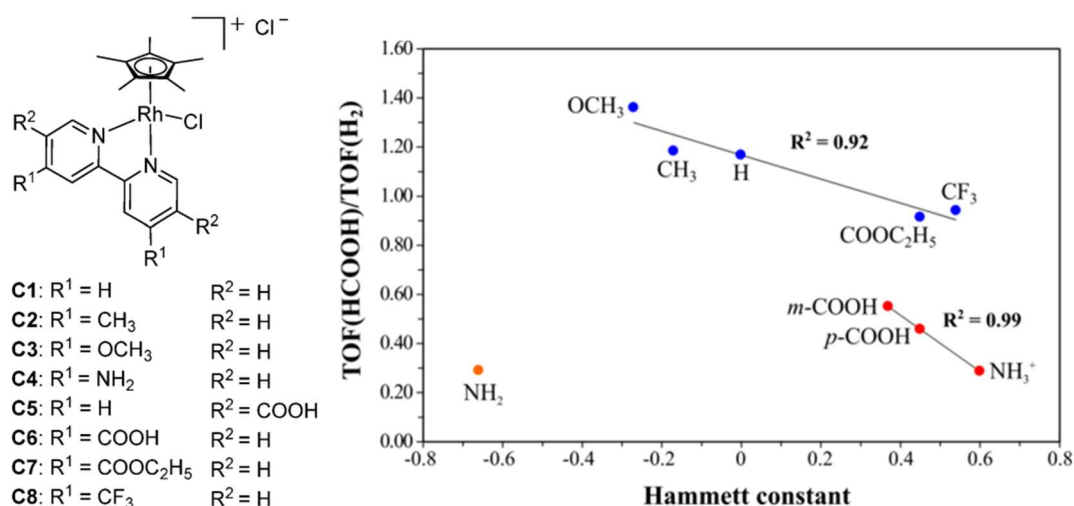


Figure 2.4: Structures of [Cp*Rh(bpy-R)Cl]Cl complexes (left) and correlation between the Hammett constant and the TOF(HCOOH)/TOF(H₂) of the complexes (right).¹³

Meanwhile, Salomon *et al.*¹⁴ have successfully immobilized a series of polyoxometalates in the same UiO-67 MOF preparing POM@MOF materials with POMs such as PW₁₁, PW₁₂ and P₂W₁₈. The authors have synthesized the POM@MOF compounds by direct solvothermal synthesis in DMF, adding both the MOF precursors and the preformed POMs. The integrity of the POMs was verified by ³¹P MAS NMR, where the chemical shifts of the polyoxometalates were maintained (-12.9 ppm for P₂W₁₈, -13.2 ppm for PW₁₁ and -15.2 ppm for PW₁₂). In addition, IR spectroscopy showed the characteristic P-O and W-O vibration bands between 850 and 1100 cm⁻¹, confirming the integrity of the incorporated POMs. The N₂ adsorption measurements were in agreement with the presence of the POM inside the pores with a decreasing adsorbed volume with empty UiO-67 > PW₁₁ > PW₁₂ > P₂W₁₈ (2400, 1400, 1390 and 1100 m²·g⁻¹ respectively) in accordance with the POM size and loading. No application has been reported for the composites by the authors.

The combination of Keggin POMs and CO₂ reduction catalyst started in 2011, when a first report from Neumann and col.¹⁵ described the photoreduction of CO₂ into CO by a rhenium phenanthroline-polyoxometalate hybrid complex. In this study the authors have used the PW₁₂ moiety to avoid the use of amines as sacrificial proton and electron donor, as they use H₂ as both electron and proton sacrificial donor. They have indeed shown that the presence of the POM in solution with the catalytic complex, and the addition of H₂ in the catalytic media, lead to the oxidation of H₂ into 2H⁺ + 2e⁻ and reduction of H₃[PW^{VI}₁₂O₄₀]. The newly formed

$\text{H}_5[\text{PW}_2^{\text{V}}\text{W}_{10}^{\text{VI}}\text{O}_{40}]$ is necessary for the reduction of CO_2 to CO catalyzed by a $[\text{Re}(\text{bpy})(\text{CO})_3]^+$ complex. The mechanism of this reaction has been later on studied by Poblet *et al.*¹⁶

In 2017, the same team has again described a similar catalyst for the reduction of CO_2 to CO .¹⁷ A dirhenium catalyst was prepared with a modified bipyridine (6,6''-(hydrazine-1,1-diyl)di-2,2'-bipyridine) (**Figure 2.5 a**). The addition of the rhenium complex ($[\text{Re-cat}]$) and the POM in acetonitrile leads to the formation of the hybrid catalyst through salt formation between the basic nitrogen of the pyridine ring and the acidic protons of the POM. This catalyst has then been reduced twice electrochemically in dimethyl acetamide (DMA) at -1.302 V vs. Fc/Fc^+ leading to the formation of $[\text{Re-cat}]\text{-H}_5\text{PW}_2^{\text{V}}\text{W}_{10}^{\text{VI}}\text{O}_{40}$. The feasibility of the electron transfer from the reduced $\text{PW}_2^{\text{V}}\text{W}_{10}^{\text{VI}}$ POM to the rhenium complex was demonstrated by UV-Vis experiment (**Figure 2.5 b**). The reduced POM (leading to a blue solution) was reacted with the rhenium catalyst showing a decrease of the large band between 600 and 900 nm characteristic of POM-reduced species. After 3h irradiation no more absorbance in this range was observed, suggesting an electron transfer from the reduced POM to the rhenium complex. Lastly, the authors have conducted photo-electro catalytic experiments where the POM was reduced at $E_{\text{app}} = -1.30$ V vs. Ag/Ag^+ , the reduced $\text{PW}_2^{\text{V}}\text{W}_{10}^{\text{VI}}$ POM thus transferring two electrons to the rhenium catalyst, allowing the further reduction of CO_2 in carbon monoxide. The presence of the POM as an electron relay thus led to a higher activity of $[\text{Re-cat}]$.

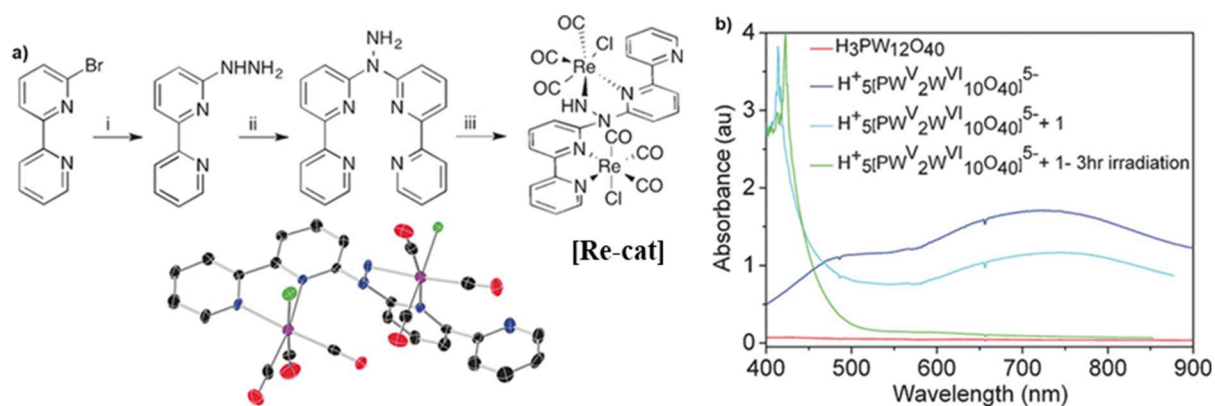


Figure 2.5: a) Strategy for the synthesis of the dirhenium complex; b) UV-Vis spectra following the reduction of $\text{H}_3\text{PW}_{12}\text{O}_{40}$ and its re-oxidation induced by visible light in the presence of $[\text{Re-cat}]$.¹⁷

Few years later, the use of a Keggin POM immobilized in a MOF porous solid as an electron and proton relay for CO_2 photoreduction was reported by Liu *et al.*¹⁸ The disubstituted $\text{K}_7\text{PW}_{10}\text{Ti}_2\text{O}_{40}$ Keggin, already known for its ability to photoreduce CO_2 ,¹⁹ has been used to

synthesize the POM-based MOF NENU-10. NENU-10 being non-catalytic, gold nanoparticles (AuNP) were co-immobilized in the POM@MOF. The study compares different systems, HKUST-1 being the POM-free MOF, NENU-3 containing the PW_{12} Keggin, NENU-10 containing $PW_{10}Ti_2$, and the gold nanoparticles loaded MOF Au@NENU-3 and Au@NENU-10 (**Figure 2.6**).

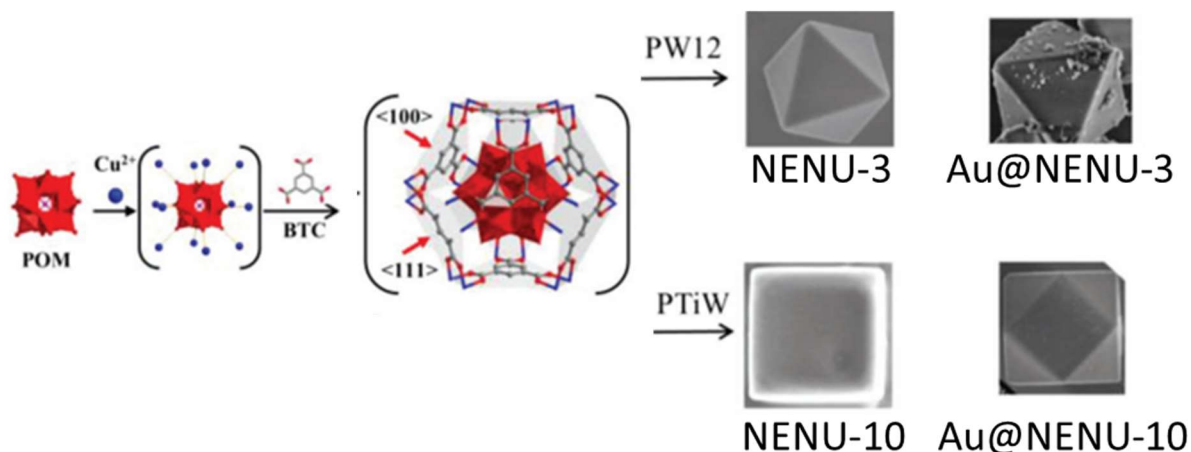


Figure 2.6: Reaction between POM, Cu^{2+} and BTC to form NENU-3 and NENU-10 MOF. HKUST-1 is the equivalent MOF without the POM inside the pores.¹⁸

The catalysts have been used as synthesized, the conversion yield of CO_2 into CO , H_2 and CH_4 being shown in **Figure 2.7 a**). The authors report $12.8 \mu mol \cdot g^{-1} \cdot h^{-1}$ for CO , 2.6 for H_2 and 2.1 for CH_4 with Au@NENU-10, whereas the yields for Au@NENU-3 are of $0.15 \mu mol \cdot g^{-1} \cdot h^{-1}$ for CO and 0.5 for H_2 with no CH_4 production, leading to an 85-fold increase in CO production and 5-fold in H_2 production. The catalytic properties in homogeneous media have also been investigated where the same effect can be observed, although the yields are lower. Indeed, having both AuNP and PW_{12} in solution produces only H_2 ($0.42 \mu mol \cdot g^{-1} \cdot h^{-1}$) whereas with AuNP and $PW_{10}Ti_2$ the whole range of products can be detected (CO 2.1, H_2 0.29 and CH_4 $0.35 \mu mol \cdot g^{-1} \cdot h^{-1}$).

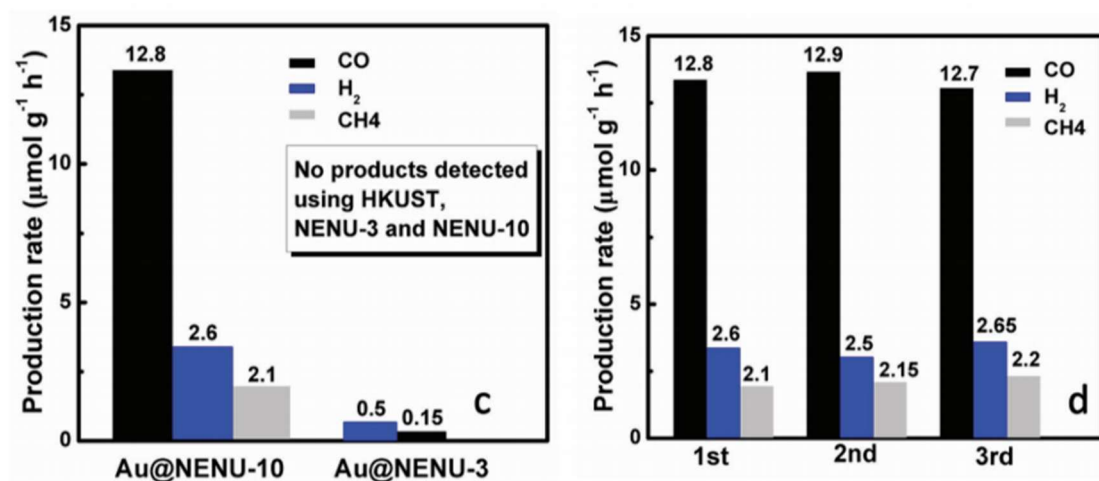


Figure 2.7: a) Production yields of CO, H₂ and CH₄ from CO₂ b) recycling tests of Au@NENU-10.¹⁸

Overall, the catalytic properties of any (POM,cat)@MOF solid rely on the integrity of its (POM, cat, MOF) components and on subtle interactions between the immobilized (POM, cat) species and the MOF host. Rietveld refinement methods from powder X-ray diffraction (PXRD) patterns, based on the Bragg peaks analysis arising from symmetry in polycrystalline solids, may be used to locate guest species while retrieving the host's crystal structure. However, such techniques - even using high-resolution synchrotron data - are not suitable when the immobilized guests exhibit a strong positional disorder in the porous host. Although many POM@MOF composites have been reported for catalysis purposes,^{20,21} there has been so far very few report of structural single-crystal data determination²² and no report on POM@MOF crystal structure determination from powders, besides the proposed positioning of PW_{12} in NU-1000 by Farha *et al.* from difference electron density maps.^{23,24} Instead, pair distribution function (PDF) data collection, which includes both Bragg and diffuse scattering, is considered as a valuable technique to overcome the above limitations as detailed below and retrieve reliable structural information on hosted molecular species.

The PDF signal reflects the probability of finding a pair of atoms at a distance r in the structure and may be described as a one-dimensional function that exhibits peaks at r -values corresponding to characteristic interatomic distances within the sample. The strength of this method lies in the quantitative structural information provided about short, middle and long-range orders, including all the deviations from the average structure.²⁵ In the present POM@MOF and (POM,cat)@MOF materials, the contributions arising from both the host and the guests are expected to induce a strong peak overlap making the interpretation of the PDF

data challenging. To overcome this limitation, an elegant approach was proposed by Chapman *et al.*, namely the differential PDF (d-PDF) method,²⁶ whereby the local structure of the guest, the host-guest interactions and the structural modifications of the host are retrieved through the subtraction of the PDF of the guest-free host (as a reference) from that of the guest-loaded PDF. In this context, Chapman *et al.* studied N_2 adsorbed in Prussian blue whereby the d-PDF refinement showed a slight expansion of the host network and a confinement of the loaded N_2 molecules close to the pore centers.²⁵ In another challenging case, Platero-Prats *et al.* demonstrated the formation of Cu-oxo clusters within the small pores of NU-1000 during the atomic layer deposition of Cu.²⁷ The further refinement of the d-PDF highlighted the formation under reducing atmosphere of metallic Cu^0 nanoparticles of 4 nm and < 1 nm sizes within the pores, followed by their transformation into cuprite Cu_2O nanoparticles under oxidative atmosphere. However, the use of PDF and d-PDF methods is still limited in the field of guest@MOF materials, with only a few reports, most of which concerning the adsorption of small molecules.^{25,28–30} To the best of our knowledge, the investigation of POM@MOF and (POM,cat)@MOF composites by differential PDF analysis is the first of the kind.

Cp^*Rh has shown great catalytic properties for CO_2 reduction to both formate and H_2 , by electroreduction at first, and more recently by photochemical ways where the catalyst has been immobilized in the UiO-67 MOF and kept its activity. Moreover, reports show that Keggin POM can be used as an electron and proton relay to increase the CO_2 reduction activity of different kinds of catalysts including a rhenium bipyridine based catalyst, which is close to rhodium bipyridine catalysts in terms of activity. Lastly, Salomon *et al.* succeeded in incorporating PW_{12} inside the same MOF where the Cp^*Rh catalyst has been immobilized.

Considering this information, we have decided to co-immobilize Cp^*Rh and PW_{12} in the same material in order to investigate its catalytic properties and the eventual effect that PW_{12} could have on the catalysis. Indeed, introducing an electron/proton relay near the Cp^*Rh catalytic center might increase the system efficiency for CO_2 reduction, as shown with NENU-10.¹⁸ Besides, the stability and structural complexity of PW_{12} @UiO-67 make it a perfect proof of concept for d-PDF studies of POM@MOF.

2. Synthesis and Characterizations of the $(\text{PW}_{12}, \text{Cp}^*\text{Rh})@ \text{UiO}-67$ composite

The $(\text{PW}_{12}, \text{Cp}^*\text{Rh})@ \text{UiO}-67$ compound was synthesized in two steps combining the two reported procedures for the synthesis of $\text{PW}_{12}@ \text{UiO}-67$ ¹⁴ and $\text{Cp}^*\text{Rh}@ \text{UiO}-67$ ¹ (**Figure 2.8**). First, the encapsulation of the POMs in the octahedral cavities of UiO-67 was achieved by *in situ* synthesis in DMF at 120°C. The resulting $\text{PW}_{12}@ \text{UiO}-67$ composite has been washed several times with heated DMF and acetone to dissolve all unreacted compounds (c.a. benzoic acid; biphenyl dicarboxylic acid) before being reacted with the molecular complex $\text{Cp}^*\text{Rh}(\text{bpydc})\text{Cl}_2$ (bpydc = 2,2'-bipyridine-5,5'-dicarboxylic acid). UiO-67 being unstable to water in oxidative conditions, in order to avoid the MOF degradation, two sealed vials were degassed with argon for 20 min, one containing the MOF and the Cp^*Rh linker, the other one filled with water. Degassed water was then added to the powder containing flask. The reaction media was stirred at RT for 24h.

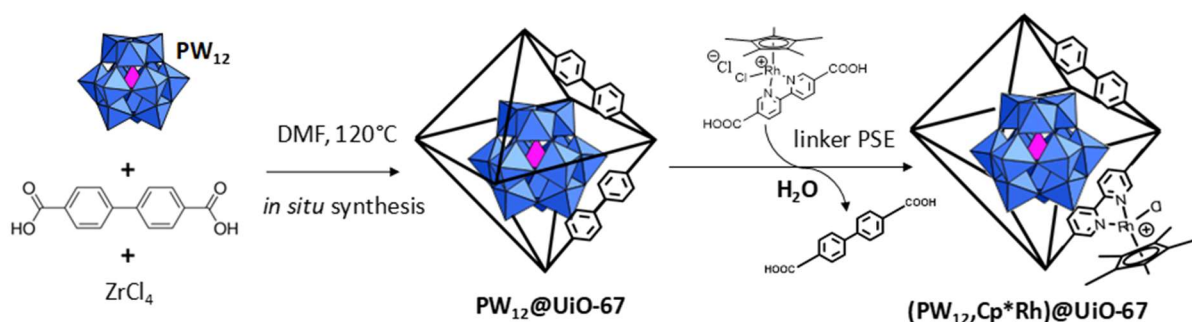


Figure 2.8: (a) Schematic representation of the two-step *in situ* synthesis and linker's post-synthetic exchange (PSE) procedure to obtain the composite material $(\text{PW}_{12}, \text{Cp}^*\text{Rh})@ \text{UiO}-67$.

The presence of PW_{12} inside the MOF cavities leads to a more difficult linker exchange during the PSE. We made the hypothesis that it might be due to some steric hindrance effects. In order to achieve similar amounts of exchanged linkers in both the POM-containing and POM-free UiO-67 materials, a higher initial amount of Cp^*Rh linker in the reactive medium was thus necessary when working with the POM@MOF than with the MOF alone (see details in experimental section). The percentage of bpdc linkers exchanged in the MOF as well as the amounts of POMs immobilized in the cavities were evaluated by EDS and elemental analyses. Firstly, EDS analysis allowed us to estimate the amount of both POM and Cp^*Rh by monitoring the W% and Rh% with respect to the Zr%.

Table 2.2: EDS Analysis

	PW ₁₂ @UiO-67	Cp*Rh@UiO-67	(PW ₁₂ ,Cp*Rh)@UiO-67
W/Zr	0.45	-	0.38
Rh/Zr	-	0.073	0.071

In the case of PW₁₂@UiO-67 the W/Zr ratio is 0.45, knowing that there is twice as much W in PW₁₂ than Zr in the UiO-67, we can consider about 0.22 POM per Zr₆ cluster. A former PhD student in our group previously demonstrated by CHN elemental analysis and EDS that the POM gets inside the pores without its counterions meaning that its charge of -3 causes a linker defect in order to ensure the electroneutrality of the compound.¹⁴ We can thus propose, for the PW₁₂@UiO composite I have synthesized, the formula: Zr₆O₄(OH)₄(C₁₄O₄H₈)_{5.67}(PW₁₂O₄₀)_{0.22}, which represents approximately the incorporation of one POM in the pores of UiO-67 every 5 Zr-clusters. As for the Cp*Rh@UiO-67, both the catalytic rhodium linker and the pristine bpdc linker are twice negatively charged. We propose a formula without linker defects, which is the following: Zr₆O₄(OH)₄(C₁₄O₄H₈)_{5.56}(RhC₂₂H₂₁N₂O₄Cl₂)_{0.44}. We compared the theoretical composition in C, H, N, W, Zr and Rh calculated from the proposed formula, to the experimental values collected by elemental analysis, ICP and EDS (Table 2.3). Considering the good correlation between calculated and experimental values, we can thus conclude that the linker exchange does not induce any linker defect. Lastly, for the (PW₁₂,Cp*Rh)@UiO-67 composite, a chlorine defect has been identified by EDS suggesting a loss of chloride ions in the Cp*Rh complex. The electroneutrality is ensured by the Zr₆ cluster contributing for 12 positive charges, by the bpdc (-2), Cp*Rh without a chloride anion (-1) and PW₁₂ (-3) for the negative charges leading to the formula Zr₆O₄(OH)₄(C₁₄O₄H₈)_{5.45}(RhC₂₂H₂₁N₂O₄Cl)_{0.44}(PW₁₂O₄₀)_{0.22}. The different components of (PW₁₂,Cp*Rh)@UiO-67 are displayed in **Figure 2.9**.

The proposed formula and metal% for (PW₁₂,Cp*Rh)@UiO-67 were confirmed by ICP-AES and elemental analysis.

Table 2.3: Calculated and experimental values of elemental analysis of (PW₁₂,Cp*Rh)@UiO-67.

	C	H	N	W	Zr	Rh
Calc.	38.22	3.17	3.28	14.48	16.33	1.29
Exp.	38.27	4.79	3.55	14.80	16.70	1.40

Once all the samples were synthesized with the same amount of guests inside the MOF pores, systematic characterization steps have been made, ranging from usual characterization methods (PXRD, IR, UV-vis, etc.) to more specialized ones (ssNMR, PDF).

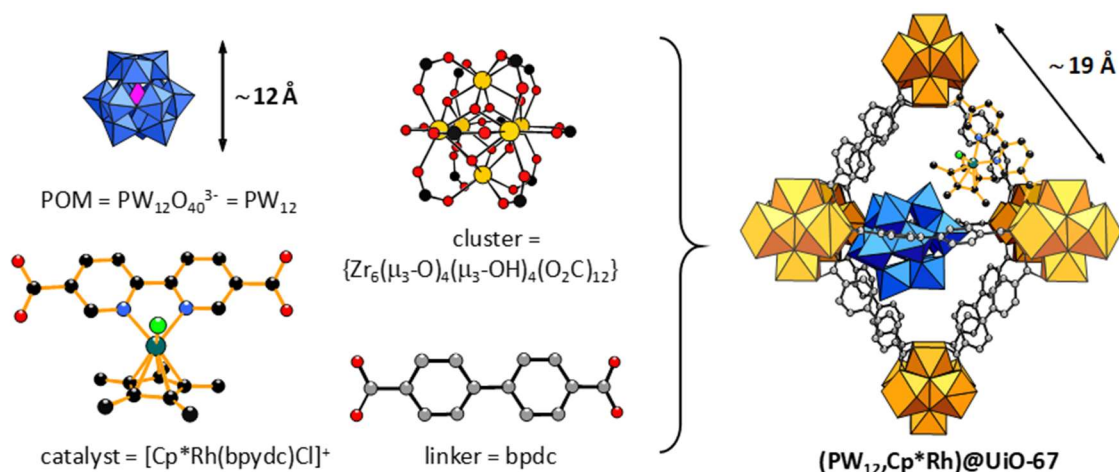


Figure 2.9: $(\text{PW}_{12}, \text{Cp}^*\text{Rh})@ \text{UiO-67}$ components: the PW_{12} polyoxometalate, the Zr-based inorganic subunit of UiO-67, the $[\text{Cp}^*\text{Rh}(\text{bpydc})\text{Cl}]^+$ molecular catalyst and the bpdC linkers. WO_6 , blue polyhedra; ZrO_8 , orange polyhedra; PO_4 , pink polyhedron; Zr, orange spheres; O, red spheres; C, gray or black spheres; N, blue spheres; Rh, dark green spheres; Cl, green spheres.

The powder X-ray diffraction measurements (**Figure 2.10**) of the $(\text{PW}_{12}, \text{Cp}^*\text{Rh})@ \text{UiO-67}$ composite, compared to those of UiO-67 and $\text{PW}_{12}@ \text{UiO-67}$, confirm that the crystallinity of the MOF host is maintained upon the *in situ* incorporation of the POM and upon the PSE of the Cp^*Rh complex. For the $\text{PW}_{12}@ \text{UiO-67}$ and $(\text{PW}_{12}, \text{Cp}^*\text{Rh})@ \text{UiO-67}$ composites, we could unambiguously assign the additional broad signal visible at low (2θ) angles (below 4°) under the Bragg peaks to the diffuse scattering signal of the encapsulated $[\text{PW}_{12}\text{O}_{40}]^{3-}$ in the MOF cavities, while excluding the possible presence of a separated amorphous phase, thanks to the PDF analysis (see below).

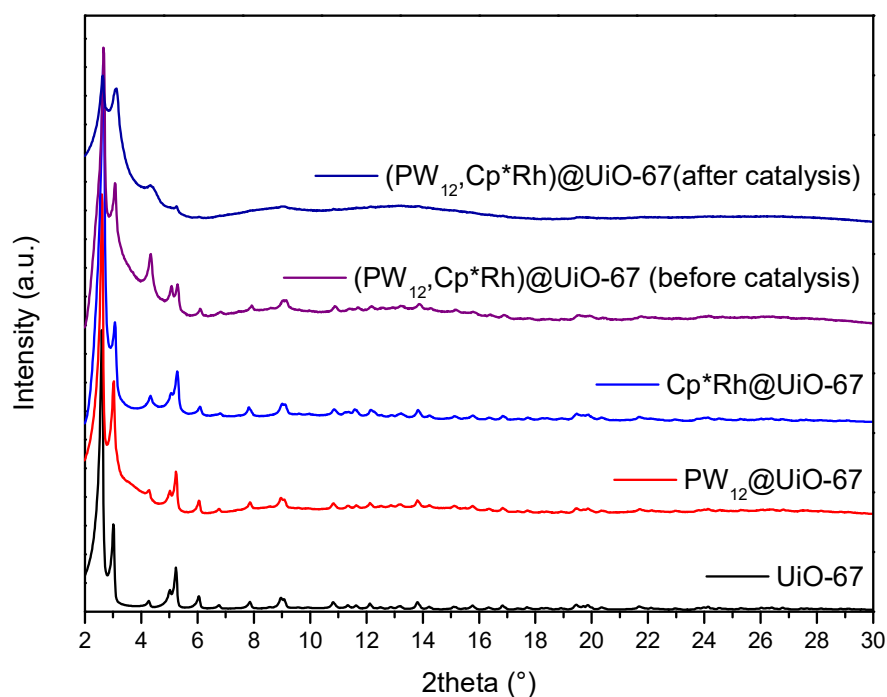


Figure 2.10: Powder X-ray diffraction patterns (PXRD) of POM@MOF and (POM,cat)@MOF composite solids. PXRD are shown for UiO-67, PW_{12} @UiO-67, Cp^*Rh @UiO-67 and $(\text{PW}_{12},\text{Cp}^*\text{Rh})$ @UiO-67 before and after catalysis.

All the diffraction peaks are unambiguously attributed to the UiO-67 crystalline structure.⁸ Apart from the diffuse scattering observed in PW_{12} @UiO-67 (common to all POM-containing composites), the PXRD patterns of UiO-67 and PW_{12} @UiO-67 are strictly comparable in terms of 2θ peak positions and intensities. However, the quality of the diagrams prohibits any further structural investigations such as Rietveld refinement. It shows here the limit of conventional PXRD analysis to retrieve structural information in the case of the immobilization of a guest inside an MOF porous network (low POM content, disorder).

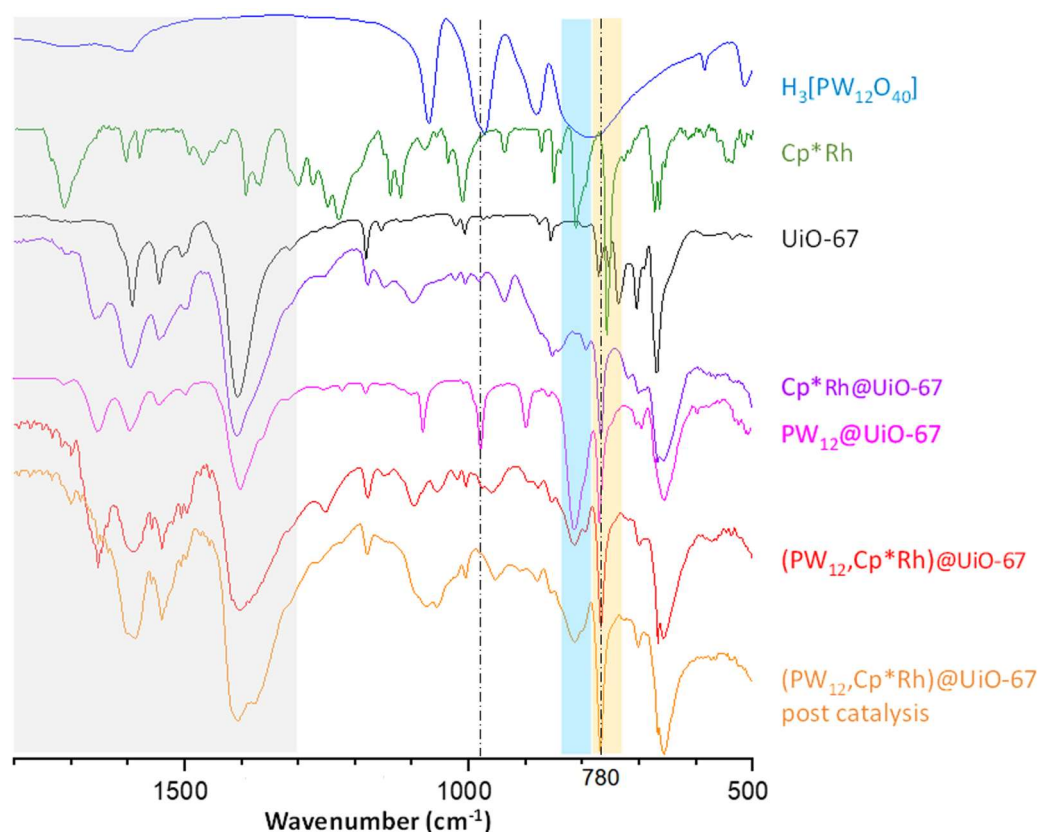


Figure 2.11: Infrared spectra of the different precursors and MOFs composites.

Infrared (IR) spectra (**Figure 2.11**) indicate both the presence of the POM and the UiO-67 MOF, with P-O vibrations around 1100 cm^{-1} , W=O vibrations around 980 cm^{-1} , W-O vibrations around 780 cm^{-1} and carboxylate vibrations between 1350 cm^{-1} and 1650 cm^{-1} but do show unambiguously the presence of Cp^*Rh . In addition, Raman spectra confirm the presence, this time, of both PW_{12} and Cp^*Rh in the related composites (**Figure 2.12**).

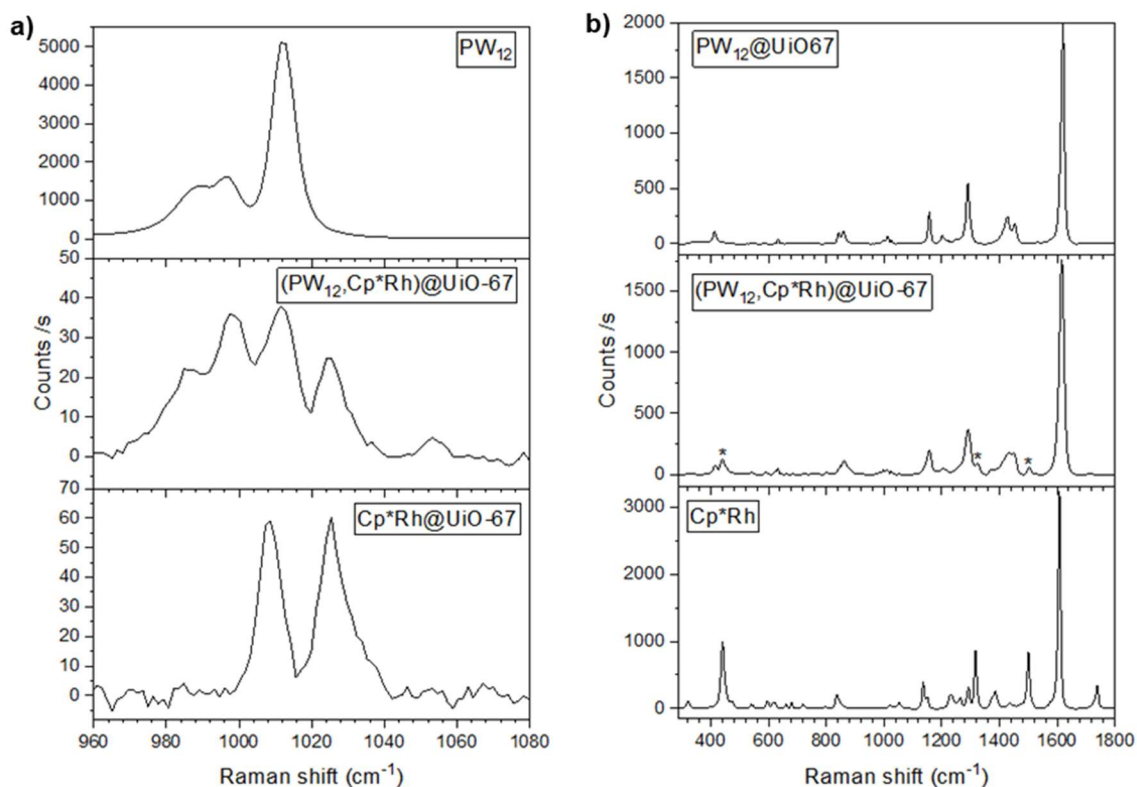


Figure 2.12: Raman spectra of POM, $(\text{PW}_{12}, \text{Cp}^*\text{Rh})@ \text{MOF}$, $\text{Cp}^*\text{Rh}@ \text{MOF}$ and PW_{12} and Cp^*Rh solids measured at 532 nm excitation wavelength.

The main bands of the POM at 1011 (stretching of P-O) and 996 cm^{-1} (stretching of W=O)³¹ are detected in the $(\text{PW}_{12}, \text{cat})@ \text{UiO}-67$. The two vibrational bands of the $\text{Cp}^*\text{Rh}@ \text{MOF}$ are still observed in the 960-1040 cm^{-1} area (**Figure 2.12 a**). The presence of Cp^*Rh in the $(\text{PW}_{12}, \text{cat})@ \text{UiO}-67$ can be observed by the characteristic bands (stars in the **Figure 2.12 b**) at 440 ($\delta(\text{N-Rh-N})$), 1324 cm^{-1} and 1506 cm^{-1} ($\nu(\text{C=N}) + \nu(\text{C=C})$).⁴ Those involving the COOH group disappear from the free Cp^*Rh molecules after its insertion into the MOF, as the C=O 1738 cm^{-1} band, as expected.

Scanning electron microscopy (SEM) images combined to energy-dispersive X-ray spectroscopy (EDS) mapping experiments (**Figure 2.13**) suggest a uniform distribution of the POM (monitored by W $\text{M}\alpha 1$) and of the Rh (Rh $\text{L}\alpha 1$) complex within the MOF crystallites (monitored by Zr $\text{L}\alpha 1$).

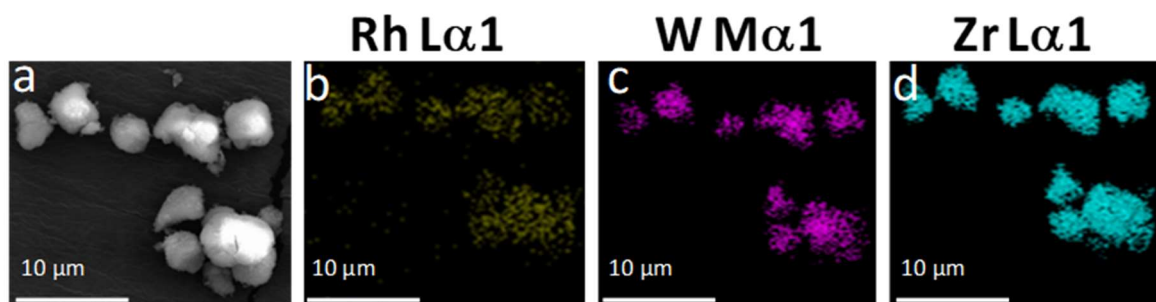


Figure 2.13: SEM image of $(\text{PW}_{12},\text{Cp}^*\text{Rh})@\text{UiO}-67$ (a) and EDS mapping of Rh $\text{L}\alpha 1$ (b), W $\text{M}\alpha 1$ (c) and Zr $\text{L}\alpha 1$ (d).

As expected, the Brunauer-Emmett-Teller (BET) surface area (**Figure 2.14 a**) calculated from the N_2 isotherm significantly decreases from UiO-67 to $\text{PW}_{12}@\text{UiO}-67$ and $(\text{PW}_{12},\text{Cp}^*\text{Rh})@\text{UiO}-67$ as a result of the successive incorporation of the POM and of the Rh complex, with $2300 \text{ m}^2\cdot\text{g}^{-1}$, $1034 \text{ m}^2\cdot\text{g}^{-1}$ and $930 \text{ m}^2\cdot\text{g}^{-1}$, respectively. The transformed UV-visible absorption spectrum of $(\text{PW}_{12},\text{Cp}^*\text{Rh})@\text{UiO}-67$ compared to that of $\text{Cp}^*\text{Rh}@\text{UiO}-67$ exhibits a slight red-shift of the Rh-localized d-d transition¹ (**Figure 2.14 b**). This suggests a direct interaction between the POM and the Cp^*Rh catalyst, which modifies its electronic structure.

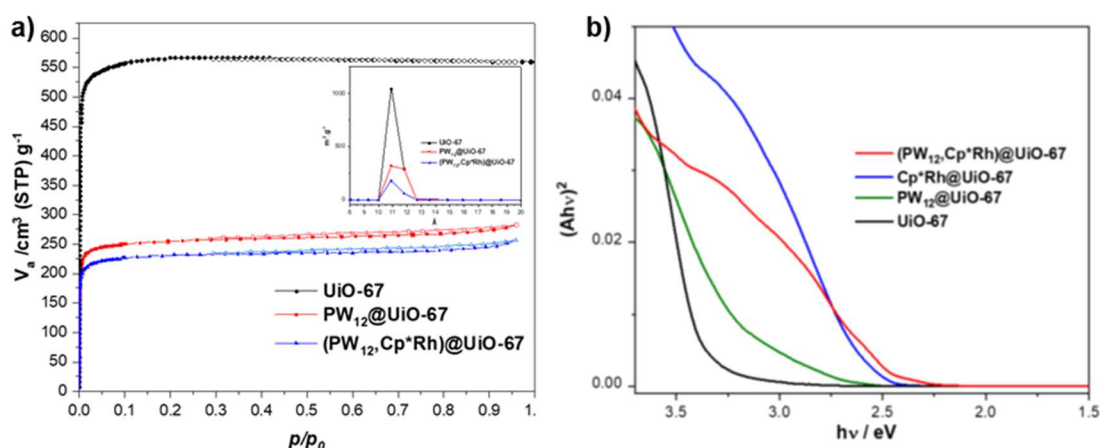


Figure 2.14: a) N_2 adsorption/desorption isotherms of UiO-67 and the $\text{PW}_{12}@\text{UiO}-67$, and $(\text{PW}_{12},\text{Cp}^*\text{Rh})@\text{UiO}-67$ composites (77K, $P/P_0 = 1 \text{ atm.}$). Inset shows the pore distributions. b) Plot of the $(Ah\nu)^2$ versus photon energy ($h\nu$) of $(\text{PW}_{12},\text{Cp}^*\text{Rh})@\text{UiO}-67$ (red), $\text{Cp}^*\text{Rh}@\text{UiO}-67$ (blue), $\text{PW}_{12}@\text{UiO}-67$ (green) and UiO-67 (black).

The ^1H and ^{13}C MAS NMR spectra (**Figure 2.15**) of $\text{Cp}^*\text{Rh}@\text{UiO}-67$ and $(\text{PW}_{12},\text{Cp}^*\text{Rh})@\text{UiO}-67$, when compared to those of Cp^*Rh , UiO-67, and $\text{PW}_{12}@\text{UiO}-67$,

confirm the incorporation of the Cp^*Rh complex into the UiO-67's framework. The ^1H NMR spectra of UiO-67 and $\text{PW}_{12}@ \text{UiO-67}$ exhibit the expected resonances of aromatic linker's protons (7.1 and 7.9 ppm) and of hydroxyl groups of the inorganic node (0.2-3.7 ppm) including those of defect sites.^{14,32} New resonances at 1.1-1.2 ppm observed in $\text{Cp}^*\text{Rh}@ \text{UiO-67}$ and $(\text{PW}_{12}, \text{Cp}^*\text{Rh})@ \text{UiO-67}$ solids correspond to methyl protons of the Cp^* moiety, however, significantly shielded with respect to the resonance at 1.9 ppm observed in the spectrum of the $\text{Cp}^*\text{Rh}(\text{bpydc})\text{Cl}_2$ precursor. Furthermore, the absence of the signal at 12.5 ppm characteristic of the acid protons of the carboxylic groups of the precursor indicates the full complexation of the bpydc linker by the inorganic node of the MOF upon the ligand exchange process, confirming the absence of unreacted $\text{Cp}^*\text{Rh}(\text{bpydc})$ inside the MOF pores. ^{13}C NMR also confirms the inclusion of both the Cp^* complex and bpydc ligand with the appearance of their characteristic resonances at ca. 9 and 98 ppm, and ca. 154 ppm, respectively. It should be mentioned that the excessive line broadening observed in both ^1H and ^{13}C spectra of $(\text{PW}_{12}, \text{Cp}^*\text{Rh})@ \text{UiO-67}$ when compared to those of $\text{PW}_{12}@ \text{UiO-67}$ or $\text{Cp}^*\text{Rh}@ \text{UiO-67}$ should indicate major disorder within the structure when the POM and the Cp^*Rh complex are introduced together.

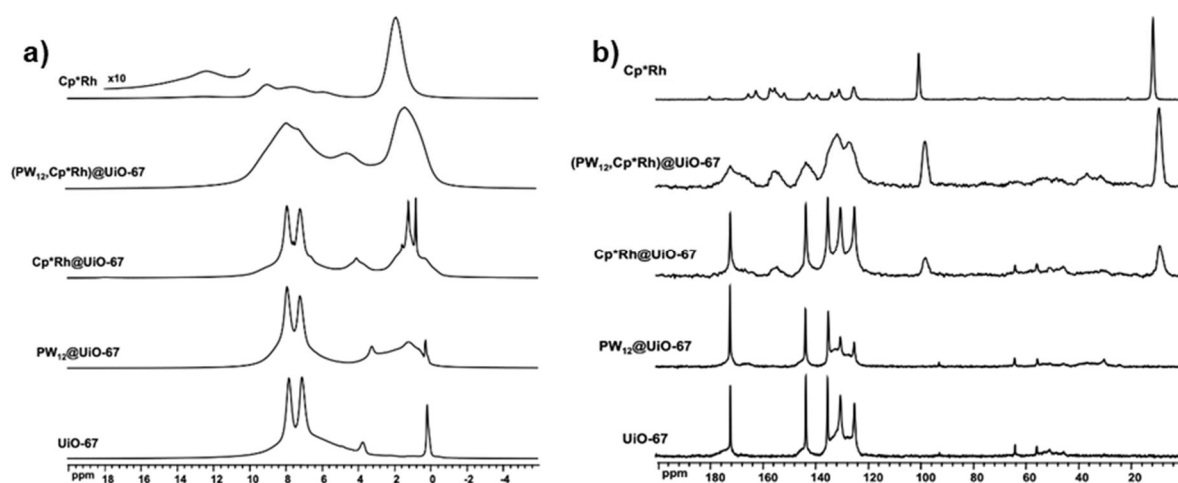


Figure 2.15: a) Solid state ^1H MAS NMR spectra of $\text{PW}_{12}@ \text{UiO-67}$, $\text{Cp}^*\text{Rh}@ \text{UiO-67}$ and $(\text{PW}_{12}, \text{Cp}^*\text{Rh})@ \text{UiO-67}$ composites compared to that of the Cp^*Rh complex precursor and UiO-67. b) Solid state $^{13}\text{C}\{^1\text{H}\}$ CPMAS NMR spectra of $\text{PW}_{12}@ \text{UiO-67}$, $\text{Cp}^*\text{Rh}@ \text{UiO-67}$ and $(\text{PW}_{12}, \text{Cp}^*\text{Rh})@ \text{UiO-67}$ composites compared to that of the Cp^*Rh complex precursor and UiO-67.

The ^{31}P MAS NMR spectra of $\text{PW}_{12}@ \text{UiO-67}$ and $(\text{PW}_{12}, \text{Cp}^*\text{Rh})@ \text{UiO-67}$ are shown in **Figure 2.16 a)** and **2.16 b)**, respectively. A single signal is observed at -15.1 ppm for $\text{PW}_{12}@ \text{UiO-67}$ reflecting a homogeneous environment of the POM in UiO-67,^{14,33} while two

main resonances at -15.2 and -14.4 ppm can be distinguished in the case of $(\text{PW}_{12},\text{Cp}^*\text{Rh})@\text{UiO}-67$. This latter result suggests that the POMs occupy two distinct structural positions within the pores of $\text{Cp}^*\text{Rh}@\text{UiO}-67$.

To attribute the two different environments of PW_{12} when in presence of the Cp^* moiety, finer characterization methods are needed. The results of those methods will be presented in the next part.

3. In-depth Characterizations of the $(\text{PW}_{12},\text{Cp}^*\text{Rh})@\text{UiO}-67$ composite

In view of the level of structural complexity reached in the $(\text{PW}_{12},\text{Cp}^*\text{Rh})@\text{UiO}-67$ solid, we use here, besides standard characterizations, an in-depth combination of Density Functional Theory (DFT) calculations and Pair Distribution Function (PDF) analysis using laboratory X-rays. Also, the mutual interactions between the MOF host and the POM and catalyst guests were probed using ^1H , ^{13}C , and ^{31}P solid-state NMR, in line with the computational chemistry findings.

3.1 2D Solid-state NMR

As seen earlier, two different ^{31}P peaks are observed in solid-state NMR suggesting two environments for the PW_{12} moiety. Further evidence of two environments was provided by 2D NMR ^{31}P - ^1H HETCOR experiments (**Figure 2.16**). The spectrum shows that the ^{31}P signal at -15.2 ppm correlates preferably with the ^1H signal of aromatic protons at 8.3 ppm, while the second ^{31}P signal at -14.4 ppm correlates with the Cp^* moiety peak at 1.6 ppm. This clearly indicates that two POM environments co-exist within the $(\text{PW}_{12},\text{Cp}^*\text{Rh})@\text{UiO}-67$ material, *i.e.* one near the Cp^* moieties (-14.4 ppm) and another closer to the bipyridine organic linker (-15.2 ppm). Quantitatively, they are distributed almost equally (47:53 for -14.4 and -15.2 ppm respectively).

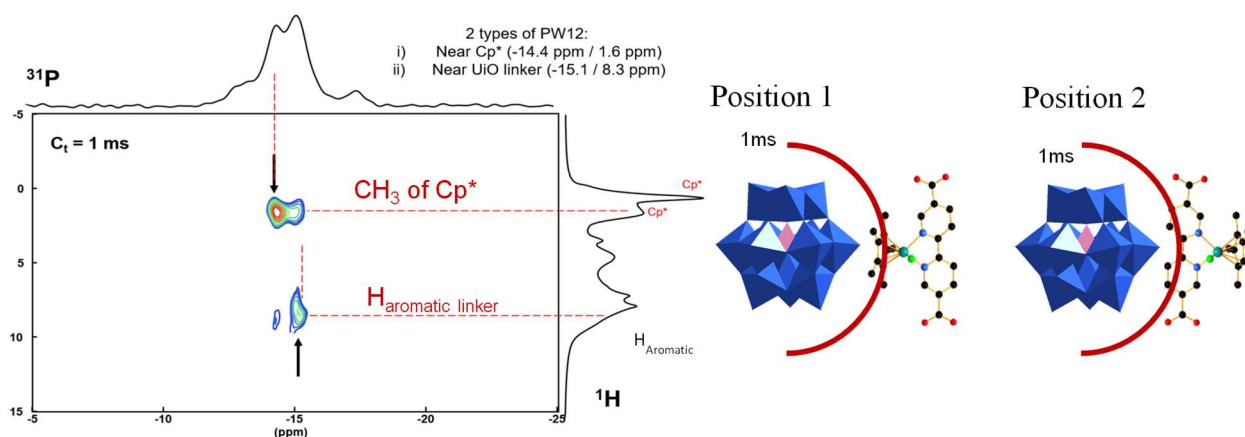


Figure 2.16: $^{31}\text{P}\{^1\text{H}\}$ CPMAS NMR, ^1H MAS NMR and $^{31}\text{P}\{^1\text{H}\}$ HETCOR spectra of $(\text{PW}_{12}, \text{Cp}^*\text{Rh})@\text{UiO}-67$ (left), proposed relative position of PW_{12} and Cp^*Rh considering the different $^{31}\text{P}\{^1\text{H}\}$ HETCOR signals (right).

3.2 DFT calculations

In a first step, simulated annealing (SA) and dispersion-corrected DFT-D3 geometry optimizations were performed by Mathis Duguet to identify the most likely position of the POM in UiO-67 and qualify its host-guest interactions with the hybrid framework. SA simulations provided recurrent successful insertion of PW_{12} in the octahedral cage of UiO-67. **Figures 2.17 a)** and **A2.2** illustrate its position and interactions in the solid. The POM is located at the center of the cavity and interacts equally with the 12 bpdc linkers of the octahedral cage. It is stabilized through a network of $(\text{PW}_{12})\text{O}\cdots\text{H}(\text{bpdc})$ van der Waals interactions between its terminal oxygen atoms and two aromatic hydrogen atoms of each bpdc linker within 2.4–2.7 Å distances. Overall, the host-guest interaction energy, which emanates from electrostatic interactions including multiple van der Waals interactions, is estimated from DFT calculations around 200 $\text{kcal}\cdot\text{mol}^{-1}$. This high affinity of the MOF for the POM results from the confinement of the POM in the rather small size pores of UiO-67.

Mathis Duguet then investigated the positioning of the Rh catalytic complex in the $\text{PW}_{12}@\text{UiO}-67$ solid considering the replacement of 1 bpdc linker per octahedral cage by one $\text{Cp}^*\text{Rh}(\text{bpydc})$ catalytic linker (**Figures 2.17** and **A2.2**). Two situations were distinguished whereby the Cp^*Rh catalytic moiety is oriented either towards an empty, *i.e.* POM-free, neighboring cage (**Figure 2.17 b**), position “out”) or towards the same cage as the PW_{12} guest (**Figure 2.17 c**), position “in”). The DFT-D3 level geometry optimization of the “out” position shows a similar {POM,

MOF} interaction energy than in the catalyst-free MOF. By contrast the comparison of the “out” and “in” models shows that interactions between the POM and the Cp*Rh component of the catalytic linker are favored by $\sim 46 \text{ kJ}\cdot\text{mol}^{-1}$ when they are located within the same cage. The calculations also show that in both “out” and “in” positions short-range interactions of the PW₁₂ with the linkers of the MOF are maintained through a series of hydrogen-bond type interactions within the 2.3-3 Å range of distances.

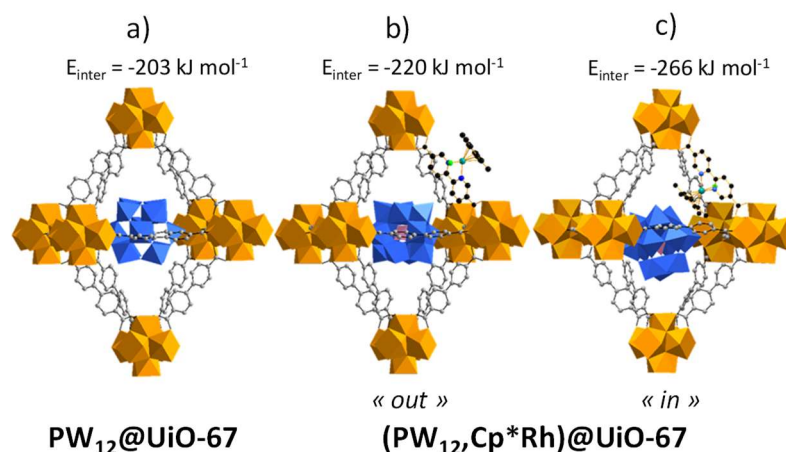


Figure 2.17: Computed PW₁₂@UiO-67 and (PW₁₂,Cp*Rh)@UiO-67 models. (a) PW₁₂ in PW₁₂@UiO-67 and (b)-(c) in (PW₁₂,Cp*Rh)@UiO-67 as obtained from SA and DFT-D3 level geometry optimizations. The POM and the Rh-catalytic center are modeled within different cages (“out” position, b) or within the same cage (“in” position, c). Interaction energies between PW₁₂ and the MOF host are given for each model. WO₆, blue polyhedra; ZrO₈, orange polyhedra; Rh, dark green sphere; O, red spheres; C, gray spheres; N, dark blue spheres; Cl, green spheres. H atoms are omitted.

The DFT calculations are thus fully consistent with the NMR experimental observations. The severe line broadening of the NMR signals reflects the structural disorder in the (POM,cat)@MOF material as the result of a loss of local symmetry when both the Keggin-POM and the Rh-catalyst are introduced into the MOF. Notably, the incorporation of either the POM or the Rh-catalyst induces much less disorder within the resulting POM@MOF or cat@MOF solids. Along this line, DFT calculations show that the POM is perfectly centered in the cage of the PW₁₂@UiO-67 solid, *i.e.* in absence of the Rh-catalyst, with thus only little effect on long- and short-range orders. By contrast, the presence of the Rh-catalyst displaces the POM of the center of the cage when the Cp* moiety points towards the PW₁₂ POM (**Figure 2.17 b**), which results in a new POM environment characterized by a ³¹P NMR signal at -14.4 ppm as revealed by the 2D ¹³P-¹H correlation experiment. The ³¹P NMR signal at -15.2 ppm is assigned to the POM centered in the cage with no close interaction with the Cp* of the Rh-

complex. This situation occurs when no Rh-catalyst is present within the cage or when the Cp^* ligand is oriented towards an adjacent neighboring cage (**Figure 2.17 c**). Finally, the experimental NMR data confirm the occurrence of the two distinct DFT local structures of the POM distributed equally.

3.3 Pair Distribution Functions analysis

In a first step, PDF analysis of the $\text{PW}_{12}@\text{UiO-67}$ composite was performed by Dr. Alex Lemarchand using UiO-67 as a reference, which will act as a proof-of-concept for the applicability of the d-PDF method to our composites. The experimental PDF profile of the UiO-67 (**Figure A2.3**) is characterized by a series of narrow peaks on the selected r -range (1–40 Å) which typically attest the high crystallinity of the sample, *i.e.* with short, middle and long-range orders. All intense peaks were assigned in a similar fashion than previously done on the related UiO-66 material,³⁴ reflecting the reported crystal structure of UiO-67.³⁵ More details may be found in the appendix. Turning to the $\text{PW}_{12}@\text{UiO-67}$ composite, its experimental PDF profile contains all the expected features of the UiO-67 host while presenting particularly intense additional peaks below 10.0 Å (**Figure 2.18 a**). Knowing the respective scattering factors of the POM and MOF atoms ($f_{\text{W}} \gg f_{\text{Zr}} \gg f_{\text{P}} > f_{\text{O}} > f_{\text{C}}$), these narrow and intense peaks clearly emanate from the heavy W scatterers and indicate their short-range structural organization in line with the presence of the encapsulated POM. Importantly, the two experimental PDF profiles perfectly overlap at long-range order (15.0 to 40.0 Å), confirming the similar high crystallinity of the UiO-67's framework upon the encapsulation of PW_{12} by in situ synthesis, as already observed from their PXRD patterns (**Figure 2.10**). This long-range feature allowed the calculation of the differential PDF in optimal conditions. The resulting d-PDF (**Figure 2.18 a**) is dominated by intense and narrow peaks in the low r region with a strong dampening above 10.0 Å.

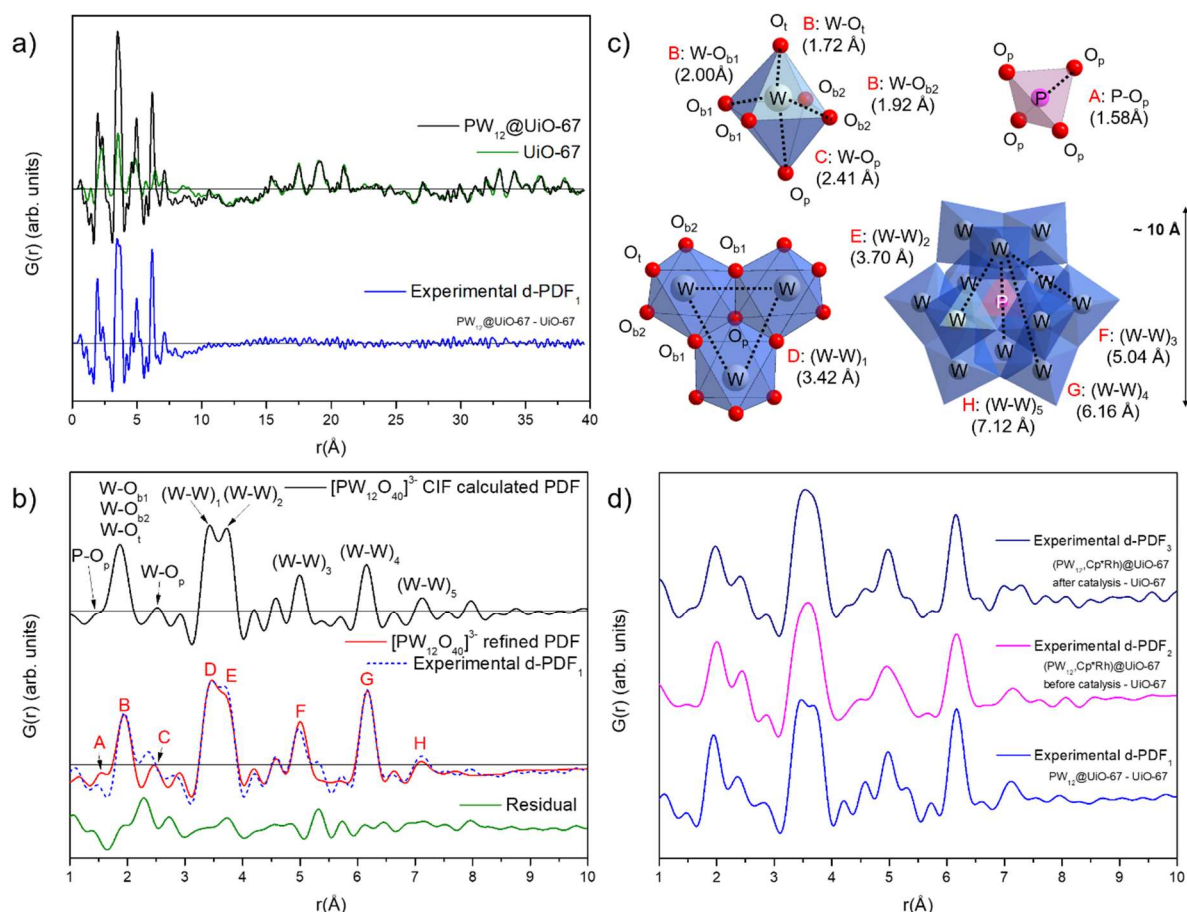


Figure 2.18: (a) Experimental PDF data for $\text{PW}_{12}@ \text{UiO-67}$ (black) and the guest-free UiO-67 (green) and the corresponding d-PDF for PW_{12} encapsulated in UiO-67 (blue) determined by subtracting the PDF of UiO-67 from the PDF of $\text{PW}_{12}@ \text{UiO-67}$. (b) Comparison of the calculated PDF of an isolated PW_{12} (black) and the experimental d-PDF of PW_{12} in UiO-67 (blue dotted lines), superimposed with the refined d-PDF (red) fitted using the $[\text{PW}_{12}\text{O}_{40}]^{3-}$ structural model from CIF files (JCPDS 00-050-0304)³⁶ and residual profile (green). A-H labels of peaks correspond to the indicated refined distances in the POM components as illustrated in (c) for the PO_4 tetrahedron, the WO_6 octahedron, the trimer of WO_6 octahedra, and within the full PW_{12} polyoxometalate structure. WO_6 , blue octahedra, PO_4 , pink tetrahedron, O, red spheres, W, gray spheres, P pink sphere. (d) Experimental d-PDFs (numbered 1 to 3) for PW_{12} in $\text{PW}_{12}@ \text{UiO-67}$ (blue), in $(\text{PW}_{12}, \text{Cp}^*\text{Rh})@ \text{UiO-67}$ before catalysis (magenta) and in $(\text{PW}_{12}, \text{Cp}^*\text{Rh})@ \text{UiO-67}$ after catalysis (navy blue) determined by subtracting the PDF of UiO-67 from the PDF of $\text{PW}_{12}@ \text{UiO-67}$, $(\text{PW}_{12}, \text{Cp}^*\text{Rh})@ \text{UiO-67}$ before and after catalysis, respectively.

Alex Lemarchand compared the d-PDF with the calculated PDF of an isolated PW_{12} extracted from reported crystallographic data (JCPDS 00-50-0304 CIF file)³⁶ over the 1–10 Å r -range (Figure 2.18 b). The two profiles match remarkably well whereby all peaks of the experimental d-PDF are equally well described (shape and position) in the calculated PDF of PW_{12} , allowing an exhaustive assignment of its characteristic interatomic distances. The first short distance peak at 1.5 Å (A) corresponds to the P-O bond length of the central PO_4 tetrahedron of the

POM. The second and third peaks (B, C) at 2.0 and 2.4 Å, respectively, correspond to the length of various W-O bonds constituting the WO_6 octahedra.

The intense peaks (D-G) at 3.5, 3.7, 5.0, 6.2 and 7.1 Å, are assigned to various W-W distances inside the PW_{12} structure. In addition, a very good agreement is found over the 1–8 Å r-range between the observed d-PDF and the theoretical one calculated from the DFT models of UiO-67 and $\text{PW}_{12}@\text{UiO-67}$ (**Figure A2.4 a**). The disagreement between the experimental and theoretical d-PDF profiles at long range (> 8 Å) emanates from the absence of POM's ordering in the $\text{PW}_{12}@\text{UiO-67}$ composite, by contrast with the virtual ordering induced by the DFT periodic models.

Overall, the structural integrity of the PW_{12} upon encapsulation in UiO-67 is thus supported by PDF analysis. Nonetheless, it can be pointed out that the lacunary polyoxotungstate PW_{11} POM would display the same W-O lengths as in PW_{12} . Solid-state NMR is thus necessary to unambiguously confirm the stability of the POM. Alex Lemarchand further attempted a refinement of the POM's atomic positions whereby it is constrained to the space group Pn-3m (**Figure 2.18 b**), **Table A2.1**). The relatively good quality of the refinement ($R_w \sim 28.2\%$) and the corresponding structural model (**Figure 2.18 c**) indicate that the original structure of the POM is indeed fully preserved upon its immobilization in UiO-67. The residual difference between experimental and calculated d-PDFs might be assigned to errors induced by the PDF subtraction step at low r-values, and/or potential positional atomic disorder and symmetry loss within the POM structure induced by the proximity of UiO-67's ligands and nodes.

In a second step, the d-PDF related to the $(\text{PW}_{12}, \text{Cp}^*\text{Rh})@\text{UiO-67}$ catalyst was investigated using UiO-67 as a reference. The PDF of the $(\text{PW}_{12}, \text{Cp}^*\text{Rh})@\text{UiO-67}$ exhibits all expected features of UiO-67 showing that the linker exchange did not induce major changes in the structure or important loss of crystallinity. The perfect overlap of $(\text{PW}_{12}, \text{Cp}^*\text{Rh})@\text{UiO-67}$'s and UiO-67's PDF profiles at large r-values (15–40 Å) allowed us to calculate the related d-PDF (**Figure 2.19**) reflecting the POM's structure. Consistently, this d-PDF is very similar to the d-PDF obtained for the POM in $\text{PW}_{12}@\text{UiO-67}$, i.e., prior to the linker exchange (**Figure 2.18 d**), confirming that the post-synthetic linker exchange has no impact on the structural integrity of PW_{12} . It is worth mentioning here that further attempts to identify the contribution of the catalytic Cp^*Rh ligand in the d-PDFs were unsuccessful due to the low amount of Rh in the sample and to the coincidence between Rh-Cl distances (~ 2.4 Å) and W-O distances characteristic of the POM.

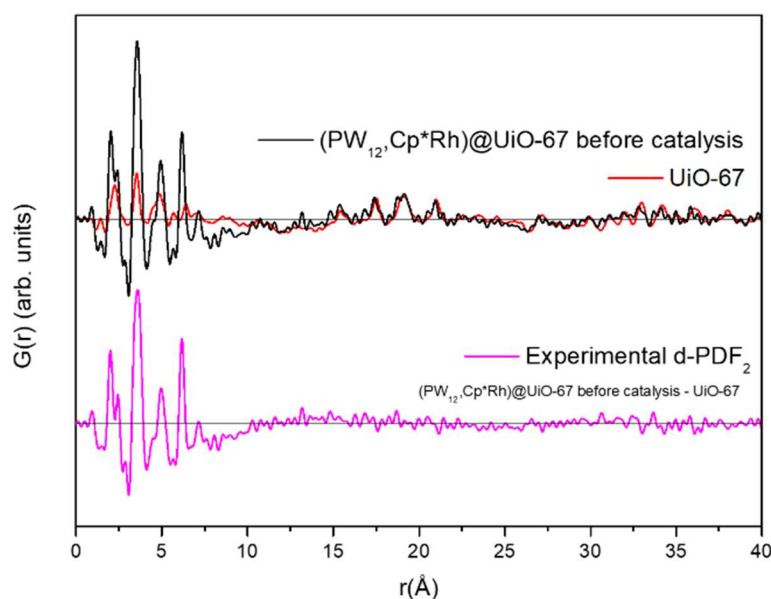


Figure 2.19: Experimental PDF data for $(\text{PW}_{12},\text{Cp}^*\text{Rh})@\text{UiO}-67$ before catalysis (black) and the POM-free UiO-67 (red). Bottom: the resulting d-PDF for PW_{12} in $(\text{PW}_{12},\text{Cp}^*\text{Rh})@\text{UiO}-67$ before catalysis (magenta) determined by subtracting the PDF of UiO-67 from the PDF of $(\text{PW}_{12},\text{Cp}^*\text{Rh})@\text{UiO}-67$ before catalysis.

4. Photocatalytic reduction of CO_2

4.1 Photocatalytic activity

Considering that $\text{Cp}^*\text{Rh}@\text{UiO}-67$ was active for the CO_2 reduction under visible-light irradiation,¹ the photocatalytic activity of the $(\text{PW}_{12},\text{Cp}^*\text{Rh})@\text{UiO}-67$ composite was investigated in the same conditions. Briefly, 0.8 mg of $\text{Cp}^*\text{Rh}@\text{UiO}-67$ or 1.4 mg of $(\text{PW}_{12},\text{Cp}^*\text{Rh})@\text{UiO}-67$ is dispersed in 0.8 mL of a 0.1 mM $\text{Ru}(\text{bpy})_3\text{Cl}_2$ $\text{CH}_3\text{CN}/\text{TEOA}$ (5:1) solution. The sample was degassed for 20 min using CO_2 before being irradiated for 3 h with a 280 Xe lamp equipped with a UV and infrared cutoff ($415 < \lambda < 800$ nm).

The production of H_2 and formate were thus compared for the $\text{Cp}^*\text{Rh}@\text{UiO}-67$ and $(\text{PW}_{12},\text{Cp}^*\text{Rh})@\text{UiO}-67$ materials (**Figure 2.20**), no other reaction products were detected neither with $\text{Cp}^*\text{Rh}@\text{UiO}-67$ nor $(\text{PW}_{12},\text{Cp}^*\text{Rh})@\text{UiO}-67$ (oxalate, methane, carbon monoxide, methanol, ethylene and ethanol were tested). The H_2 production performed by the $(\text{Cp}^*\text{Rh},\text{PW}_{12})@\text{UiO}-67$ catalyst increases progressively before reaching a plateau after 3 h, in a similar fashion than observed with $\text{Cp}^*\text{Rh}@\text{UiO}-67$ (**Figure 2.20 a**). Remarkably, we estimate at 3 h that the H_2 production is enhanced by a factor of ~ 2.5 in the

$(\text{PW}_{12}, \text{Cp}^*\text{Rh})@\text{UiO}-67$ composite with respect to that of the POM-free $\text{Cp}^*\text{Rh}@\text{UiO}-67$ composite (**Figure 2.21 b**). The production of formate follows the same trend, being similarly enhanced but by a factor of ~ 2 (**Figure 2.21 b**). Thus, the presence of the POM in the $\text{Cp}^*\text{Rh}@\text{UiO}-67$ photosystem seems to enhance both the hydrogen and formate production. The same trend is also observed on the initial TOF values: for H_2 , without POM the TOF is 6.8 h^{-1} with the POM it increases to 17.8 h^{-1} ; as for formate without the TOFs are 4.2 and 8.4 h^{-1} for $\text{Cp}^*\text{Rh}@\text{UiO}-67$ and $(\text{PW}_{12}, \text{Cp}^*\text{Rh})@\text{UiO}-67$ respectively. The TOFs were calculated at 30min.

The amount of $(\text{PW}_{12}, \text{Cp}^*\text{Rh})@\text{MOF}$ catalysts used during the photochemical tests has been adapted to have the same catalyst molarity as $\text{Cp}^*\text{Rh}@\text{UiO}-67$ system. The presence of the POM contributing to the compound mass, a higher amount of powder is needed with $(\text{PW}_{12}, \text{Cp}^*\text{Rh})@\text{UiO}-67$ (1.4 mg vs. 0.8 mg for the POM free composite). Control experiments without irradiation did not show any formate production nor hydrogen production. A very minor H_2 production can be observed with the Rh-catalyst-free $\text{PW}_{12}@\text{UiO}-67$ (**Figure 2.20 a**). By comparison with the experiment in absence of composites, this production can be fully assigned to some catalytic activity of the $\text{Ru}(\text{bpy})_3\text{Cl}_2$ complex (**Figure 2.20 a**). Furthermore, blank experiments with argon instead of carbon dioxide led to no formate production, the catalyst was still active for proton reduction. Photoreduction experiments with ^{13}C could be planned to confirm the formic acid production is not coming from the catalyst or the MOF degradation.

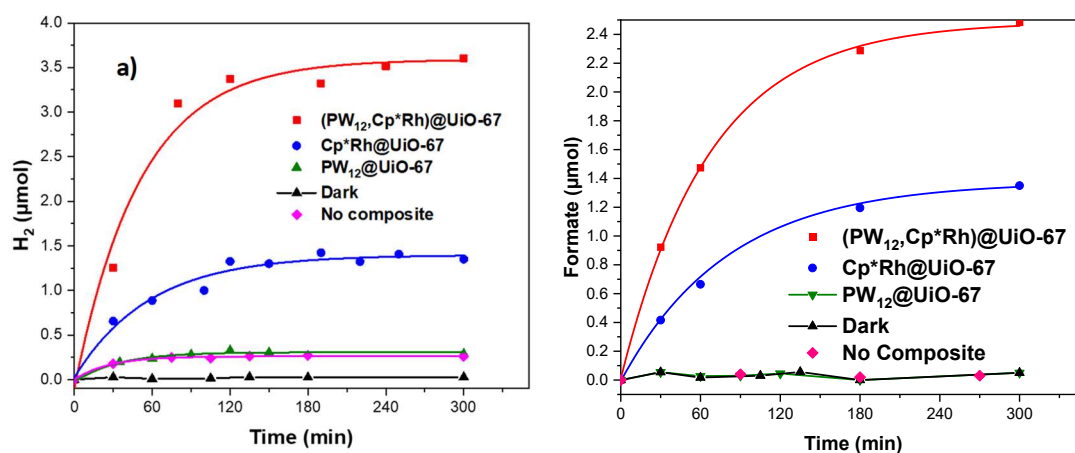


Figure 2.20: Kinetics of (a) H_2 and (b) HCOO^- production during CO_2 photoreduction reaction by $(\text{PW}_{12}, \text{Cp}^*\text{Rh})@\text{UiO}-67$ compared to $\text{Cp}^*\text{Rh}@\text{UiO}-67$. Reactions conditions: $0.17 \mu\text{mol}$ of catalyst, 0.8 mL of $\text{CH}_3\text{CN}/\text{TEOA}$ 5:1, 1 mM $\text{Ru}(\text{bpy})_3\text{Cl}_2$, 280 W , $\lambda > 415 \text{ nm}$.

The addition of a fresh solution of $\text{Ru}(\text{bpy})_3\text{Cl}_2$ after 2h of reaction results in a new cycle of H_2 production with similar initial TOF ($\sim 0.30 \text{ min}^{-1}$, **Figure 2.21 a**), clearly showing that the

system is mainly limited by the consumption of the photosensitizer and not by the catalyst deactivation.

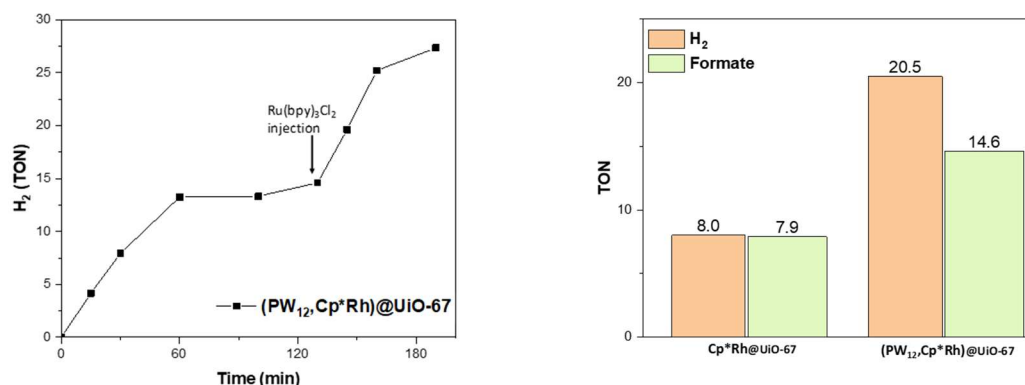


Figure 2.21: a) Photoreduction of CO_2 overtime by a $(\text{PW}_{12}, \text{Cp}^*\text{Rh})@ \text{UiO}-67$ composite. A fresh solution of $\text{Ru}(\text{bpy})_3\text{Cl}_2$ photosensitizer was added to the reaction after 120 min b) Formate (green) and H_2 (orange) TONs during a CO_2 photoreduction reaction by $(\text{PW}_{12}, \text{Cp}^*\text{Rh})@ \text{UiO}-67$ and $\text{Cp}^*\text{Rh}@ \text{UiO}-67$ composites after 180 min illumination.

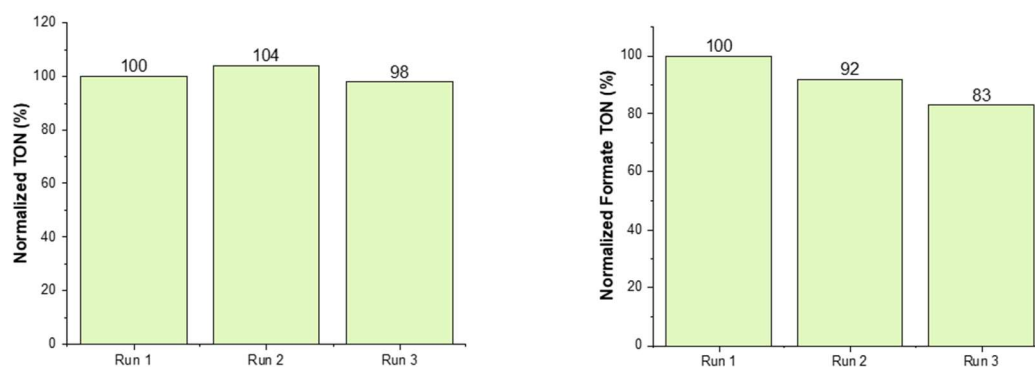


Figure 2.22: Recyclability of $(\text{PW}_{12}, \text{Cp}^*\text{Rh})@ \text{UiO}-67$ thin films for photocatalytic CO_2 reduction. Normalized formate TONs (a) after 30 min illumination, (b) after 180 min ($\text{CH}_3\text{CN}/\text{TEOA}$ 5:1, $\text{Ru}(\text{bpy})_3\text{Cl}_2$ 1 mM, 280 W, $\lambda > 415$ nm). The TON after 180 min is equal to 175 for the first run for $(\text{PW}_{12}, \text{Cp}^*\text{Rh})@ \text{UiO}-67$ thin films and 126 for $(\text{Cp}^*\text{Rh})@ \text{UiO}-67$ thin films.

As MOFs are obtained mostly as polycrystalline powders, depositing them on transparent conducting supports allows developing easy-to-use and recyclable setups. Investigating the stability of the catalyst on the powder often causes catalyst's mass loss after recollection by centrifugation. Moreover, the catalyst being highly porous, weighing the powder after each catalytic test would lead to a bias since the solvent uptake would contribute non-innocently to the composite mass. Having this in mind, the stability and recyclability of the

$(\text{PW}_{12}, \text{Cp}^*\text{Rh})@\text{UiO}-67$ composite upon photocatalysis were assessed utilizing thin films rather than suspensions, by drop casting (DC) $(\text{PW}_{12}, \text{Cp}^*\text{Rh})@\text{UiO}-67$ on an indium tin oxide (ITO) plate. Only a slight decrease of the formate production was detected after the first run (8%) and the second run of irradiation (9%) (**Figure 2.22**). Furthermore, it can be noticed that much higher formate TONs are achieved with DC-thin films than with the suspension (175 compared to 14.6, at 3h). This can be assigned to the better illumination of the crystallites deposited on the ITO plate in contrast with usual photocatalytic experiments performed on a suspension, as we recently observed for the $\text{P}_2\text{W}_{18}\text{Co}_4@\text{MOF}-545$ photosystem (**Figure 2.23**).³⁷ Indeed, while all particles deposited on ITO are exposed to light, the less efficient exposure of crystallites to light when in suspension (random orientation of crystallites, light diffusion by the suspension...) may be responsible for the lower TONs observed.

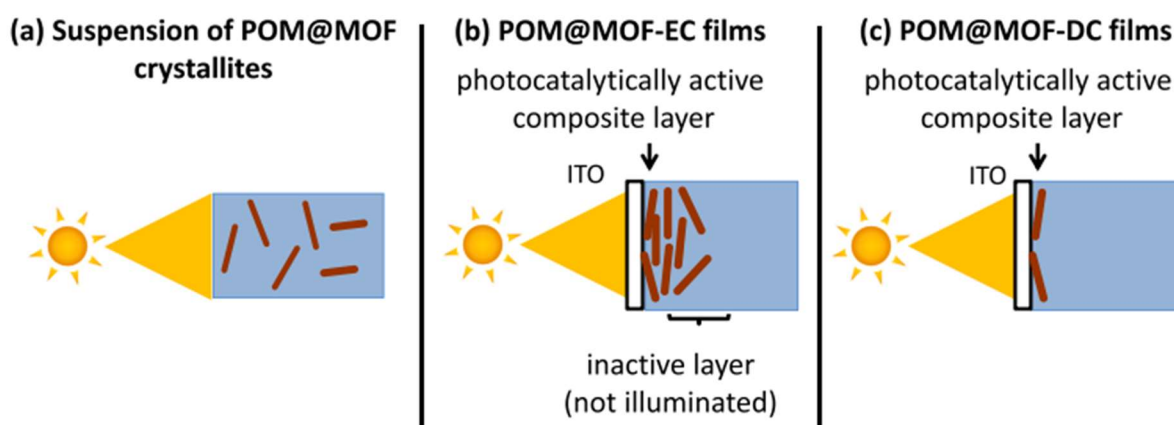


Figure 2.23: Schematic representation of the $\text{P}_2\text{W}_{18}\text{Co}_4@\text{MOF}-545$ photosystem under various setups upon light illumination: (a) in suspension, light capture by the crystallites is not optimal (random orientation of crystallites, light diffusion); (b) as a thick layer on ITO obtained using electrophoresis (EP); the absorption of light is limited to the fraction of the crystallites in contact with ITO; (c) deposited on ITO by drop casting; DC allows depositing small amounts of $\text{POM}@\text{MOF}$ dispersed on ITO so that all crystallites may be illuminated.³⁷

4.2 Post-catalysis characterization

Importantly, no significant differences are detected in the XRD (**Figure 2.10**), IR (**Figure 2.11**) and EDS-SEM analyses (**Figure 2.24**) between the composite before and after the photocatalytic reaction, confirming its stability upon both illumination and the catalytic event.

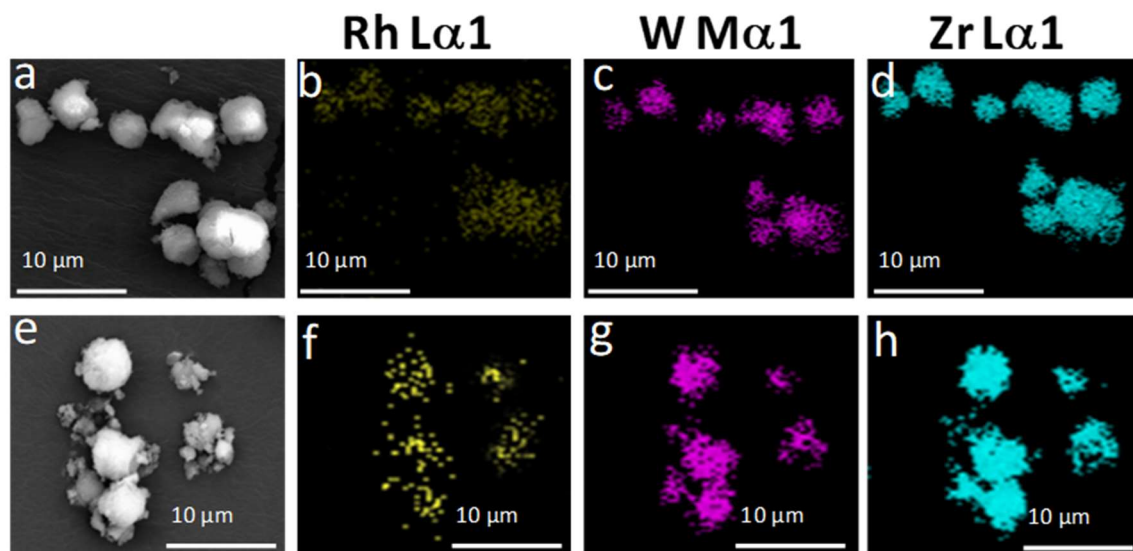


Figure 2.24: a) SEM image of $(\text{PW}_{12}, \text{Cp}^*\text{Rh})@\text{UiO}-67$, b), c), d) EDS mapping of Rh, W and Zr, respectively, before catalysis and e) SEM image, f), g), h) EDS mapping of Rh, W and Zr, respectively, after catalysis.

The PDF data collection of the $(\text{PW}_{12}, \text{Cp}^*\text{Rh})@\text{UiO}-67$ composite after photocatalysis showed no modification of the d-PDF profile associated to the POM, demonstrating that it remains intact upon the photocatalytic step (**Figure 2.25**).

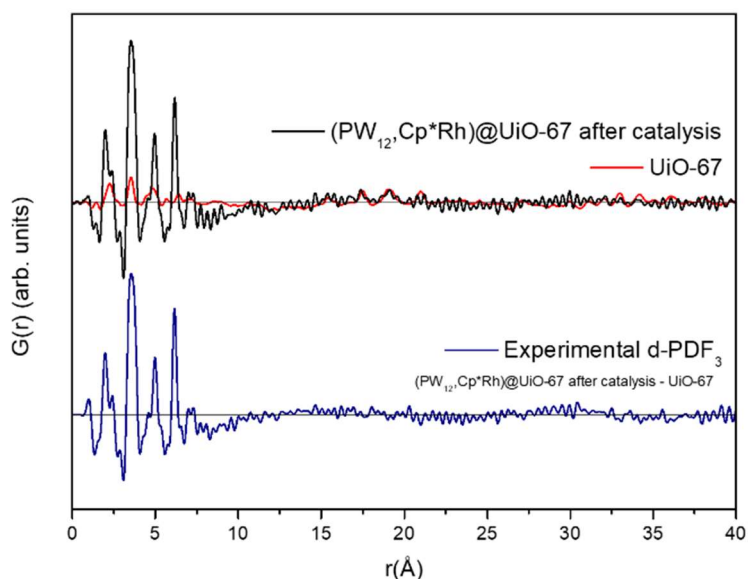


Figure 2.25: Experimental PDF data for $(\text{PW}_{12}, \text{Cp}^*\text{Rh})@\text{UiO}-67$ after catalysis (black) and the POM-free UiO-67 (red). Bottom: the resulting d-PDF for PW_{12} encapsulated in $(\text{PW}_{12}, \text{Cp}^*\text{Rh})@\text{UiO}-67$ after catalysis.

4.3 Mechanistic investigation

This subpart describes DFT calculations performed by Albert Solé-Daura in view of our results in photocatalysis, aiming at understanding the possible role of each component of the complex $(\text{PW}_{12}, \text{Cp}^*\text{Rh})@\text{UiO}-67$ system. They are briefly summarized here in order to provide key comparative features between the POM-free and the POM-containing catalyst for CO_2 reduction.

$[\text{Ru}(\text{bpy})_3]\text{Cl}_2$ is used as an external photosensitizer. When irradiated by visible light, an electron from the ruthenium complex is promoted to the bipyridine linker as a result of a metal ligand charge transfer, forming an MLCT excited singlet state, which rapidly evolves to a long-lived triplet MLCT via intersystem crossing.³⁸ The reduced bipyridine in the $^3\text{MLCT}$ state can act as an electron donor to reduce the POM with up to 2 electrons in a step-wise process that involves two different molecules of photosensitizer. This $^3\text{MLCT}$ is also reducing enough to transfer electrons to the Cp^*Rh catalyst, yielding a $\text{Rh}(\text{I})$ complex and releasing the Cl^- ligand, while consuming two molecules of photoexcited $\text{Ru}(\text{bpy})_3$. The oxidized form of the photosensitizer can be then reduced by TEOA in solution, regenerating the $\text{Ru}(\text{II})\text{bpy}_3$ species while generating $\text{TEOA}^{+\bullet}$ radical cation. The latter $\text{TEOA}^{+\bullet}$ is then quenched by a second TEOA molecule, leading to the formation of HTEOA^+ which was found to act as the source of protons, and a neutral TEOA^\bullet radical, a reducing agent able to reduce both PW_{12} and Cp^*Rh . These preliminary steps are the same no matter the presence of PW_{12} .

Starting from the $\text{Cp}^*\text{Rh}(\text{I})$ shown in **Figure 2.26**, in presence of HTEOA^+ a proton exchange can occur and form the $\text{Cp}^*\text{Rh}(\text{III})\text{H}$ intermediate. From this species, we can envisage two possible processes to occur: the first one (in black) where no POM is near the Cp^*Rh , and the second one (in blue) with a doubly-reduced $\text{PW}_{12}(2e^-)$ immobilized near the catalyst.

i) In the absence of POM (black pathway in **Figure 2.26**), an intramolecular hydrogen transfer from the Rh center to the Cp^* ligand is expected to be faster than the direct bpy ligand reduction by the electron donor (leading to $\text{Cp}^*\text{Rh}(\text{III})\text{H}(\text{bpy}^\bullet)$) to form the active species of the catalyst. This is due to the low concentration of electron donors in solution (namely TEOA^\bullet and photoactivated $\text{Ru}(\text{bpy})_3$). Thus, it is expected that an equilibrium between $\text{Cp}^*\text{Rh}(\text{III})\text{H}$ (at $-2.4 \text{ kcal}\cdot\text{mol}^{-1}$) and $(\text{Cp}^*\text{H})\text{Rh}(\text{I})$ (at $-7.2 \text{ kcal}\cdot\text{mol}^{-1}$) is reached, the latter being more stable. Interaction between $(\text{Cp}^*\text{H})\text{Rh}(\text{I})$ and an electron donor, followed by another intramolecular hydrogen transfer from the Cp^* moiety to the Rh leads to the formation of the catalyst in its

active form ($-3.6 \text{ kcal}\cdot\text{mol}^{-1}$). This last intramolecular hydrogen transfer is the reaction limiting step with a relatively high ΔG^\ddagger of $26.3 \text{ kcal}\cdot\text{mol}^{-1}$ (shown in red arrow). This limiting step could be avoided with a higher concentration of electron donors since the reduction would occur before the first intramolecular hydrogen exchange.

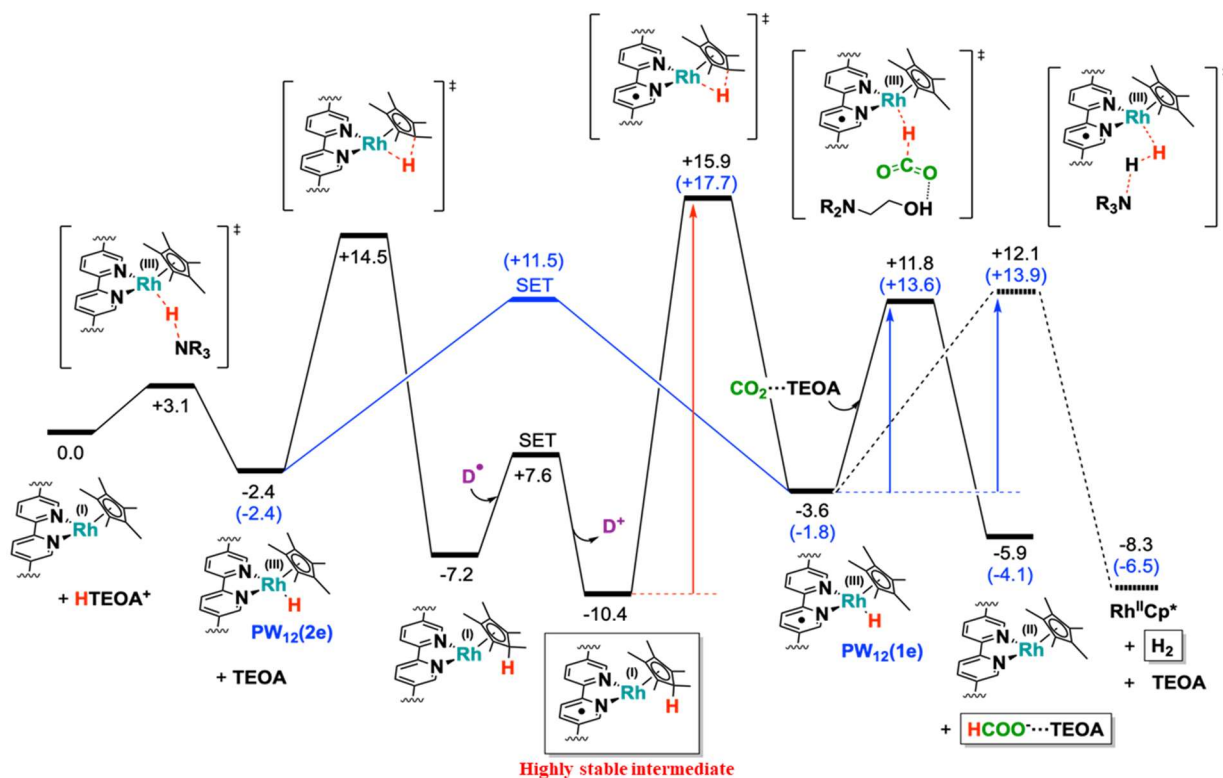


Figure 2.26: Proposed mechanism for CO_2 photoreduction by $\text{Cp}^*\text{Rh}@ \text{UiO-67}$ (in black and red) and $(\text{PW}_{12}, \text{Cp}^*\text{Rh})@ \text{UiO-67}$ (in blue). Relative Gibbs free energies are given in $\text{kcal}\cdot\text{mol}^{-1}$.

ii) The presence of the doubly-reduced $\text{PW}_{12}(2\text{e}^-)$ (blue pathway in **Figure 2.26**) plays a huge role in the catalytic process, by being confined next to the Cp^*Rh and able to act as an electron donor. The free-energy barrier for the single-electron transfer (SET) from the doubly-reduced POM to the Rh-catalyst ($+13.9 \text{ kcal}\cdot\text{mol}^{-1}$) is lower than that for the POM-free process whereby an H-transfer allows forming the $\text{Rh}(\text{I})$ species ($+16.9 \text{ kcal}\cdot\text{mol}^{-1}$). Thus the presence of the POM allows bypassing the formation of the highly stable intermediate highlighted in **Figure 2.26** and going directly from the $\text{Cp}^*\text{Rh}(\text{III})\text{H}(\text{bpy})$ to the active $\text{Cp}^*\text{Rh}(\text{III})\text{H}(\text{bpy}^\bullet)$ at a lower activation energy cost. The new limiting step (arrows in blue) is then either the CO_2 transformation into HCOO^- or the H_2 formation with $\Delta G = 13.6 \text{ kcal}\cdot\text{mol}^{-1}$ for the CO_2 reduction and $\Delta G = 13.9 \text{ kcal}\cdot\text{mol}^{-1}$ for proton reduction. This change in the nature of the limiting step

and the significant reduction of the overall free-energy barrier by ca. $12 \text{ kcal}\cdot\text{mol}^{-1}$ can qualitatively explain the experimentally observed enhancement of the catalytic activity induced by the presence of the POM. Moreover, the fact that the POM acts as an electron relay suggests that any POM with suitable energy levels may be approachable to increase the activity of the catalyst without significantly altering its reactivity or selectivity (**Figure 2.27**).

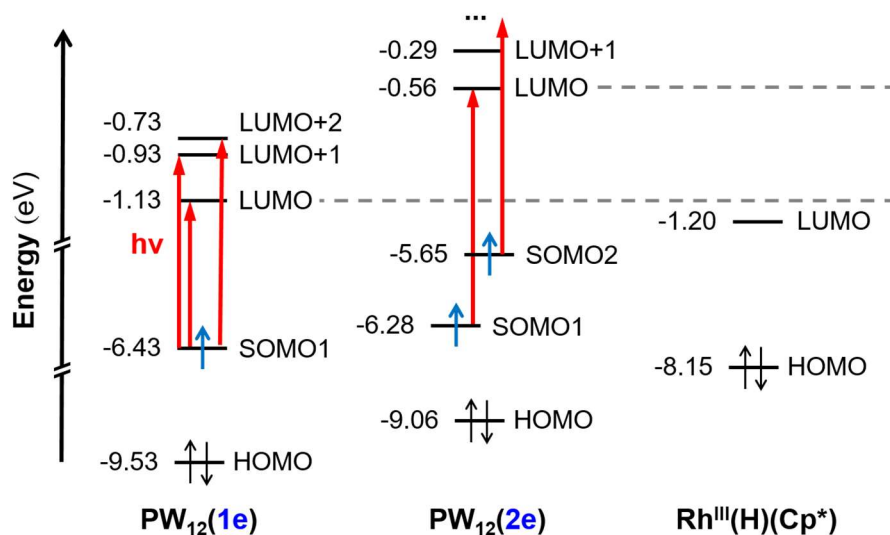


Figure 2.27: HOMO and LUMO levels of reduced $\text{PW}_{12}(1\text{e})$, two times reduced $\text{PW}_{12}(2\text{e})$ and $\text{Rh}(\text{III})(\text{H})(\text{Cp}^*)$.

It is important to keep in mind that this mechanism occurs once the POM is reduced twice, meaning that the nature of the POM still has an impact on the overall properties. The POM should be easily reducible in order to be reduced twice, but also able to transfer electron easily in order to act as an electron relay. Building a similar system with other Keggin POMs would help us better understand the role of each moiety.

5. Conclusions and perspectives

We successfully co-immobilized a POM entity and a Cp^*Rh catalyst in the $(\text{PW}_{12}, \text{Cp}^*\text{Rh})@\text{UiO}-67$ material and showed that the reduction of CO_2 into formate and the production of H_2 are significantly enhanced when compared to those observed with the POM-free $\text{Cp}^*\text{Rh}@\text{UiO}-67$ material. Catalytic studies were performed on crystallites in suspensions. The $(\text{PW}_{12}, \text{Cp}^*\text{Rh})@\text{UiO}-67$ composite was also deposited as films on ITO plates, providing evidence for the stability and the recyclability of the system as well as improved performances compared to those of suspensions. Importantly, differential Pair Distribution Function analysis

was used for the first time to characterize a POM@MOF composite and allowed to prove the integrity of the POM before and after catalysis. Also, solid-state NMR nicely confirmed the two environments of the POMs within the MOF's cavities as determined from Monte Carlo and DFT calculations, with the Cp^*Rh moiety pointing either towards a POM-free cavity or towards a POM. Such POM- Cp^*Rh interactions might explain the beneficial role of the POMs in the photocatalytic reduction of CO_2 . DFT calculations also helped to provide a plausible mechanism. However, the precise role of the POM in the catalytic reaction remains to be confirmed. With this goal in mind, we started different projects detailed in the next part.

As mentioned in the conclusion above, and at the time of the publication of this study, the investigations on the mechanism and on the role of each component of our complex system were still at an early stage. Different hypotheses on how the PW_{12} could play a role in this catalytic system, the most plausible one being a role of either electron or proton relay, were envisioned.

5.1 $\text{PMo}_{12}\text{@UiO-67}$

In order to confirm the role of the POM in the system, we tried to change the nature of the Keggin anion immobilized in the Rh-MOF. Changing the red/ox properties of the POM, where PMo_{12} is easier to reduce than PW_{12} ,^{39,40} would influence its capacity to transfer electrons to the Cp^*Rh moiety. Considering the proposed mechanism, the limiting step is not the electron transfer from the POM to the catalyst but from the active form of the catalyst to the CO_2 or H^+ . The presence of reduced POM allows to bypass the previous limiting step. Thus, having an increased amount of reduced POM near the catalyst, either by having a higher loading, or by having a POM that is more easily reduced, should increase furthermore the system efficiency for CO_2 reduction. If no change is to be observed in the catalytic performances between the two different $(\text{Keggin}, \text{Cp}^*\text{Rh})\text{@UiO-67}$ composites, here $(\text{PMo}_{12}, \text{Cp}^*\text{Rh})\text{@UiO-67}$ and $(\text{PW}_{12}, \text{Cp}^*\text{Rh})\text{@UiO-67}$, that would lead to two hypotheses. The first one is that even though PMo_{12} can be reduced more easily, it might not transfer the electron as well as PW_{12} , and the second that the effect on the catalysis does not depend on the nature of the POM immobilized inside the pore.

The first step to test this hypothesis was to synthesize $\text{PMo}_{12}\text{@UiO-67}$. The $\text{PMo}_{12}\text{@UiO-67}$ system has already been studied by a former PhD student at Institut Lavoisier de Versailles, William Salomon. He has shown that a direct synthesis, such as the one used for the

incorporation of PW_{12} inside the UiO-67 frameworks, was unsuccessful. The “POM@MOF” PXRD pattern indeed did not match with that of the pristine UiO-67 (**Figure 2.28**). In addition, the peaks were compared to those of the simulated XRD pattern obtained with the CIF of Strandberg *et al.* and do not match with those of $\text{H}_3\text{PMo}_{12}\text{O}_{40}$ neither.⁴¹ Moreover, a color change corresponding to the reduced PMo_{12} could be observed. The *in-situ* reduction of the POM can be the reason why the final composite is amorphous. In order to avoid this process, we tried to add a strong oxidizing agent in the reaction media, Br_2 . However, the final compound was still amorphous. We thus turn to another POM, nonetheless trying other synthetic conditions, such as ambient temperature synthesis, or microwave synthesis could maybe solve the crystallinity issues.

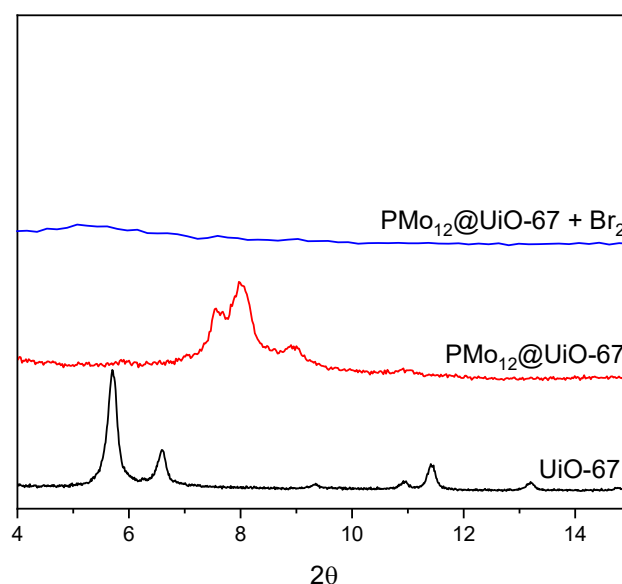


Figure 2.28: PXRD of UiO-67 and $\text{PMo}_{12}@UiO-67$.

5.2 $\text{PW}_{10}\text{Ti}_2@UiO-67$

We have thus started to study the incorporation of the $\text{PW}_{10}\text{Ti}_2$ POM inside the UiO-67. The idea was also to work with a POM showing better electron/proton relay properties¹⁸ than PW_{12} and able to reduce CO_2 by itself.¹⁹ To synthesize the $\text{PW}_{10}\text{Ti}_2@UiO-67$, we have used the same method as for $\text{PW}_{12}@UiO-67$. The proportion of $\text{PW}_{10}\text{Ti}_2$ was adapted to have a similar stoichiometry with respect to ZrCl_4 . The PXRD data show that the MOF is still crystalline after the synthesis. Infrared spectra show no additional peak that could be attributed to $\text{PW}_{10}\text{Ti}_2$ in the POM@MOF composite, probably due to the low POM loading. Nevertheless, the presence of $\text{PW}_{10}\text{Ti}_2$ inside the MOF and the loading has been confirmed by EDS analysis, with a W/Zr

ratio of 0.18. EDS analysis also revealed the presence of KCl (with ~30% K and 30% Cl compared to 32% Zr, 6% W and 1.5% Ti). Several washing with EtOH (96%) were necessary to get rid of the KCl without harming the POM@MOF integrity.

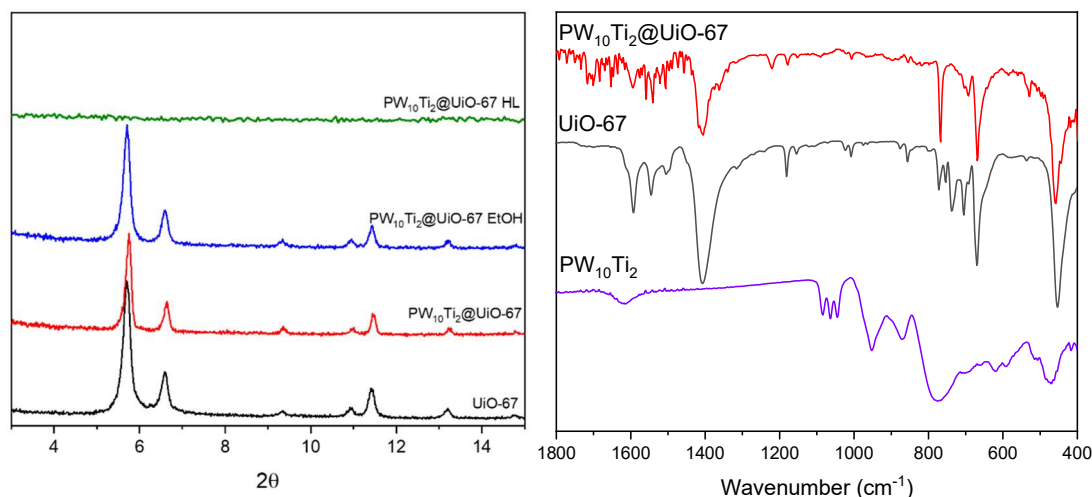


Figure 2.29: PXRD patterns of UiO-67 and the $\text{PW}_{10}\text{Ti}_2@\text{UiO-67}$ composites, in blue after the EtOH washing, and in green with increase amount (HL stands for High Loading) of $\text{PW}_{10}\text{Ti}_2$ during the synthesis (left), and IR spectra of UiO-67, $\text{PW}_{10}\text{Ti}_2$ and $\text{PW}_{10}\text{Ti}_2@\text{UiO-67}$ (right).

The first problem we encountered with this sub-project was the low content in $\text{PW}_{10}\text{Ti}_2$ in the MOF. As seen previously in this chapter, the POM is meant to be immobilized in the MOF without its counterions, meaning that a certain amount of the MOF's linkers is removed to guarantee an electroneutral composite. The necessity of those defects to immobilize the POM could thus lead to a lower loading when the POM has a higher charge. $\text{PW}_{10}\text{Ti}_2$ bears seven negative charges, more than twice that of PW_{12} . It results that the POM@MOF loading is only equal to 0.1 POM per Zr_6 cluster (about one POM every ten cavities). We tried to increase the loading by adding a higher amount of $\text{PW}_{10}\text{Ti}_2$ (from one to three times the initial amount) but the resulting powder became amorphous. However, the next step would still be to exchange the biphenyl linkers for the catalytic Cp^*Rh on the low-content POM@MOF composite and to test the composite activity for CO_2 reduction. Although the loading is low, as the POM could show better CO_2 boosting effect, a significant improved catalytic effect could not be excluded even at low loading.

5.3 $(\text{PW}_{12}, \text{Cp}^*\text{Rh})@ \text{POP}$

Lastly, we have worked in collaboration with the group of Dr. Jérôme Canivet in IRCElyon to co-immobilize the Cp^*Rh and PW_{12} in another kind of porous material. The objective was to see if the impact of the PW_{12} POM observed in the UiO-67 on CO_2 photocatalytic reduction could be reproduced on another similar porous however non-crystalline polymer. Dr. Ashta Chandra Ghosh thus worked on the immobilization of the POM in a bipyridine/viologen based porous organic polymer (POP) as a first step before adding the Cp^*Rh catalyst by post synthetic modification methods (**Figure 2.30**).

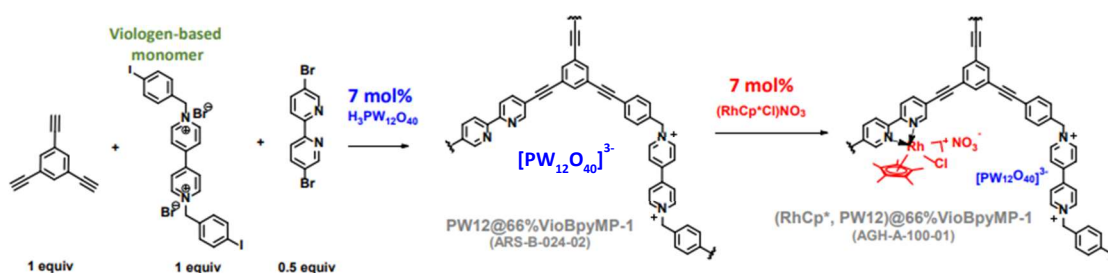


Figure 2.30: Synthesis steps of $(\text{PW}_{12}, \text{Cp}^*\text{Rh})@66\% \text{VioBpyMP-1}$

I performed the CO_2RR catalytic tests on the obtained composite. Preliminary results are shown in **Figure 2.31**, where R values are the amount of H_2 produced considering 1g of composites for one hour. Interestingly, we can see an increase in the H_2 production when the POM is added to the complex when compared to the POM-free polymer. Also, the catalyst is still active after three catalytic cycles. However, surprisingly, the formate production is not enhanced by the presence of the POM (**Figure A2.5**) while both the formate and H_2 productions were increased when PW_{12} and Cp^*Rh were co-immobilized in the MOF. Co-immobilization of the POM and Cp^*Rh catalyst in the POP did once again increase the system efficiency for CO_2 reduction, confirming that the use of POM to enhance the catalysis can be used with other supports. Interestingly the H_2 production increase is similar in both UiO-67 and POP system; however, we are still working to understand the reasons of this increase in H_2 only by DFT calculations.

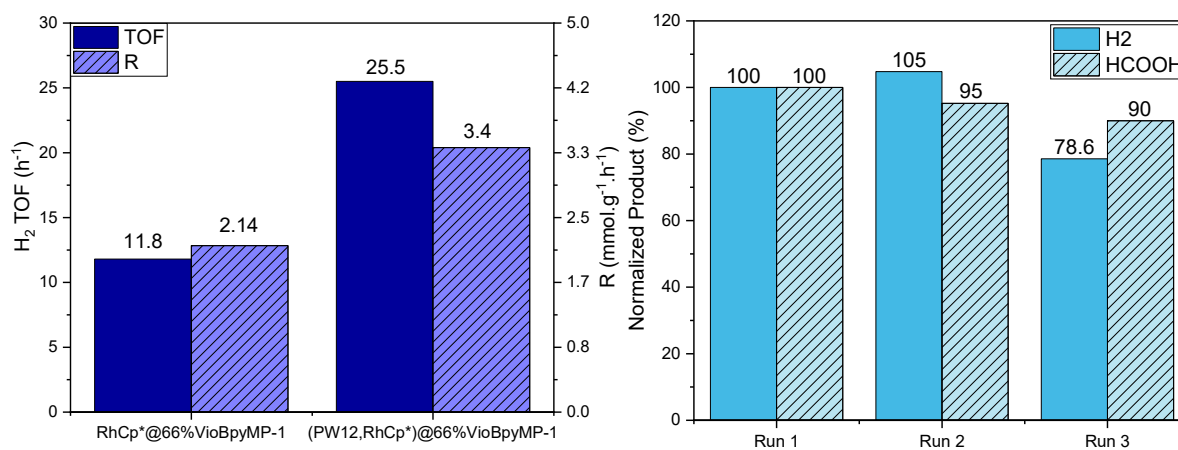


Figure 2.31: Production yield of H_2 with RhCp^* @66%VioBpyMP-1 and $(\text{PW}_{12}, \text{RhCp}^*)$ @66%VioBpyMP-1 (left) and recyclability tests with $(\text{PW}_{12}, \text{RhCp}^*)$ @66%VioBpyMP-1 as a catalyst (right).

6. Experimental Section

If no contrary indication, all chemicals have been bought either from Sigma, TCI Chemicals or Alfa Aesar and used without any further purification.

Synthesis of Keggin POMs.

H₃PW₁₂O₄₀ was synthesized as previously described in Ions minéraux condensés.⁴² H₃PMo₁₂O₄₀ and K₇PW₁₀Ti₂O₄₀ were synthesized following reported procedures.^{19,43}

Synthesis of Cp*Rh(bpydc).

Cp*Rh(bpydc) was synthesized according to the protocol described by Chambers *et al.*¹ A 50 mL reaction flask was charged with 0.506 g (0.820 mmol, 1 equivalent) of [Cp*RhCl₂]₂ and 0.400g (1.64 mmol, 2 equivalent) of 2,2'-bipyridine-5,5'-dicarboxylic acid. 25 mL of MeOH was added to the reaction flask and the mixture was allowed to stir at room temperature. After one hour, the homogeneous deep orange solution was concentrated under vacuum. Excess diethyl ether was added to the reaction flask to yield a yellow precipitate and a colorless solution. The yellow precipitate was collected on a Buchner funnel and dried under vacuum for 2 hours at which point the dried powder was transferred to a vial.

Synthesis of UiO-67.

UiO-67 was synthesized as described by Salomon *et al.*¹⁴ ZrCl₄ (116 mg, 0.5 mmol), biphenyl-dicarboxylic acid (121 mg, 0.5 mmol) and benzoic acid (1.83 g, 15 mmol, 30 equivalents) were dissolved in 10 mL of dimethylformamide (DMF) in a 23 mL polytetrafluoroethylene-lined stainless steel container. Hydrochloric acid 37% (83 μ L) was then added to the solution. All reactants were stirred briefly before heating. The mixture was heated to 120 °C over a period of 1 h, kept at 120 °C for 24 h, and allowed to cool down to room temperature. The solid was filtrated, washed with dry DMF and dry acetone and dried in an oven at 90°C overnight. The presence of chlorine has not been detected by EDX analysis indicating that the linker deficiency has been compensated by hydroxyl ligands in the formula. Final mass: 102 mg (yield 60% based on Zr).

Synthesis of Cp*Rh@UiO-67.

Cp*Rh@UiO-67 with a Cp*Rh loading of 7% was synthesized by a slight variation of the reaction conditions used for the synthesis of the Cp*Rh@UiO-67 with a Cp*Rh loading of 10%.

¹ In a 10 mL glass flask, UiO-67 (50 mg) and $\text{Cp}^*\text{Rh}(\text{bpydc})\text{Cl}_2$ (17 mg, $3 \cdot 10^{-5}$ mol) were suspended in 10 mL of degassed deionized water. The solution was stirred at room temperature for 24 h. The solid was isolated by centrifugation and thus suspended in 5 mL of DMF. After standing at room temperature for 1 h, the suspension was centrifuged and the solvent was decanted. The obtained yellow solid (~ 40 mg) was then washed with ethanol and finally dried under reduced pressure at room temperature.

Synthesis of $(\text{PW}_{12}, \text{Cp}^*\text{Rh})@\text{UiO}-67$.

In a 10 mL glass flask, $\text{PW}_{12}@\text{UiO}-67$ (50 mg, $1.87 \cdot 10^{-5}$ mol) and $\text{Cp}^*\text{Rh}(\text{bpydc})\text{Cl}_2$ (17 mg, $3 \cdot 10^{-5}$ mol) were suspended in 5 mL of degassed deionized water. This solution was stirred at room temperature for 24 h. The solid was isolated by centrifugation and suspended in 5 mL of DMF. After standing at room temperature for 1 h, the suspension was centrifuged and the solvent was decanted. The obtained yellow solid (40 mg) was then washed with ethanol and finally dried under reduced pressure at room temperature.

Synthesis of $\text{PMo}_{12}@\text{UiO}-67$.

The synthesis of $\text{PMo}_{12}@\text{UiO}-67$ follows the same protocol as $\text{PW}_{12}@\text{UiO}-67$ but using $\text{H}_3\text{PMo}_{12}\text{O}_{40}$ instead of $\text{H}_3\text{PW}_{12}\text{O}_{40}$.

Synthesis of $\text{PW}_{10}\text{Ti}_2@\text{UiO}-67$.

The synthesis of $\text{PW}_{10}\text{Ti}_2@\text{UiO}-67$ follows the same protocol as $\text{PW}_{12}@\text{UiO}-67$ but using $\text{K}_7\text{PW}_{10}\text{Ti}_2\text{O}_{40}$ instead of $\text{H}_3\text{PW}_{12}\text{O}_{40}$.

Thin film preparation.

Indium thin oxide 4 cm^2 was bought from SOLEMS and cut in $0.6 \text{ cm} \times 2 \text{ cm}$ plates. A plate was sonicated in ethanol for 20 min and then dried under airflow. A solution of $1 \text{ mg} \cdot \text{mL}^{-1}$ of catalyst ($\text{Cp}^*\text{Rh}@\text{UiO}-67$ or $(\text{PW}_{12}, \text{Cp}^*\text{Rh})@\text{UiO}-67$) was sonicated for 20 min in parallel. After the sonication, $10 \mu\text{L}$ of the suspension was drop-cast on the ITO plates, dried under air and then in an oven at 100°C .

General photocatalytic procedure.

Photochemical Reactions were performed using a 280 W, high-pressure Xe arc lamp (Newport Instruments). The beam was passed through a water infrared filter, a collimating lens and a filter holder equipped with a 415 nm band pass filter (Asahi Spectra). Samples were prepared in a 1 cm path length quartz sealed cuvette (Hellma) which was placed in a temperature-

controlled cuvette holder (Quantum Northwest) maintained at 20 °C with a circulated water bath. A CH_3CN /TEOA mixture 5:1 was used as a solvent (CH_3CN and TEOA purchased from Sigma Aldrich and used without further purification). The photosensitizer utilized was a 1.0 mM solution of $\text{Ru}(\text{bpy})_3\text{Cl}_2$ (purchased from Sigma Aldrich and used without further purification). 1.4 mg of $(\text{PW}_{12}, \text{Cp}^*\text{Rh})@\text{UiO}-67$ and 0.9 mg of $\text{Cp}^*\text{Rh}@\text{UiO}-67$, which corresponds to 0.17 μmol of Cp^*Rh catalyst, were used for the photocatalytic studies. Samples were saturated with CO_2 via directly bubbling CO_2 through the solution mixture for 20 min. During irradiation, the samples were vigorously stirred and aliquots of gas and liquid were analyzed. H_2 measurements (aliquots of 50 μL of the headspace) were performed by gas chromatography on a Shimadzu GC-2014 equipped with a Quadrex column, a Thermal Conductivity Detector and using N_2 as a carrier gas. The formate concentration was determined using a Metrohm 883 Basic IC plus ionic exchange chromatography instruments, using a Metrosep A. Supp 5 column and a conductivity detector. A typical measurement requires the sampling of 200 μL of solution, followed by 100-time dilution in deionized 18 $\text{M}\Omega$ water and injection of 20 μL into the IC chromatograph. All TONs and TOFs were assessed by normalizing the production of H_2 and HCOO^- with the number of nmol of Cp^*Rh catalyst.

7. References

1. Chambers, M. B. *et al.* Photocatalytic Carbon Dioxide Reduction with Rhodium-based Catalysts in Solution and Heterogenized within Metal-Organic Frameworks. *ChemSusChem* **8**, 603–608 (2015).
2. Bolinger, C. M. *et al.* Electrocatalytic reduction of CO₂ based on polypyridyl complexes of rhodium and ruthenium. *J. Chem. Soc. Chem. Commun.* 796–797 (1985) doi:10.1039/C39850000796.
3. Bolinger, C. M., Story, N., Sullivan, B. P. & Meyer, T. J. Electrocatalytic reduction of carbon dioxide by 2,2'-bipyridine complexes of rhodium and iridium. *Inorg. Chem.* **27**, 4582–4587 (1988).
4. Kölle, U. & Grützel, M. Organometallic Rhodium(III) Complexes as Catalysts for the Photoreduction of Protons to Hydrogen on Colloidal TiO₂. *Angew. Chem. Int. Ed. Engl.* **26**, 567–570 (1987).
5. Caix, C., Chardon-Noblat, S. & Deronzier, A. Electrocatalytic reduction of CO₂ into formate with [(η⁵-Me₅C₅)M(L)Cl]⁺ complexes (L = 2,2'-bipyridine ligands; M = Rh(III) and Ir(III)). *J. Electroanal. Chem.* **434**, 163–170 (1997).
6. Wang, C., Xie, Z., deKrafft, K. E. & Lin, W. Doping Metal–Organic Frameworks for Water Oxidation, Carbon Dioxide Reduction, and Organic Photocatalysis. *J. Am. Chem. Soc.* **133**, 13445–13454 (2011).
7. Li, L. *et al.* Effective visible-light driven CO₂ photoreduction via a promising bifunctional iridium coordination polymer. *Chem. Sci.* **5**, 3808–3813 (2014).
8. Cavka, J. H. *et al.* A New Zirconium Inorganic Building Brick Forming Metal Organic Frameworks with Exceptional Stability. *J. Am. Chem. Soc.* **130**, 13850–13851 (2008).
9. Luo, Y.-H., Dong, L.-Z., Liu, J., Li, S.-L. & Lan, Y.-Q. From molecular metal complex to metal-organic framework: The CO₂ reduction photocatalysts with clear and tunable structure. *Coord. Chem. Rev.* **390**, 86–126 (2019).
10. Pullen, S., Fei, H., Orthaber, A., Cohen, S. M. & Ott, S. Enhanced Photochemical Hydrogen Production by a Molecular Diiron Catalyst Incorporated into a Metal–Organic Framework. *J. Am. Chem. Soc.* **135**, 16997–17003 (2013).
11. Wang, X., Wisser, F. M., Canivet, J., Fontecave, M. & Mellot-Draznieks, C. Immobilization of a Full Photosystem in the Large-Pore MIL-101 Metal–Organic Framework for CO₂ reduction. *ChemSusChem* **11**, 3315–3322 (2018).
12. Feng, X., Ren, Y. & Jiang, H. Metal-bipyridine/phenanthroline-functionalized porous crystalline materials: Synthesis and catalysis. *Coord. Chem. Rev.* **438**, 213907 (2021).
13. Todorova, T. K., Huan, T. N., Wang, X., Agarwala, H. & Fontecave, M. Controlling Hydrogen Evolution during Photoreduction of CO₂ to Formic Acid Using [Rh(R-bpy)(Cp*)Cl]⁺ Catalysts: A Structure–Activity Study. *Inorg. Chem.* **58**, 6893–6903 (2019).
14. Salomon, W. *et al.* Immobilization of polyoxometalates in the Zr-based metal organic framework UiO-67. *Chem. Commun.* **51**, 2972–2975 (2015).
15. Eppedgi, J., Diskin-Posner, Y., Weiner, L. & Neumann, R. Photoreduction of Carbon Dioxide to Carbon Monoxide with Hydrogen Catalyzed by a Rhenium(I) Phenanthroline–Polyoxometalate Hybrid Complex. *J. Am. Chem. Soc.* **133**, 188–190 (2011).
16. Ci, C., Carbó, J. J., Neumann, R., Graaf, C. de & Poblet, J. M. Photoreduction Mechanism of CO₂ to CO Catalyzed by a Rhenium(I)–Polyoxometalate Hybrid Compound. *ACS Catal.* **6**, 6422–6428 (2016).
17. Haviv, E., Shimon, L. J. W. & Neumann, R. Photochemical Reduction of CO₂ with Visible Light Using a Polyoxometalate as Photoreductant. *Chem. – Eur. J.* **23**, 92–95 (2017).
18. Liu, S.-M. *et al.* Ti-Substituted Keggin-Type Polyoxotungstate as Proton and Electron Reservoir Encaged into Metal–Organic Framework for Carbon Dioxide Photoreduction. *Adv. Mater. Interfaces* **5**, 1801062 (2018).

19. Yamase, T. & Sugeta, M. Photoreduction of CO₂ to CH₄ in water using dodecatungstophosphate as multielectron transfer catalyst. *Inorganica Chim. Acta* **172**, 131–134 (1990).
20. Samaniyan, M., Mirzaei, M., Khajavian, R., Eshtiagh-Hosseini, H. & Streb, C. Heterogeneous Catalysis by Polyoxometalates in Metal–Organic Frameworks. *ACS Catal.* **9**, 10174–10191 (2019).
21. Du, D.-Y., Qin, J.-S., Li, S.-L., Su, Z.-M. & Lan, Y.-Q. Recent advances in porous polyoxometalate-based metal–organic framework materials. *Chem. Soc. Rev.* **43**, 4615–4632 (2014).
22. Yang, L., Naruke, H. & Yamase, T. A novel organic/inorganic hybrid nanoporous material incorporating Keggin-type polyoxometalates. *Inorg. Chem. Commun.* **6**, 1020–1024 (2003).
23. Buru, C. T. *et al.* Adsorption of a Catalytically Accessible Polyoxometalate in a Mesoporous Channel-type Metal–Organic Framework. *Chem. Mater.* **29**, 5174–5181 (2017).
24. Buru, C. T. *et al.* Thermally induced migration of a polyoxometalate within a metal–organic framework and its catalytic effects. *J. Mater. Chem. A* **6**, 7389–7394 (2018).
25. Egami, T. & Billinge, S. J. L. *Underneath the Bragg Peaks: Structural Analysis of Complex Materials*. (Elsevier, 2003).
26. Chapman, K. W., Chupas, P. J. & Kepert, C. J. Selective Recovery of Dynamic Guest Structure in a Nanoporous Prussian Blue through in Situ X-ray Diffraction: A Differential Pair Distribution Function Analysis. *J. Am. Chem. Soc.* **127**, 11232–11233 (2005).
27. Platero-Prats, A. E. *et al.* Addressing the characterisation challenge to understand catalysis in MOFs: the case of nanoscale Cu supported in NU-1000. *Faraday Discuss.* **201**, 337–350 (2017).
28. Sava Gallis, D. F. *et al.* Selective O₂ Sorption at Ambient Temperatures via Node Distortions in Sc-MIL-100. *Chem. Mater.* **28**, 3327–3336 (2016).
29. Rangwani, S. *et al.* Adsorptive removal of Sb(V) from water using a mesoporous Zr-based metal–organic framework. *Polyhedron* **151**, 338–343 (2018).
30. Sava, D. F. *et al.* Capture of Volatile Iodine, a Gaseous Fission Product, by Zeolitic Imidazolate Framework-8. *J. Am. Chem. Soc.* **133**, 12398–12401 (2011).
31. Caliman, E., Dias, J. A., Dias, S. C. L. & Prado, A. G. S. Solvent effect on the preparation of H₃PW₁₂O₄₀ supported on alumina. *Catal. Today* **107–108**, 816–825 (2005).
32. Lawrence, M. C., Schneider, C. & Katz, M. J. Determining the structural stability of UiO-67 with respect to time: a solid-state NMR investigation. *Chem. Commun.* **52**, 4971–4974 (2016).
33. Chang, T. NMR characterization of the supported 12-heteropoly acids. *J. Chem. Soc. Faraday Trans.* **91**, 375–379 (1995).
34. Bennett, T. D. *et al.* Connecting defects and amorphization in UiO-66 and MIL-140 metal–organic frameworks: a combined experimental and computational study. *Phys. Chem. Chem. Phys.* **18**, 2192–2201 (2016).
35. Øien, S. *et al.* Detailed Structure Analysis of Atomic Positions and Defects in Zirconium Metal–Organic Frameworks. *Cryst. Growth Des.* **14**, 5370–5372 (2014).
36. Kremenović, A. *et al.* Keggin’s ion structural modification and expansion of dodecatungstophosphoric acid hexahydrate induced by temperature treatment: In situ X-ray powder diffraction and raman investigations. *Solid-State Ion.* **132**, 39–53 (2000).
37. Paille, G. *et al.* Thin Films of Fully Noble Metal-Free POM@MOF for Photocatalytic Water Oxidation. *ACS Appl. Mater. Interfaces* **11**, 47837–47845 (2019).
38. Kuramochi, Y., Ishitani, O. & Ishida, H. Reaction mechanisms of catalytic photochemical CO₂ reduction using Re(I) and Ru(II) complexes. *Coord. Chem. Rev.* **373**, 333–356 (2018).

39. Song, I. K. & Barteau, M. A. Redox properties of Keggin-type heteropolyacid (HPA) catalysts: effect of counter-cation, heteroatom, and polyatom substitution. *J. Mol. Catal. Chem.* **212**, 229–236 (2004).
40. Himeno, S., Takamoto, M., Santo, R. & Ichimura, A. Redox Properties and Basicity of Keggin-Type Polyoxometalate Complexes. *Bull. Chem. Soc. Jpn.* **78**, 95–100 (2005).
41. Strandberg, R. *et al.* Multicomponent Polyanions. The Crystal Structure of a Hydrated Dodecamolybdophosphoric Acid, $H_3Mo_{12}PO_{40}(H_2O)$. *Acta Chem. Scand.* **29a**, 359–364 (1975).
42. Souchay, P. *Ions minéraux condensés*,. (Masson et Cie, 1969).
43. Rocchiccioli-Deltcheff, C., Fournier, M., Franck, R. & Thouvenot, R. Vibrational investigations of polyoxometalates. 2. Evidence for anion-anion interactions in molybdenum(VI) and tungsten(VI) compounds related to the Keggin structure. *Inorg. Chem.* **22**, 207–216 (1983).

8. Appendix

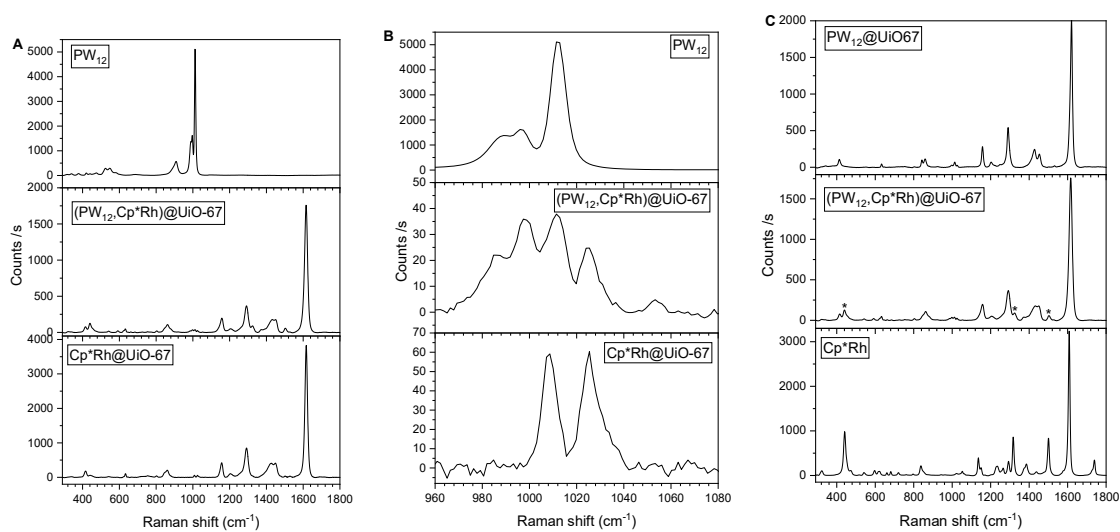


Figure A2.1: Raman spectra of A, B) PW_{12} , $(PW_{12},Cp^*Rh)@UiO-67$ and $Cp^*Rh@UiO-67$ and C) $PW_{12}@UiO-67$, $(PW_{12},Cp^*Rh)@UiO-67$ and Cp^*Rh solids measured at 532 nm excitation wavelength.

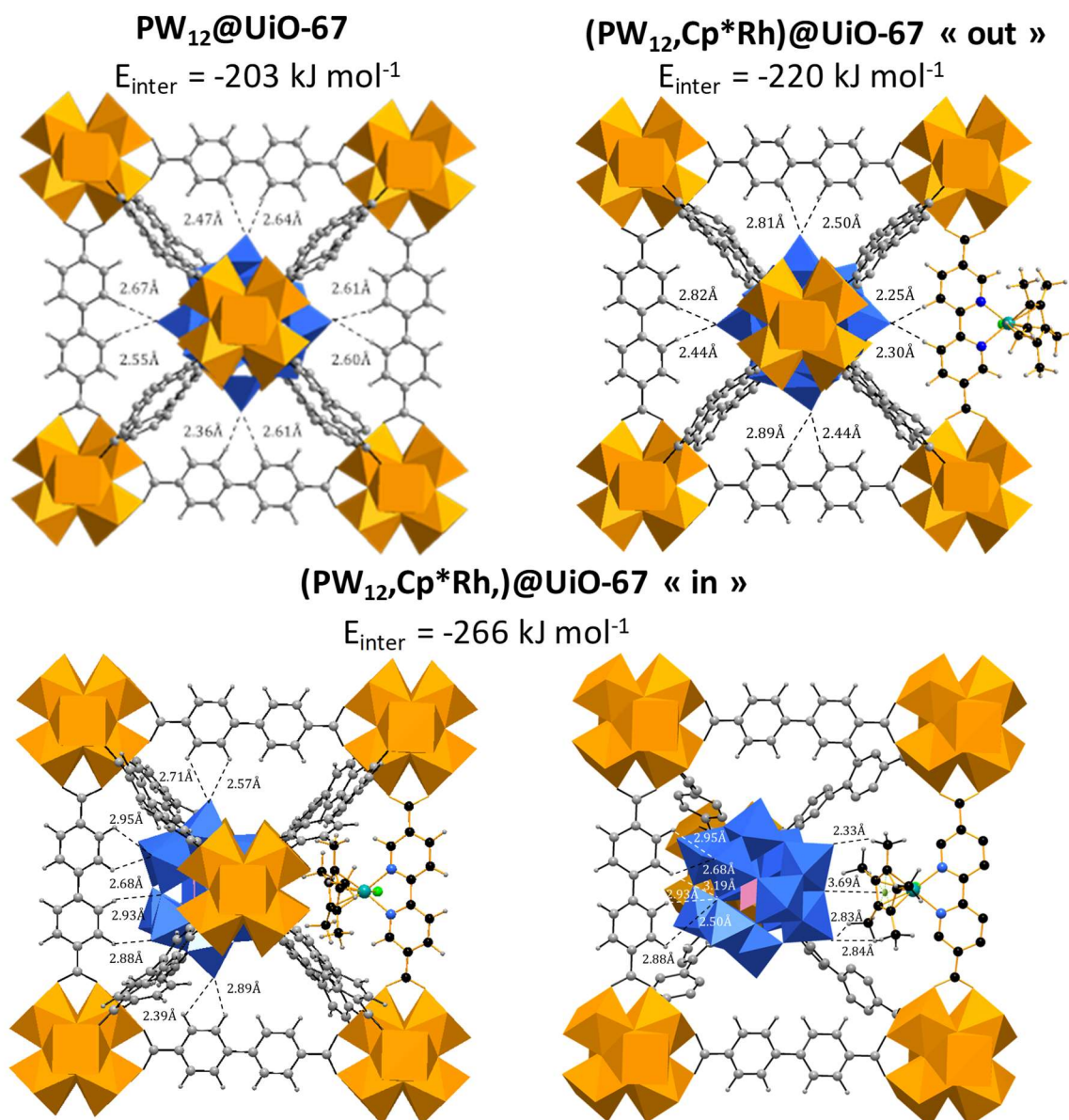


Figure A2.2: Computed $\text{PW}_{12}@\text{UiO-67}$ and $(\text{PW}_{12},\text{Cp}^*\text{Rh})@\text{UiO-67}$ models. Computed position of PW_{12} in $\text{PW}_{12}@\text{UiO-67}$ and $(\text{PW}_{12},\text{Cp}^*\text{Rh})@\text{UiO-67}$ as obtained from SA and DFT-D3 level geometry optimizations. The POM and the Rh-catalytic center are modeled within the same cage (“in” position) or different cages (“out” position). For describing the “out” position, one inorganic Zr-cluster was disregarded to illustrate the interactions of the POM with the Cp^*Rh moiety. Interatomic distances and interaction energies between PW_{12} and the MOF host are given for each model. WO_6 , blue polyhedra; ZrO_8 , yellow polyhedra; Rh, dark green sphere; O, red spheres; C, H, gray; N, dark blue; Cl, green spheres.

PDF Data Description and Peak Assignment for UiO-67

For the r -range from 1 Å to 6.5 Å, all the peaks could be assigned to characteristic distances within the $\text{Zr}_6\text{O}_4(\text{OH})_4$ clusters (**Figure A2.3 a**). The first chemically relevant peak (A) at ~ 1.3

Å corresponds to covalent C-C (benzene ring) and C-O (carboxylate group) bond lengths from the bpdc linkers. The second peak at 2.0 Å (B) corresponds to the Zr first coordination sphere, i.e., Zr-O bond lengths. The third peak at 3.5 Å (C) is assigned to the Zr-Zr second coordination sphere distances between two neighboring Zr atoms of a Zr_6 -cluster. The next peaks below 6.0 Å (D, E and F) are attributed to clearly identified Zr-O and Zr-Zr distances within the $\text{Zr}_6\text{O}_4(\text{OH})_4$ cluster. The longer r-range from 6.5 Å to 15.0 Å exhibits many overlapping peaks of lower intensities characteristics of C-C, C-O and Zr-C distances. However, the higher scattering power of Zr atoms compared to that of O or C atoms implies we mainly observe the peaks corresponding to Zr-C distances. The peak broadening induced by the overlapping of the many contributions of close Zr-C distances renders nevertheless precise assignment challenging. Intense peaks (G to K) are visible from 15.0 Å to 22.0 Å and are clearly attributed to Zr-Zr distances between two $\text{Zr}_6\text{O}_4(\text{OH})_4$ clusters separated by one bpdc linker (**Figure A2.2 b**). The other peaks at higher r value were assigned to Zr-Zr distances between further distant Zr clusters, in line with the excellent crystallinity of the UiO-67 framework.

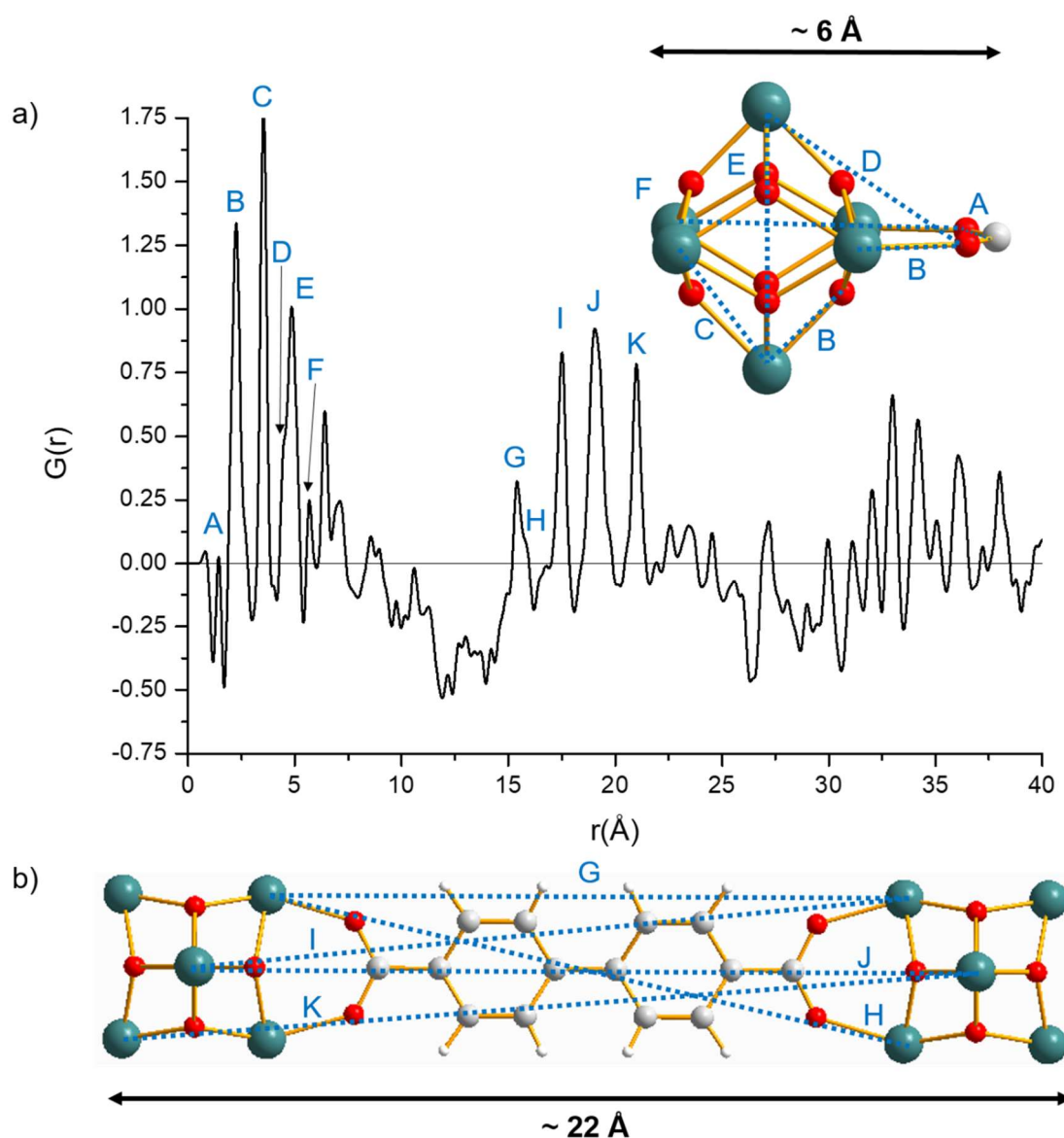


Figure A2.3: PDF analysis of UiO-67. (a) PDF data of UiO-67. A-F labels of peaks below 6.5 \AA correspond to the indicated correlations within the $\text{Zr}_6\text{O}_4(\text{OH})_4$ clusters. (b) Two $\text{Zr}_6\text{O}_4(\text{OH})_4$ units connected by a bpdc linker and relevant Zr-Zr distances corresponding to the longer r features (G-K). Zr, gray spheres; O, red spheres; C, light gray spheres; H, white spheres. Presentation inspired from Bennett *et al.*⁵

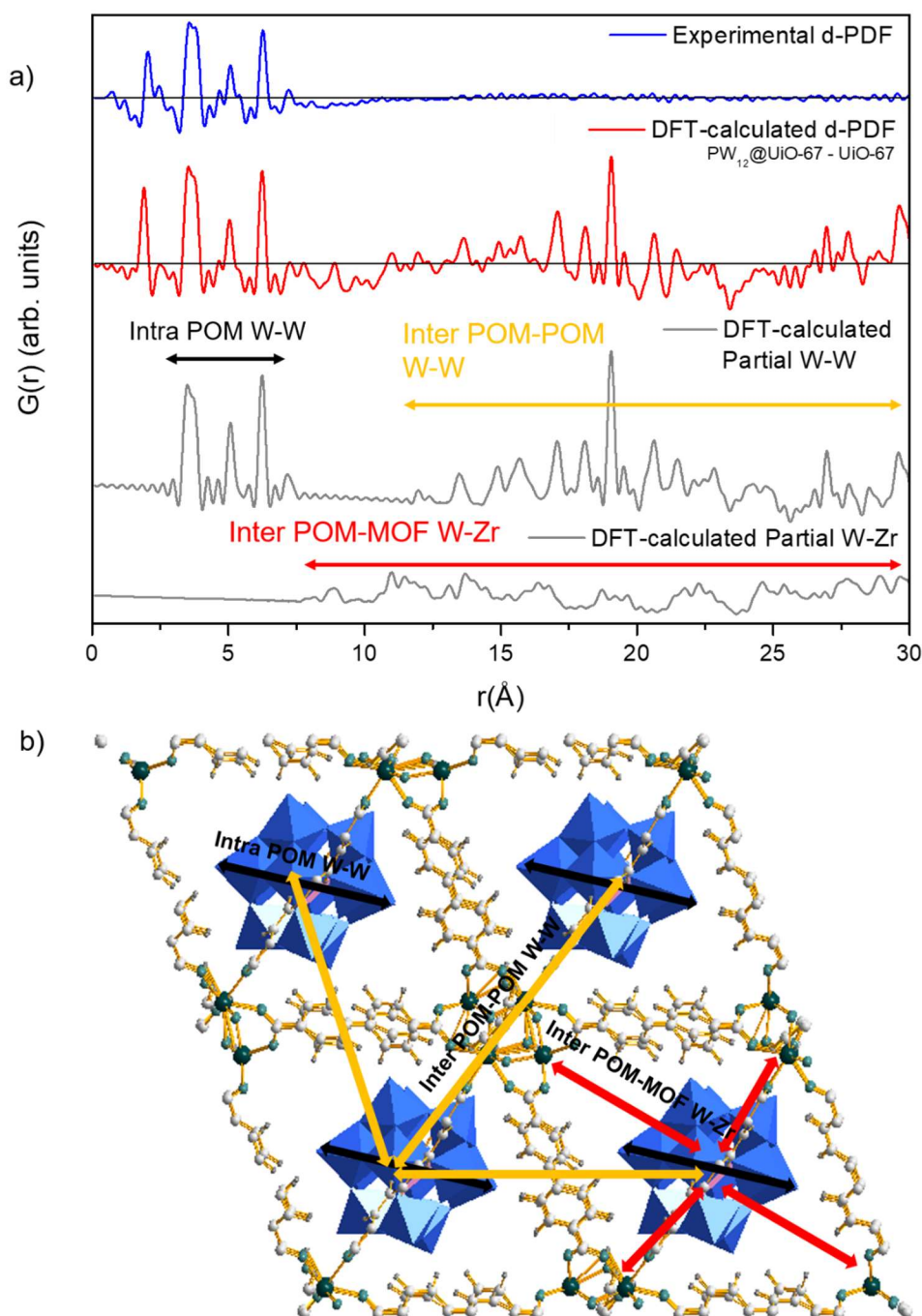


Figure A2.4: Differential PDF for PW_{12} encapsulated in UiO-67. (a) Red: Experimental d-PDF (red) for PW_{12} encapsulated in UiO-67 determined by subtracting the PDF of UiO-67 from the PDF of $\text{PW}_{12}@UiO-67$, Black: theoretical d-PDF determined by subtracting the PDF of UiO-67 (DFT-calculated) from the PDF of $\text{PW}_{12}@UiO-67$ (DFT-calculated). The corresponding partial W-W and W-Zr calculated pair distribution functions are shown below in black. (b) Structural model of $\text{PW}_{12}@UiO-67$ obtained from DFT. The black, orange and red arrows are used as a guideline to highlight respectively the intra-POM W-W distances, the inter POM-POM W-W distances and the inter POM-MOF Zr-distances.

Comments on the Coupling Between PDF and DFT

As expected, for the short-range order (1–8 Å), the experimental d-PDF and the DFT-calculated d-PDF are very similar showing a good agreement (**Figure A2.4 a**). All the peaks of the DFT-calculated d-PDF can thus be attributed to the [PW₁₂O₄₀]³⁻ characteristic distances. However, extra-contributions are observable for higher radial distances on the DFT-calculated d-PDF (**Figure A2.4 a**). As the UiO-67 peaks are erased by the d-PDF, only the [PW₁₂O₄₀]³⁻ contributions, namely POM-POM and POM-MOF interactions, are here represented. Knowing the atomic diffusion factors, we expect that the most intense and distinguishable peaks mainly arise from distances involving heavy atoms such as W and Zr. The distance analysis from the model obtained from DFT (**Figure A2.4 a,b**) confirms that they mainly correspond to inter-POM [PW₁₂O₄₀]³⁻ W-W distances and [PW₁₂O₄₀]³⁻-UiO-67 W-Zr distances. This phenomenon comes from an ordering of the POM inside the MOF network induced by the DFT calculations. The peak absence at middle- and long-range order on the experimental d-PDF can then be explained on one hand by the random immobilization of the POM inside the UiO-67 network and, on the other hand, by the POM rotational disorder from one octahedron to another one.

Structural data		Refined values	Reference (JCPDS 00-50-0304) ⁶
Structural parameters	a (Å)	12.156	12.156
	P _x P _y = Z _p	0.750; 0.750; 0.750	0.750; 0.750; 0.750
	O _p X _{O1} = Y _{O1} = Z _{O1}	0.825	0.820
	O ₂ X _{Ob1} = Y _{Ob1} ; Z _{Ob1}	0.675; 0.490	0.656; 0.507
	O ₃ X _{Ob2} = Y _{Ob2} ; Z _{Ob2}	0.872; 0.027	0.870; 0.026
	O _t X _{O4} ; Y _{O4} = Z _{O4}	0.730; 0.055	0.735; 0.053
	W _x W _y ; Y _W = Z _W	0.758; 0.957	0.758; 0.957
	B _{iso} P (Å ²)	1.13	0.50
	B _{iso} O (Å ²)	1.65	0.47
	B _{iso} W (Å ²)	0.48	1.57
First distances	P-O _t (Å)	1.58	1.47
	W-O _{octahedron} (Å)	1.72 <d _{w-o} <2.41	1.69 <d _{w-o} <2.45
	W-W (Å)	3.42; 3.70	3.40; 3.68
Refinement quality (R _w)		0.282	/

Table A2.1: Structural parameters and characteristic distances of the [PW₁₂O₄₀]³⁻ polyoxometalate obtained from d-PDF refinement from a PW₁₂@UiO-67. For a comparison purpose, the structural parameters of the Keggin [PW₁₂O₄₀]³⁻ reference are reminded.

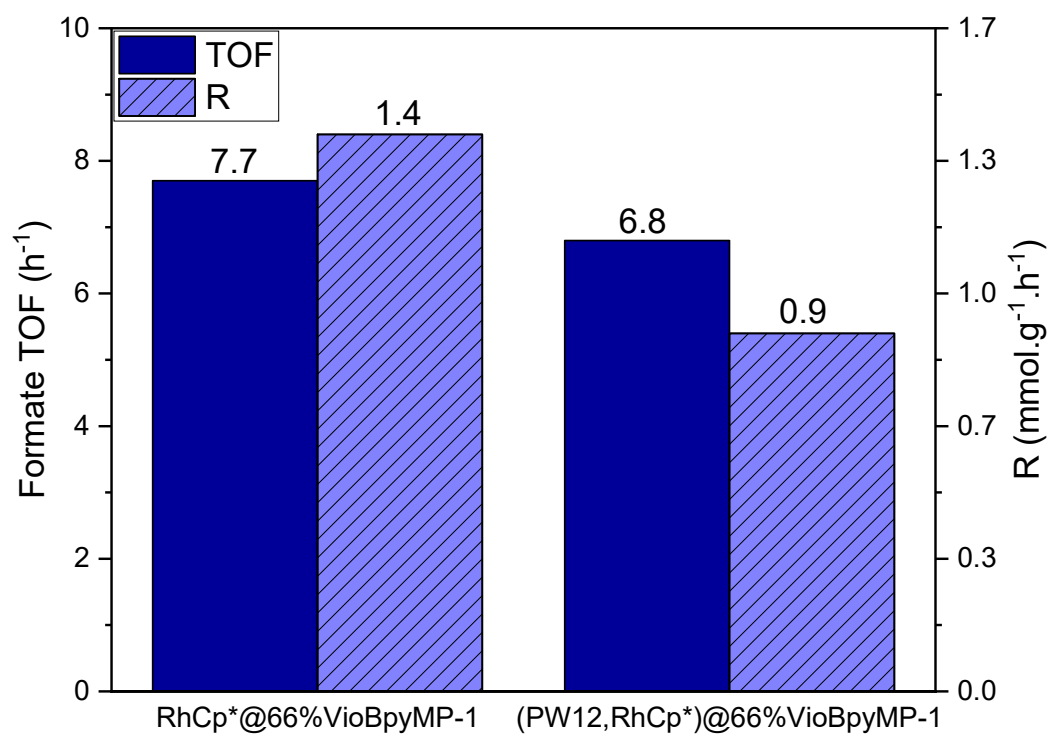


Figure A2.5: Production yield of formate with $\text{RhCp}^*\text{@66\%VioBpyMP-1}$ and $(\text{PW}_{12}, \text{RhCp}^*)\text{@66\%VioBpyMP-1}$

Chapter 3: Photocatalytic reduction of CO₂ by Porphyrinic Metal-Organic Framework

As mentioned in the previous chapter, the (PW₁₂Cp*Rh)@UiO-67 catalytic system had two major limitations: i) the use of noble metal (Rh, Ru), which potentially limits its large scale utilization and ii) the necessity of an external photosensitizer (PS), Ru(bpy)₃Cl₂, that deactivates itself after few hours due to its relative unstability. The use of noble metal-free Zr₆-TCPP (TCPP = tetrakis(4-carboxyphenyl)porphyrin) porphyrinic MOFs could solve these two problems at once as MOFs incorporating Zr₆ oxoclusters (**Figure 3.1** left) have been already reported to be able to reduce CO₂¹⁻³ while Zr₆-TCPP MOFs, (**Figure 3.1** right) can act as PSs as they bear TCPP linkers.⁴

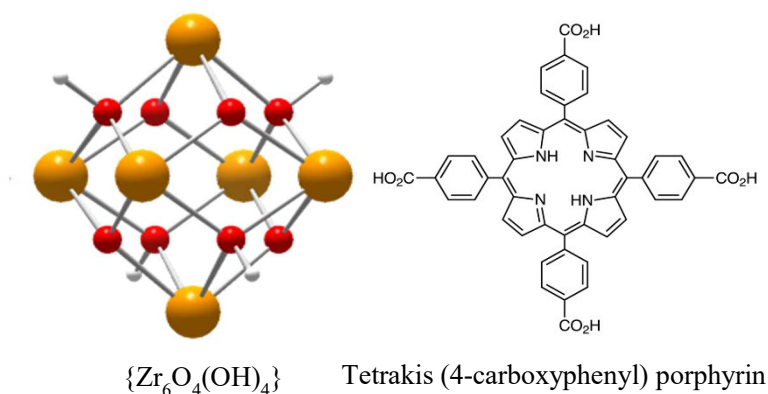


Figure 3.1: Structure of the Zr₆ oxocluster (left) and the TCPP linker (right)

As presented in the first chapter, depending on the Zr₆ oxocluster coordination (6, 8 or 12 TCPP linker per Zr₆ node) a large variety of Zr₆-TCPP MOFs have been synthesized so far (**Figure 3.2**).⁵⁻¹² Moreover, the TCPP linker can obviously be metalated with a wide range of transition metal cations (Mn³⁺, Co²⁺, Cu²⁺, Zn²⁺, Fe³⁺, Pd²⁺, Rh³⁺,...) leading to an even greater chemical variety of Zr₆-TCPP MOFs. Importantly, previous reports have shown that MOF-525, MOF-545, PCN-223 and PCN-224 are able to reduce CO₂ into different products (CO, CH₄ and/or formate) without any additional co-catalyst or PS.¹³

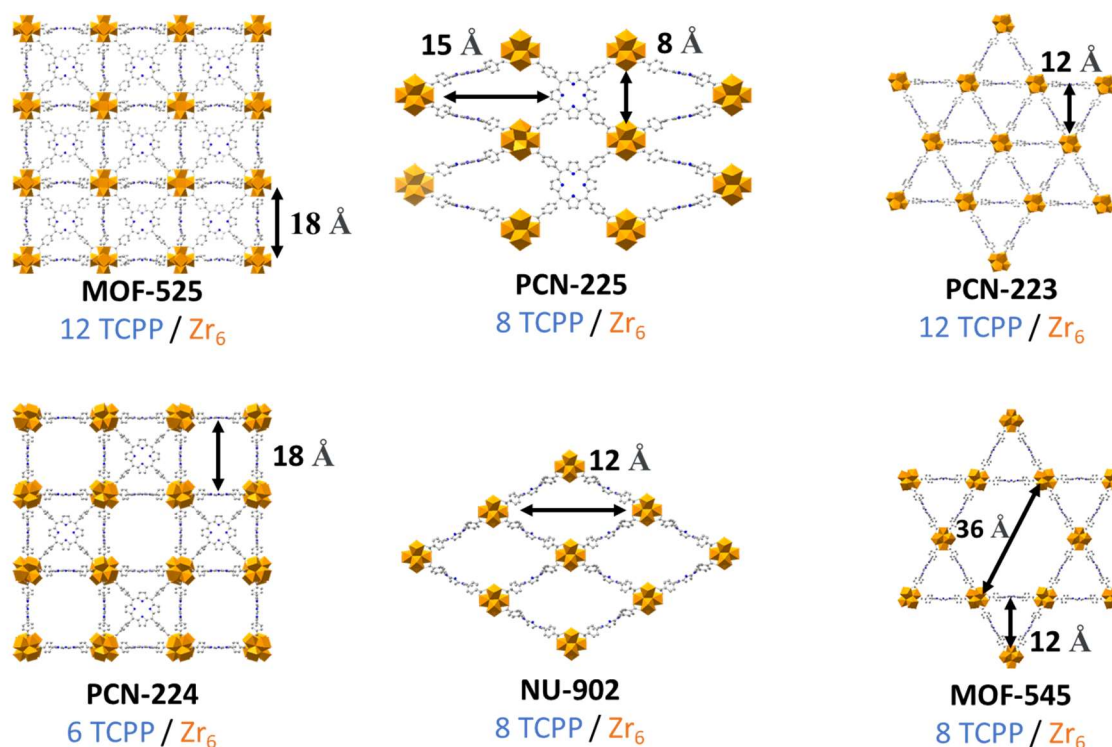


Figure 3.2: Topology of the different Zr₆ porphyrinic MOFs.

Despite these reports,¹³ the mechanism for CO₂ reduction with these composites remains unclear. So far, three different mechanisms have been proposed:

- TCPP acts as a PS, transferring an electron to the Zr₆ oxocluster which plays the role of a catalyst.
- TCPP acts both as a PS and a catalytic center.
- The MOF is a dual catalyst, whereby TCPP acts as PS and both Zr₆ and TCPP act as catalysts.

The different mechanisms will be developed in the next part, as well as our approach to clarify the mechanism we believe is at work in our system.

1. State of the art of Zr₆-TCPP MOFs for CO₂ reduction

The first report on the photocatalytic reduction of CO₂ by Zr₆-TCPP MOFs has been published in 2015. Xu *et al.*¹ have shown that the MOF-545 can photoreduce CO₂ into formate in acetonitrile with TEOA as both electron and proton donor. MOF-545 produces a significantly greater amount of formate than the homogeneous TCPP counterpart, going from 2 to 30 μmol (or 120 μmol.g⁻¹.h⁻¹ considering 10h reaction time and 25 mg of catalyst) of formate

respectively. This is also much higher than the previously reported values for the UiO-66-NH₂ (26.4 $\mu\text{mol}\cdot\text{g}^{-1}\cdot\text{h}^{-1}$) and MIL-125-NH₂ (16.3 $\mu\text{mol}\cdot\text{g}^{-1}\cdot\text{h}^{-1}$) MOFs under similar conditions. The authors propose that the presence of deep trap states on the porphyrin, when immobilized in the MOF, increases the lifetime of the photoinduced electrons in MOF-545 and thus the formate production. Transient absorption spectroscopy combined to steady-state photoluminescence measurements supports this hypothesis, but no additional details about the trap states are given. Nonetheless, they propose a mechanism where the porphyrin acts only as a PS, the catalyst being the Zr₆ oxocluster. Besides, electron paramagnetic resonance (EPR) measurements suggest the formation of Zr(III) centers, implying that an electron would be transferred from TCPP to the Zr₆ cluster (**Figure 3.3**), in a similar fashion to the Ti(IV)→Ti(III) reduction observed in the titanium-based MOF, MIL-125-NH₂, in photocatalytic conditions.¹⁴

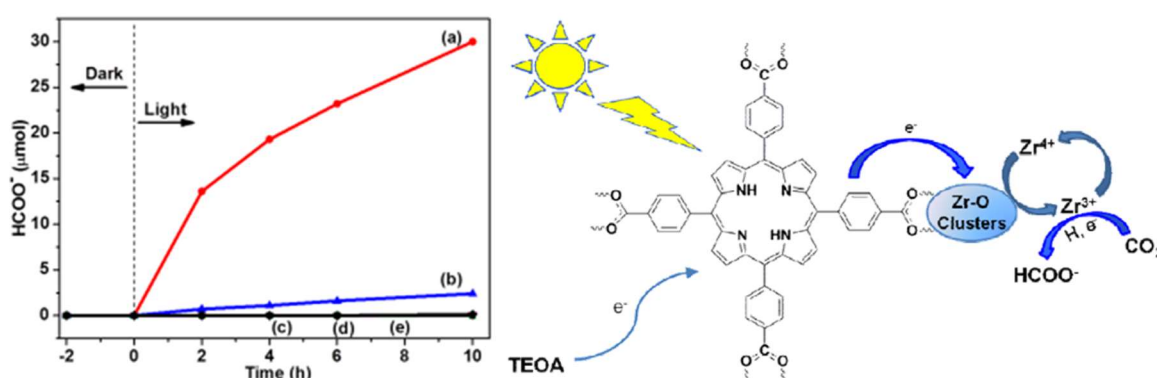


Figure 3.3: CO₂ photoreduction with MOF-545 (red), the homogeneous TCPP (blue) and blank experiments without TEOA, CO₂ or catalyst (black) (left) and proposed mechanism for the reaction (right).¹

Recently, Gao *et al.*¹⁵ reported the dual photooxidation of water and photoreduction of CO₂ to CO and CH₄ using a mixed-metal Ti/Zr-MOF-525 where Zr(IV) centers of the Zr₆-oxoclusters (shown in **Figure 3.1**) were partially exchanged with Ti(IV) ones. They have shown that, in the gas phase and without any sacrificial organic agent such as the widely used TEOA, the substituted Ti/Zr MOF could achieve a production of 1200 ppm of CO and 4000 ppm of CH₄ per gram of MOF after 6h. Indeed, the CO₂ reduction reaction is coupled with water oxidation releasing O₂, H⁺ and electrons, thus making water the reducing agent. Noticeably, the initial undoped zirconium-based MOF-525 was only able to achieve an approximately 200 ppm production of both CO and CH₄ per gram of MOF. The authors propose a similar mechanism as Xu *et al.*¹ where the porphyrin acts as both a photosensitizer and a catalyst able to oxidize

water providing the necessary electrons for the CO₂ reduction on the inorganic nodes (**Figure 3.4**).

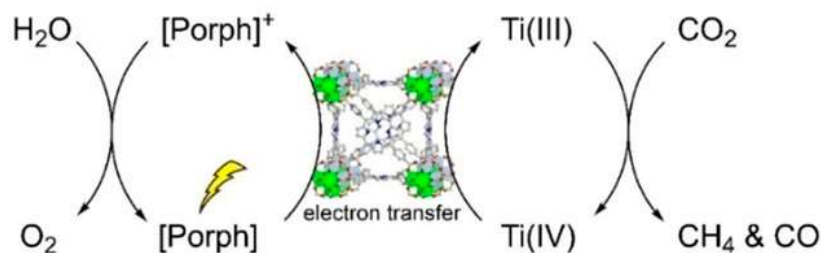


Figure 3.4: Proposed mechanism for coupled water oxidation and CO₂ reduction with Zr/TiMOF-525.¹⁵

These two publications sum up the work that has been published claiming that the inorganic node is the actual catalyst for CO₂ photoreduction with Zr₆-TCPP MOFs. But knowing the catalytic properties of metalated porphyrins in homogeneous conditions for CO₂ reduction (mainly giving CO as a product), both via electro and photochemical ways, it cannot be excluded that in our systems, when metalated, the porphyrin center acts as the catalyst.

This has been proposed in 2016 by Zhang *et al.*³ They report the CO₂ photoreduction of metalated MOF-525, namely MOF-525(Co) and MOF-525(Zn), compared to its free-base homologue. They have shown that under visible light, in acetonitrile with TEOA as an electron/proton donor, MOF-525(M) is able to reduce CO₂ to a mixture of CO and CH₄. The nature of the metal in the porphyrin plays a key role in the catalyst efficiency, with the range of performances as follows: MOF-525(Co) > MOF-525(Zn) > MOF-525 >> TCPP in homogeneous conditions (**Figure 3.5**). As in the previous reports,^{1,15} their EPR experiments show the presence of a signal at $g = 2.0048$ which has been attributed to the formation of Zr(III) and at $g = 1.9984$ which has been attributed to the formation of Co(I), coinciding to an electron transfer from the excited porphyrin to the Zr nodes in absence of CO₂. Nonetheless, under irradiation and in presence of CO₂ the signal corresponding to Zr(III) disappears, suggesting that the electron transfer from Co(II) to Zr(IV) is quenched in presence of the substrate. The authors thus suggest, with the support of DFT calculations, a mechanism where the porphyrin acts as both photosensitizer and catalyst in the MOF-525 system.

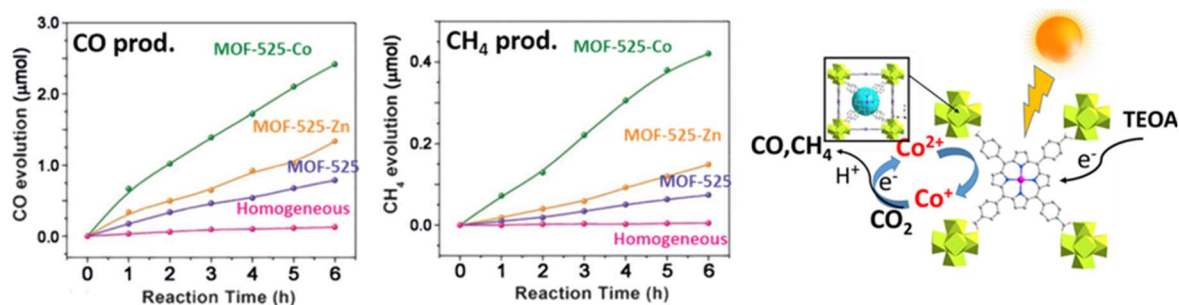


Figure 3.5: CO₂ photoreduction with metalated or free-base MOF-525 composites (left) and proposed mechanism for the reaction (right).³

Liu *et al.*¹⁶ claimed in 2018 a different dual catalytic MOF, PCN-224(Rh), with two active sites able to reduce CO₂ to formate: the Zr₆ node, and the Rh^{II} metal on the porphyrin. The reaction takes place under visible-light irradiation, in acetonitrile with TEOA as electron and proton donor (**Figure 3.6**). They confirm by Mott-Shottky measurements the ability of the metalated Zr-porphyrinic MOF to catalytically reduce CO₂. It was proposed that PCN-224(Rh) acts as an n-type semiconductor, the authors estimating the LUMO at -0.57V vs. NHE, which is more negative than the CO₂ reduction potentials. With the same measurement, they have shown that TCPP(Rh) and PCN-224 are able to achieve the same reaction. In terms of efficiency, PCN-222(Rh) is able to achieve a TON of 6 after 18h while TCPP(Rh) and PCN-224 display the same efficiency, with approximately a TON of 2 after 16h.

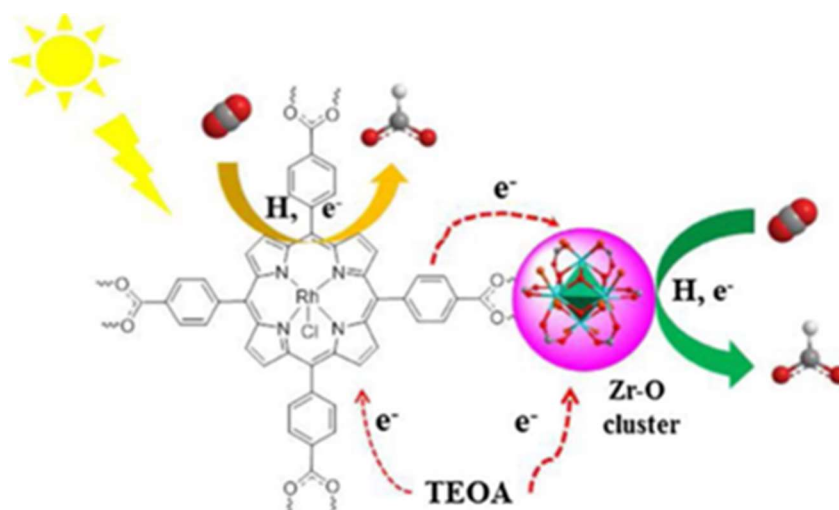


Figure 3.6: Proposed mechanism for the CO₂ photoreduction with PCN-224(Rh).¹⁶

Lastly, Jin¹⁷ reported in 2020 the CO₂ reduction with MOF-545(Zn) where the amount of metalated porphyrin is equal to 5%, 15% and 25%. The resulting MOFs are able to reduce CO₂

to formate, under visible light in 20 mM ethylene glycol aqueous solution. Interestingly, all metalated MOFs are greater catalysts than their unmetalated homologue, but the lower the metalation the better the performances. Indeed, MOF-545(5%Zn) > MOF-545(15%Zn) > MOF-545(25%Zn) > MOF-545. The author reports a production of 354 $\mu\text{mol}\cdot\text{g}^{-1}\cdot\text{h}^{-1}$ for MOF-545(5%Zn) and 28.6 $\mu\text{mol}\cdot\text{g}^{-1}\cdot\text{h}^{-1}$ for MOF-545.

The same author reported few months later, CO₂ reduction with PCN-223(Zn) and PCN-224(Zn). He used the same strategy consisting in the partial metalation of the MOF with Zn²⁺ ions.² The same trends as in the previous work can be observed, MOF-545(Zn) produces 120 $\mu\text{mol}\cdot\text{g}^{-1}\cdot\text{h}^{-1}$. As for the mechanism, they propose a dual catalytic route for all three MOFs where both the Zr₆ node and the metalated porphyrin are able to reduce CO₂ to formate.

Importantly, the effect of a co-catalyst immobilization in porphyrin MOFs has been studied by a few teams.^{18–20} For example, Choi *et al.*²⁰ grafted covalently the Re(bpy)(CO)₃Cl complex, known to yield CO in homogeneous conditions. It was observed that the grafting of the catalyst changed the selectivity toward CO₂ reduction. While the catalyst free MOF-545 was reported to produce only formate, once the Re(I) catalyst immobilized the cat@MOF is indeed selective for CO production, reaching TONs of 1900 and a production rate of 1070 $\mu\text{mol}\cdot\text{g}^{-1}\cdot\text{h}^{-1}$. In our attempts to rationalize the CO₂ photoreduction behavior of porphyrin MOFs, we will not consider the particular case of cat@MOF systems as the presence of the cat can influence the MOF selectivity.

We can summarize the different work with Zr₆-porphyrin MOFs for CO₂ reduction, their obtained products and claimed catalytic centers in the following table (**Table 3.1**). Noticeably, Zr₆-porphyrin MOFs can reduce CO₂ to both liquid (formate) and gas products (CO/CH₄). Moreover, the literature is still unclear on which part of the MOF plays the role of a catalyst.

Table 3.1: Zr₆-TCPP MOF selectivity toward CO₂ photoreduction

MOF	Product	Solvent (Sacrificial agent)	Claimed catalytic center
MOF-545 ¹	HCOOH	Acetonitrile (TEOA)	Zr ₆ node
MOF-525 ¹⁵	CO / CH ₄ / O ₂	Gas phase (Water)	Zr/Ti node
MOF-525(M) (M= Zn, Co) ³	CO / CH ₄	Acetonitrile (TEAO)	Porphyrin
PCN-224(Rh) ¹⁶	HCOOH	Acetonitrile (TEOA)	Zr ₆ node + porphyrin
MOF-545(Zn) ¹⁷	HCOOH	H ₂ O (Ethyleneglycol)	Zr ₆ node + porphyrin
MOF-545(Zn), PCN-223(Zn), PCN-224 (Zn) ²	HCOOH	H ₂ O (Ethyleneglycol)	Zr ₆ node + porphyrin

Taking advantage of the modularity of these systems, our objective was to synthesize a series of metalated MOF-545(TM) (TM = Mn, Fe, Co, Cu, Zn) and investigate their visible-light photocatalytic activity towards CO₂RR in acetonitrile using triethanolamine (TEOA) as sacrificial donor in order to go deeper in the understanding of the CO₂RR mechanism in these systems. Overall, we can consider two distinct cases: i) the metalated porphyrin acts as a co-catalyst, and a mixture of CO/CH₄ and HCOOH is expected or ii) the porphyrin acts only as a photosensitizer, and HCOOH is thus the only product. Still, the MOF-545(TM) efficiency as PS may vary according to the metal center at the porphyrin linker. We have also considered a nanosized MOF-545-based system with the aim of boosting the catalytic activity as the result of i) a higher density of catalytic sites available due to a significant increase in specific surface area and ii) a faster and more facile substrate-catalyst interaction due to lower diffusion barriers and shorter diffusion distances.²¹ Moreover, thanks to Albert Solé-Daura, we present a comprehensive mechanistic study by means of DFT calculations which reveals a new and unexpected role for TEOA in such catalytic systems as CO₂ reducing agent once photo-oxidized by the MOF linkers. Very recently, Fujita and co-workers described several supportive roles played by TEOA in the photo-reduction of CO₂ by Ru-based molecular catalysts.²² However, this is to our knowledge the first time that TEOA is proposed to play the role of CO₂ reducing agent within a mechanistic scenario that redefines it as an *up to three-electron* donor.

In a second part, we will describe our preliminary results concerning the immobilization of potential co-catalysts and of POMs for CO₂ reduction. Indeed, metalation and size effect being optimized, adding a co-catalyst able to assist the MOF during the CO₂ reduction would be a

way to increase to a higher step the MOF efficiency for CO₂RR. Furthermore, as described in Chapter 2, POMs can act as an electron/proton relays and boost the catalytic activity. Three catalysts were selected for this purpose, as well as a series of POMs. The selected catalysts for encapsulation will be described in the beginning of the second subpart of this chapter.

2. Synthesis and characterizations of metalated and nanosized MOF-545

MOF-545 was synthesized following a reported synthetic procedure using 1,2-dichloroacetic acid as modulator.²³ Metalated MOF-545(TM) (TM = Mn, Fe, Co, Cu, Zn) were obtained via an analogous protocol but using the required (TM)TCPP ligand instead of the non-metalated porphyrin derivative as starting reactants. Powder X-ray diffraction (PXRD) patterns and infrared (IR) spectra (**Figure 3.7**) support the formation of the targeted materials. It can be noticed that the additional peak at $\sim 1000\text{ cm}^{-1}$ present in most of the IR spectra of MOF-545(TM) corresponds to N-TM vibrations.

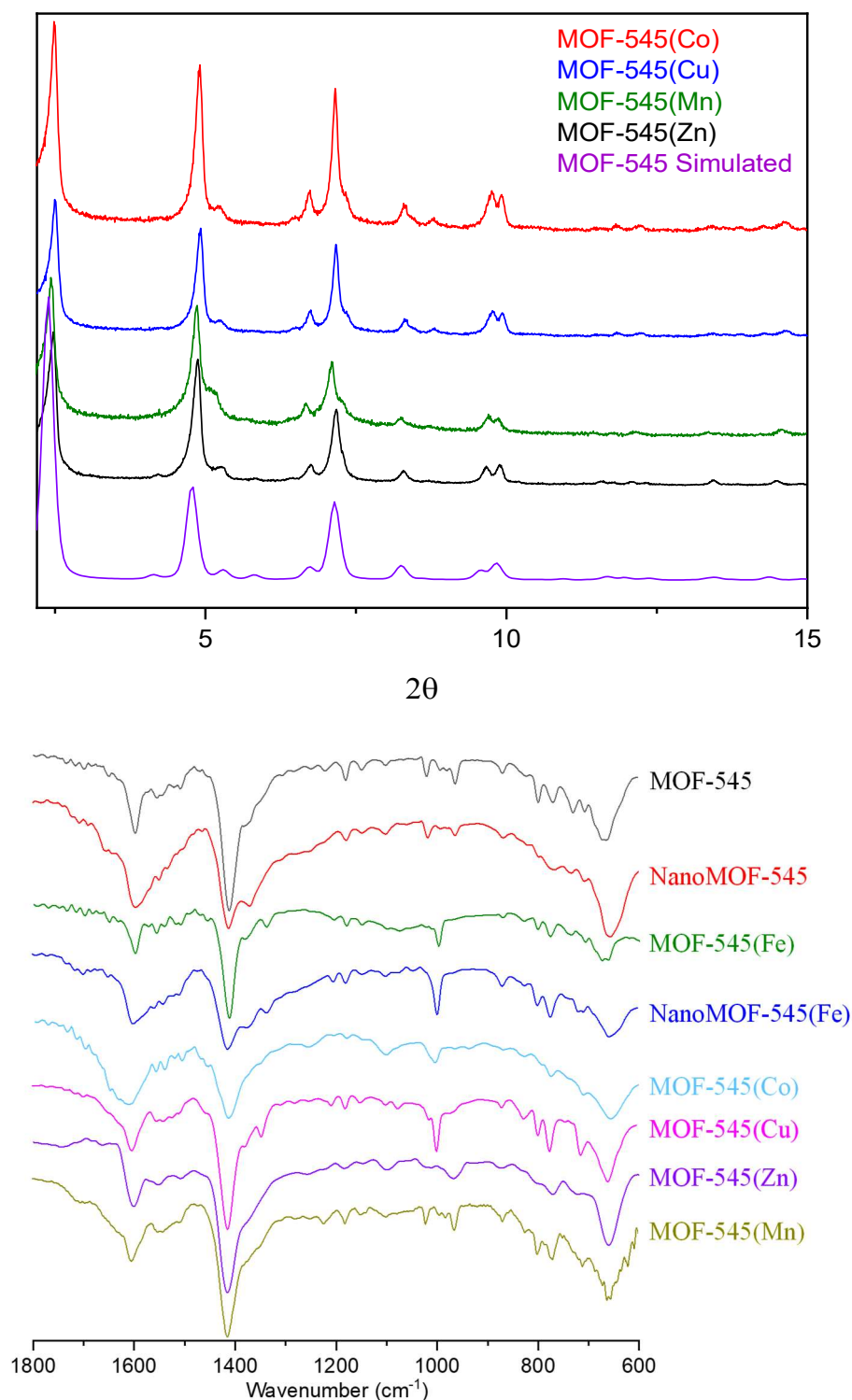


Figure 3.7: Left: Comparison of the experimental X-ray powder patterns of MOF-545(Co) (red), MOF-545(Cu) (blue), MOF-545(Mn) (green), MOF-545(Zn) (black) and of the powder pattern calculated from the structure solved from single-crystal X-ray diffraction data⁵ for MOF-545 (purple). Right: FT-IR spectra of MOF-545 (black), NanoMOF-545 (red), MOF-545(Fe) (green), NanoMOF-545(Fe) (blue), MOF-545(Co) (cyan), MOF-545(Cu) (pink), MOF-545(Zn) (purple) and MOF-545(Mn) (khaki).

Solid-state UV-Vis spectra evidence the porphyrin ligands Soret band at ca. 420 nm and the Q bands in the 500–800 nm range (**Figure 3.8**).

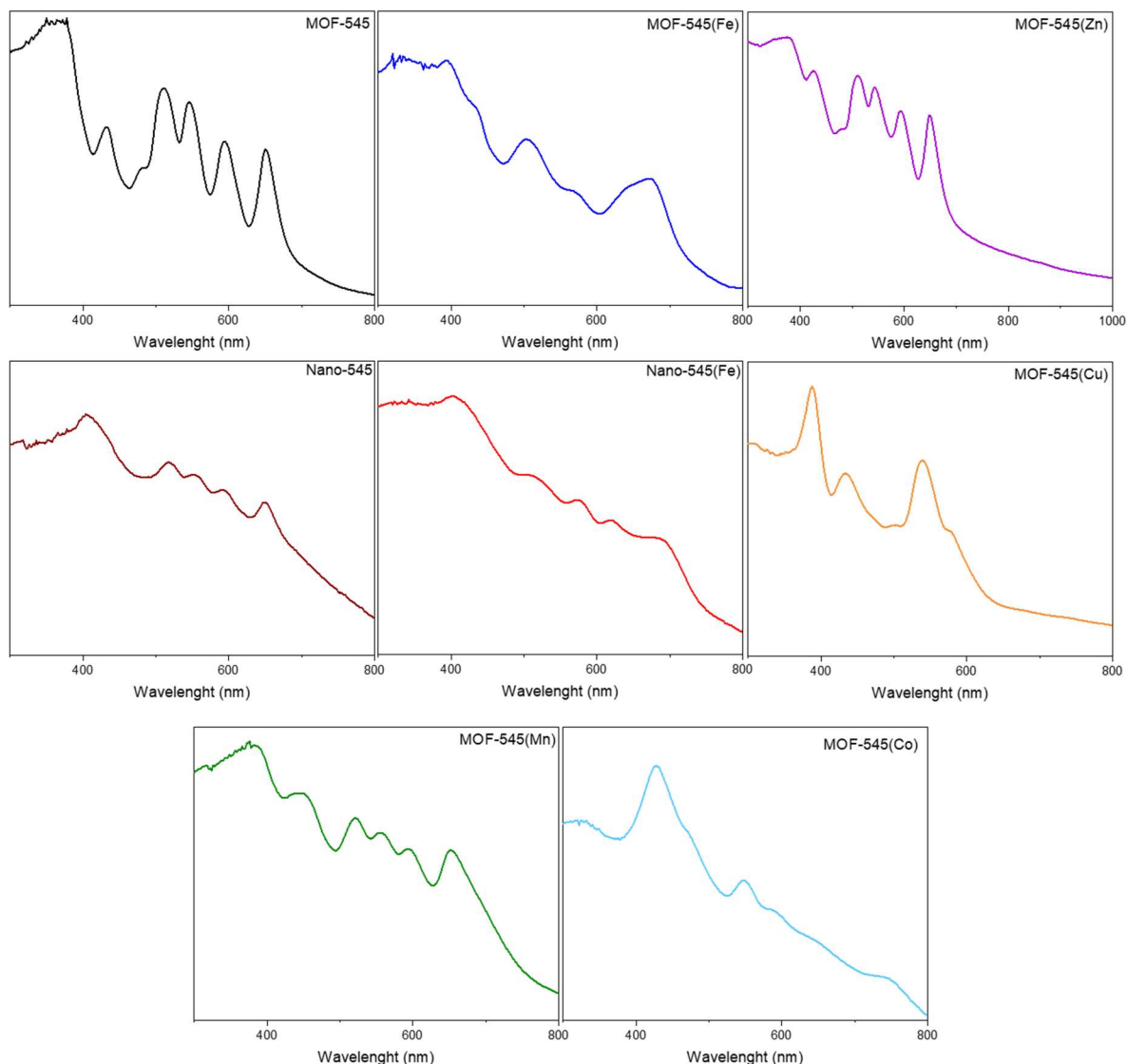


Figure 3.8: Electronic absorption spectra of MOF-545 (black), MOF-545(Fe) (blue), MOF-545(Zn) (purple), NanoMOF-545 (brown), NanoMOF-545(Fe) (red), MOF-545(Cu) (orange), MOF-545(Mn) (green) and MOF-545(Co) (cyan).

Regarding the synthesis of nanosized crystals of MOF-545, following a high-throughput screening study,²⁴ it has been reported in DMF at 130°C and later applied for the preparation of nanocomposite reverse osmosis membranes.²⁵ Also, the use of various amounts of acetic acid as a modulator allowing the control of the crystals size in DMF at 65°C was reported.²⁶ Still, the reported yields are quite low in both syntheses. Furthermore, there has been no report, to our knowledge, on the synthesis of nanosized MOF-545(Fe). Thus, we developed a synthetic protocol to obtain NanoMOF-545 and NanoMOF-545(Fe) under microwave conditions (130°C,

800 W, 20 min) allowing getting ~30 mg of NanoMOF for each MOF analog (see Experimental section). The PXRD patterns are in full agreement with those of MOF-545, with an expected widening of the Bragg peaks (**Figure 3.9 a**). The IR spectrum of NanoMOF-545(Fe) exhibits the characteristic Fe-N vibration at 997 cm⁻¹, close to that of MOF-545(Fe) (1001 cm⁻¹) (**Figure 3.9 b**).²⁷ SEM images indicate sizes of ca. 3000, 200 and 150 nm for MOF-545(Fe), NanoMOF-545 and NanoMOF-545(Fe), respectively (**Figure 3.9 c**).

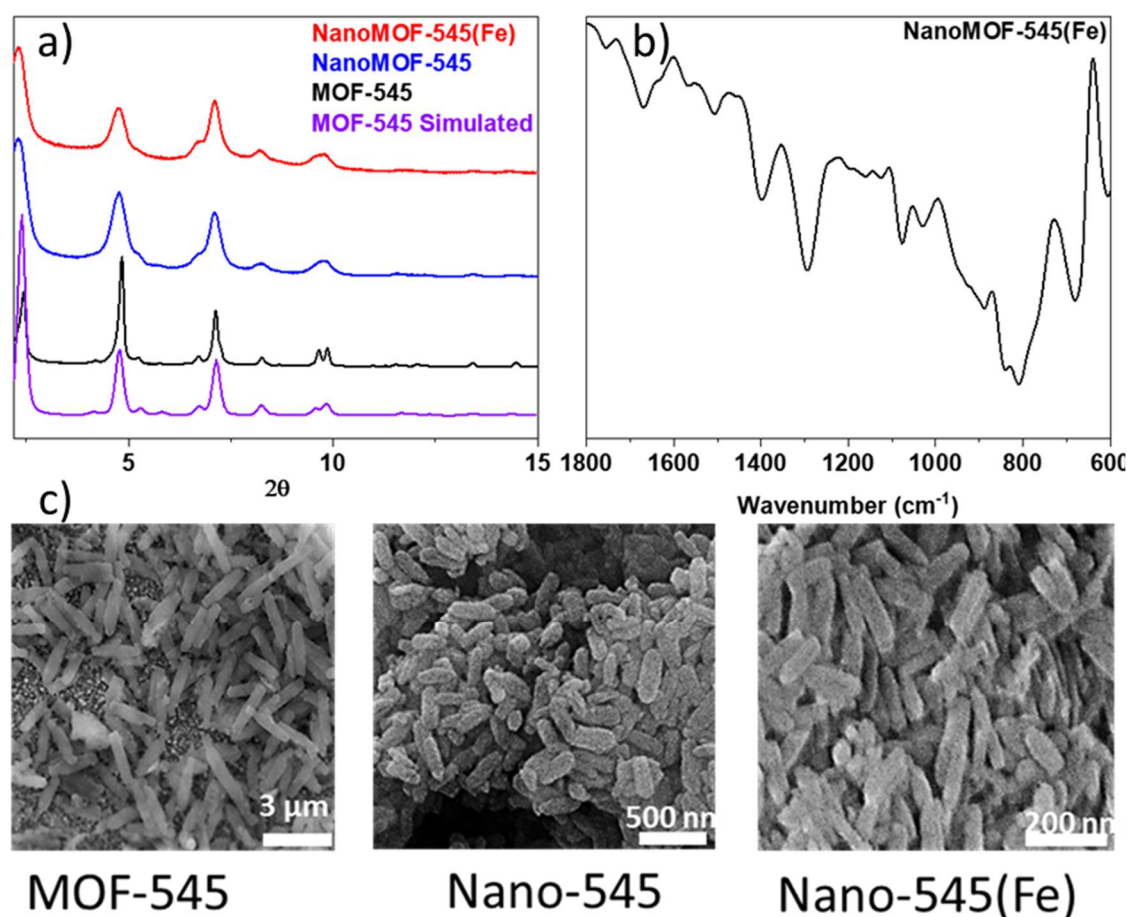


Figure 3.9: a) Comparison of the experimental X-ray powder patterns of NanoMOF-545(Fe) (red), NanoMOF-545 (blue), MOF-545 (black) and of the simulated powder pattern of MOF-545 (purple). b) IR spectrum of NanoMOF-545(Fe). c) SEM images of MOF-545, NanoMOF-545 and NanoMOF-545(Fe).

Persistence of the porphyrin's metallation during MOF synthesis was attested by EDX measurements. Thermogravimetric analysis curves of NanoMOF-545 and NanoMOF-545(Fe) are depicted in **Figure 3.10**, showing weight losses at 500°C of 67.9% and 65.8%, respectively. These weight losses are assigned to the linker's decomposition along with the formation of inorganic oxides, the experimental values agreeing with those predicted from the molecular formulae (69.0 and 64.5%, respectively).

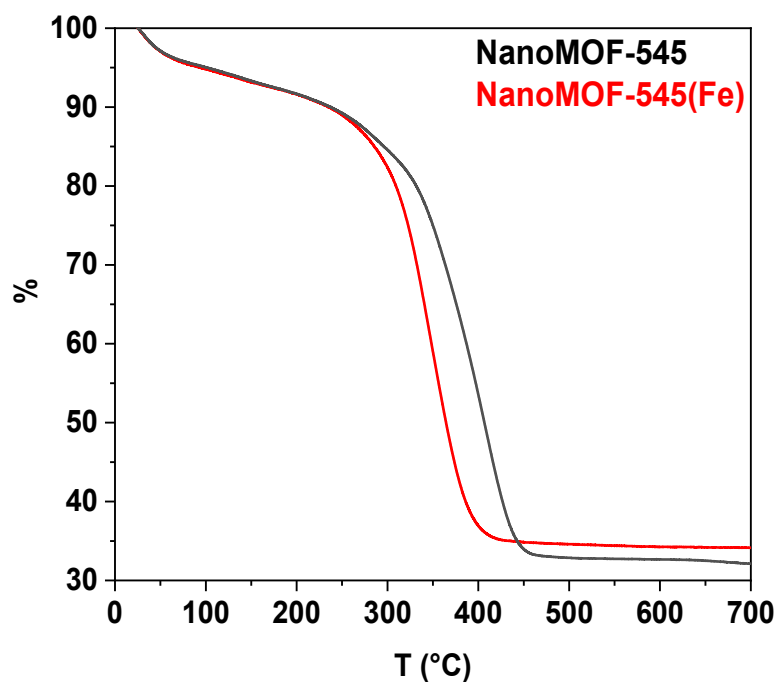


Figure 3.10: TGA curves of NanoMOF-545 (black) and NanoMOF-545(Fe) (red).

The N₂ adsorption/desorption isotherms of MOF-545(Fe), NanoMOF-545 and NanoMOF-545(Fe) have been measured (**Figure 3.11**). A Brunauer–Emmett–Teller (BET) surface area of 1434 m²·g⁻¹ was determined for NanoMOF-545(Fe), comparable to those determined for MOF-545(Fe) (1396 m²·g⁻¹) and NanoMOF-545 (1698 m²·g⁻¹). Finally, the pore diameters in all these materials are similar, with ca. 1.7 and 3.7 nm.

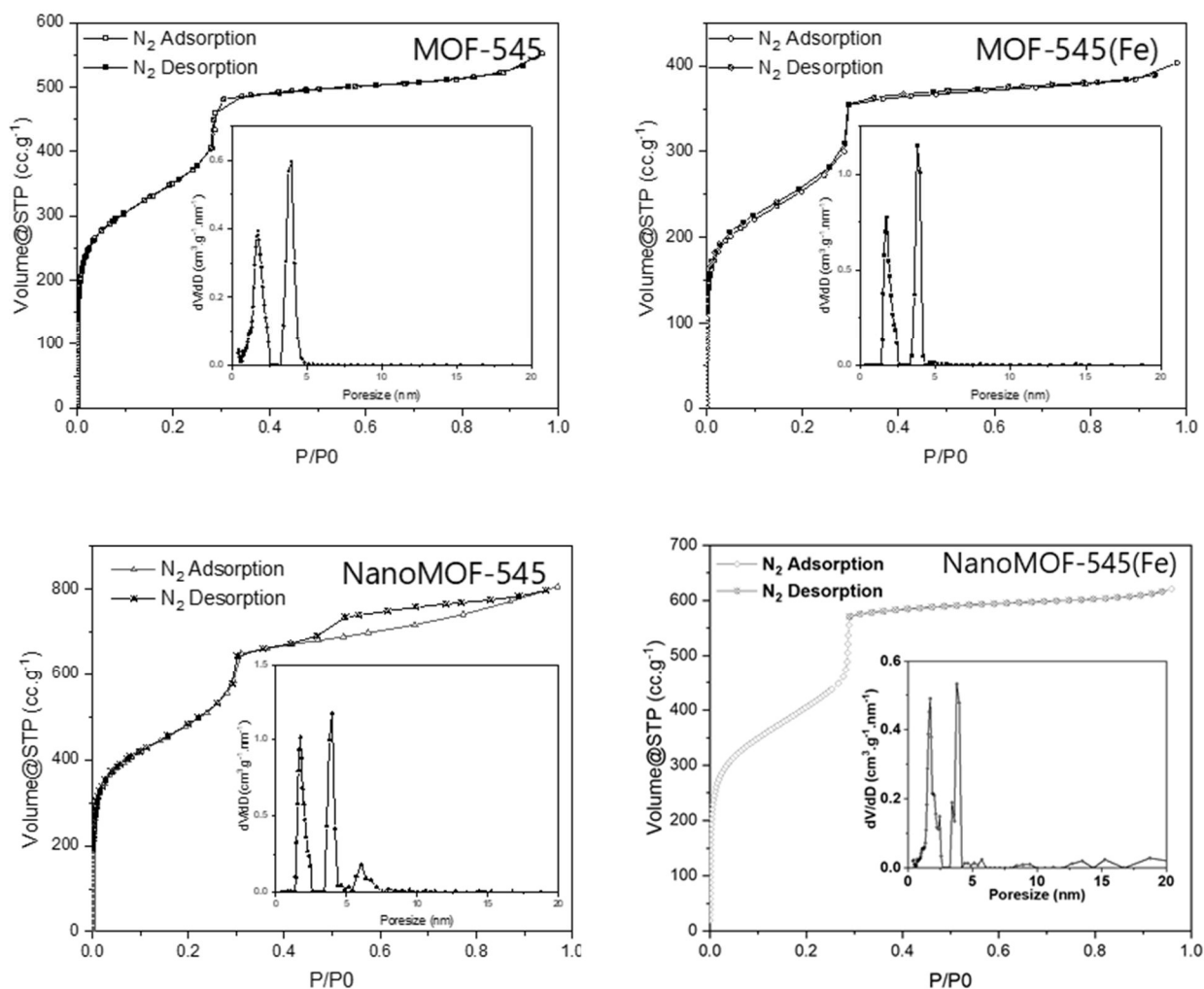


Figure 3.11: BET N₂ adsorption/desorption isotherms (77 K, P/P₀ = 1 atm.) of MOF-545, MOF-545(Fe), NanoMOF-545 and NanoMOF-545(Fe). Insert: pore size distributions.

3. Photocatalytic reduction of CO₂

The photocatalytic activities of the MOF-545(TM) (TM = Mn, Fe, Co, Cu, Zn) series of solids for CO₂RR were investigated in acetonitrile with TEOA as sacrificial electron/proton donor under visible light illumination. In all cases, it has been observed that no dihydrogen was produced. Blank experiments in the absence of light, of CO₂ or of catalyst have been conducted, with close to no formate production (**Table 3.2**).

Table 3.2: CO₂ photoreduction with 2 mg of catalyst in 2 mL of ACN:TEOA (10:1 v/v), 4h irradiation, 280W Xe lamp, $\lambda > 415$ nm, 20°C.

Catalyst	Comment	Formate yield (μmol)	Rate $\mu\text{mol}\cdot\text{g}^{-1}\cdot\text{h}^{-1}$
-	No catalyst	0.26	-
MOF-545	No light	0.34	42
MOF-545	No CO ₂ (N ₂)	0.34	42
MOF-545		1.28	159
MOF-545(Cu)		1.34	167
MOF-545(Co)		1.80	225
MOF-545(Mn)		3.06	382
MOF-545(Zn)		3.50	417
MOF-545(Fe50%)		3.67	437
MOF-545(Fe)		4.52	566
NanoMOF-545		3.20	400
NanoMOF-545(Fe)		9.28	1160

Moreover, in all cases, the selective formation of formate was systematically observed, with no CO nor methane production. Interestingly, we observe that the production of HCOO⁻ increases with TM = Cu < Co < Mn < Zn < Fe50% < Fe, reaching a maximum of 566 $\mu\text{mol}\cdot\text{g}^{-1}\cdot\text{h}^{-1}$ with the MOF-545(Fe) photocatalyst (**Figure 3.12**). The MOF-545(Fe50%) activity is slightly higher than the expected value of ~ 380 $\mu\text{mol}\cdot\text{g}^{-1}\cdot\text{h}^{-1}$. However the determination of the iron content was estimated by EDX which is not a very precise technique, meaning that the metalation might be slightly underestimated.

The metallation of the porphyrin with Fe was thus selected as the best candidate for investigating further the effect of nanosized particles on the photocatalytic performances of metalated MOF for CO₂RR.

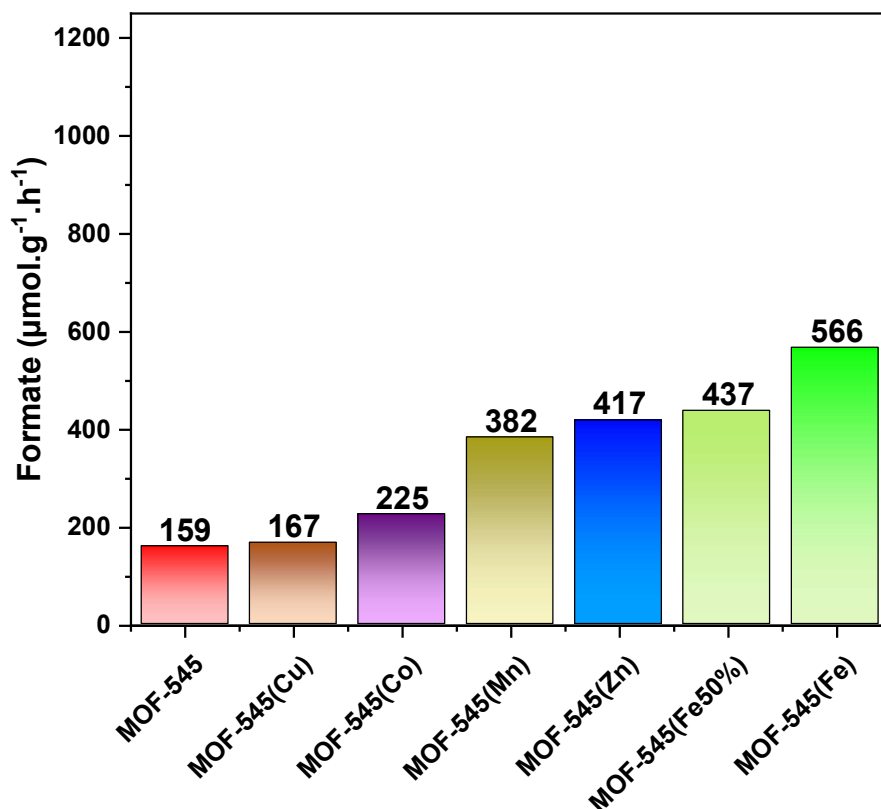


Figure 3.12: Formate production for a) MOF-545 (light red), MOF-545(Cu) (brown), MOF-545(Co) (violet), MOF-545(Mn) (khaki), MOF-545(Zn) (blue), MOF-545(Fe50%) (light green) and MOF-545(Fe) (green). Reaction conditions: catalyst 2 mg, CH₃CN/TEOA (10:1) 2 mL ($\lambda > 415$ nm, 280 W).

NanoMOF-545(Fe) exhibits indeed a remarkable formate production of 1160 $\mu\text{mol}\cdot\text{g}^{-1}\cdot\text{h}^{-1}$, well above that of MOF-545(Fe) (**Figure 3.13**). This value also exceeds by far those previously reported for most MOF-based photocatalytic systems (**Table A3.1**). Analogously, the non-metalated NanoMOF-545 possesses a higher activity than that of MOF-545 (400 vs 159 $\mu\text{mol}\cdot\text{g}^{-1}\cdot\text{h}^{-1}$, respectively) (**Figure 3.13**). These results highlight how the photocatalytic activity of MOF-545(TM) for CO₂RR can be optimized by playing both on the nature of the porphyrin metal center and the size of the catalyst particles.

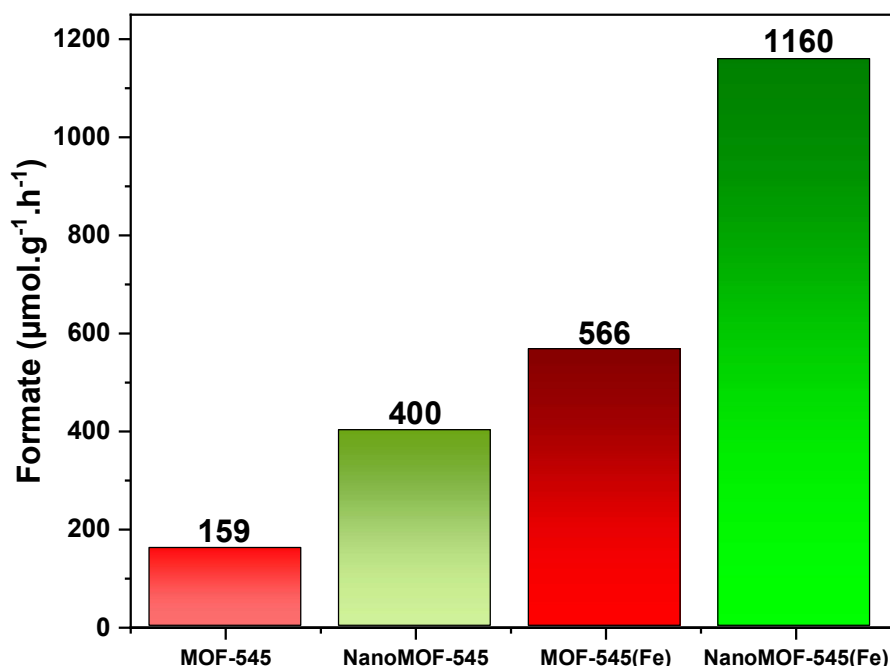


Figure 3.13: Formate production for MOF-545 (light red), MOF-545(Fe) (dark red), NanoMOF-545 (dark green) and NanoMOF-545(Fe) (dark green). Reaction conditions: catalyst 2 mg, CH₃CN/TEOA (10:1) 2 mL ($\lambda > 415$ nm, 280 W).

Kinetics of visible-light-driven formate production was investigated for NanoMOF-545(Fe) (**Figure 3.14**). Importantly, it appeared that a significant amount of the formate produced during the catalytic process remained adsorbed into the MOF. Indeed, on the first attempts of making the kinetic study, we noticed that the amount of formate produced was not only non-linear, but also sometimes decreasing (**Figure A3.1**). Considering the porous nature of metal-organic framework, and their affinity toward HCOOH, we concluded that part of the formate produced was stuck in the pores of the MOF. The yields presented in **Figure 3.14** (left) were thus obtained by considering the amount of formate measured both in the supernatant and retrieved upon washing the MOF with water at 60°C at the end of each photocatalytic test. It is observed that the formation of HCOO⁻ is slowed down after ca. 2 h. This phenomenon may be assigned to the poisoning of active sites in the pores by the formed carboxylate, in agreement with its experimentally observed strong affinity for the MOF, as mentioned above and discussed in the following sections. Finally, recyclability experiments evidence that the catalyst remains stable after 3 runs (**Figure 3.14** right). The small loss of activity observed is probably due to powder loss after the several washing steps and not to catalyst degradation.

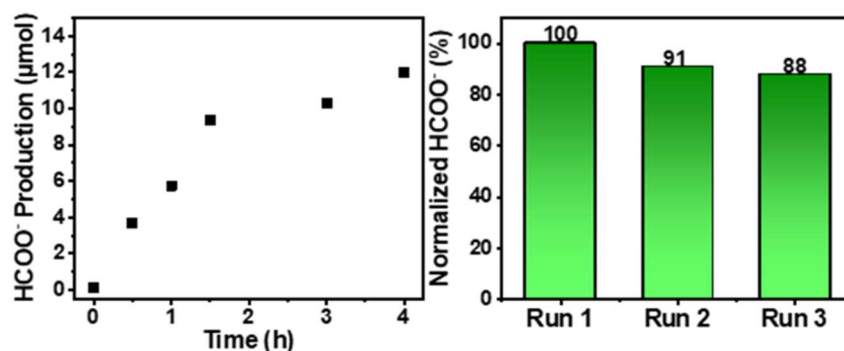


Figure 3.14: HCOO⁻ production over time with 2 mg of NanoMOF-545(Fe) (left) and recyclability test of the NanoMOF-545(Fe) (right).

Finally, the post-catalytic PXRD pattern of NanoMOF-545(Fe) shows only a slight crystallinity loss (**Figure 3.15**).

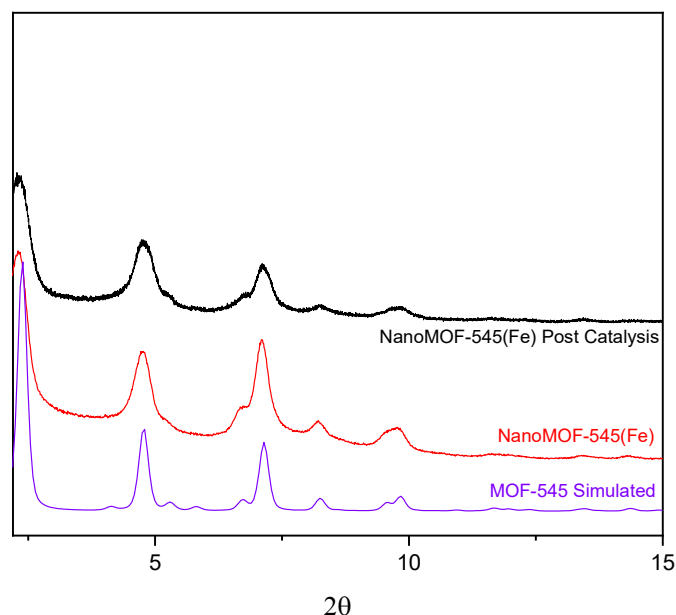


Figure 3.15: Experimental PXRD patterns of NanoMOF-545(Fe) before catalysis (red) and after 4h catalytical run (black) and simulated PXRD pattern of MOF-545 (purple).

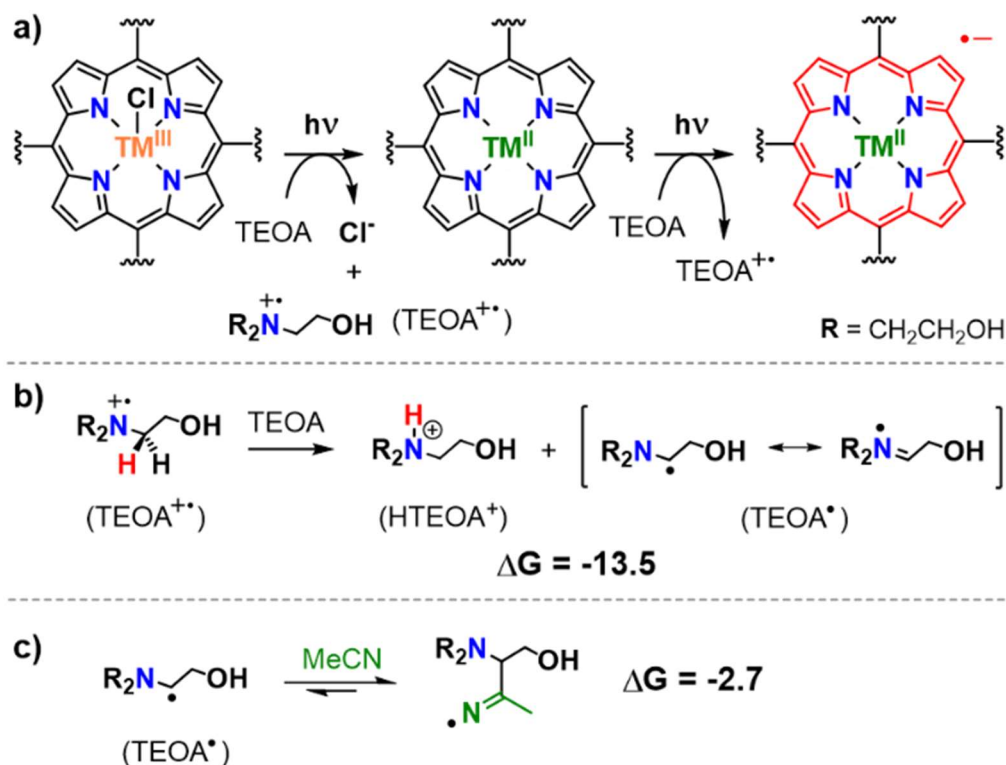
4. Reaction mechanism for CO₂ reduction to formate in MOF-545

4.1. DFT Calculation

After the gained knowledge from the above experimental study, Albert Solé-Daura next conducted DFT calculations to investigate the reaction mechanism governing the reduction of CO₂ to formate at an atomistic level. Previous computational studies have shown that the

reduction of CO₂ to formate typically involves the initial protonation of an electron-rich catalyst to form a metal hydride that can hydrogenate an incoming CO₂ molecule.^{28–30} However, this mechanism cannot apply in unmetalated MOF-545 or MOF-545(TM) (supposing that the same mechanism would be at play in unmetalated and metalated MOFs), since, as discussed above, d(Zr) orbitals are too high in energy to accommodate electrons for the subsequent reduction of a proton, in line with the absence of H₂ as a byproduct. It is also unlikely that a porphyrinic metal hydride participates in the reaction mechanism, as CO₂ is also reduced to formate when using the free-base MOF-545 as the catalyst¹ or even with other MOFs such as NNU-28,³¹ PCN-136,³² and the aminated UiO-66,³³ which are built on the same Zr-oxo cluster but lack metal centers in their linkers. Altogether, the joint analysis of the preceding works strongly suggests that the Zr-oxo clusters are involved in the reaction mechanism, although their role is not that of reducing CO₂. Instead, we propose a new mechanism for CO₂ reduction that benefits from the Lewis acidity of Zr^{IV} sites and the unprecedented role of the photo-generated TEOA• radical species as a *hydride-donor*. This mechanism was characterized and comprehensively studied by means of DFT calculations as detailed below. Its feasibility was then further evaluated with additional experimental assays presented in the following subsection.

Figure 3.16 represents the calculated Gibbs free-energy profile for the reduction of CO₂ to formic acid catalyzed by the Zr₆ nodes of MOF-545 and MOF-545(TM). After the photo-reduction of the linker to generate a TEOA• radical (**Scheme 3.1**), the thermally-activated reduction of CO₂ starts with the displacement of a labile aqua ligand from an open Zr-site of the Zr₆ cluster **1**. Ligand displacement generates a coordination vacancy in **1'** where CO₂ can bind through one of its oxygen atoms to the Zr center to give species **2**. The stepwise process is endergonic by 12.6 kcal·mol⁻¹. In species **2**, the polarization of the C=O bond of CO₂ by the effect of the Zr^{IV} ion acting as a Lewis acid increases the electrophilicity of the carbon atom, *i.e.* activating it towards receiving a nucleophilic attack from an external hydride.

Scheme 3.1: Photochemical reduction of the (TM)TCPP linkers and chemical evolution of the one-electron oxidized donor.

Interestingly, our DFT calculations reveal a mechanism whereby the neutral TEOA[•] radical plays the role of the reducing species that transfers a nucleophilic hydride to the activated CO₂ molecule. Following the formation of the **2-TEOA[•]** non-covalent adduct, the hydride-transfer step involves one of the allylic protons in TEOA[•] (highlighted in red in **Figure 3.16**) that migrates as a formal hydride to the carbon atom of the Zr-bound CO₂, triggering the abstraction of the hydroxyl proton of TEOA (highlighted in blue) by a basic Zr-OH site of the MOF. This concerted process takes place through **TS₂₋₄** overcoming a smooth free-energy barrier of 10.9 kcal·mol⁻¹ from the **2-TEOA[•]** species and yields species **4** where the formate product remains coordinated to the Zr center.

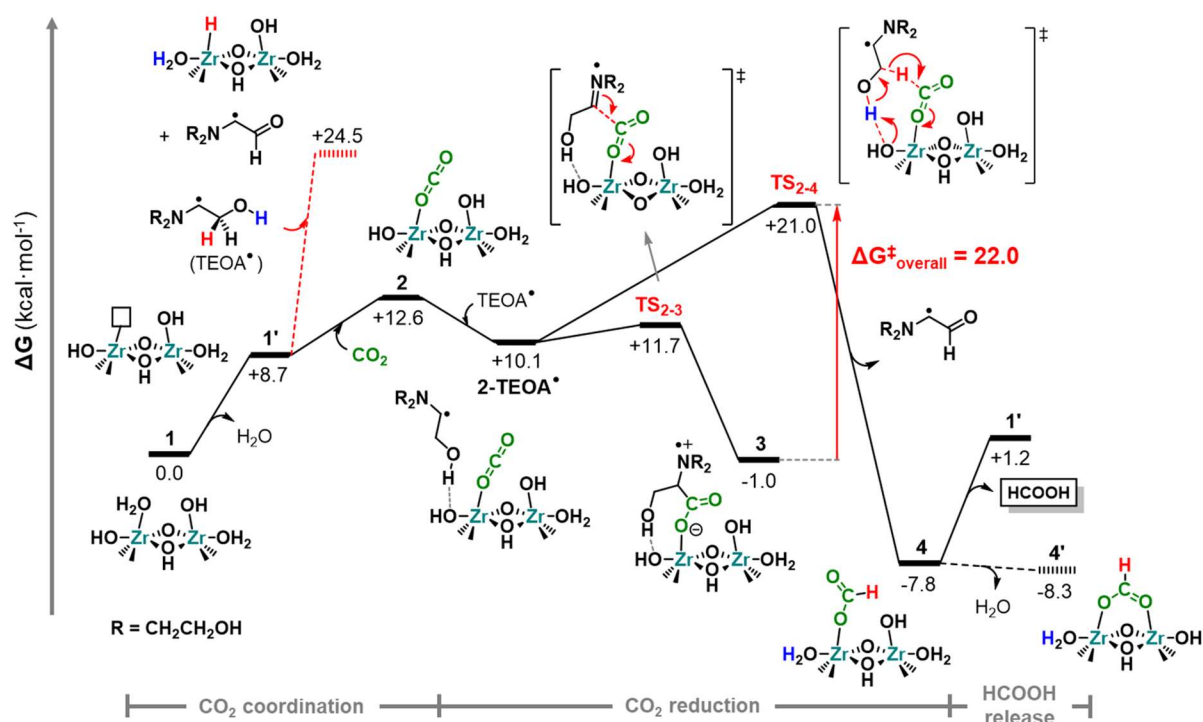


Figure 3.16: Gibbs free-energy profile (kcal·mol⁻¹) for the reduction of CO₂ to HCOOH catalyzed by MOF-545. The red arrow highlights the overall free-energy barrier (3→TS₂₋₄). Relative energies of species that contain a TEOA[•] fragment account for the energy penalty of 2.7 kcal·mol⁻¹ associated to displacing the equilibrium depicted in Scheme 3.1.c towards the free reducing agent in solution. The free-energy cost for the product release considers the product as a non-covalent HCOOH···TEOA adduct in solution. Red-dashed lines represent an alternative, less favorable mechanism that is higher in energy.

The geometry of TS₂₋₄ is represented in **Figure 3.17**. Although the organic hydroxyl proton is still attached to TEOA in the transient species structure, we were unable to locate any intermediate in the reaction coordinate between TS₂₋₄ and the product. This indicates that this proton is spontaneously transferred to the hydroxyl group of the Zr₆ cluster after the hydride transfer from TEOA[•] to CO₂, forming an aqua ligand.

Thanks to the Lewis acidity of Zr^{IV}, the free-energy barrier for the hydride-transfer is decreased by 14.1 kcal·mol⁻¹ with respect to the non-catalyzed process, which entails an overall barrier of 25.0 kcal·mol⁻¹. The non-catalyzed process corresponds to the hydride transfer from TEOA[•] radical to a non-activated CO₂. It is worth noting, though, that despite being relatively high, the latter is still affordable at room temperature and might explain the small yield of formate produced by the homogeneous porphyrin (*vide infra*). Importantly, the initial oxidation of TEOA is strictly required to create reactive allylic protons near a heteroatom. Such a pattern facilitates the hydride-transfer by delocalizing the positive charge generated in the process, as

recently observed for structurally similar allylic alcohols capable of transferring a hydride to an electrophilic peroxo group.³⁴ This pinpoints that every component in the reaction mixture plays an essential role in this complex reaction mechanism, which altogether allows the efficient reduction CO₂ when synergistically combined within the three-dimensional structure of the MOF.

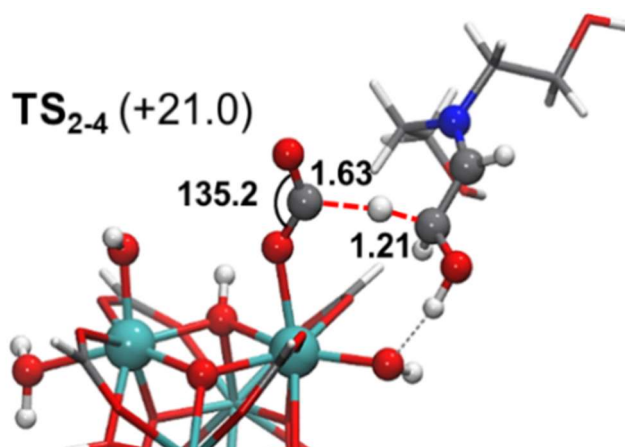


Figure 3.17: Optimized geometry for TS₂₋₄, in which a TEOA[•] molecule transfers a formal hydride to CO₂ to generate a formate anion coordinated to the Zr₆ cluster. The relative Gibbs free energy with respect to the reactants is given in parentheses in kcal·mol⁻¹. Main distances and angles are given in Å and degrees.

Notably, the formation of coordinated formate in **4** is rather exergonic and confers an irreversible character to the reaction, with a reverse free-energy barrier of ~30 kcal·mol⁻¹. Upon releasing an aqua ligand, species **4** may evolve to the slightly more stable species **4'** where the formate anion coordinates two neighboring Zr ions in a bridged fashion. After reducing CO₂, TEOA[•] turns into a depleted, aldehyde-like radical species that can be reductively quenched by the reduced linker or by a second TEOA[•] molecule and protonated by HTEOA⁺ (**Scheme A3.1**) to form an aldehyde by-product, previously reported as a photo-degradation product of TEOA.³⁵ Post catalytic ¹H NMR of the solution confirms the presence of the aldehyde (**Figure A3.2**). The final de-coordination of formic acid from species **4** to regenerate **1'** is endergonic by 9 kcal·mol⁻¹, in agreement with the experimental observations reporting the strong adsorption of the product in MOF-545. Owing to the large excess of TEOA in solution, this energy cost was computed assuming the formation of a H-bonded adduct between formic acid and TEOA that stabilizes the product by 4.4 kcal·mol⁻¹, facilitating its release as pointed out by Fujita and coworkers in a recent contribution.²² This energy cost is then compensated by the reduction of

another CO₂ molecule, which provides the thermodynamic driving force for completing the reaction.

Despite **TS₂₋₄** governing formate production, it is not necessarily the fastest interaction that **2** and TEOA[•] may undergo. We characterized another transient species lower in energy, **TS₂₋₃**, that leads to species **3** through the formation of a C-C bond between the Zr-O=C=O group and the vinylic C atom of TEOA[•] overcoming a very smooth barrier of 1.6 kcal·mol⁻¹ from 2-TEOA[•] (vs. 10.9 kcal·mol⁻¹ to reach **TS₂₋₄**). Species **3** is a zwitterionic complex where both positive and negative charges are stabilized by the electron-donating and electron-withdrawing character of the alkyl chains and of the Zr^{IV} center, respectively. Notably, this makes **3** lie slightly below the reactants in terms of free energy, and therefore, it is expected to act as the resting state of the catalytic cycle. Thus, the overall free-energy barrier (**3**→**TS₂₋₄**, highlighted with a red arrow in **Figure 3.16**) accounts for a moderate value of 22.0 kcal mol⁻¹ that can be overcome at the experimental conditions.

Alternatively, we have evaluated whether TEOA[•] acting as a hydride donor could serve to generate a Zr-hydride from species **1'**. As shown in **Figure 3.15**, the Zr-hydride intermediate is already 3.5 kcal·mol⁻¹ higher in energy than **TS₂₋₄**, suggesting that this pathway might not be operative. A sequential electron transfer and proton transfer mechanism from **2** + TEOA[•] was also predicted to be unlikely, involving a one-electron reduced Zr-(OCO^{•-}) intermediate that lies 30.9 kcal·mol⁻¹ above the reactants.

Finally, we sought for an explanation for experimental catalytic trends. Thanks to the gained knowledge on the reaction mechanism, the outperformance of metalated MOFs over MOF-545 might be rationalized by the ability of metalated porphyrins to coordinate TEOA through the N atom,³⁶ allowing a more efficient inner-sphere photo-oxidation and leading in turn, to a higher concentration of TEOA[•]. Among them, the high catalytic activity of MOF-545(Fe) and MOF-545(Mn) might be attributed to the fast and highly efficient metal-centered photo-reduction (from TM^{III} to TM^{II}) of the porphyrin linkers to produce TEOA[•]. On the other hand, the higher activity of MOF-545(Zn) compared to its TM^{II}-containing partners may be also explained by a boost in the concentration of TEOA[•], caused either by a more favorable association with TEOA or by a superior light-harvesting ability.³⁷⁻³⁹

4.2. Complementary photocatalytic tests

To validate the role of TEOA in our mechanistic proposal, we performed a new set of catalytic tests with the free-base MOF-545 in the presence of an additional amount of molecular Fe^{III}Cl-TCPPOMe (TCPPOMe = tetramethoxyphenylporphyrin) in solution, the iron derivative being the material providing the highest formate yield in the present work. The ester form of the porphyrin was used for solubility reasons. According to our mechanism, the porphyrin added in solution is expected to act as an auxiliary electron acceptor boosting the concentration of the TEOA[•] and in turn, accelerating the rate of the CO₂RR. **Figure 3.18** shows that indeed, the addition of the iron-porphyrin increases the yield of formate produced by the free-base MOF-545 by a factor of 1.75. This enhancement cannot be ascribed to the iron-porphyrin acting as an additional catalytic site by itself, because i) the formate production of the {MOF-545, Fe^{III}Cl-TCPPOMe} system exceeds by far the sum of the individual formate production of MOF-545 and Fe^{III}Cl-TCPPOMe and, ii) experiments with the Fe-porphyrin alone give much lower amounts of formate than with the MOF-545. This indicates much slower kinetics of CO₂ reduction when using Fe^{III}Cl-TCPPOMe rather than MOF-545, whereby the catalytic pathway involving the MOF should prevail over that involving the molecular porphyrin in the mixed {MOF-545, Fe^{III}Cl-TCPPOMe} system.

In line with experiments, our calculations indicate that the consumption of reactants (CO₂ and TEOA[•]) should be much faster on the Zr₆ nodes of the MOF than with the molecular Fe-porphyrin in solution. Therefore, the yield obtained experimentally by combining both MOF-545 and Fe^{III}Cl-TCPPOMe species should be attributed to the catalytic activity of the MOF exclusively, while the Fe-porphyrin added in solution allows increasing the concentration of the reducing agent by accelerating the one-electron oxidation of TEOA.

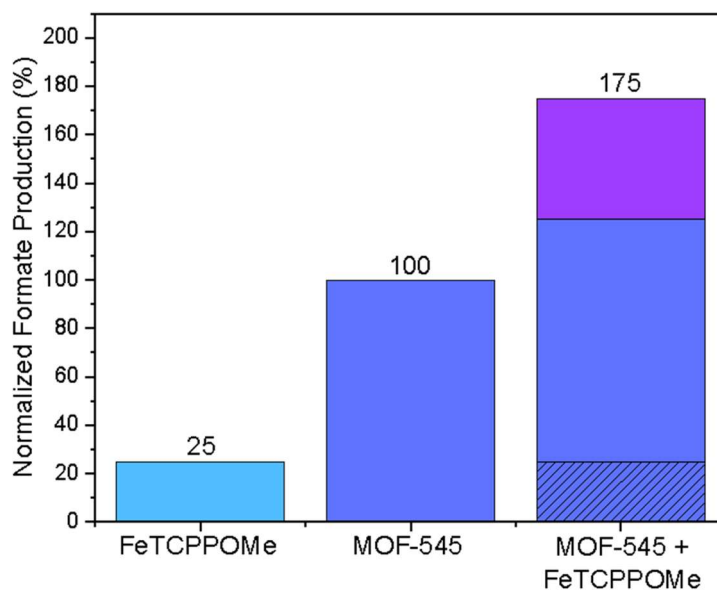


Figure 3.18: Formate production upon CO₂ reduction with Fe-TCPPOMe (1.2 mg) and/or free-base MOF-545 (2 mg) allowing ~1:1 ratio between porphyrins in solution and in the MOF. Experiments were conducted in 2 mL CH₃CN/TEOA (10:1) for 4h under 280 W Xenon Lamp. The amount of formate detected was normalized regarding MOF-545.

In fact, according to a $\Delta\Delta G^\ddagger$ of 3 kcal·mol⁻¹ (22.0 vs 25.0 kcal·mol⁻¹ for the Zr₆-catalyzed and non-catalyzed paths, respectively), the formate produced on the Zr sites would account for the 99.4 % of the overall yield at 25 °C. Further supporting our mechanistic proposal, we noticed that most of the experimental works that reported the formation of formate with Zr-based porphyrinic MOFs also employed TEOA as “sacrificial donor” (**Table A3.1**). The remaining ones performed the catalytic experiments in the presence of other aliphatic alcohols structurally similar to TEOA that might display analogous reactivity, such as ethylene glycol² or triisopropanolamine.³²

To conclude, a computational study supported by experimental data allowed proposing for the first time a full description of the reaction mechanism at play in the photocatalytic reduction of CO₂ into formate by Zr-oxo-clusters in a porphyrinic MOF in presence of TEOA, which is depicted in **Figure A3.3**. The proposed mechanism consists of three main processes: i) the photo-generation of the active reducing species at the porphyrinic linkers; ii) the thermally-activated reduction of CO₂ on the Zr₆ nodes and iii) the termination via radical quenching. It appears that the photoreduction of the linkers by TEOA yields a TEOA• radical, which, beyond being a mere depleted sacrificial donor, was identified as the *real reducing species*, being able to transfer a hydride to a CO₂ molecule activated on a Zr^{IV} Lewis acid center of the Zr₆ node.

The relative catalytic activity of the different materials is rationalized on the basis of their ability to oxidize TEOA under visible-light irradiation: Fe^{III}- and Mn^{III}-containing MOFs, with an oxidation state of +3, permit a highly efficient metal-centered photoreduction, whilst the coordination of TEOA to metalated linkers allows more efficient inner-sphere charge-transfer process compared to free base TCPP linkers.

Overall, these findings represent a step forward towards understanding the catalytic processes that make use of photo-active materials in combination with TEOA (or structurally similar) “sacrificial donors” and is expected to inspire the design of new multi-component catalytic platforms for photo-reduction reactions with improved activity and selectivity.

5. Co-catalyst immobilization in MOF-545

Another way to increase the activity of MOF-545 would be to use its porous character in order to immobilize a co-catalytic guest able to reduce CO₂. The large 36 Å long pore allows the incorporation of a wide variety of catalysts, from small molecules to larger complexes.⁴⁰ The combination of the photosensitive porphyrin and a catalytic guest could allow the reduction of CO₂ without addition of external photosensitizer, in contrast with (PW₁₂,Cp*Rh)@UiO-67 seen in the previous chapter. The choice of the catalyst is a crucial step to build the photoactive composite. A molecular catalyst already reported to reduce CO₂ in presence of porphyrins as PS would be the best choice. Nonetheless, as shown by Paille *et al.*,⁴⁰ the heterogenization of the TCPP porphyrin in metal-organic frameworks can change its photoactivity. Indeed, the molecular [(PW₉O₃₄)₂(H₂O)₂Co₄]¹⁰⁻ (Co₄) polyoxometalate catalyst reported for H₂O oxidation could not, in homogeneous conditions with TCPP, oxidize water in O₂. However, once Co₄ was immobilized in MOF-545, the system could act as a heterogeneous catalyst for water splitting, showing that the energy levels of the TCPP can be modified between the molecular species in homogeneous conditions and the PS immobilized in the MOF as linker. Considering these facts, we have turned to three catalysts previously reported for CO₂ reduction: Mn(bpy)(CO)₃Br^{41,42} (noted Mn(bpy)), Ni(cyclam)Cl₂⁴³⁻⁴⁵ (noted Ni(cyclam)) and 5,10,15,20-tetrakis(pentafluorophenyl)porphyrin (noted F₂₀) (**Figure 3.19**). We have immobilized Ni(cyclam) and Mn(bpy) in MOF-545(Zn). This MOF was chosen because Zn(TPP) is known to be the best PS^{46,47} among the metalated porphyrins. The immobilization of F₂₀ was first performed in the unmetalated MOF-545 to test the possibility of encapsulating this porphyrin catalyst in a porphyrinic MOF.

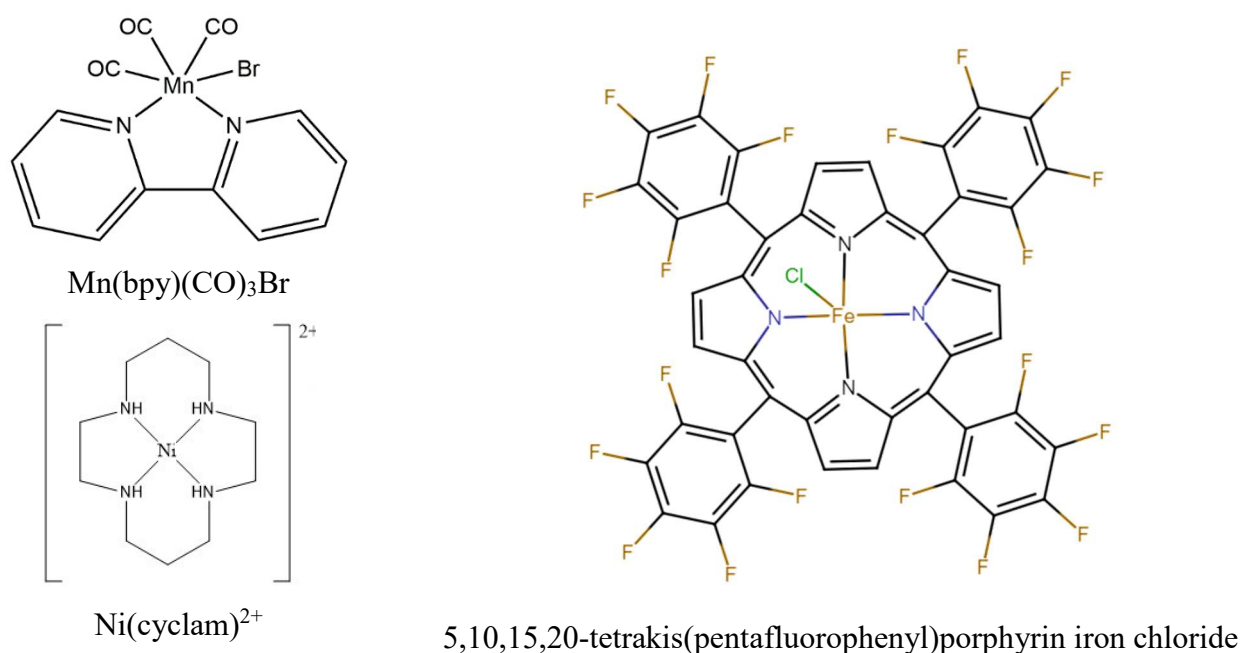


Figure 3.19: Representation of $\text{Mn}(\text{bpy})$, $\text{Ni}(\text{cyclam})$ and F_{20} considered for immobilization in MOF-545

In 2016, Zhang *et al.*⁴¹ reported the photoreduction of CO₂ by a $\text{Mn}(\text{bpy})(\text{CO})_3\text{Br}$ complex in homogeneous conditions with the zinc tetrakis(phenyl)porphyrin as a photosensitizer. The reaction was carried out in CH₃CN/H₂O (20:1) with 0.1 M of triethylamine as an electron donor and 0.5 mM of catalyst. The catalyst over ZnTPP ratio was modulated ranging from 1:2 to 4:1. Surprisingly, the lower the amount of ZnTPP, the higher the catalyst efficiency. Indeed, the 4:1 ratio reached remarkable TONs of 119 for CO and 19 for HCOOH compared to 8 and 6 for CO and HCOOH, respectively, when the $\text{Mn}(\text{bpy})$:ZnTPP ratio was 1:2 (**Table 3.3**). The authors did not propose any explanation for this ratio effect.

Table 3.3: Photocatalytic CO₂ reduction with Mn(bpy)(CO)₃Br and ZnTPP. 3h irradiation, 500W Xe Lamp, CH₃CN/H₂O (20:1), TEA 0.1 M.⁴¹

Group Number	<i>fac</i> -[Mn(phen)(CO) ₃ Br]/ZnTPP ^a	TON ^b	
		CO	HCOOH
1	4:1	119	19
2	3:1	97	18
3	2:1	64	16
4	1:1	12	10
5	1:2	8	6
6	Only <i>fac</i> -[Mn(phen)(CO) ₃ Br] ^c	2	1
7	Only ZnTPP ^d	0	0

Fei *et al.*⁴² reported in 2015 the immobilization of Mn(bpy) in UiO-67 MOF. They used a mixed linker UiO-67 including a bipyridine moiety to act as an anchoring site for the Mn(bpy) catalyst. The Mn(bpy)@UiO-67 activity was compared to that of the Mn(bpy) and Mn(bpydc) (bpydc = bipyridine dicarboxylate) complexes dissolved in a DMF/TEOA (4:1) solution and photosensitized by a ruthenium complex, with additional BNAH (BNAH = 1-benzyl-1,4-dihydronicotinamide) as an electron donor. After 18h, the cat@MOF was close to twice more active than the complexes in homogeneous conditions. However, the homogeneous catalyst only shows a slight deactivation after a few catalytic runs⁴¹ whereas the Mn(bpy)@UiO-67 composite loses half its efficiency after only one catalytic run. The authors indicate that the loss of activity is due to the loss of CO ligands from the Mn catalytic sites and to the degradation of the MOF framework.

Regarding Ni(cyclam), it was first described for CO₂ reduction in 1987 by Grant *et al.*⁴³ Ni(cyclam) was used in water with ascorbic acid as an electron donor and [Ru(bpy)₃]Cl₂ as the photosensitizer. The catalyst was highly stable; however, the catalyst was poorly efficient reaching TONs of 4.8 after 22h for CO and was poorly selective as 90% of the product was H₂. Moreover, the sample was irradiated at 1000W, which is a far more powerful output than any of the studies presented so far. Few reports on Ni(cyclam) immobilization, on ZrO₂⁴⁴ or in a Gd MOF,⁴⁵ show a significant increase in the catalyst efficiency.

F₂₀ was selected to serve as a proof of concept of porphyrin molecular catalyst immobilization in a porphyrin MOF because, although F₂₀ has not been reported for CO₂ photoreduction, closely related porphyrins have shown interesting catalytic performances.⁴⁸ Furthermore, F₂₀ is commercial and relatively cheap and easy to quantify thanks to the 20 fluor born by the phenyl rings. We can note also that several publications dedicated to catalytic reactions involving the cobalt metalated F₂₀ have been published, including oxygen evolution reactions,⁴⁹ cyclohexane oxidation⁵⁰ or hydroalkoxylation of alkynes.⁵¹ This study was performed in collaboration with Julien Bonin and Marc Robert (Laboratoire d'Electrochimie Moléculaire, Université de Paris)

5.1. Synthesis, characterization and photocatalytic activity of the cat@MOF composites

To synthesize the cat@MOF-545 composites, we adapted the protocol described by Paille *et al.*⁴⁰ Briefly, 10 mg of MOF-545(TM) are dispersed and stirred for 24h in a 5 mM solution of the molecular catalyst. For Ni(cyclam)Cl₂ and Mn(bpy)(CO)₃Br, the catalysts were dissolved in acetonitrile and heated at 25 or 60°C. The cat@MOF composites were collected by centrifugation and washed several times with the same solvent than the one used for the encapsulation. A last washing step with acetone was necessary before drying the powder in the oven at 100°C. The quantity of catalyst immobilized in the MOF was estimated by EDS, through the evaluation of the Mn/Zr and Ni/Zr ratios for Mn(bpy) and Ni(cyclam), respectively (Table 3.4). We thus propose the following formulas: Zr₆O₁₆H₁₈(C₄₈H₂₄N₄O₈Zn)₂Cl₂(Mn(bpy))_{0.8} Zr₆O₁₆H_{17.2}(C₄₈H₂₄N₄O₈Zn)₂Cl₂(Ni(cyclam))_{0.4} at room temperature and Zr₆O₁₄H₁₀(C₄₈H₂₄N₄O₈Zn)₂(Ni(cyclam))_{4.0} at 60°C. The previous formula considers the charge compensation by a proton loss on the zirconium cluster as no additional chlorine has been detected by EDS, meaning Ni(cyclam) is encapsulated as a cation.

Table 3.4: EDS analysis of Mn(bpy)@MOF-545(Zn) and Ni(cyclam)@MOF-545(Zn).

	Mn/Zr	Ni/Zr
Mn(bpy)@MOF-545(Zn)	0.13	-
Ni(cyclam)@MOF-545(Zn) RT	-	0.07
Ni(cyclam)@MOF-545(Zn) 60°C	-	0.66

The different compounds were characterized by usual means, PXRD and infrared spectroscopy. For all the composites, the PXRD exhibited the four major peaks of MOF-545 around $2\theta = 2.4$, 4.8, 7.1 and 9.8° (**Figures 3.20**), assessing the structural integrity of the composites during the encapsulation process. However, no peaks of the molecular catalysts were visible in IR no matter the loading ($\text{cat}/\text{Zr}_6 = 0.8$ for Mn(bpy) and $\text{cat}/\text{Zr}_6 = 4$ for Ni(cyclam)).

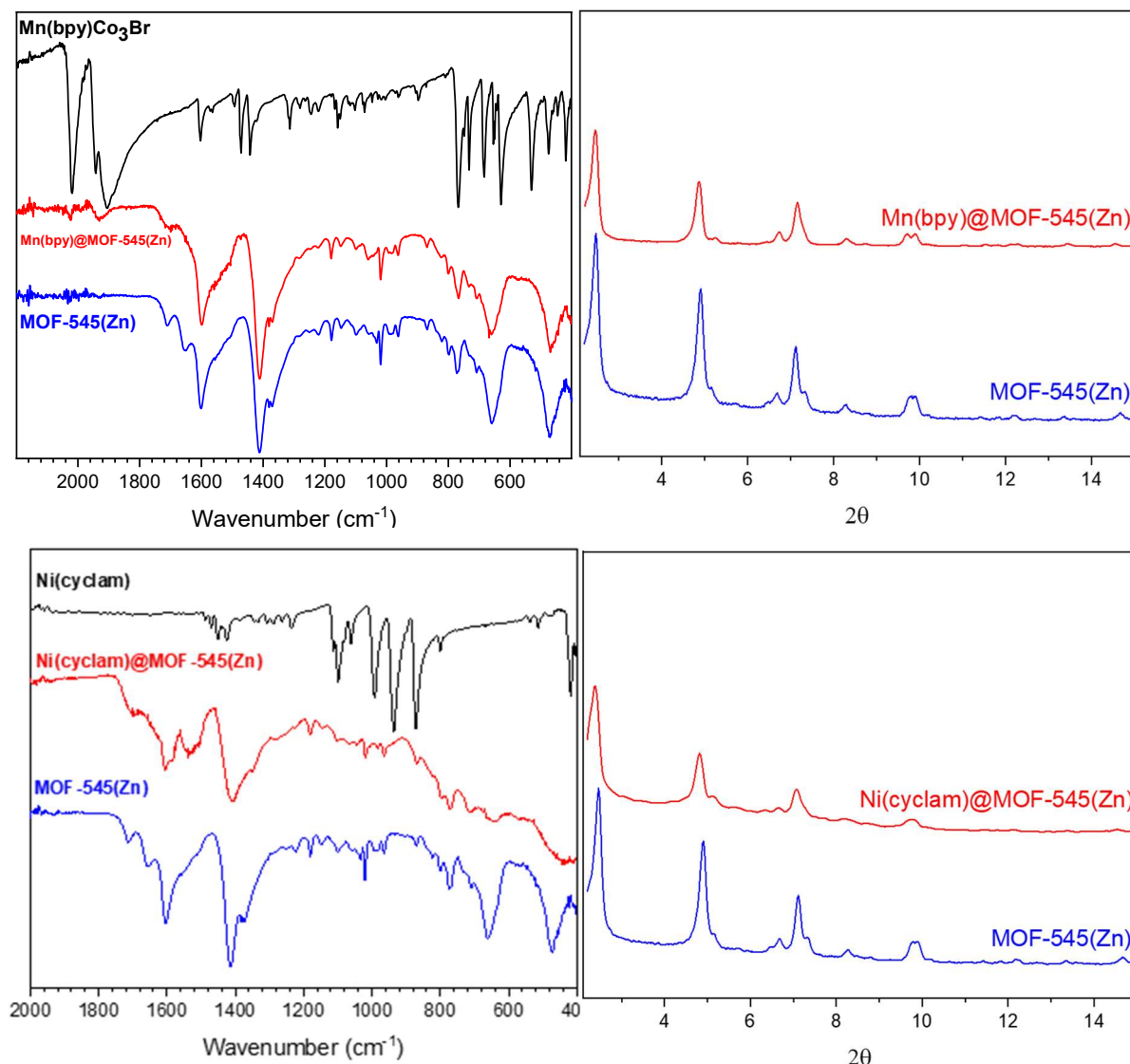


Figure 3.20: IR spectra and PXRD diagrams of MOF-545(Zn), Mn(bpy)@MOF-545(Zn) and Ni(cyclam)@MOF-545(Zn).

Considering F₂₀, the catalyst was purchased from Sigma and used as received. The encapsulations were conducted in DMF rather than acetonitrile to heat the solution at a higher temperature. A first encapsulation attempt was carried at 80°C for 24h. However, the EDS analysis showed a negligible amount of F₂₀ incorporated into MOF-545. In order to increase

the amount of impregnated F₂₀, the temperature was increased to 120°C, leading only to a clearly insufficient F₂₀/Zr₆ ratio of 0.04. We thus turned to a “successive encapsulation” method. After each 24h encapsulation, the solid was collected by centrifugation and washed several times. The same solid was then dispersed in a fresh solution of 5 mM F₂₀ in DMF and stirred for 24h at 120°C. This way, we obtained larger F₂₀/Zr₆ ratio up to 0.2 after the third cycle. (**Table 3.5**).

Table 3.5: EDS analysis of F₂₀@MOF-545 composites obtained after one (F₂₀@MOF-545-1), two (F₂₀@MOF-545-2) and three (F₂₀@MOF-545-3) impregnation cycles in DMF (24h, 120°C, 5mM F₂₀).

	F/Zr	F ₂₀ /MOF
F ₂₀ @MOF-545-1	0.14	0.04
F ₂₀ @MOF-545-2	0.47	0.14
F ₂₀ @MOF-545-3	0.69	0.20

The composites have been characterized at each step by infrared spectroscopy and PXRD (**Figure 3.21**). As for Mn(bpy)@MOF-545(Zn) and Ni(cyclam)@MOF-545(Zn), the different PXRD patterns are similar to that of MOF-545, assessing the structural integrity of the composite even after 72h at 120°C and several washing steps. Like for the two previous cat@MOF composites, it was not possible to identify the presence of the catalysts on the IR spectra.

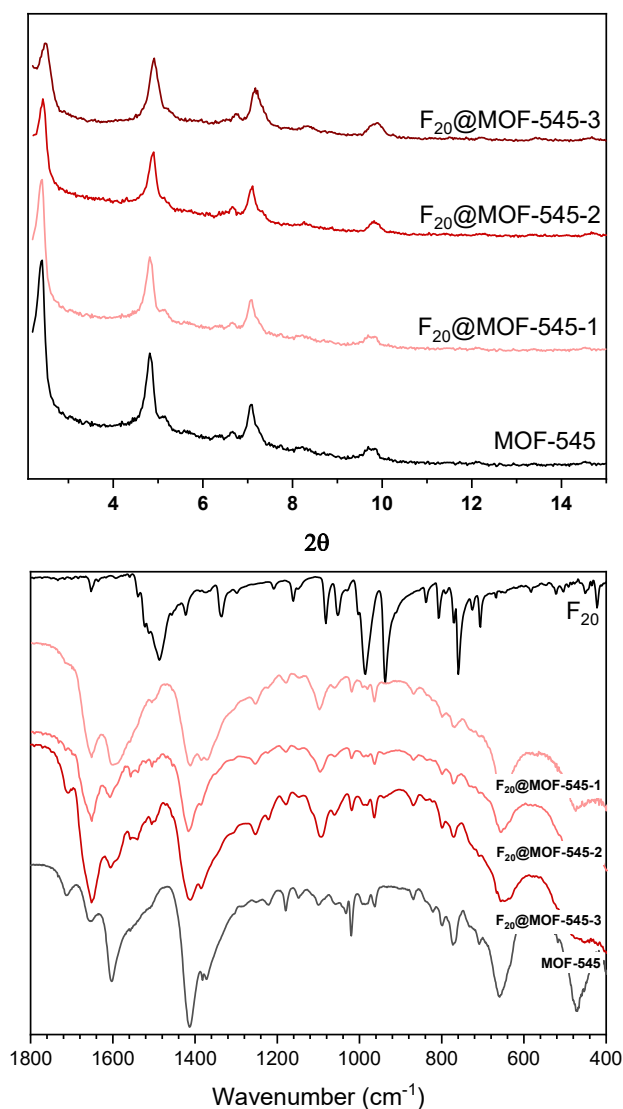


Figure 3.21: PXRD (left) and infrared spectra (right) of the successively encapsulated $F_{20}@MOF-545$.

Next, the activity for CO₂ reduction of the three cat@MOF composites were tested. We have considered different combinations between water and acetonitrile as solvent and TEA, TEOA and ascorbic acid as sacrificial electron donors. For both $F_{20}@MOF-545$ and Ni(cyclam)@MOF-545(Zn), no matter the combination, no CO₂ reduction product were detected after several hours of irradiation. Nonetheless, for Mn(bpy)@MOF-545(Zn) a large amount of CO was detected by gas chromatography using acetonitrile as solvent and TEOA as an electron donor (**Figure 3.22**). In order to confirm the catalytic nature of the reaction, we performed blank experiments. Without light, no CO was detected. However, we could still detect CO without bubbling CO₂ in the solution, meaning that the CO detected by GC is not issued from CO₂ reduction but from the Mn(bpy)(CO)₃Br decomposition. Indeed, after 8h

irradiation, the CO production measured without CO₂ and the CO production found when bubbling CO₂ were similar (640 nmol).

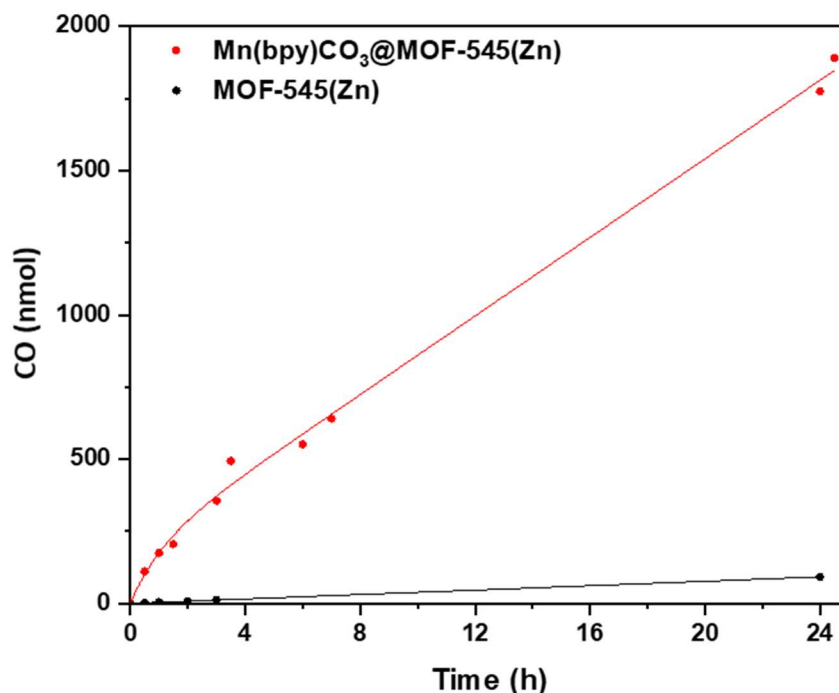


Figure 3.22: CO release in presence of CO₂ of a 2 mL of CH₃CN/TEOA (5:1) mixture with 0.5 mg of Mn(bpy)@MOF-545(Zn) (24 h irradiation with a 280W Xe lamp equipped with a 415nm UV cut-off).

5.2. Synthesis and characterization and photocatalytic activity of POM@MOF composites

As seen in the previous chapter, the presence of an electron-rich POM near the catalytic center can enhance greatly the catalytic performances of the composite. Moreover, the pores of MOF-545 being large enough to proceed to post synthetic encapsulations, we worked on immobilizing various POM anions in the MOF-545.

In a preliminary study conducted before the MOF-545 CO₂RR catalytic activity optimization seen in subpart two, we investigated the effect on the catalysis of the immobilization of four POMs which differ by their composition, charge and shape: [(PW₉O₃₆)₂(H₂O)₂Ni₄]¹⁰⁻ (Ni₄), [(PW₉O₃₆)₂(H₂O)₂Co₄]¹⁰⁻ (Co₄), [PW₁₀Ti₂O₄₀]⁷⁻ (PW₁₀Ti₂) and [SiW₁₂O₄₀]⁴⁻ (SiW₁₂) (**Figure 3.23**).

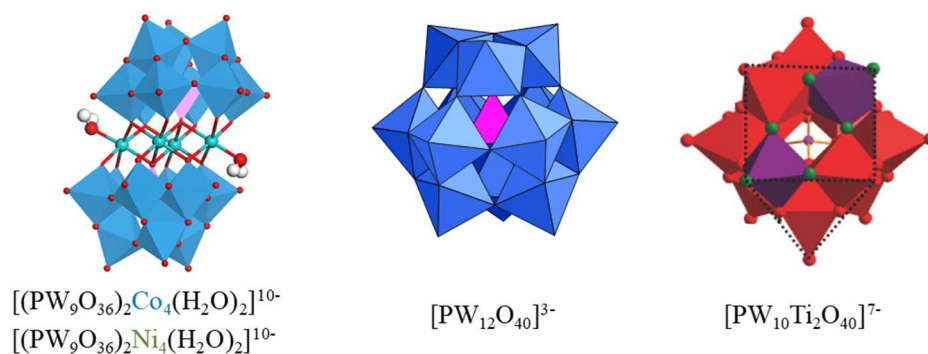


Figure 3.23: Structure of Ni₄/Co₄, PW₁₂ and PW₁₀Ti₂

The synthesis of the POM@MOF-545 composites was performed using 5 mM of POM DMF/H₂O (1:1 v/v) mixtures. We quantified the formate production rates in two ways, first by considering the whole sample as the catalyst and thus presenting the rate in $\mu\text{mol}\cdot\text{g}^{-1}\cdot\text{h}^{-1}$, second by considering that the POM does not act as catalyst and thus presenting the rates in $\mu\text{mol}\cdot\text{g}^{-1}\cdot\text{h}^{-1}_{\text{MOF}}$ (**Table A3.2**).

Two POM@MOFs, Ni₄@MOF-545 and SiW₁₂@MOF-545, present a significant boosting effect on the catalysis compared to the POM-free MOF, whereas the two others (Co₄@MOF-545 and PW₁₀Ti₂@MOF-545) have proven a limited increase. The value of the HCOOH production in $\mu\text{mol}\cdot\text{g}^{-1}\cdot\text{h}^{-1}$ of Ni₄@MOF-545 is greater than that of SiW₁₂@MOF-545 (268 vs 218). In contrary, when considering the MOF only, SiW₁₂@MOF-545 shows the greatest increase (378 vs 423) (**Figure 3.24**).

We thus decided to investigate the incorporation of different Keggin anions in MOF-545, the main purpose of this study being to rationalize the effect of the POM charge, redox potential and acidity on the catalysis. The compounds K₅[BW₁₂O₄₀], Na₄[SiW₁₂O₄₀], Na₂H[PW₁₂O₄₀], Na₂H[PMo₁₂O₄₀] and K₄[SiMo₁₂O₄₀], were considered. Also, based on the results described above, the nano version of the MOF-545 was considered.

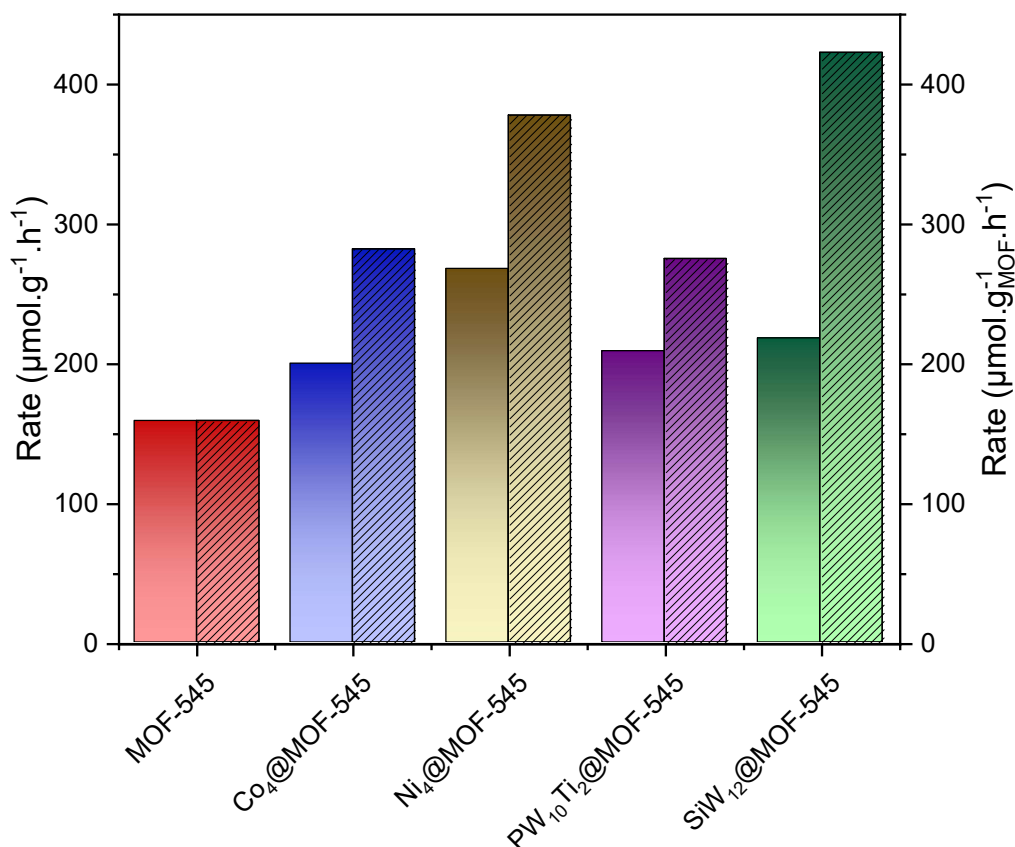


Figure 3.24: CO₂ photoreduction rates for the studied POM@MOF composites. The plain bars correspond to the rates in $\mu\text{mol}\cdot\text{g}^{-1}\cdot\text{h}^{-1}$ and the hatched bars in $\mu\text{mol}\cdot\text{g}^{-1}_{\text{MOF}}\cdot\text{h}^{-1}$.

The first impregnation procedure was adapted from the previously described ones. Briefly, 10 mg of NanoMOF-545 was dispersed in 2 mL of a 5 mM POM solution in a DMF/HCl (0.1M) (1:1 v/v) mixture. This medium was chosen because the alkaline salts of the Keggin POMs considered for this study are not soluble in organic solvent and are only stable in acidic aqueous solutions while the MOF is more stable in DMF than in aqueous solutions. The solutions were stirred for 5h, the composites were collected by centrifugation and washed several times. The PXRD patterns of the synthesized POM@NanoMOF-545 composites were collected and are presented in **Figure 3.25**.

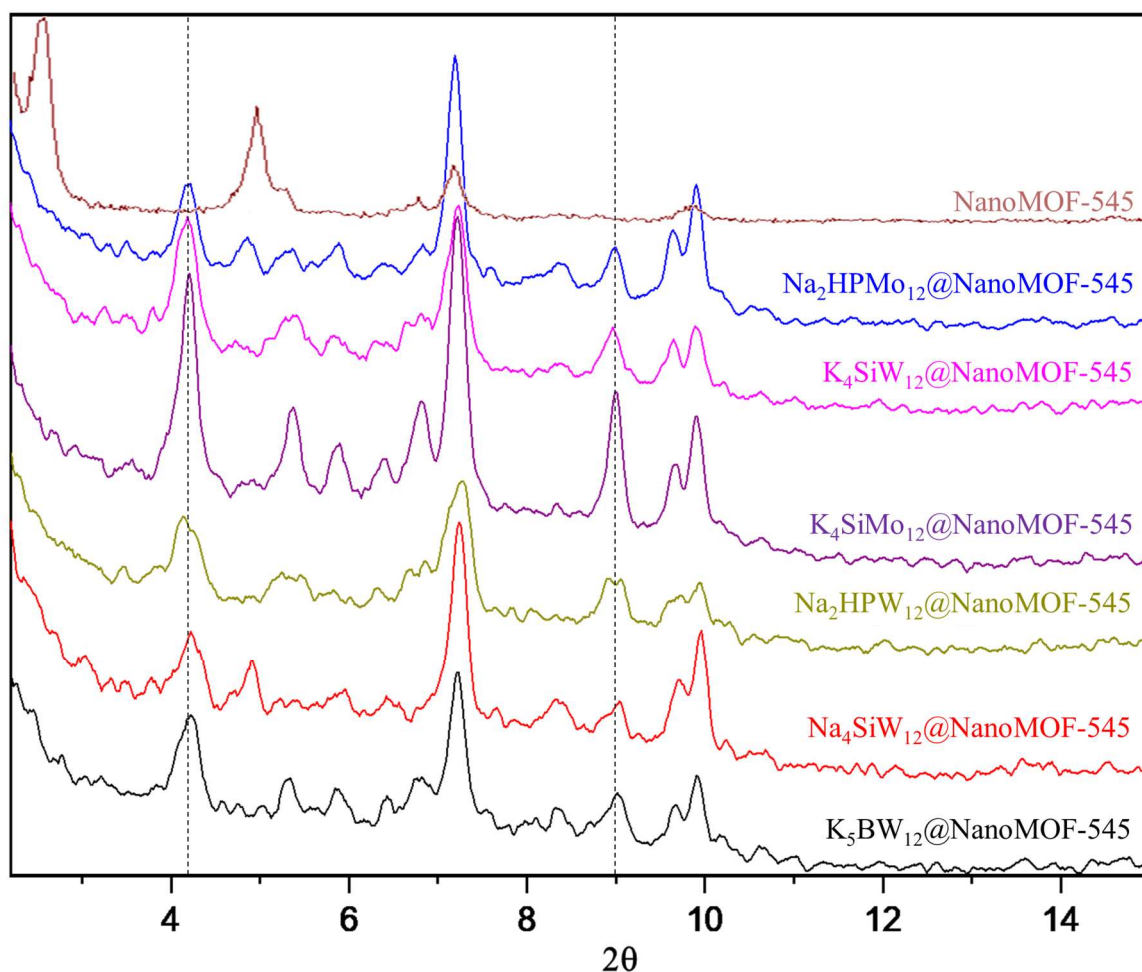


Figure 3.25: Experimental PXRD patterns of the POM@NanoMOF-545 composites.

All six POM@NanoMOF-545 show similar features. It can be seen that the two main peaks at $2\theta = 2.4$ and 4.8° completely disappeared while the peaks at 7.1 and 9.8° are still observed. Moreover, two new peaks at 4.1 and 9.0° appeared. To date, these peaks could not be attributed to known porphyrinic MOF phases nor to the initial POMs. The reason of the drastic changes in the PXRD pattern could be attributed to the highly concentrated solutions of POMs used during the impregnation steps probably resulting in high loading of POMs. Indeed, for POM@MOF composites, the negative POM charge is often compensated by linker defects and thus high loadings can lead to a partial destruction of the MOF.

Next, we tried to play around the impregnation protocol to avoid the changes in PXRD patterns. We thus decided to decrease the amount of POM in solution during the encapsulation processes, even if this could lead to significantly lower loadings in POM. We performed the encapsulations with three different concentrations (1, 0.5 or 0.25 equivalents of Na₂HPMo₁₂O₄₀ per Zr₆ units). This corresponds to concentrations of 2, 1 and 0.5 mM of POM. The new PXRD patterns are

shown in **Figure 3.26**. It is indeed observed that the lower the POM concentration, the closer to the NanoMOF-545 PXRD pattern. To compromise between the crystallinity and the POM loading we have decided to work with the 0.5 eq encapsulation methods.

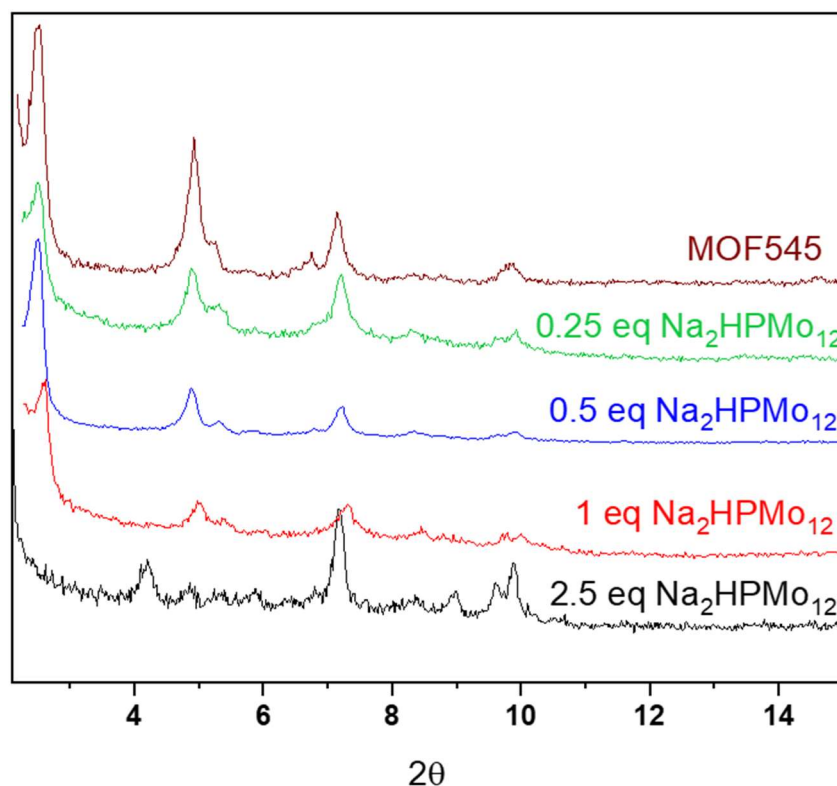


Figure 3.26: PXRD patterns of PMo₁₂@nanoMOF-545 composites prepared from solution incorporating 2.5 (black), 1 (red), 0.5 (blue), 0.25 (green) equivalent of POM per Zr₆ units.

The POM@NanoMOF-545 composites activity for CO₂ reduction has been tested. Unfortunately, no significant CO₂ reduction has been found. This is highly surprising as the MOF alone has shown to be active (see above). Thus, this could be due to the presence of the POM but also to the POM impregnation conditions. To check this last hypothesis, the POM-free NanoMOF-545 has thus been stirred in DMF/HCl (0.1M) solution (i.e. the impregnation conditions for the obtaining of the POM@MOF materials). Despite being highly crystalline, the resulting MOF has shown only a small activity (**Table 3.6**), strongly suggesting that the loss of activity is indeed due to its treatment in DMF/HCl (0.1M).

Table 3.6: Photocatalytic CO₂ reduction of NanoMOF-545 after different treatments in 10:1 CH₃CN/TEOA solutions.

Impregnation solvent	Activation	[Formate] after 2h.
No impregnation	No activation	1052 μ M
DMF/HCl (0.1 M) (1:1)	No activation	339 μ M
Borate buffer pH 8.0	No activation	238 μ M
Borate buffer pH 8.0	Supercritical CO ₂	460 μ M
DMF/H ₂ O (1:1)	No activation	723 μ M
DMF/H ₂ O (1:1)	Supercritical CO ₂	867 μ M

The NanoMOF-545 has also been stirred in a DMF/H₂O mixture, a medium where alkaline Keggin salts are soluble. Interestingly, a slighter activity loss can be observed, going from 1050 μ M of formate for the starting NanoMOF-545 to 723 μ M after the DMF/H₂O treatment. This supports that the loss of activity is due to the acidity of the medium used for POM encapsulation. Moreover, it has been found that supercritical CO₂ treatment can help the NanoMOF-545 to recover partially its activity after the DMF/H₂O treatment as the formate produced increases from 723 to 867 μ M (with and without supercritical CO₂ activation respectively).

To conclude this study, we have seen that the impregnation conditions could lead to a drastic loss of activity of the MOF. Conditions where the MOF is both crystalline and active after POM encapsulation still have to be clearly established. Further investigations on the encapsulation conditions are thus necessary. We could think of working with monosubstituted Keggin. Monosubstituted PW₁₁M Keggin anions are indeed stable at pH higher than non-substituted ones. This pH can, depending on the nature of the heterometal M, reach pH 7;⁵² thus, encapsulation in DMF/H₂O can be considered for these species.

6. Conclusions

The photocatalytic activity of non-metalated and metalated MOF-545(TM) towards CO₂RR in 10:1 CH₃CN/TEOA solutions has been evaluated by systematically varying the transition metal coordinated to the porphyrinic linkers. All the prepared catalysts showed 100% selectivity towards formate production and the yield increases from free-base to Cu^{II} < Co^{II} < Mn^{III} < Zn^{II} < Fe^{III}, reaching 566 μ mol·g⁻¹·h⁻¹ for MOF-545(Fe). The activity of MOF-545(Fe) could be

boosted thanks to the preparation of nanocrystals (150 nm length) allowing an increased density of accessible catalytic sites. This strategy enabled reaching a formate production of 1160 $\mu\text{mol}\cdot\text{g}^{-1}\cdot\text{h}^{-1}$, being one of the highest productions of formate amongst MOF catalysts reported to date. Recyclability tests show that the MOFs maintain their catalytic activity over several runs.

Concerning the encapsulation of Mn(bpy) and Ni(cyclam), a high loading in porphyrinic MOFs can be reached in rather mild conditions (60°C in acetonitrile). The resulting cat@MOF-545(Zn) have been characterized and tested for their catalytic CO₂ reduction properties but, unfortunately, did not give promising results. Indeed, no products were detected when working with Ni(cyclam). Besides, with Mn(bpy) a high amount of CO was detected but corresponded to the catalyst degradation, releasing its former covalently bound CO ligands. Considering the high loading of both catalysts, it could however be interesting to test the cat@MOF-545(Zn) composites for CO₂ electroreduction as it has been reported that Ni(cyclam)⁵³ is more active and Mn(bpy)⁵⁴ more stable in such conditions than under photocatalytic conditions. As for F₂₀, we successfully encapsulated the porphyrin in MOF-545. The encapsulation is more challenging than Mn(bpy) and Ni(cyclam) as it involves several successive encapsulations to reach a loading of 0.20 F₂₀/MOF, but again, no significant CO₂RR activity has been observed.

Lastly, we attempted to encapsulate Keggin anions in NanoMOF-545. Due to the low stability of the polyoxometalates used in non-acidic conditions and the stability issues of MOF-545 toward water, simple encapsulation in pure aqueous media was excluded. Reactions have thus been performed in DMF/HCl (0.1M) (1:1 v/v). A very high POM loading has been obtained, greatly affecting the crystallinity of the MOF as evidenced by the PXRD patterns which are altered, with in particular the appearance of two new intense peaks. Moreover, the resulting POM@MOF composites are inactive for CO₂ reduction. We assume that treatments in acidic media deactivate the MOF. A non-acidic DMF/H₂O mixture has thus been considered as potential solvent for further impregnation experiments. Interestingly, it has been found that this time, the NanoMOF-545 conserves its activity, which makes it possible to obtain in future studies active POM@MOF composites.

7. Experimental section

NanoMOF-545 synthesis. 137 mg of ZrOCl₂.8H₂O, 30 mg of TCPP and 300 µL of 1,2-dichloroacetic acid were dissolved in 10 mL DMF in a 100 mL Teflon vial. The mixture was heated for 20 min under microwave (130°C, 800 W) with vigorous stirring. After cooling to room temperature, a powder was collected by centrifugation. The MOF was then heated at 130°C for two hours in a 10 mL DMF / 1 mL 1M HCl mixture. After centrifugation, the obtained material was rinsed twice with DMF and twice with acetone. Lastly, the powder was dispersed in 20 mL of acetone and stirred overnight. The final compound was collected by centrifugation and rinsed twice with acetone then dried at 100°C (m = 28 mg).

NanoMOF-545(Fe) Synthesis. 137 mg of ZrOCl₂.8H₂O, 32 mg of (Fe)TCPP and 900 µL of 1,2-dichloroacetic acid were dissolved in 10 mL DMF in a 100 mL Teflon vial. The mixture was heated for 20 min under microwave (130°C, 800 W) with vigorous stirring. After cooling to room temperature, a powder was collected by centrifugation. The MOF was then heated at 130°C for two hours in a 30 mL DMF / 3 mL 1M HCl mixture. After centrifugation, the obtained material was rinsed twice with DMF and twice with acetone. Lastly, the powder was dispersed in 20 mL of acetone and stirred overnight. The final compound was collected by centrifugation and rinsed twice with acetone then dried at 100°C (m = 30 mg). EDX calcd. (exp.): Fe/Zr 0.33 (0.32).

Photocatalysis experiments. 2 mg of catalyst and 2 mL of a CH₃CN/TEOA (10:1) mixture were added to a 4 mL sealed quartz cuvette and sonicated for 10 min. The cuvette was then submitted to a CO₂ flux for 20 min before being irradiated for 4 h with a 280 W Xenon lamp equipped with a 415 nm UV cutoff. Gas products were analyzed via gas chromatography while liquid products were assessed by ionic chromatography. After the catalytic process, the catalyst was recollected by centrifugation, dispersed in 2 mL of milli-Q water and stirred at 60°C for 1 h. An aliquot of the liquid phase was collected and analyzed by ionic chromatography to quantify the remaining formate leached by the MOF.

8. References

1. Xu, H.-Q. *et al.* Visible-Light Photoreduction of CO₂ in a Metal–Organic Framework: Boosting Electron–Hole Separation via Electron Trap States. *J. Am. Chem. Soc.* **137**, 13440–13443 (2015).
2. Jin, J. Porphyrin-based metal–organic framework catalysts for photoreduction of CO₂: understanding the effect of node connectivity and linker metalation on activity. *New J. Chem.* **44**, 15362–15368 (2020).
3. Zhang, H. *et al.* Efficient Visible-Light-Driven Carbon Dioxide Reduction by a Single-Atom Implanted Metal–Organic Framework. *Angew. Chem. Int. Ed.* **55**, 14310–14314 (2016).
4. Birel, Ö., Nadeem, S. & Duman, H. Porphyrin-Based Dye-Sensitized Solar Cells (DSSCs): a Review. *J. Fluoresc.* **27**, 1075–1085 (2017).
5. Morris, W. *et al.* Synthesis, Structure, and Metalation of Two New Highly Porous Zirconium Metal–Organic Frameworks. *Inorg. Chem.* **51**, 6443–6445 (2012).
6. Liu, T.-F. *et al.* Topology-Guided Design and Syntheses of Highly Stable Mesoporous Porphyrinic Zirconium Metal–Organic Frameworks with High Surface Area. *J. Am. Chem. Soc.* **137**, 413–419 (2015).
7. Feng, D. *et al.* Construction of Ultrastable Porphyrin Zr Metal–Organic Frameworks through Linker Elimination. *J. Am. Chem. Soc.* **135**, 17105–17110 (2013).
8. Feng, D. *et al.* A Highly Stable Porphyrinic Zirconium Metal–Organic Framework with shp-a Topology. *J. Am. Chem. Soc.* **136**, 17714–17717 (2014).
9. Feng, D. *et al.* Zirconium-Metalloporphyrin PCN-222: Mesoporous Metal–Organic Frameworks with Ultrahigh Stability as Biomimetic Catalysts. *Angew. Chem. Int. Ed.* **51**, 10307–10310 (2012).
10. Chen, Y., Hoang, T. & Ma, S. Biomimetic Catalysis of a Porous Iron-Based Metal–Metalloporphyrin Framework. *Inorg. Chem.* **51**, 12600–12602 (2012).
11. Jiang, H.-L. *et al.* An Exceptionally Stable, Porphyrinic Zr Metal–Organic Framework Exhibiting pH-Dependent Fluorescence. *J. Am. Chem. Soc.* **135**, 13934–13938 (2013).
12. Deria, P., Yu, J., Balaraman, R. P., Mashni, J. & White, S. N. Topology-dependent emissive properties of zirconium-based porphyrin MOFs. *Chem. Commun.* **52**, 13031–13034 (2016).
13. Yu, K., Won, D.-I., Lee, W. I. & Ahn, W.-S. Porphyrinic zirconium metal-organic frameworks: Synthesis and applications for adsorption/catalysis. *Korean J. Chem. Eng.* **38**, 653–673 (2021).
14. Fu, Y. *et al.* An Amine-Functionalized Titanium Metal–Organic Framework Photocatalyst with Visible-Light-Induced Activity for CO₂ Reduction. *Angew. Chem. Int. Ed.* **51**, 3364–3367 (2012).
15. Gao, W.-Y. *et al.* A Mixed-Metal Porphyrinic Framework Promoting Gas-Phase CO₂ Photoreduction without Organic Sacrificial Agents. *ChemSusChem* **13**, 6273–6277 (2020).
16. Liu, J. *et al.* A porous rhodium(III)-porphyrin metal-organic framework as an efficient and selective photocatalyst for CO₂ reduction. *Appl. Catal. B Environ.* **231**, 173–181 (2018).
17. Jin, J. Highly stable and efficient visible-light-driven carbon dioxide reduction by zirconium–metalloporphyrin PCN-222 via dual catalytic routes. *React. Kinet. Mech. Catal.* **131**, 397–408 (2020).
18. Wu, L.-Y. *et al.* Encapsulating Perovskite Quantum Dots in Iron-Based Metal–Organic Frameworks (MOFs) for Efficient Photocatalytic CO₂ Reduction. *Angew. Chem. Int. Ed.* **58**, 9491–9495 (2019).

19. Guo, Y. *et al.* Charge separation in hybrid metal–organic framework films for enhanced catalytic CO₂ conversion. *J. Mater. Chem. A* **9**, 2694–2699 (2021).
20. Choi, S. *et al.* Rapid Exciton Migration and Amplified Funneling Effects of Multi-Porphyrin Arrays in a Re(I)/Porphyrinic MOF Hybrid for Photocatalytic CO₂ Reduction. *ACS Appl. Mater. Interfaces* **13**, 2710–2722 (2021).
21. Majewski, M. B., Noh, H., Islamoglu, T. & Farha, O. K. NanoMOFs: little crystallites for substantial applications. *J. Mater. Chem. A* **6**, 7338–7350 (2018).
22. Sampaio, R. N., Grills, D. C., Polyansky, D. E., Szalda, D. J. & Fujita, E. Unexpected Roles of Triethanolamine in the Photochemical Reduction of CO₂ to Formate by Ruthenium Complexes. *J Am Chem Soc* **16** (2020).
23. Paille, G. *et al.* A Fully Noble Metal-Free Photosystem Based on Cobalt-Polyoxometalates Immobilized in a Porphyrinic Metal–Organic Framework for Water Oxidation. *J. Am. Chem. Soc.* **140**, 3613–3618 (2018).
24. Kelty, M. L. *et al.* High-throughput synthesis and characterization of nanocrystalline porphyrinic zirconium metal–organic frameworks. *Chem. Commun.* **52**, 7854–7857 (2016).
25. PCN-222 Metal–Organic Framework Nanoparticles with Tunable Pore Size for Nanocomposite Reverse Osmosis Membranes | ACS Applied Materials & Interfaces. <https://pubs.acs.org/doi/10.1021/acsami.0c04349>.
26. Bůžek, D. *et al.* Nanoscaled porphyrinic metal–organic frameworks: photosensitizer delivery systems for photodynamic therapy. *J. Mater. Chem. B* **5**, 1815–1821 (2017).
27. Fidalgo-Marijuan, A., Barandika, G., Bazán, B., Urtiaga, M.-K. & Arriortua, M.-I. Self-assembly of iron TCPP (meso-tetra(4-carboxyphenyl)porphyrin) into a chiral 2D coordination polymer. *Polyhedron* **30**, 2711–2716 (2011).
28. Waldie, K. M., Ostericher, A. L., Reineke, M. H., Sasayama, A. F. & Kubiak, C. P. Hydricity of Transition-Metal Hydrides: Thermodynamic Considerations for CO₂ Reduction. *ACS Catal.* **8**, 1313–1324 (2018).
29. Ceballos, B. M. & Yang, J. Y. Directing the reactivity of metal hydrides for selective CO₂ reduction. *Proc. Natl. Acad. Sci.* **115**, 12686–12691 (2018).
30. Todorova, T. K., Huan, T. N., Wang, X., Agarwala, H. & Fontecave, M. Controlling Hydrogen Evolution during Photoreduction of CO₂ to Formic Acid Using [Rh(R-bpy)(Cp*)Cl]⁺ Catalysts: A Structure–Activity Study. *Inorg. Chem.* **58**, 6893–6903 (2019).
31. Chen, D., Xing, H., Wang, C. & Su, Z. Highly efficient visible-light-driven CO₂ reduction to formate by a new anthracene-based zirconium MOF via dual catalytic routes. *J. Mater. Chem. A* **4**, 2657–2662 (2016).
32. Qin, J.-S. *et al.* Creating Well-Defined Hexabenzocoronene in Zirconium Metal–Organic Framework by Postsynthetic Annulation. *J. Am. Chem. Soc.* **141**, 2054–2060 (2019).
33. Sun, D. *et al.* Studies on Photocatalytic CO₂ Reduction over NH₂-Uio-66(Zr) and Its Derivatives: Towards a Better Understanding of Photocatalysis on Metal–Organic Frameworks. *Chem. – Eur. J.* **19**, 14279–14285 (2013).
34. Zhang, T. *et al.* Reaction Pathway Discrimination in Alkene Oxidation Reactions by Designed Ti-Siloxy-Polyoxometalates. *ChemCatChem* **13**, 1220–1229 (2021).
35. Pellegrin, Y. & Odobel, F. Sacrificial electron donor reagents for solar fuel production. *Comptes Rendus Chim.* **20**, 283–295 (2017).
36. Gabrielsson, A., Smith, J. R. L. & Perutz, R. N. Remote site photosubstitution in metalloporphyrin-rhenium tricarbonylbipyridine assemblies: photo-reactions of molecules with very short lived excited states. *Dalton Trans.* 4259–4269 (2008) doi:10.1039/b806267f.

37. Campbell, W. M., Burrell, A. K., Officer, D. L. & Jolley, K. W. Porphyrins as light harvesters in the dye-sensitised TiO₂ solar cell. *Coord. Chem. Rev.* **248**, 1363–1379 (2004).
38. Chen, D., Yang, D., Geng, J., Zhu, J. & Jiang, Z. Improving visible-light photocatalytic activity of N-doped TiO₂ nanoparticles via sensitization by Zn porphyrin. *Appl. Surf. Sci.* **255**, 2879–2884 (2008).
39. Chaitanya, K., Ju, X.-H. & Heron, B. M. Theoretical study on the light-harvesting efficiency of zinc porphyrin sensitizers for DSSCs. *Rsc Adv.* **4**, 26621–26634 (2014).
40. Paille, G. *et al.* A Fully Noble Metal-Free Photosystem Based on Cobalt-Polyoxometalates Immobilized in a Porphyrinic Metal–Organic Framework for Water Oxidation. *J. Am. Chem. Soc.* **140**, 3613–3618 (2018).
41. Zhang, J.-X., Hu, C.-Y., Wang, W., Wang, H. & Bian, Z.-Y. Visible light driven reduction of CO₂ catalyzed by an abundant manganese catalyst with zinc porphyrin photosensitizer. *Appl. Catal. Gen.* **522**, 145–151 (2016).
42. Fei, H., Sampson, M. D., Lee, Y., Kubiak, C. P. & Cohen, S. M. Photocatalytic CO₂ Reduction to Formate Using a Mn(I) Molecular Catalyst in a Robust Metal–Organic Framework. *Inorg. Chem.* **54**, 6821–6828 (2015).
43. Grant, J. L., Goswami, K., Otvos, J. W. & Calvin, M. Photochemical Reduction of Carbon Dioxide to Carbon Monoxide in Water using a Nickel(II) Tetra-azamacrocyclic Complex as Catalyst. *J CHEM SOC DALTON TRANS* **5** (1987).
44. Neri, G. *et al.* Photochemical CO₂ reduction in water using a co-immobilised nickel catalyst and a visible light sensitiser. *Chem. Commun.* **52**, 14200–14203 (2016).
45. Wu, P. *et al.* Photoactive Metal–Organic Framework and Its Film for Light-Driven Hydrogen Production and Carbon Dioxide Reduction. *Inorg. Chem.* **55**, 8153–8159 (2016).
46. Baskin, J. S., Yu, H.-Z. & Zewail, A. H. Ultrafast Dynamics of Porphyrins in the Condensed Phase: I. Free Base Tetraphenylporphyrin. *J. Phys. Chem. A* **106**, 9837–9844 (2002).
47. Yu, H.-Z., Baskin, J. S. & Zewail, A. H. Ultrafast Dynamics of Porphyrins in the Condensed Phase: II. Zinc Tetraphenylporphyrin. *J. Phys. Chem. A* **106**, 9845–9854 (2002).
48. Rao, H., Schmidt, L. C., Bonin, J. & Robert, M. Visible-light-driven methane formation from CO₂ with a molecular iron catalyst. *Nature* **548**, 74–77 (2017).
49. Qin, H. *et al.* Cobalt porphyrins supported on carbon nanotubes as model catalysts of metal-N₄/C sites for oxygen electrocatalysis. *J. Energy Chem.* **53**, 77–81 (2021).
50. Mo, L.-Q., Huang, X.-F., Huang, G., Yuan, G.-P. & Wei, S.-J. Highly Active Catalysis of Cobalt Tetrakis(pentafluorophenyl)porphyrin Promoted by Chitosan for Cyclohexane Oxidation in Response-Surface-Methodology-Optimized Reaction Conditions. *ChemistryOpen* **8**, 104–113 (2019).
51. Ushimaru, R., Nishimura, T., Iwatsuki, T. & Naka, H. A Fluorinated Cobalt(III) Porphyrin Complex for Hydroalkoxylation of Alkynes. *Chem. Pharm. Bull. (Tokyo)* **65**, 1000–1003 (2017).
52. I. Gumerova, N. & Rompel, A. Polyoxometalates in solution: speciation under spotlight. *Chem. Soc. Rev.* **49**, 7568–7601 (2020).
53. Froehlich, J. D. & Kubiak, C. P. The Homogeneous Reduction of CO₂ by [Ni(cyclam)]⁺: Increased Catalytic Rates with the Addition of a CO Scavenger. *J. Am. Chem. Soc.* **137**, 3565–3573 (2015).
54. Bourrez, M., Molton, F., Chardon-Noblat, S. & Deronzier, A. [Mn(bipyridyl)(CO)₃Br]: An Abundant Metal Carbonyl Complex as Efficient Electrocatalyst for CO₂ Reduction. *Angew. Chem. Int. Ed.* **50**, 9903–9906 (2011).

9. Appendix

Table A3.1: Comparative table of CO₂ photoreduction with pure MOF composites.

Material	Wave length (nm)	Reaction medium	HCOOH production ($\mu\text{mol g}^{-1} \text{h}^{-1}$)	Ref.
NanoMOF-545(Fe)	>415	CH ₃ CN/TEOA (10/1)	1160	This work
PCN-222	420-800	CH ₃ CN/TEOA (10/1)	60	Zhang, Liang and coll. <i>J. Am. Chem. Soc.</i> 2015 , 137, 13440
PCN-224	420-800	Ethyleneglycol 20 mM	45.2	Jin <i>New. J. Chem.</i> 2020 , 44, 15362
PCN-222	420-800	Ethyleneglycol 20 mM	10.2	Jin <i>New. J. Chem.</i> 2020 , 44, 15362
PCN-222(Zn)	420-800	Ethyleneglycol 20 mM	120.2	Jin <i>New. J. Chem.</i> 2020 , 44, 15362
PCN-224	>400	CH ₃ CN/TEOA (4/1)	25	Zhang and coll. <i>Applied. Catal. B: Environmental</i> 2018 , 231, 173
PCN-136	>420	CH ₃ CN/H ₂ O/TIPA ¹ (40/5/5)	45	Lan, Alsalmeh, Zhou and coll. <i>J. Am. Chem. Soc.</i> 2019 , 141, 2054
Rh-PMOF-1	>400	CH ₃ CN/TEOA (4/1)	74	Zhang and coll. <i>Applied. Catal. B: Environmental</i> 2018 , 231, 173
NH₂-UiO-66	420-800	CH ₃ CN/TEOA (5/1)	26.4	Li and coll., <i>Chem. Eur. J.</i> 2013 , 19, 14279
NNU-28	420-800	CH ₃ CN/TEOA (30/1)	52.8	Xing, Zu and coll., <i>J. Mat. Chem. A</i> 2016 , 4, 2657
Cp*Rh@UiO-67 + Ru(bpy)₃	415-800	CH ₃ CN/TEOA (5/1)	464 ²	Fontecave and coll. <i>ChemSusChem.</i> 2015 , 8, 603
UiO-66-CrCAT	420-800	CH ₃ CN/TEOA (4/1), BNAH	1724	Kang, Cohen and coll. <i>Chem. Commun.</i> 2015 , 51, 16549
NH₂-UiO-66(Zr/Ti)	420-800	CH ₃ CN/TEOA (4/1), BNAH	1052	Kang, Cohen and coll. <i>Chem. Commun.</i> 2015 , 51, 5735
NH₂-MIL-125(Ti)	420-800	CH ₃ CN/TEOA (5/1)	16.28	Li and coll. <i>Angew. Chem. Int. Ed.</i> 2012 , 51, 3364
MIL-101(Fe)	420-800	CH ₃ CN/TEOA (5/1)	147.5	Li and coll. <i>ACS Catal.</i> 2014 , 4, 4254

Scheme A3.1: Proposed pathway and transient intermediates involved in the formal hydride-transfer process from TEOA[•] to CO₂.

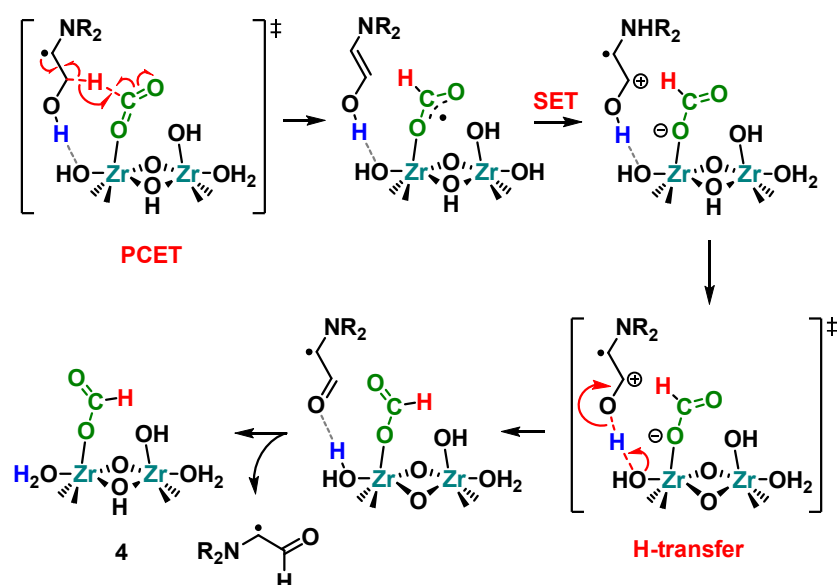


Table A3.2: Photocatalytic reduction of CO₂ with POM@MOF composites. 4h irradiation, 280W Xe, $\lambda > 415$ nm, 2 mg of catalyst in 2 mL of CH₃CN/TEOA (10:1), 20°C.

Catalyst	Loading (POM/Zr ₆)	$\mu\text{mol} \cdot \text{g}^{-1} \cdot \text{h}^{-1}$	$\mu\text{mol} \cdot \text{g}^{-1}_{\text{MOF}} \cdot \text{h}^{-1}$	TON
MOF-545	-	159	159	1.53
MOF-545(Fe)	-	566	566	5.84
Co ₄ @MOF-545	0.2	200	282	2.73
Ni ₄ @MOF-545	0.2	268	378	3.66
PW ₁₀ Ti ₂ @545	0.3	209	275	2.67
SiW ₁₂ @545	0.8	218	423	4.09

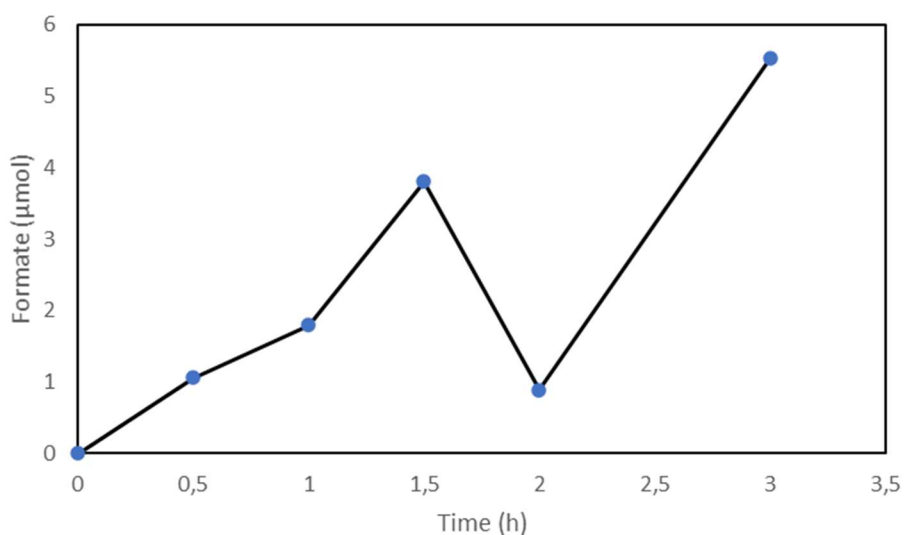


Figure A3.1: Formate production over time with NanoMOF-545(Fe), 280W Xe, CH₃CN/TEOA (10:1), 2 mg of catalyst. Results are before formate desorption protocol.

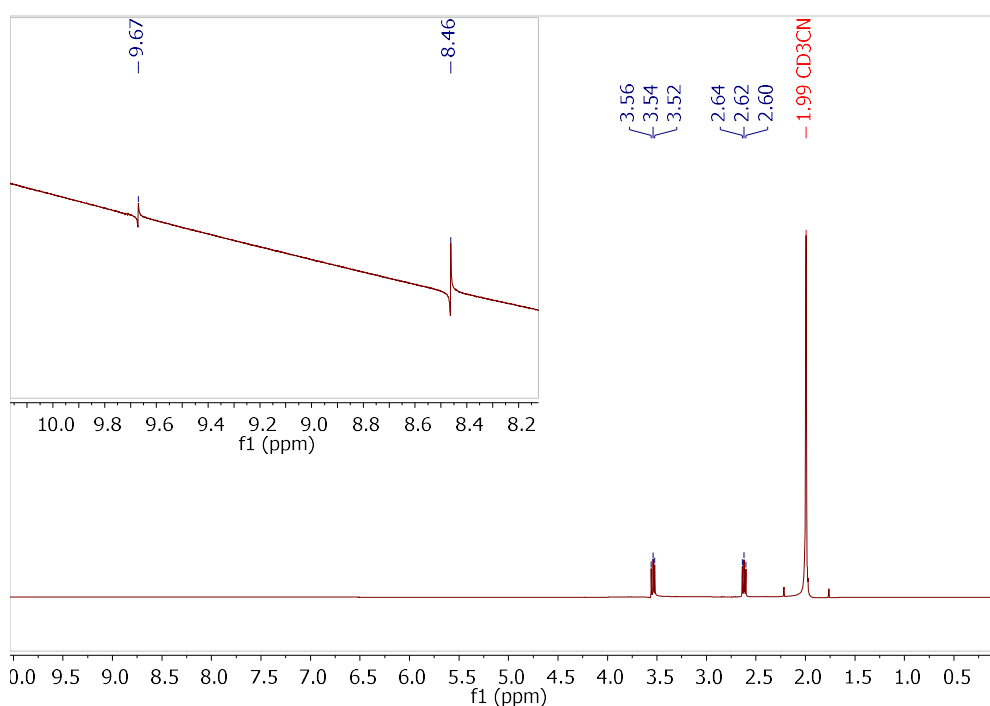


Figure A3.2: ¹H NMR spectrum of the reaction mixture after the catalysis. The triplets at 2.62 and 3.54 ppm are assigned to the alkyl protons in TEOA; whereas smaller peaks at 8.46 and 9.67 ppm are assigned to the C-bound proton of formic acid and the proton of the aldehyde function in the oxidized form of TEOA respectively.

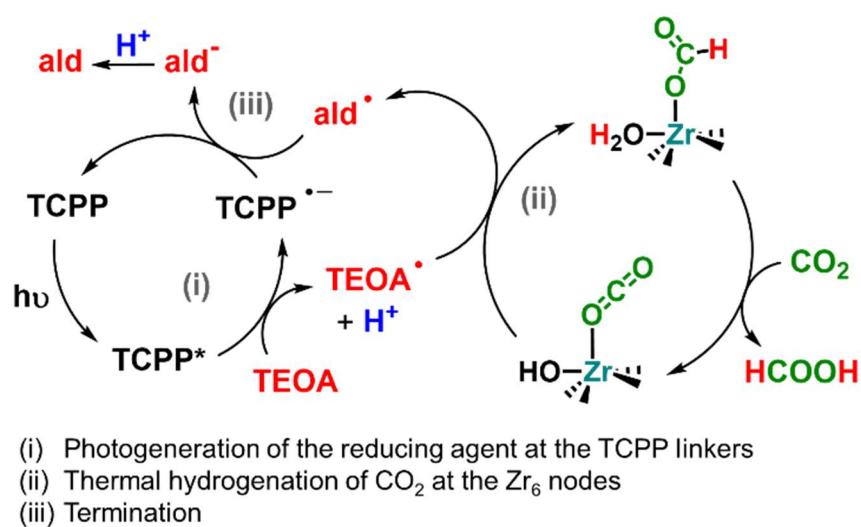


Figure A3.3. Schematic summary of the proposed reaction mechanism for the photocatalytic reduction of CO₂ to formic acid with TEOA promoted by Zr-based porphyrinic MOFs.

Chapter 4: P₄Mo₆-based polyoxometalates for CO₂ heterogeneous photoreduction

In this chapter, we will focus on POMs for the CO₂ reduction in heterogeneous conditions. Noticeably, although numerous studies have revealed their potentialities as catalysts for water splitting,^{1–3} there have been only few reports on POMs for CO₂RR.⁴ However, besides rare examples of transition metal (M)-substituted polyoxotungstates^{5–7} as seen in Chapter 2, reduced polyoxomolybdates (i.e. containing Mo^V ions) emerged in 2019 as promising candidates. Illustratively, {ε-Mo^V₁₂Mo^{VI}₄O₅₂} reduces CO₂ into formaldehyde under UV-light in homogeneous conditions in water⁸ and the related {ε-PMo^V₈Mo^{VI}₄Zn₄O₅₂}, as the building unit of a POM-based Metal-Organic Framework (POMOF) NNU-29, selectively reduces CO₂ into formate in heterogeneous conditions under visible light in water, with [Ru(bpy)₃]²⁺ as a photosensitizer.⁹ Another family of solids made of reduced POM building units have been recently evidenced as heterogeneous photocatalysts for CO₂RR; these solids made of {P₄Mo^V₆} POM units connected by Mn^{II} or Co^{II} ions can reduce CO₂ into CO and CH₄ in the presence of [Ru(bpy)₃]²⁺.^{10–12}

1. Polyoxometalates for CO₂ photoreduction

P₄Mo₆ oxoclusters were first described in 1989 by Haushalter *et al.*¹³ who report a structure containing [Mo₆P₄O₂₄(OH)₇]⁵⁻ anionic clusters. In this anion, three {Mo^V₂O₄} dimeric units are connected by edges around a central phosphate group (**Figure 4.1**). Three peripheral phosphate groups complete the molecular structure. The Mo(V) ions form short Mo-Mo bonds (~2.6 Å) within the dimeric unit. The central and the three peripheral phosphate groups lie in the same side of the plane defined by the six Mo ions. The P₄Mo₆ subunits are linked together by bridging Na⁺ cations forming 1D strings. In the following decade several groups have reported a variety of related structures with different transition metals (Zn^{II}, Fe^{II/III}, Co^{II}, Mn^{II}) as bridging cations for the P₄Mo₆ subunits.^{14–1}

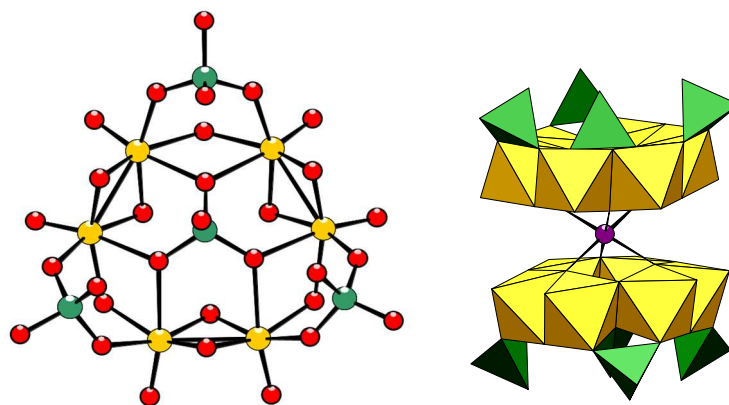


Figure 4.1: Ball and stick representation of the $[(\text{Mo}_2\text{O}_4)_3(\text{HPO}_4)_x(\text{PO}_4)_{4-x}(\text{OH})_3]^{(9-x)-}$ (P_4Mo_6) anion (left) Polyhedral representation of the sandwich-type structure formed by the connection of two P_4Mo_6 anions (right)

The hydrothermal synthesis of insoluble solids with P_4Mo_6 polyoxometalates units connected to transition metal ions has been previously studied in our group by a former PhD student, Charlotte du Peloux. In 2004 our group thus reported the partial substitution of the bridging metal cations in order to give bi-metallic P_4Mo_6 derivatives.¹⁸ Six out of ten manganese atoms in the $\text{Na}_{15}\text{Mn}_{10}[(\text{Mo}_2\text{O}_4)_3(\text{HPO}_4)(\text{PO}_4)_3(\text{OH})_3]_4(\text{PO}_4) \cdot 48\text{H}_2\text{O}$ solid were replaced by Fe ions. To date, this composite had only been studied for its magnetic properties. In fact, reducing CO₂ was not a concerning topic at that time.

The first report of P_4Mo_6 -based material active for CO₂ reduction was published fifteen years later. Xie et al.¹¹ reported the reduction of CO₂ into CH₄ in water by two new compounds: NENU-605 and NENU-606. NENU-605 is a purely inorganic material with four P_4Mo_6 polyoxometalate subunits connected to 10 manganese metal centers, while NENU-606 is a bi-metallic POM-based material containing 7.5 Mn and 2.5 Co centers every four P_4Mo_6 units.

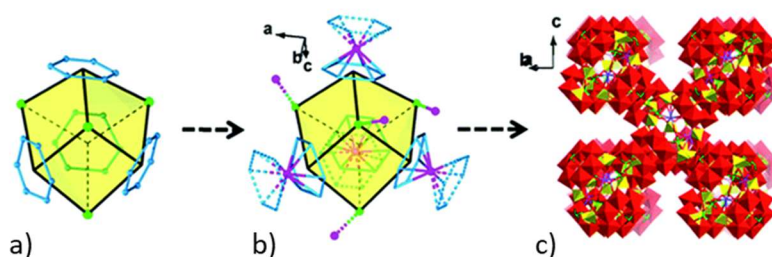


Figure 4.2: a) Simplified cluster constitutive of NENU-605, with Mn in green dots and Mo₆ rings in blue; b) surrounding environment of the simplified cluster, with outer Mn in purple; c) 3D Structure of NENU-605.¹¹

The authors compare the activity of both systems in water in presence of $[Ru(bpy)_3]Cl_2$ as an external photosensitizer and TEOA as a sacrificial electron donor. Both composites are able to reduce CO_2 , leading to methane as a major product and a selectivity approaching 80% for CH_4 over CO (**Figure 4.3**). The presence of Co in NENU-606 increases the overall activity going from 160 to 350 nmol of CH_4 after 20h. A plateau around 20h can be observed for the two POMs. A classic mechanism where the $Ru(bpy)_3$ acts as a photosensitizer and the POM as a catalyst has been proposed but without any supporting DFT calculations.

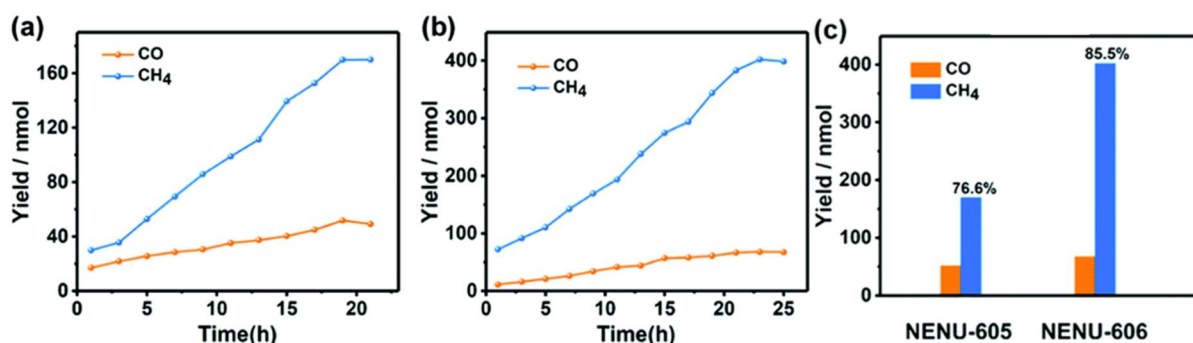


Figure 4.3: Amounts of CH_4 and CO produced as a function of the time of visible-light irradiation using (a) NENU-605 and (b) NENU-606; (c) total product yield and the selectivity of gaseous products in the photocatalytic CO_2RR .¹¹

Few months later, Du et al.¹⁰ compared the activity for CO_2 reduction of three POM-based materials: $Na\{P_4Mo_6\}_2$ and two homologues $Co\{P_4Mo_6\}_2(bib)$ and $Co\{P_4Mo_6\}_2(tib)$ ($bib = 1,4$ -bis(1-H-imidazol-4-yl)benzene and $tib = 1,3,5$ -tris(1-imidazolyl)benzene, both being used as structuring agents) where the Na^+ bridging cations have been substituted by cobalt cations. They have confirmed the beneficial effect of the cobalt ions in the P_4Mo_6 -based materials, both Co containing composites being active for CO_2 photoreduction while their Na equivalent showed no activity. Their hypothesis for the difference in activity is that the cobalt containing solids have a conducting band higher in energy than that of $Ru(bpy)_3$ (**Figure 4.4 a**). It thus allows a photoinduced electron transfer from $Co\{P_4Mo_6\}_2$ to $Ru(bpy)_3$ where the ruthenium may then act as a catalyst for CO_2 reduction. In addition, the photoinduced hole in the POM-based material can react with the sacrificial electron donor (TEOA) and inhibit the recombination of photoinduced electron/hole pairs in $Ru(bpy)_3$. In contrast, the conducting band of $Na\{P_4Mo_6\}_2$ being lower than the conducting band of $Ru(bpy)_3$, the electron transfer operates from $Ru(bpy)_3$ to the POM, which is in turn unable to reduce CO_2 (**Figure 4.4 b**). To summarize, the cobalt-based composites act as a photosensitizer reducing $Ru(bpy)_3$ that is the actual catalyst, while in

the absence of cobalt the $\text{Ru}(\text{bpy})_3$ complex is the photosensitizer while $\text{Na}\{\text{P}_4\text{Mo}_6\}_2$ is unable to reduce CO_2 making the $\text{Ru}(\text{bpy})/\text{Na}\{\text{P}_4\text{Mo}_6\}$ system inactive.

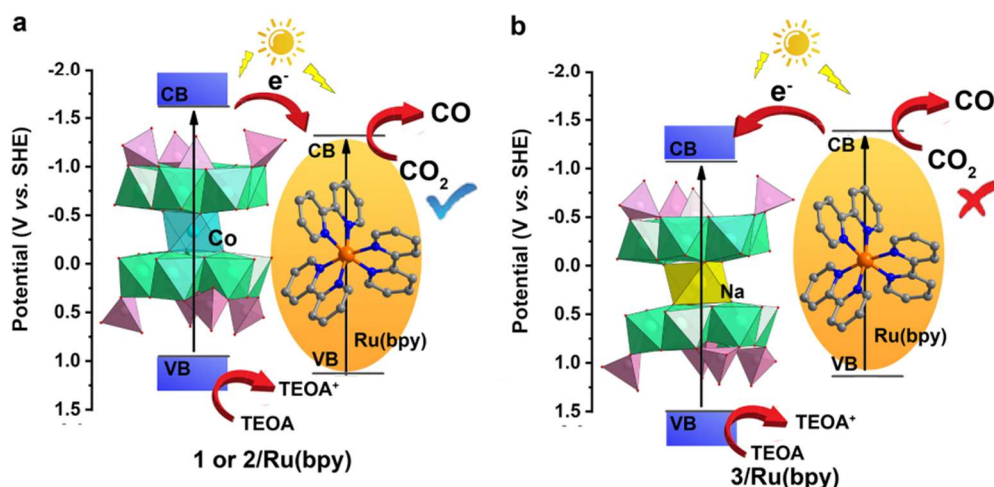


Figure 4.4: Proposed mechanism for CO_2 photoreduction by $\text{Co}\{\text{P}_4\text{Mo}_6\}_2$ (a) and $\text{Na}\{\text{P}_4\text{Mo}_6\}_2$ (b).¹⁰

Furthermore, the use of organic molecules as counter cations and shaping agents has been previously described for polyoxometalates-related composites (i.e. crown ether complexes, organometallic salts).^{19,20} Considering the photocatalytic CO_2 reduction reaction, it is potentially interesting to use $[\text{Ru}(\text{bpy})_3]^{2+}$ as a counterion whereby it could play the role not only of a photosensitizer but also of a catalyst, as pointed by Du et al. with their $\text{Co}\{\text{P}_4\text{Mo}_6\}$ system and in other studies.^{21,10,22} This strategy has been in particular explored for POMOFs exhibiting catalytic properties for proton reduction.²³ Another example is the transformation of the cesium salt of the $[\text{Co}_9(\text{H}_2\text{O})_6(\text{OH})_3(\text{HPO}_4)_2(\text{PW}_9\text{O}_{34})_3]^{16-}$ POM into the corresponding $[\text{Ru}(\text{bpy})_3]^{2+}$ salt. This compound was studied as a heterogeneous photocatalyst for water oxidation and showed improved performances when compared to those of the cesium salt, the authors proposing that the formation of the photosensitizer/catalyst pair in the solid state is beneficial for the electron transfer event and for the long-term stability of the photosensitizer.²⁴

Our objective was thus to synthesize new P_4Mo_6 -based materials with a varying range of bridging cations in order to try to rationalize the effect of the metal center for the CO_2 reduction. Moreover, we used $[\text{Ru}(\text{bpy})_3]^{2+}$ and $[\text{Ni}(\text{cyclam})]^{2+}$, small active cations for CO_2 photoreduction,^{25,26} as counterions with the aim to increase the overall activity. The synthesis protocols and the characterization of the new crystalline solids will be presented in the following section, then we will focus on the photocatalytic activity of the synthesized systems before finally focusing on the mechanism for CO_2 reduction with P_4Mo_6 based POMs.

2. Synthesis and characterization

2.1 Synthesis

Hydrothermal synthesis is the method of choice for the preparation of heterometallic molybdenum(V) phosphates. Indeed, these conditions are necessary to promote the reduction of Mo(VI) by metallic Mo to form the {Mo^V₂O₄} dinuclear fragments. Phosphate ions are added in excess. An acidic pH, between 2 and 4, is also crucial to promote the formation of the molybdenum(V) phosphates. A mixture of Na₂MoO₄, Mo, concentrated H₃PO₄ and metallic salts (Fe(II), Co(II), Ni(II) or Mn(II)) in aqueous solution is thus heated at 180°C for 70 h. In addition, [Ru(bpy)₃]²⁺ (noted Ru(bpy)) and [Ni(cyclam)]²⁺ (noted Ni(cyclam)) have been introduced in the reaction medium to play the role of counterions. Finally, iminodiacetic acid [HN(CH₂COO)₂]²⁻ has been added in some syntheses to improve the crystallization process, following previous observations.^{27,28} We modulated the metal salt and the amount of salt used as described in **Table 4.1**.

Table 4.1: Synthesis protocol of Ru(bpy)-Mn, Fe-Mn, Ru(bpy)-Co and Ni(cyclam)-Mn.

Reactants	Ru(bpy)-Mn	Fe-Mn	Ru(bpy)-Co	Ni(cyclam)-Mn
Mo	30 mg	30 mg	30 mg	30 mg
Na ₂ MoO ₄	470 mg	470 mg	235 mg	470 mg
H ₃ PO ₄ (85%)	290 µL	530µL (8M)	73 µL	290 µL
Fe(SO ₄) ₂ (NH ₄) ₂ .6H ₂ O		280 mg		
CoCl ₂ .6H ₂ O			420 mg	
NiCl ₂ .6H ₂ O	148 mg			
MnCl ₂ .4H ₂ O	119 mg	58 mg		119 mg
Iminodiacetic acid	100 mg	100 mg		100 mg
Ni(cyclam)Cl ₂				50 mg
Ru(bpy) ₃ Cl ₂	100 mg		200 mg	
H ₂ O	4 mL	4 mL	4 mL	4 mL
pHi	2.5	2.5	2	4

We tried over 60 different combinations of metals/counterions, many of them did not lead to any crystal formation. We mainly focused on Mn, Co, Fe and Ni as bridging metals for the POMs. Out of the 60 conditions screened less than 20 yielded crystals (**Table 4.2**), but only four of them gave reproducible synthesis with homogeneous crystals suitable for single crystal diffraction.

Those four crystals are labeled **Ru(bpy)-Mn**, **Fe-Mn**, **Ru(bpy)-Co** and **Ni(cyclam)-Mn** (highlighted in light orange in **Table 4.2**) will be the main focus of this chapter, their synthesis is described in **Table 4.1**. The four composite formula, obtained from combining monocrystal XRD and TGA, are the following:

- Ru(bpy)-Co: $[\text{Ru}(\text{bpy})_3]_2\text{Co}^{\text{II}}_5[\text{P}_4\text{Mo}_6\text{O}_{26}(\text{OH})_5]_2 \cdot 22\text{H}_2\text{O}$
- Ru(bpy)-Mn: $\text{Na}_2[\text{Ru}(\text{bpy})_3]_2\text{Mn}^{\text{II}}_3[\text{P}_4\text{Mo}_6\text{O}_{25}(\text{OH})_6]_2 \cdot 20\text{H}_2\text{O}$
- Fe-Mn: $\text{Na}_7\text{Mn}^{\text{II}}_2\text{Fe}^{\text{II}}_4\text{Fe}^{\text{III}}_4[\text{P}_4\text{Mo}_6\text{O}_{26}(\text{OH})_5]_4(\text{PO}_4) \cdot 52\text{H}_2\text{O}$
- Ni(cyclam)-Mn: $\text{Na}_2[\text{Ni}(\text{cyclam})]_3\text{Mn}^{\text{II}}_2[\text{P}_4\text{Mo}_6\text{O}_{25}(\text{OH})_6]_2 \cdot 12\text{H}_2\text{O}$

In parallel, despite several attempts, we never managed to synthesize NENU-605 and NENU-606 in order to compare their photocatalytic activity to those of our systems in the same conditions. Detailed synthesis conditions can be found in the experimental section.

Table 4.2: Crystals obtained by solvothermal synthesis, expected and final composition.

Label	Expected composition	Found composition	Comment	Photoactivity
1-D	MnCoRu(bpy) ₃	-	Not homogeneous	-
1-E	MnFeRu(bpy) ₃	MnRu / MnFe	Two kinds of crystals	No
1-F	MnFeRu(bpy) ₃ with more Mn	MnFeRu(bpy) ₃ / MnRu(bpy) ₃	Not reproducible	Yes
1-G	MnCoRu	MnCoRu	-	No
1-H	FeCoRu(bpy) ₃	FeCoRu(bpy) ₃	Low Fe	No
1-J	MnNiRu(bpy) ₃	MnRu(bpy) ₃	No Ni	Yes
2-B	MnCoRu(bpy) ₃	MnCoRu(bpy) ₃	-	No
2-C	NiRu(bpy) ₃	Ni ₇ Ru ₃	Not P ₄ Mo ₆	-
2-E	NiFeRu(bpy) ₃	NiFeRu(bpy) ₃	Varying amount of Ni and Fe	Yes
2-F	NiRu(bpy) ₃	P ₄ Mo ₃ Ni ₂	No Ru(bpy) ₃ as counterion	-
3-A	Mn ₄ Fe ₆	MnFe	More Fe than Mn	Yes
3-C	(Mn(Ni)Ru(bpy) ₃)	-	Not P ₄ Mo ₆ , no Ru(bpy) ₃	-
3-D	NiRu(bpy) ₃	NiRu(bpy) ₃	Few Ru, not P ₄ Mo ₆	-
3-G	MnCoRu(bpy) ₃	CoRu(bpy) ₃	No Mn in the crystals	No
4-E	MnNiNi(cyclam)	MnNi ₂ Ni(Cyclam)	Two types of crystals	-
5-E	MnNi(cyclam)	MnNi(cyclam)	-	No

2.2 Structure description

The four structures contain the $[(\text{Mo}_2\text{O}_4)_3(\text{HPO}_4)_x(\text{PO}_4)_{4-x}(\text{OH})_3]^{(9-x)-}$ ($x = 2-3$) (P₄Mo₆) anion. In all four structures, as almost exclusively observed with heterometallic molybdenum(V) phosphates containing P₄Mo₆ anions, the P₄Mo₆ units are connected in pairs by a metallic ion (Co(II) or Mn(II)) in octahedral coordination, forming a sandwich-type, sometimes called “hour-glass”, structure (**Figure 4.5**).

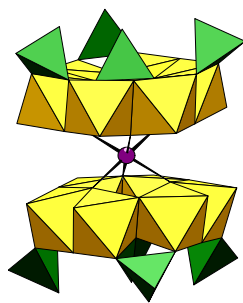


Figure 4.5: Polyhedral representation of the sandwich-type structure formed by the connection of two P_4Mo_6 anions by a $Co(II)$ or $Mn(II)$ ion in octahedral coordination.

In the structure of **Ru(bpy)-Co**, two P_4Mo_6 anions are sandwiched by a $Co(II)$ ion (Co1). These sandwich-type POMs are connected to each other by dimers of $Co(II)$ ions and form a 1D chain (**Figure 4.6 a**). Co2 and Co3 adopt a distorted octahedral coordination, being connected to three oxygen atoms of phosphate ions, two terminal water ligands and one bridging water molecule (**Figure A4.1 a** in Appendix). The Co2-Co3 distance is quite short (2.91 Å) within a $Co(II)$ dimer. The anionic charge of the chains is compensated by neighboring $[Ru(bpy)_3]^{2+}$ counterions (**Figures 4.6 b** and **c**).

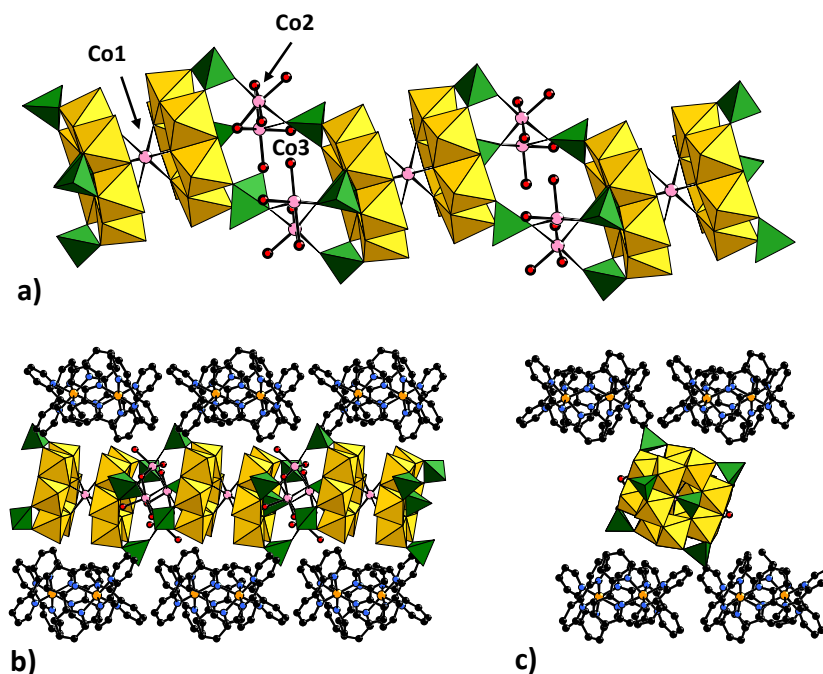


Figure 4.6: a) View of the chain formed by the connection of $Co(P_4Mo_6)_2$ sandwich-type POMs by $Co(II)$ ions in the structure of **Ru(bpy)-Co**; b) side view and c) top view of the chain surrounded by $[Ru(bpy)_3]^{2+}$ cations.

The structure of **Ru(bpy)-Mn** has similarities with that of **Ru(bpy)-Co**, with Mn(II) ions replacing Co(II) ions. However, the two compounds are not isostructural and present some differences. In **Ru(bpy)-Mn**, there are two independent P₄Mo₆ units with two independent Mn(II) ions (Mn1 and Mn4) connecting them (**Figure 4.7 a**). These Mn(P₄Mo₆) sandwich-type ions stack into chains like Co(P₄Mo₆)₂ analogues in **Ru(bpy)-Co** but while these entities are parallel in **Ru(bpy)-Co**, the chain adopts a zig-zag shape in **Ru(bpy)-Mn** with tilted anionic units. Furthermore, the POMs are connected by four Co(II) ions in **Ru(bpy)-Co** but there are only two Mn(II) ions linking the anionic entities in **Ru(bpy)-Mn**. Mn2 and Mn3 are in a pseudo-octahedral coordination environment, being connected to three terminal water ligands and to three oxygen atoms of phosphate ions (**Figure A4.1 b**). Contrarily to what is observed in the structure of the Co analogue, the two Mn ions are not directly connected via an oxygen atom of a bridging water molecule but are separated by a sodium ion. The chains are surrounded by [Ru(bpy)₃]²⁺ counterions (**Figures 4.7 b and c**).

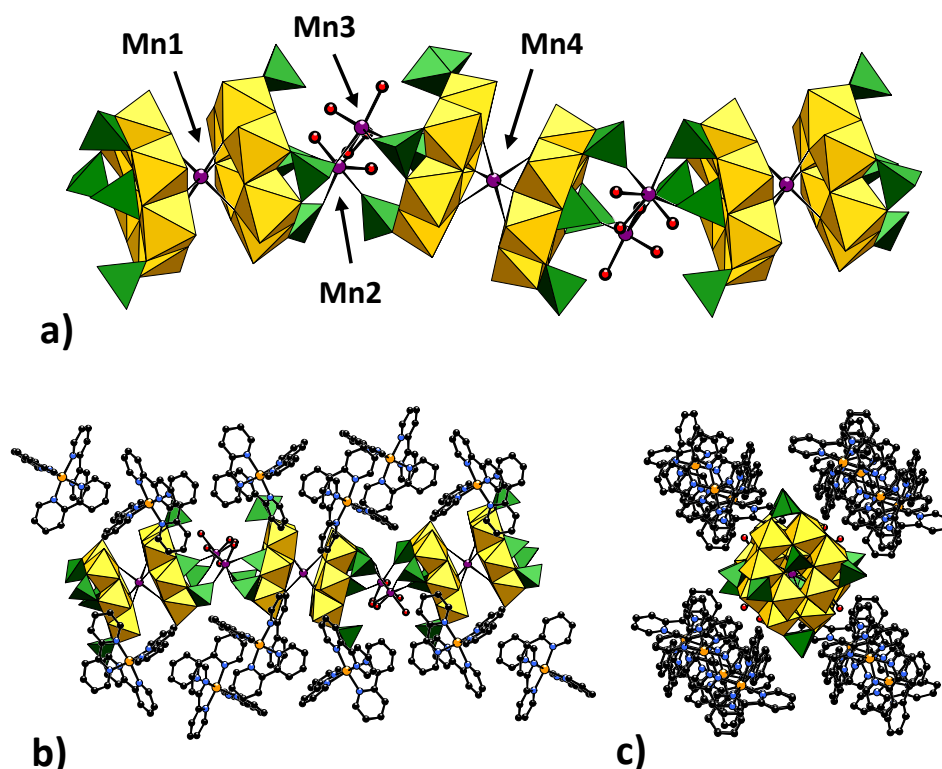


Figure 4.7: a) View of the chain formed by the connection of Mn(P₄Mo₆) sandwich-type POMs by Mn(II) ions in the structure of **Ru(bpy)-Mn**, b) side view and c) top view of the chain surrounded by [Ru(bpy)₃]²⁺ cations.

In the structure of **Ni(cyclam)-Mn**, there is only one crystallographically independent P₄Mo₆ unit which forms a sandwich with one independent Mn(II) ion (Mn1). The sandwich-type anionic entities are parallel to each other and are linked to each other by only one extra Mn(II) ion (Mn2), forming a straight chain (**Figure 4.8 a**). Mn2 is bound to four phosphate ions and to two water ligands (**Figure A4.1 c**). These two water molecules are linked to two sodium ions which thus also ensure the connection of the POMs within the chain. Each P₄Mo₆ unit is weakly connected to two [Ni(cyclam)]²⁺ complexes via long Ni-O bonds (Ni1-O7 = 2.894(3) Å, Ni2-O8 = 2.839(3) Å) between the Ni(II) ions and a terminal oxygen atom of a MoO₆ octahedron of the POM (**Figure 4.8 b**). The connection of the Ni complexes and the POMs thus generate a supramolecular structure (**Figure 4.8 c**).

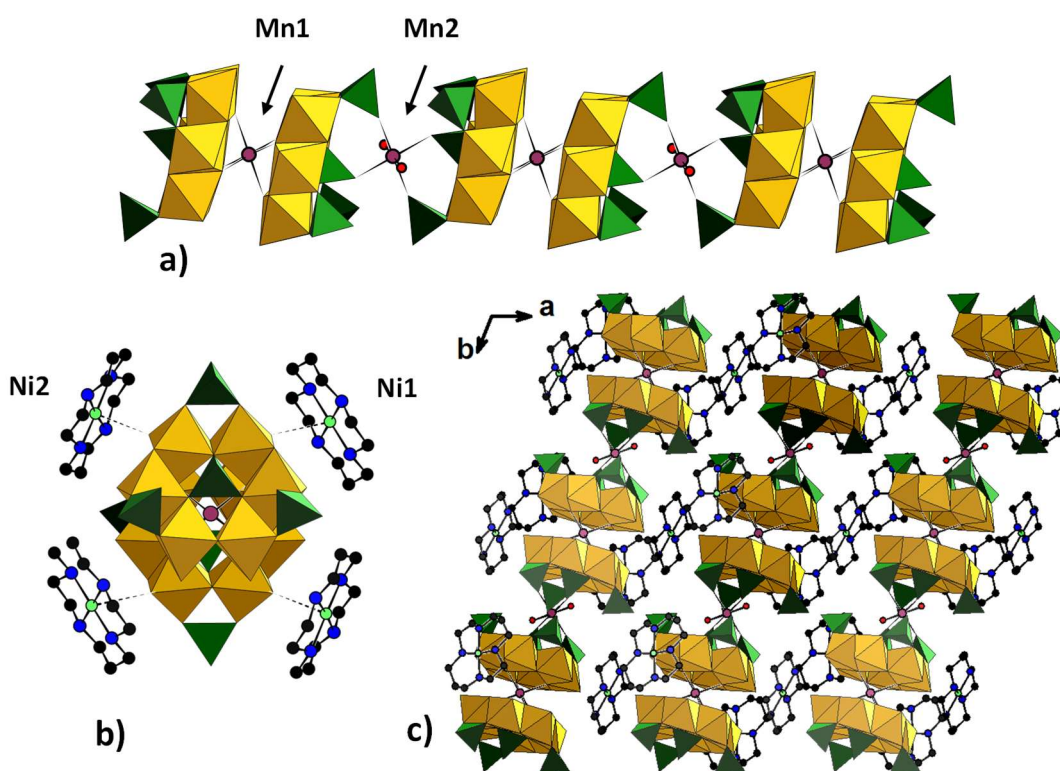


Figure 4.8: a) View of the chain formed by the connection of Mn(P₄Mo₆)₂ sandwich-type POMs by Mn(II) ions in the **Ni(cyclam)-Mn** crystal structure ; b) view of one sandwich-type POM surrounded by four Ni(II) complexes and c) view along the *c* axis of the supramolecular structure formed by the connection of the POMs and the [Ni(cyclam)]²⁺ cations.

Finally, **Fe-Mn** does not contain additional transition metal complexes as counterions as it is the case for the three other structures reported herein. It is thus a fully inorganic structure with P₄Mo₆ units linked by Fe and Mn metal ions. Its structure is reminiscent of that of the previously reported molybdenum(V) phosphates Na₁₅Mn₁₀[(Mo₂O₄)₃(HPO₄)(PO₄)₃(OH)₃]₄(PO₄)₂₈,

Na₇Mn₄Fe₆[(Mo₂O₄)₃(HPO₄)₂(PO₄)₂(OH)₃]₄(PO₄),²⁷ NENU-605¹¹ and NENU-606,¹¹ which all crystallize in the tetragonal *I*4₁/*acd* space group and contain Mn(P₄Mo₆)₂ sandwich-type units. One additional common feature of these structures is the presence of an extra phosphate ion which does not belong to a P₄Mo₆ unit. The difference between them lies in the nature of the transition metal ions connecting these units. In **Fe-Mn**, the Mn(P₄Mo₆)₂ sandwich-type units are connected to each other and to the extra phosphate group via Fe(II) and Fe(III) ions (**Figure 4.9 a**). BVS calculations unambiguously allowed to determine that Fe1 is a Fe(III) ion while Fe2 is in the +II oxidation state, Fe1 and Fe2 being in octahedral environments. Fe1 is connected to six oxygen atoms of phosphate groups and Fe2 is bound to four oxygen atoms of phosphate groups and to two water molecules (**Figure A4.1 d**). The four oxygen atoms of the extra PO₄ group are bound to Fe1 ions. The Fe2 ions connect directly phosphate groups of P₄Mo₆ units. The connection of the POMs via these Fe-O(PO₃) bonds generates a compact 3D structure (**Figure 4.9 b and c**).

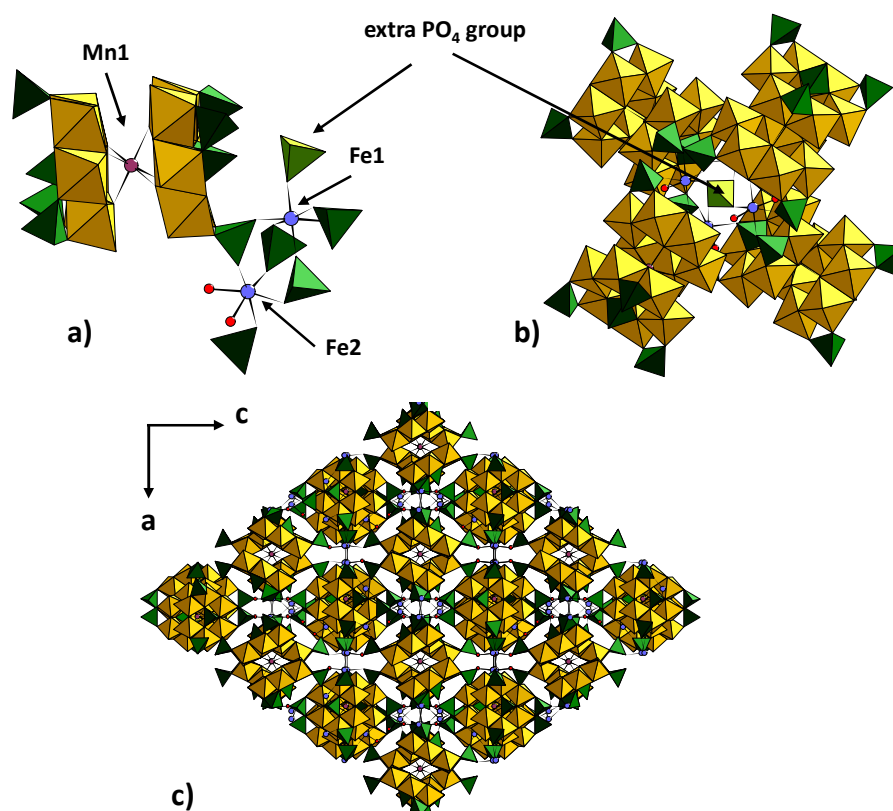


Figure 4.9: a) View of the structural unit in **Fe-Mn**, which consists in a Mn(P₄Mo₆)₂ sandwich-type anion, one Fe(III) ion (Fe1), one Fe(II) ion (Fe2) and one extra PO₄ group; b) view highlighting the extra PO₄ group bound to four Mn(P₄Mo₆)₂ sandwich-type anions via Fe-O(PO₃) bonds; c) view along the *b* axis of the 3D structure.

2.3 Characterization

All four compounds form dark red crystals, a common feature of structures containing {Mo^V₂O₄} units. The UV-vis spectra of the four compounds (**Figure 4.10**) exhibit two intense absorption bands with maxima around 240 and 300 nm attributed to Mo → Mo charge-transfer transitions (*vide infra*).²⁹ As expected, the UV-vis spectra of **Ru(bpy)-Co** and **Ru(bpy)-Mn** are very close and the broad band around 450 nm, not present in the other two compounds, can be attributed to MLCT transitions in the [Ru(bpy)₃]²⁺ complex.

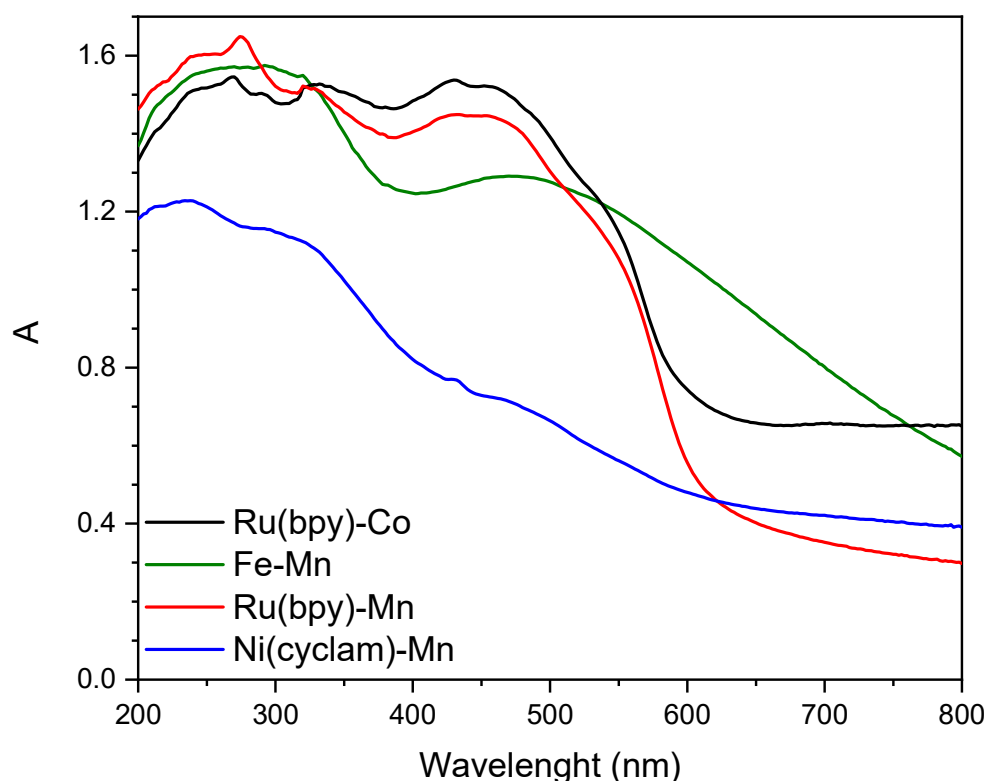


Figure 4.10: Solid-state UV-vis spectra of **Ru(bpy)-Co** (black), **Fe-Mn** (green), **Ru(bpy)-Mn** (red) and **Ni(cyclam)-Mn** (blue).

EDX analyses allow confirming the formula determined by single-crystal analysis for the three compounds (see experimental section). TGA analyses (**Figure 4.11**) indicate the number of crystallization water molecules and the comparison of the calculated and experimental mass of oxides formed at high temperature also confirm the proposed formula.

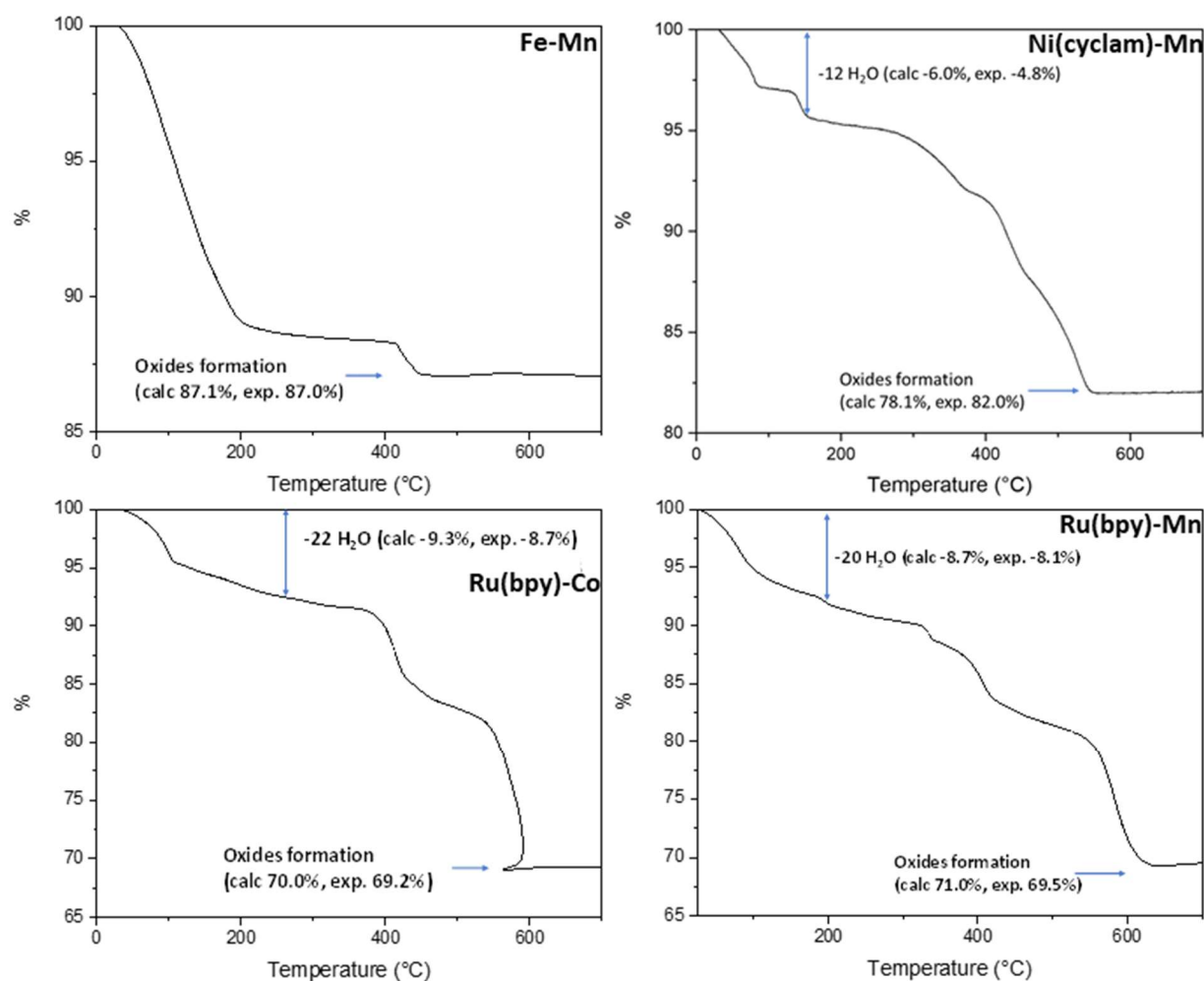


Figure 4.11: TGA curves of **Fe-Mn**, **Ni(cyclam)-Mn**, **Ru(bpy)-Co** and **Ru(bpy)-Mn** (air, heating rate 5°C/min).

The IR spectra of the four compounds (**Figure 4.12**) display strong similarities with P-O vibrations in the 1000-1150 cm⁻¹ region, Mo=O vibrations in the 900-1000 cm⁻¹ region and Mo-O vibrations below 800 cm⁻¹. The presence of [Ru(bpy)₃]²⁺ cations in **Ru(bpy)-Mn** and **Ru(bpy)-Co** is confirmed by the comparison of their IR spectra with that of [Ru(bpy)₃]Cl₂, showing the presence of characteristic bands attributed to ν_{C-N} and ν_{C-C} vibrations between 1350 and 1500 cm⁻¹.

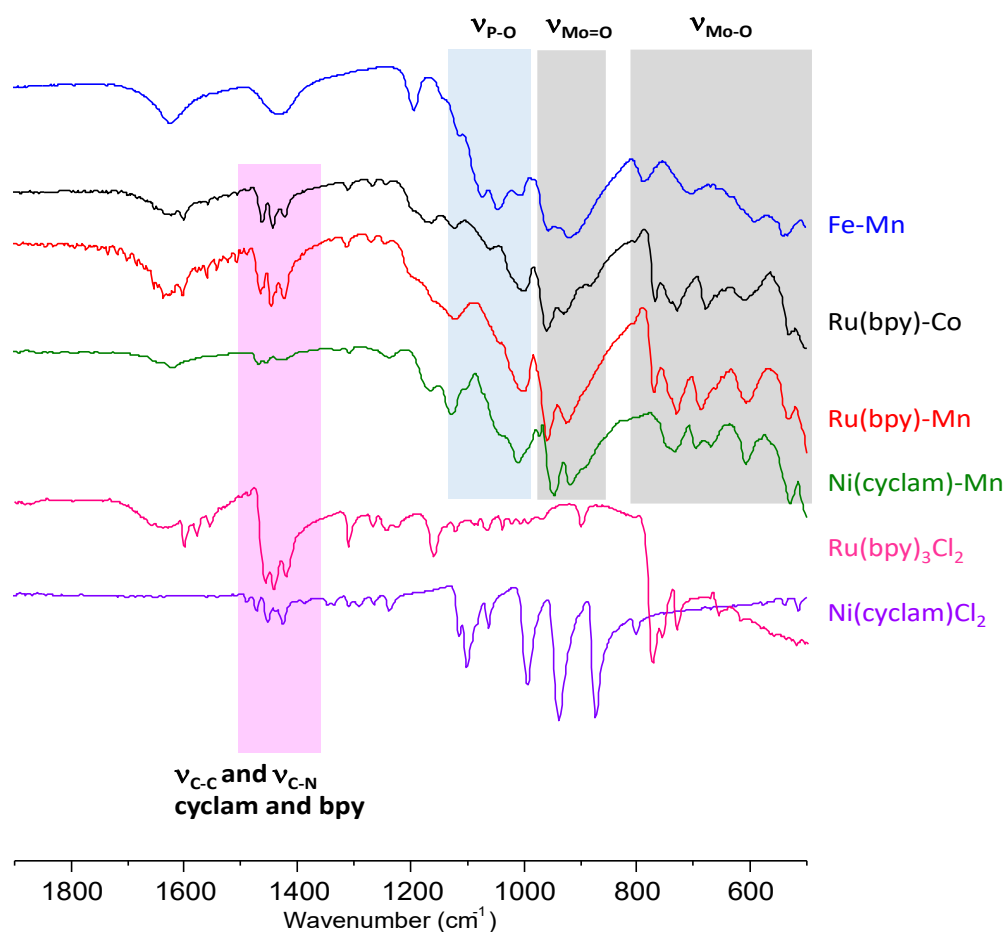


Figure 4.12: Infrared spectra of **Ru(bpy)-Co** (black), **Fe-Mn** (blue), **Ru(bpy)-Mn** (red), **Ni(cyclam)-Mn** (green), **Ni(cyclam)-Cl₂** (purple) and **[Ru(bpy)₃]Cl₂** used for the synthesis (pink).

The experimental X-ray powder patterns and of the powder pattern calculated from the structure solved from single-crystal X-ray diffraction data (**Figure 4.13**) are in accordance, showing no crystalline impurities mixed with the crystals after the several washing steps.

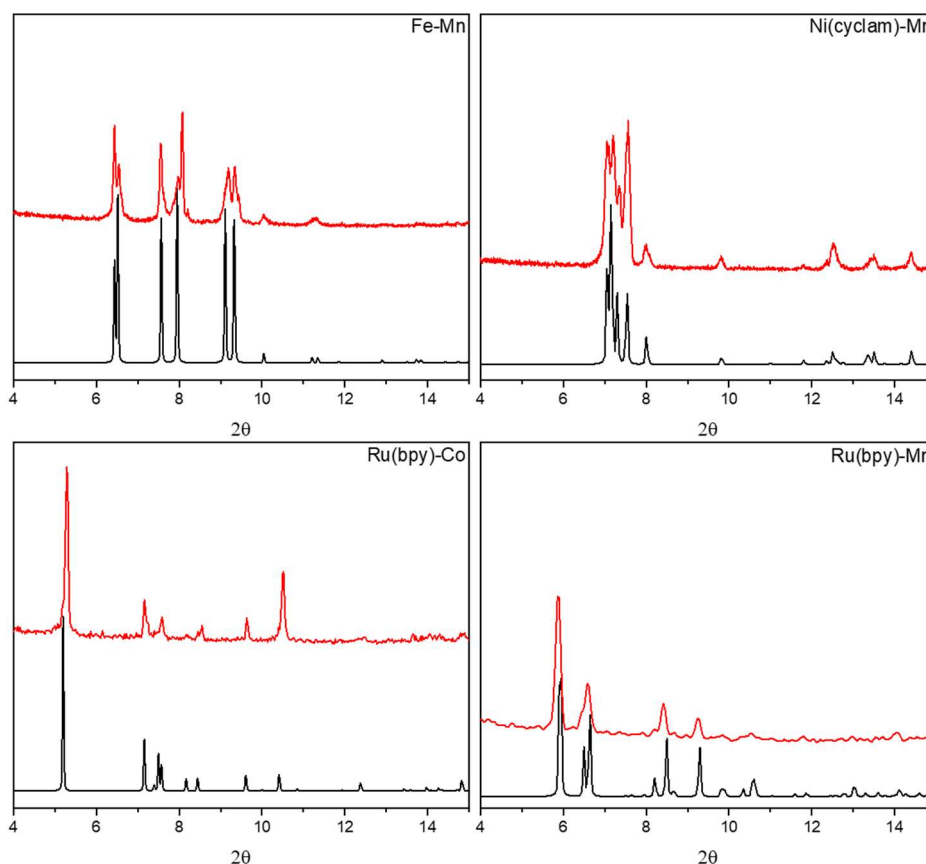


Figure 4.13: PXRD for **Ru(bpy)-Co**, **Ru(bpy)-Mn**, **Ni(cyclam)-Mn** and **Fe-Mn**, in red experimental data, in black simulated data.

3. Photocatalytic properties

The photocatalytic properties of the four compounds were studied in aqueous suspensions of ground crystals, with triethanolamine (TEOA) as an electron donor ($\text{H}_2\text{O}/\text{TEOA} = 14:1$). Despite the presence of $[\text{Ru}(\text{bpy})_3]^{2+}$ species in the framework of **Ru(bpy)-Co** and **Ru(bpy)-Mn**, neither the formation of gaseous products nor that of formate in the liquid phase was observed under visible light irradiation in absence of additional photosensitizer (PS). However, in presence of $[\text{Ru}(\text{bpy})_3]\text{Cl}_2$ dissolved in the catalytic medium, the formation of CO and CH₄ could be observed in the gas phase for **Ru(bpy)-Mn** and **Fe-Mn**, but not for **Ru(bpy)-Co** and **Ni(cyclam)-Mn**. For the two former compounds, CH₄ is the major product and its production increases almost linearly with the irradiation time (**Figure 4.14**). In contrast, the production of CO is much lower and stops after a few hours. The CH₄ production amounts to 48.0 nmol (i.e. $600 \text{ nmol} \cdot \text{g}^{-1} \cdot \text{h}^{-1}$) and 115.2 nmol (i.e. $1440 \text{ nmol} \cdot \text{g}^{-1} \cdot \text{h}^{-1}$) after 8 h, with selectivity of 85.2% and 92.6% for **Ru(bpy)-Mn** and **Fe-Mn**, respectively. **Fe-Mn** is thus the most efficient catalyst, and its activity is comparable to that observed for the related fully inorganic P₄Mo₆-based

heterometallic molybdenum(V) compounds NENU-605 (894.7 nmol·g⁻¹·h⁻¹) and NENU-606 (1747.8 nmol·g⁻¹·h⁻¹) studied in similar conditions.¹¹ However, the selectivity of **Fe-Mn** for CH₄ (92.6%) is better than the selectivity of these two compounds (76.6% and 85.5% for NENU-605 and NENU-606, respectively).

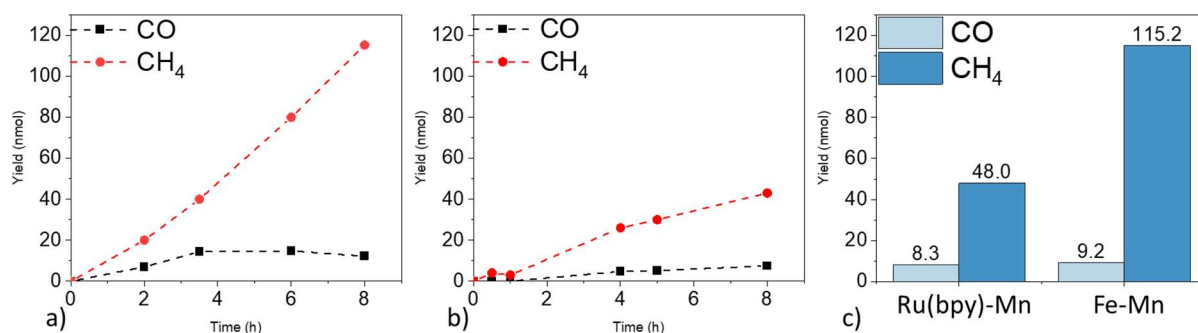


Figure 4.14: CO and CH₄ production from CO₂ over time with **Fe-Mn** (a), **Ru(bpy)-Mn** (b), H₂O:TEOA and (c) compared yield at 8h. (14:1 v/v), [Ru(bpy)₃]Cl₂ 0.01 mmol, 280 W, λ > 415 nm.

Furthermore, there is no deactivation even after 48 h of the CH₄ production of **Ru(bpy)-Mn** (Figure 4.15, left) while a *plateau* was observed after 24 h for NENU-605 and NENU-606. In addition, after three catalytic cycles no significant loss of activity has been assessed. After each catalytic run (8h) the catalyst has been indeed collected by centrifugation, washed abundantly with water and reused in a fresh H₂O:TEOA solution containing 0.01 mmol of [Ru(bpy)₃]Cl₂, and only a slight loss of activity was observed compared to the first run (Figure 4.15, right).

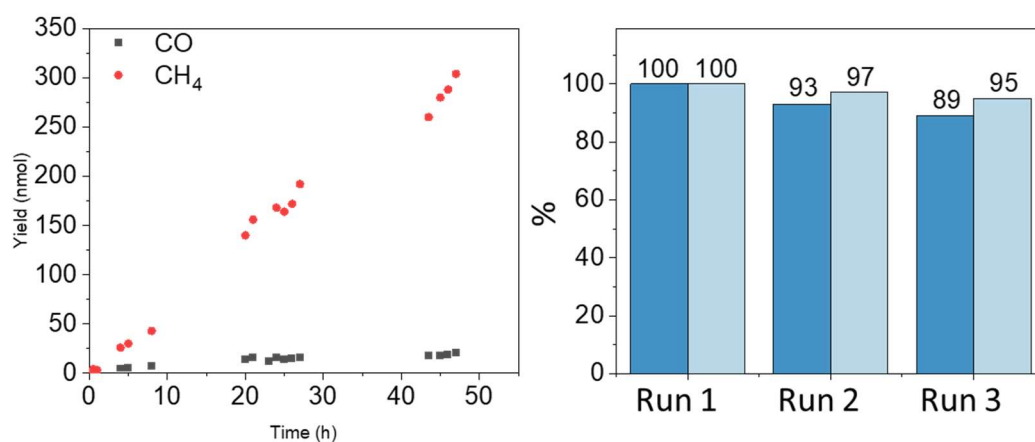


Figure 4.15: 48h catalytic CO₂ photoreduction (left) and recyclability tests (right) with **Ru(bpy)-Mn** as a catalyst.

Also, IR spectra and X-ray powder patterns of **Ru(bpy)-Mn** and **Fe-Mn** before and after catalysis are quite similar (Figures 4.16), confirming the relative stability of these materials

under catalytic conditions. Nonetheless, for $Ru(bpy)-Mn$ composite PXRD displays an additional peak at $13.3^\circ 2\theta$ that we could not attribute.

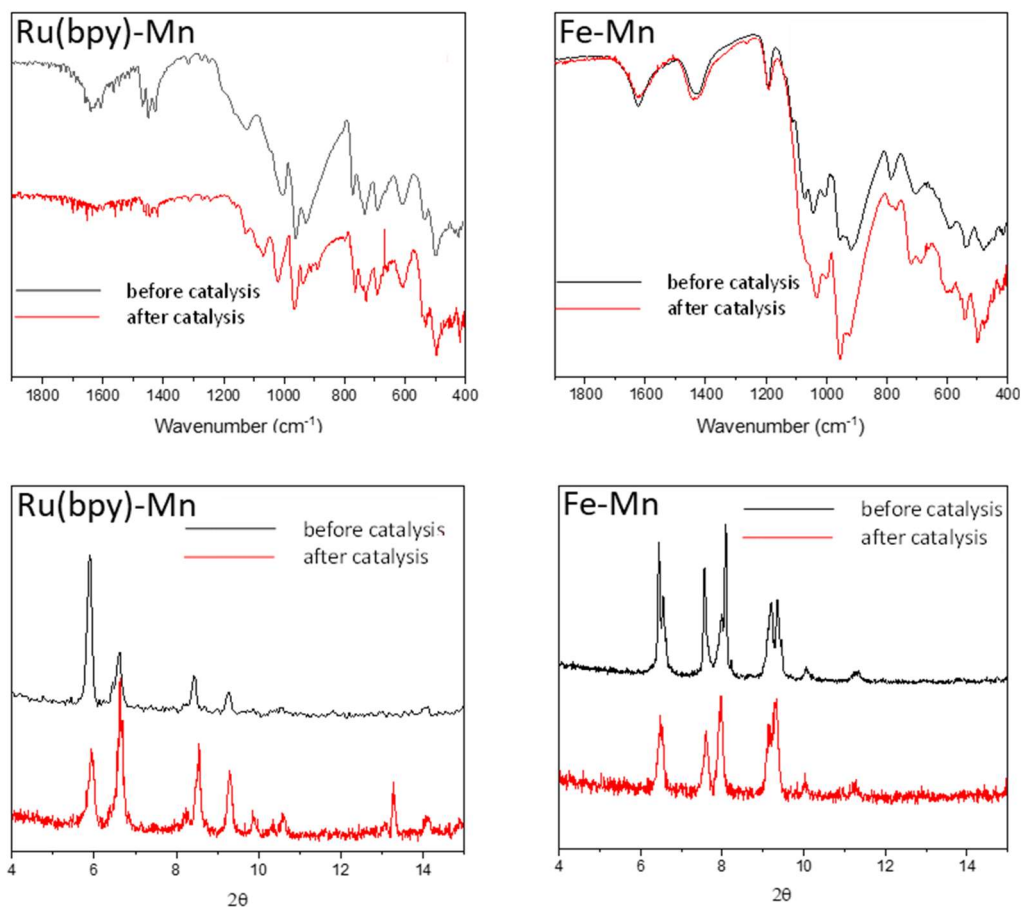


Figure 4.16: Infrared spectra and PXRD of $Ru(bpy)-Mn$ and $Fe-Mn$ before (black) and after (red) catalysis.

Aiming to shed light onto the mechanism responsible for the reduction of CO_2 by these multi-component catalytic platforms and to understand why $Ru(bpy)-Co$ and $Ni(cyclam)-Mn$ composites are inactive while $Ru(bpy)-Mn$ and $Fe-Mn$ are, Dr. Albert Solé-Daura, a post-doctoral student in Collège de France, conducted a thorough computational analysis by means of DFT. The results will be presented in the next section.

4. Mechanistic study

Previous computational studies have shown that the reduction of CO_2 to CO requires the coordination of CO_2 to an active metal center through the carbon atom to induce the charge transfer from electron-rich ligands or from the metal itself to form a $M-COO^{\bullet-}$ intermediate.^{30–}

³⁸ In our system, phosphate-coordinated metals bearing labile aqua ligands are more accessible

and in turn, more likely to participate in the reaction mechanism compared to those sandwiched between two P₄Mo₆ units, which are hexacoordinated to bridging oxygen of the POM.

Owing to the presence of *d* electrons in fully reduced polyoxomolybdates such as {P₄Mo^V₆}, it was initially postulated that upon light absorption, POMs may be able to transfer electrons to interstitial metal centers to generate a M(I) ion where CO₂ molecule could be then reduced upon coordination.^{12,39} In such a scenario, the role of the [Ru(bpy)₃]²⁺ would be that of regenerating the fully reduced POM complex with the help of a sacrificial electron donor. More recently, photophysical studies suggested that the reduction of CO₂ is attained by the [Ru(bpy)₃]²⁺ complex rather than by {P₄Mo^V₆}-containing materials, as the transient photovoltage of [Ru(bpy)₃]²⁺ is quenched in the presence of CO₂, whereas that of {P₄Mo^V₆}-based crystals was not significantly altered.¹⁵ Similar findings were also reported for larger Mo(V)-phosphate-containing POMs.²¹

To investigate the processes that may occur when irradiating such a complex multi-component system, we evaluated the feasibility of possible interactions between the POM catalyst, the Ru-photosensitizer and the TEOA sacrificial donor. On the one hand, [Ru(bpy)₃]²⁺ is well-known to undergo a metal-to-ligand charge transfer (MLCT) upon visible-light absorption, leading to a singlet MLCT state that rapidly evolves towards a long-lived triplet MLCT state, ³[Ru^{III}(bpy)₂(bpy^{•-})]^{2+,*}.⁴⁰ On the other hand, the {P₄Mo₆} POMs can also interact with visible light, leading to internal transitions of metal-centered (MC) and metal-to-metal charge transfer (MMCT) character that involve the Mo(V) ions of the cluster. Our DFT calculations predicted that both the POM and the [Ru(bpy)₃]²⁺ systems are susceptible of generating a hole at a suitable energy level to be quenched by TEOA after absorbing a photon, in agreement with previous photophysical measurements.^{10,21} It is also important to note that the ³[Ru^{III}(bpy)₂(bpy^{•-})]^{2+,*} excited state is not reducing enough to spontaneously transfer an electron to the ground state of the POM, although an excited state of {P₄Mo₆} may reduce [Ru(bpy)₃]²⁺. Overall, this analysis indicates that the Ru complex is the species that acts as electron acceptor, while the {P₄Mo₆} clusters in the crystal could act as electron shuttles, facilitating a formal electron transfer from TEOA to [Ru(bpy)₃]²⁺.

The gained knowledge about the charge-transfer processes underlying to the {P₄Mo₆}/Ru(bpy)₃ photosystem prompted us to propose a novel mechanism for the reduction of CO₂ to CO in which [Ru(bpy)₃]²⁺ acts as the catalyst and the POM-based material as a co-catalyst. This mechanistic proposal is schematically represented in **Figure 4.17** and evaluated by means of theoretical and experimental approaches. First, the formation of the one-electron reduced forms

of the POM and [Ru(bpy)₃]²⁺ (highlighted in yellow and green, respectively) occurs photochemically as described above. The absorption of a second photon by [Ru^{II}(bpy)₂(bpy^{•-})]⁺ could promote its photoionization via a *ligand-to-solvent charge transfer* (LSCT), generically known as *charge transfer to solvent* (CTTS), to regenerate the initial [Ru^{II}(bpy)₃]²⁺ species yielding a solvated electron (e⁻_{aq}). In the presence of CO₂, solvated electrons tend to localize in an empty π* MO of CO₂, resulting in a CO₂^{•-} radical anion of bent structure,^{41,42} and accomplishing the first electron injection.

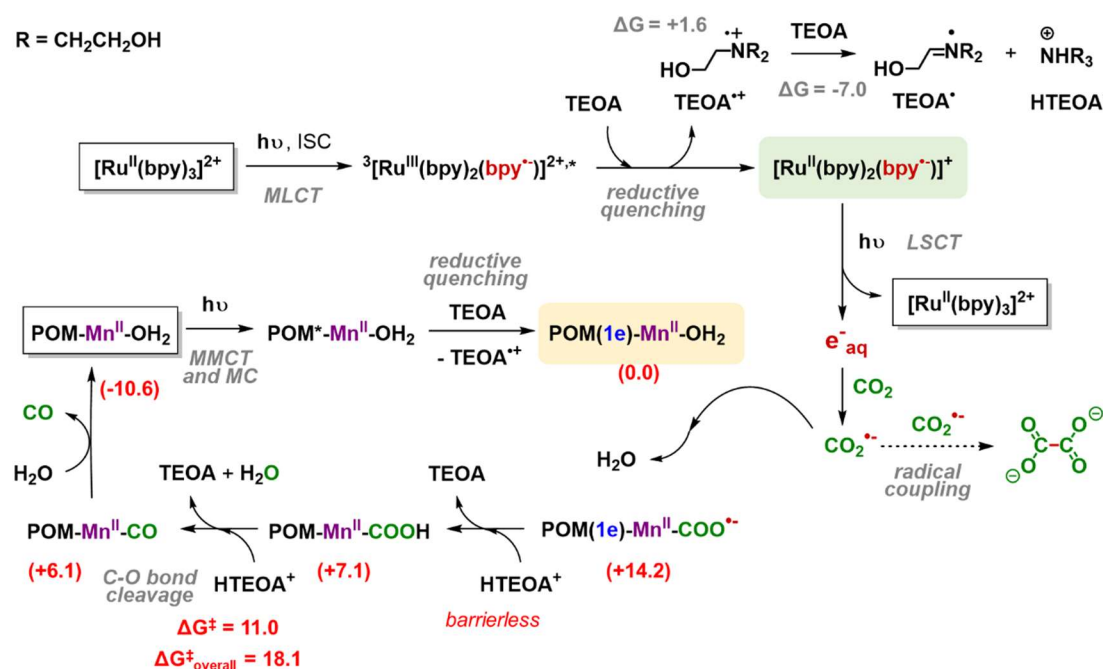


Figure 4.17: Proposed mechanism for the photoreduction of CO₂ to CO catalyzed by {P₄Mo₆}/Ru(bpy)₃ systems using TEOA as sacrificial donor. Reaction Gibbs free energies are given in kcal·mol⁻¹. Values in parentheses indicate relative Gibbs free energies. MLCT, ISC, MMCT, MC and LSCT stand for *metal-to-ligand* charge transfer, *intersystem crossing*, *metal-to-metal* charge transfer, *metal-centered* and *ligand-to-solvent* charge transfer, respectively.

After generating CO₂^{•-} in solution, this can coordinate through the C atom to a Mn(II) center of the **Ru(bpy)-Mn** crystal replacing a labile aqua ligand and generating a Mn-COO^{•-} intermediate. The Mn-COO^{•-} species can then take a proton from a protonated TEOA molecule (HTEOA⁺) through a rapid process in which one electron from a {P₄Mo₆}(1e) cluster of the material is spontaneously transferred to the CO₂ moiety to yield a Mn^{II}-COOH species. Finally, the protonation of the Mn-COOH species by a second HTEOA⁺ molecule promotes the cleavage of the C-O(H) bond. The C-O bond scission releases a water molecule and leads to the CO product coordinated to a sixfold coordinated Mn(II) center. The CO product is released

to the solution, being replaced by a water molecule to regenerate the Mn-OH₂ species, rendering the whole process irreversible, with a reverse free-energy barrier of ca. 29 kcal·mol⁻¹.

Aside from evolving to CO on the crystal surface, we can envisage an alternative pathway that CO₂^{•-} may undergo, which is the radical coupling with another CO₂^{•-} to form an oxalate anion (C₂O₄²⁻), which may prevail in the absence of coordination sites. In view of this possible route, we re-performed blank experiments in the absence of POM-based crystals, not only verifying the absence of CO and CH₄, but more importantly revealing the formation of oxalate anions as demonstrated by ¹³C NMR (Figure 4.18) and also confirmed by IC measurements, thus supporting the generation of CO₂^{•-} anions in solution by the Ru complex. Furthermore, this also evidences that [Ru^{II}(bpy)₃]²⁺ alone is not sufficient for yielding CO and thus, in absence of metal centers where CO₂^{•-} can bind to carry on with the reaction, the generated CO₂^{•-} ions quench among them to form oxalate, which is fully consistent with the proposed reaction mechanism and the roles of the Ru complex and the POM crystal as catalyst and co-catalyst, respectively.

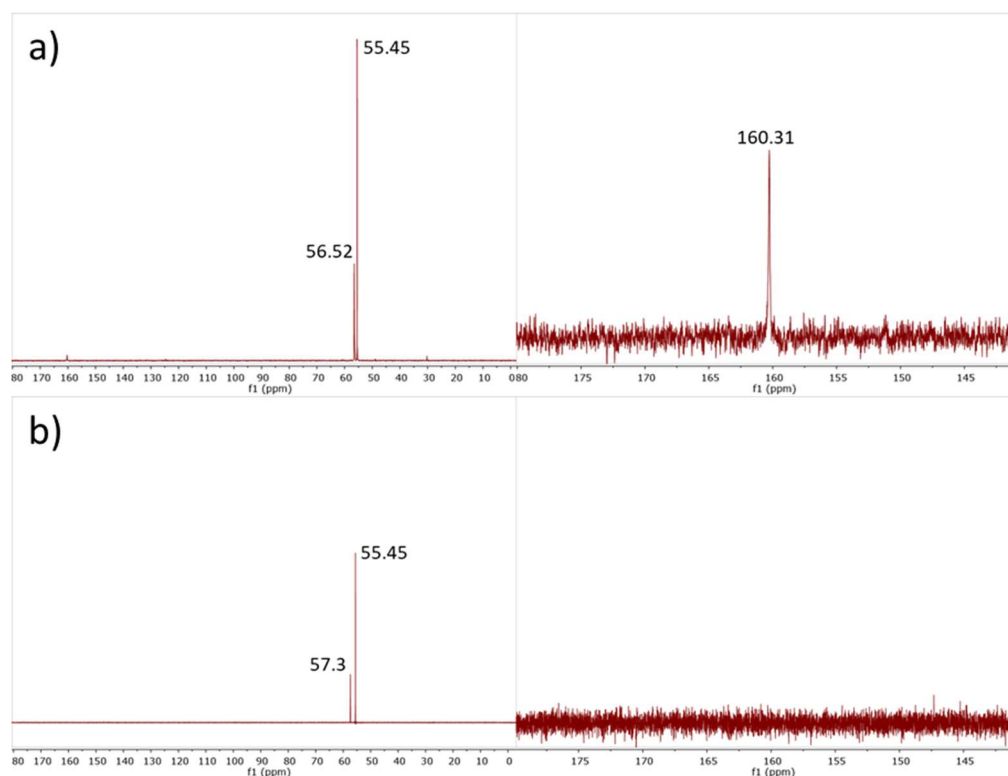


Figure 4.18: a) ¹³C NMR of 0.01 mmol Ru(bpy)₃.Cl₂ in 30 mL H₂O:TEOA (14:1) after overnight irradiation; b) DEPT 135 NMR of the same solution.

The peak at 160 ppm in the ¹³C NMR spectrum of the overnight irradiated ruthenium solution can indeed be attributed to oxalate. However, formic acid shift being close to 160 ppm in the

same conditions, we performed a DEPT 135 NMR experiment in order to confirm the nature of the product. The disappearance of the peak in DEPT 135 assesses the absence of H bond to the carbon, excluding the presence of formate.

Finally, we attempted to propose a plausible mechanism to explain the subsequent reduction of CO to CH₄. Very recently, we have characterized the TEOA[•] species that originates from the oxidation of TEOA as a hydride-donor that is capable of hydrogenating a Lewis-acid activated CO₂ to formic acid (see Chapter 3). Although we have not studied this process in detail, a preliminary analysis of the reaction profile suggests that CO could be reduced to formaldehyde, then to methanol and finally to methane on Mn(II) sites via sequential hydride-transfer steps from the allylic carbon of TEOA[•] to the carbon atom of the substrate. According to this, homogeneous [Ru(bpy)₃]²⁺ would not be strictly required to reduce any of these intermediates to methane and indeed, additional catalytic experiments showed that in aqueous solutions with TEOA, **Ru(bpy)-Mn** is capable of reducing methanol to methane by itself (**Figure 4.19**). Nonetheless, when [Ru(bpy)₃]²⁺ is added to the reaction mixture the yield of CH₄ increases significantly due to an enhanced photooxidation of TEOA caused by the electron flow from reduced POMs to [Ru(bpy)₃]²⁺ and by the role of the latter as an additional TEOA photo-oxidant.

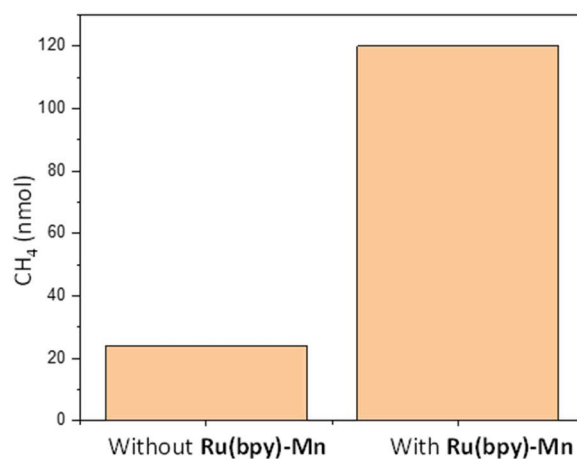


Figure 4.19: Methanol photocatalytic reduction to CH₄ in presence (right) or in absence (left) of **Ru(bpy)-Mn**. Experiments were conducted for 50 h under 280W Xenon Lamp equipped with a 415 nm cutoff, with or without 10 mg of catalyst, in 30 mL of H₂O/TEOA/MeOH (13/1/1), in the absence of additional [Ru(bpy)₃]Cl₂.

Although these facts are consistent with TEOA[•] being related to the CO to CH₄ reduction, further experimental and theoretical analyses are required to fully understand this process.

However, this is beyond the scope of this work aimed at reporting and understanding how these new photo-systems activate and reduce CO₂.

Finally, concerning our two new structures not reducing CO₂, the absence of activity for **Ru(bpy)-Co** despite previous reports^{10,11} showing that Co bridging cation helps the CO₂ photoreduction, supports the importance of the crystalline assembly. This importance can be confirmed with **Ni(cyclam)-Mn**: looking at the structure carefully we can notice that Mn(II) ions of Ni(cyclam)-Mn are scarcely accessible to an incoming CO₂ molecule and thus a mechanism similar to that observed for **Ru(bpy)-Mn** is not possible.

As for [Ni(cyclam)]²⁺, it does not play the role of co-catalyst as the POM-based composite cannot reduce CO₂. However, it must be recalled that the activity of this complex towards CO₂ reduction depends strongly on the nature of the electron donor as well as of the solvent.⁴³

5. Conclusion

In conclusion, four novel structures containing the P₄Mo₆ anionic building unit connected by first-row transition metal ions were successfully isolated by hydrothermal synthesis. Their dimensionality depends on the nature of the counterions. **Ru(bpy)-Co**, **Ru(bpy)-Mn** and **Ni(cyclam)-Mn** exhibit a 1D structure with M(P₄Mo₆)₂ (M = Co or Mn) sandwich-type POMs connected by additional Co(II) or Mn(II) ions. The [Ru(bpy)₃]²⁺ cations introduced in the synthesis of **Ru(bpy)-Mn** to play the role of counterions do not act as photosensitizer, and additional Ru complexes must be added in the catalytic solution. Since it does not play any catalytic role either, comparing the **Ru(bpy)-Mn** to its homologue without Ru(bpy) would provide useful information concerning its necessity, as addition of Ru(bpy)₃.Cl₂ might be mandatory to obtain the POM-based crystals..

DFT calculations allowed giving insights into the photocatalytic CO₂RR mechanism. Analysis of the electronic structure and photochemical properties of the different species revealed that both the POM units of the crystals and [Ru(bpy)₃]²⁺ can photooxidize the TEOA sacrificial donor and in turn, reduced POMs can reductively quench a photoexcited [Ru(bpy)₃]²⁺. As Ru-bpy complexes with delocalized electrons in the bpy ligands are known for being photo-ionized, we propose that the absorption of a photon by the one-electron reduced Ru complex, i.e. [Ru^{II}(bpy)₂(bpy^{•-})]⁺, generates a solvated electron, which can then reduce a CO₂ molecule to form a CO₂^{•-} anion in solution. In the presence of metal sites with labile ligands and suitable energy levels such as Mn(II) ions in **Ru(bpy)-Mn**, CO₂^{•-} can coordinate to the metal center,

being further reduced with one electron by the material and protonated to generate a Mn-COOH intermediate. The protonation of the latter induces the C-O(H) bond cleavage to yield a Mn-coordinated CO product releasing a water molecule. This step determines the overall cost of the thermally activated process, which needs to overcome a moderate free-energy barrier of ca. 18 kcal·mol⁻¹. Remarkably, this mechanism is consistent with three key experimental facts: i) the reduction of CO₂ to CO does not take place in the absence of any of the components; ii) oxalate is the sole product in the absence of POM crystal, since [Ru(bpy)₃]²⁺ can promote the formation of solvated electrons and CO₂^{•-} ions (which quench each other to give oxalate) but it cannot accomplish the formation of CO; iii) despite having very similar structures, Ru(bpy)-Co does not yield CO because the coordination of CO₂^{•-} to Co(II) centers results in a spontaneous electron transfer to form a Co-Co bond, regenerating an oxidized CO₂ molecule (more details can be found in the appendix). Understanding the following steps for the reduction of CO to CH₄ requires additional experimental and computational work that is under way in our groups, although preliminary studies point towards the critical role of a photogenerated TEOA[•] species as hydride donors.

Overall, this study further evinces that heterometallic molybdenum(V) phosphates can act as stable heterogeneous catalysts for the photocatalytic reduction of CO₂ into the high-valued CH₄ hydrocarbon with high selectivity. Moreover, it provides insights into the complex mechanism governing the photo-reduction of CO₂ at an atomic level, which might serve for designing a next generation of more efficient catalysts.

6. Experimental section

$[\text{Ru}(\text{bpy})_3]\text{Cl}_2 \cdot 6\text{H}_2\text{O}$ ⁴⁴ was synthesized according to reported procedures. All other reagents were purchased from commercial sources and used as received. Molybdenum powder 1-5 μm with purity >99.9% was used for the synthesis. Hydrothermal syntheses were carried out in 23 mL polytetrafluoroethylene lined stainless steel containers under autogenous pressure. All reactants were briefly stirred before heating. The mixture was heated to 180 °C over a period of 1 h, kept at 180 °C for 70 h and cooled down to room temperature over a period of 20 h. The product was isolated by filtration after sonication and washed with ethanol.

Preparation of $[\text{Ru}(\text{bpy})_3]_2\text{Co}^{\text{II}}_5[\text{P}_4\text{Mo}_6\text{O}_{26}(\text{OH})_5]_2 \cdot 22\text{H}_2\text{O}$ (Ru(bpy)-Co):

A mixture of $\text{Na}_2\text{MoO}_4 \cdot 2\text{H}_2\text{O}$ (0.235 g, 0.98 mmol), metallic Mo (0.030 g, 0.31 mmol), concentrated (85 wt%) H_3PO_4 (73 μL , 1.11 mmol), $\text{CoCl}_2 \cdot 6\text{H}_2\text{O}$ (0.420 g, 1.76 mmol), $[\text{Ru}(\text{bpy})_3]\text{Cl}_2 \cdot 6\text{H}_2\text{O}$ (0.200 g, 0.27 mmol) and H_2O (4 mL) was stirred and the pH was adjusted to 2.0 with 4 M HCl ($\text{pH}_f = 2.0$). Red crystals were isolated after filtration and sonication in ethanol (0.067 g, 14.7 % based on Mo). Metal composition was checked by EDX analysis: P/Mo = 0.55 (calc 0.67); Ru/P = 0.29 (calc 0.25); Co/P = 0.70 (calc 0.62). IR (v/cm^{-1}): 1624 (w), 1601 (w), 1460 (w), 1441 (w), 1421 (w), 1310 (m), 1166 (w), 1122 (w), 1060 (m), 1001 (s), 959 (s), 926 (s), 882 (s), 769 (m), 729 (m), 677 (m), 608 (w), 530 (m).

Preparation of $\text{Na}_2[\text{Ru}(\text{bpy})_3]_2\text{Mn}^{\text{II}}_3[\text{P}_4\text{Mo}_6\text{O}_{25}(\text{OH})_6]_2 \cdot 20\text{H}_2\text{O}$ (Ru(bpy)-Mn):

A mixture of $\text{Na}_2\text{MoO}_4 \cdot 2\text{H}_2\text{O}$ (0.470 g, 1.95 mmol), metallic Mo (0.030 g, 0.31 mmol), concentrated (85 wt%) H_3PO_4 (290 μL , 4.42 mmol), $\text{MnCl}_2 \cdot 4\text{H}_2\text{O}$ (0.119 g, 0.59 mmol), iminodiacetic acid (0.100 g, 0.75 mmol), $[\text{Ru}(\text{bpy})_3]\text{Cl}_2 \cdot 6\text{H}_2\text{O}$ (0.100 g, 0.13 mmol) and H_2O (4 mL) was stirred and the pH was adjusted to 2.5 with 4 M HCl ($\text{pH}_f = 2.5$). Red crystals were isolated after filtration and sonication in ethanol (0.065 g, 8.8 % based on Mo). Metal composition was checked by EDX analysis: P/Mo = 0.61 (calc 0.67); Ru/P = 0.30 (calc 0.25); Mn/P = 0.30 (calc 0.37); Na/P = 0.14 (calc. 0.25). IR (v/cm^{-1}): 1634 (w), 1600 (w), 1464 (w), 1441 (w), 1421 (w), 1118 (m), 1001 (s), 958 (s), 923 (s), 768 (m), 726 (s), 687 (m), 603 (m), 528 (m).

Preparation of $\text{Na}_7\text{Mn}^{\text{II}}_2\text{Fe}^{\text{II}}_4\text{Fe}^{\text{III}}_4[\text{P}_4\text{Mo}_6\text{O}_{26}(\text{OH})_5]_4(\text{PO}_4) \cdot 52\text{H}_2\text{O}$ (Fe-Mn):

A mixture of $\text{Na}_2\text{MoO}_4 \cdot 2\text{H}_2\text{O}$ (0.470 g, 1.95 mmol), metallic Mo (0.030 g, 0.31 mmol), 8 M H_3PO_4 (530 μL , 4.22 mmol), $\text{Fe}(\text{SO}_4)_2(\text{NH}_4)_2 \cdot 2\text{H}_2\text{O}$ (0.280 g, 0.70 mmol) and H_2O (4 mL) was

stirred and the pH was adjusted to 2.5 with 4 M HCl ($\text{pH}_f = 2.6$). Dark red hexagonal crystals were isolated after filtration and sonication in ethanol (0.270 g, 44.0 % based on Mo). Metal composition was checked by EDX analysis: P/Mo = 0.71 (calc.: 0.67); Mn/Fe = 0.25 (calc 0.25); Fe/Mo = 0.33 (calc :0.48); Fe/Na 1.10 (1.14). IR (v/cm^{-1}): 1624 (m), 1427 (m), 1190 (m), 1112 (sh), 1073 (s), 1043 (s), 1001 (s), 955 (s), 918 (s), 785 (m), 701 (m), 595 (m), 537 (m).

Preparation of Na₂[Ni(cyclam)]₃Mn^{II}₂[P₄Mo₆O₂₅(OH)₆]₂·12H₂O (Ni(cyclam)-Mn):

A mixture of Na₂MoO₄·2H₂O (0.470 g, 1.95 mmol), metallic Mo (0.030 g, 0.31 mmol), concentrated (85 wt%) H₃PO₄ (290 μL , 4.42 mmol), MnCl₂·4H₂O (0.119 g, 0.59 mmol), iminodiacetic acid (0.100 g, 0.75 mmol), [Ni(cyclam)]Cl₂ (0.050 g, 0.25 mmol) and H₂O (4 mL) was stirred and the pH was adjusted to 4.0 with 8 M NaOH ($\text{pH}_f = 3.9$). Bright red hexagonal crystals were isolated after filtration and sonication in ethanol (0.070 g, 10.4 % based on Mo). Metal composition was checked by EDX analysis: P/Mo = 0.60 (calc 0.67); Mn/P = 0.25 (calc 0.25); Mn/Ni = 0.49 (calc. 0.67); Na/Mn = 1.03 (calc 1.00). IR (v/cm^{-1}): 1620 (w), 1468 (w), 1449 (w), 1425 (w), 1234 (w), 1164 (w), 1127 (m), 1007 (s), 947 (s), 915 (s), 733 (m), 691 (m), 668 (m), 608 (m), 527 (m).

Other attempts in P₄Mo₆ based POM synthesis.

Table 4.1: Synthesis protocol for 1-A to 4-J. All mass values are in mg.

	1-A	1-B	1-C	1-D	1-E
Mo	30	30	30	30	30
Na ₂ MoO ₄	235	175	117	117	470
H ₃ PO ₄ (85%)	73 μL	37 μL	37 μL	37 μL	290 μL
Fe(SO ₄) ₂ (NH ₄) ₂ ·6H ₂ O					240
CoCl ₂ ·6H ₂ O	420	105		52	
MnCl ₂ ·4H ₂ O			176	132	60
Iminodiacetic acid					100
Ru(bpy) ₃	200	100	100	100	100
H ₂ O (mL)	4	4	4	4	4
pH _i	2	2	2	2	2.5

	1-F	1-G	1-H	1-I	1-J
Mo	30	30	30	30	30
Na ₂ MoO ₄	470	470	470	470	470
H ₃ PO ₄ (85%)	290 μL	290 μL	290 μL	290 μL	290 μL
Fe(SO ₄) ₂ (NH ₄) ₂ ·6H ₂ O	118		118	118	

Chapter 4: P₄Mo₆ based POM for CO₂ photoreduction

CoCl ₂ .6H ₂ O		148	148		
NiCl ₂ .6H ₂ O				148	148
MnCl ₂ .4H ₂ O	119	119			119
Iminodiacetic acid	100	100	100	100	100
Ru(bpy) ₃	100	100	100	100	100
H ₂ O (mL)	4 mL	4 mL	4 mL	4 mL	4 mL
pH _i	2.5	2.5	2.5	2.5	2.5

	2-A	2-B	2-C	2-D	2-E
Mo	30	30	30	30	30
Na ₂ MoO ₄	470	470	470	470	470
H ₃ PO ₄ (85%)	530 μL (8M)	530 μL (8M)	290 μL	290 μL	290 μL
Fe(SO ₄) ₂ (NH ₄) ₂ .6H ₂ O	280				118
NiCl ₂ .6H ₂ O				148	148
MnCl ₂ .4H ₂ O	58	200	119		
Iminodiacetic acid	100	100	100	100	100
Ru(bpy) ₃		100	100	100	100
H ₂ O (mL)	4 mL	4 mL	4 mL	4 mL	4 mL
pH _i	2.5	5.5	2.5	2.5	2.5

	2-F	2-G	3-A	3-B	3-C
Mo	30	100	30	30	30
Na ₂ MoO ₄	470	330	470	470	470
H ₃ PO ₄ (85%)	290 μL		530 μL (8M)	530 μL (8M)	290 μL
H ₃ PO ₃		100			
Fe(SO ₄) ₂ (NH ₄) ₂ .6H ₂ O			280		
CoCl ₂ .6H ₂ O		120			
NiCl ₂ .6H ₂ O	266				
MnCl ₂ .4H ₂ O		100	58	200	119
Iminodiacetic acid	100		100	100	100
Imidazole		100			
2-aminoterephthalic acid		50			
Ru(bpy) ₃	100			100	100
H ₂ O	4 mL	8 mL	4 mL	4 mL	4 mL
pH _i	2.5	3	2.5	5.5	2.5

	3-D	3-E	3-F	3-G	4-A
Mo	30	30	30	30	30
Na ₂ MoO ₄	470	470	470	470	470
H ₃ PO ₄ (85%)	290 μL	290 μL	290 μL	290 μL	290 μL
Fe(SO ₄) ₂ (NH ₄) ₂ .6H ₂ O		118			

Chapter 4: P₄Mo₆ based POM for CO₂ photoreduction

CoCl ₂ .6H ₂ O				50	
NiCl ₂ .6H ₂ O	148	148	266		
MnCl ₂ .4H ₂ O				119	119
Iminodiacetic acid	100	100	100	100	100
Ru(bpy) ₃	100	100	100	100	100
H ₂ O (mL)	4 mL	4 mL	4 mL	4 mL	4 mL
pH _i	2.5	2.5	2.5	2.5	2.5

	4-B	4-C	4-D	4-E	4-F
Mo	30	30	30	30	30
Na ₂ MoO ₄	470	470	470	470	470
H ₃ PO ₄ (85%)	290 µL	290 µL	290 µL	290 µL	290 µL
NiCl ₂ .6H ₂ O	148		148		148
MnCl ₂ .4H ₂ O	119	119	119	119	119
Iminodiacetic acid	100	100	100	100	100
Ru(bpy) ₃	100				
Co(bpy) ₃		100	100		
Ni(cyclam)				50	50
H ₂ O (mL)	4 mL	4 mL	4 mL	4 mL	4 mL
pH _i	2.5	2.5	2.5	4	5.5

	4-G	4-H	4-I	4-J	5-A
Mo	30	30	30	30	30
Na ₂ MoO ₄	470	470	470	470	470
H ₃ PO ₄ (85%)	290 µL	290 µL	530 µL (8M)	530 µL (8M)	290 µL
Fe(SO ₄) ₂ (NH ₄) ₂ .6H ₂ O	118	118			
NiCl ₂ .6H ₂ O	148	148			74
MnCl ₂ .4H ₂ O			200	200	160
Iminodiacetic acid	100	100	100	100	100
Ru(bpy) ₃	100	100			100
H ₂ O (mL)	4 mL	4 mL	4 mL	4 mL	4 mL
pH _i	2.5	2.5	5.5	5.5	2.5

	5-B	5-C	5-D	5-E	5-F
Mo	30	30	30	30	30
Na ₂ MoO ₄	470	470	470	470	470
H ₃ PO ₄ (85%)	290 µL	290 µL	290 µL	290 µL	290 µL
CoCl ₂ .6H ₂ O		148	74		
NiCl ₂ .6H ₂ O	148				
MnCl ₂ .4H ₂ O	119	119	160	119	160
Iminodiacetic acid	100	100	100	100	100
Ru(bpy) ₃	60	100	100		

Ni(cyclam)				50	50
H ₂ O (mL)	4 mL	4 mL	4 mL	4 mL	4 mL
pH _i	2.5	2.5	2.5	4	4

	5-G	5-H	5-I	5-J
Mo	30	30	30	30
Na ₂ MoO ₄	470	470	470	470
H ₃ PO ₄ (85%)	290 μ L	290 μ L	530 μ L (8M)	530 μ L (8M)
CoCl ₂ .6H ₂ O		50		
MnCl ₂ .4H ₂ O	119	119	170	170
Iminodiacetic acid	100	100	200	200
Ru(bpy) ₃		100		
Ni(cyclam)	50			
H ₂ O (mL)	4 mL	4 mL	4 mL	4 mL
pH _i	5.5	2.5	5.5	5.5

Photocatalytic experiments.

If no contrary indication, all photocatalytic experiments were run in H₂O/TEOA 14:1 (v/v), with 30 mL of solution, 10 mg of catalyst finely ground in a mortar and 0.01 mmol (7.48 mg) of [Ru(bpy)₃]Cl₂. Photochemical reactions were performed using a 280 W, high-pressure Xe arc lamp (Newport Instruments). The beam was passed through a water infrared filter, a collimating lens, and a filter holder equipped with a 415 nm band-pass filter (Asahi Spectra). Samples were saturated with CO₂ via directly bubbling CO₂ through the solution mixture for 30 min. During irradiation, the samples were vigorously stirred and aliquots of gas were analyzed..

Single crystal X-ray diffraction

Data collections were carried out by using a Bruker AXS BV diffractometer equipped with a CCD bidimensional detector using the monochromatised wavelength $\lambda(\text{Mo K}\alpha) = 0.71073 \text{ \AA}$. Absorption corrections were based on multiple and symmetry-equivalent reflections in the data set using the SADABS program based on the method of Blessing. The structures were solved by direct methods and refined by full-matrix least-squares using the SHELX-TL package. In the structure of **Ru(bpy)-Co**, one of the Co ions is disordered over two positions (Co3A and Co3B, with space occupation factors equal to 0.7 and 0.3 respectively) as well as one of the P atoms (P4A and P4B with space occupation factors equal to 0.5 and 0.5 respectively). A disorder on one of the phosphate groups is also observed in the structure of **Ru(bpy)-Mn**.

Crystallographic data are given in Table A4. Selected bond distances and valence bond calculations are given in Figures A4.1-A4.4. Valence bond calculations confirm the oxidation state of the Mo, Mn, Co and Fe ions and indicate the presence of protons on bridging oxygen atoms of the POMs.

Powder X-ray diffraction data were obtained on a Brüker D5000 diffractometer using Cu radiation (1.54059 Å). EDX measurements were performed on a JEOL JSM 5800LV apparatus. Thermogravimetry analyses (TGA) were performed on a Mettler Toledo TGA/DSC 1, STARe System apparatus under oxygen flow (50 mL·min⁻¹) at a heating rate of 5°C min⁻¹ up to 700°C.

7. References

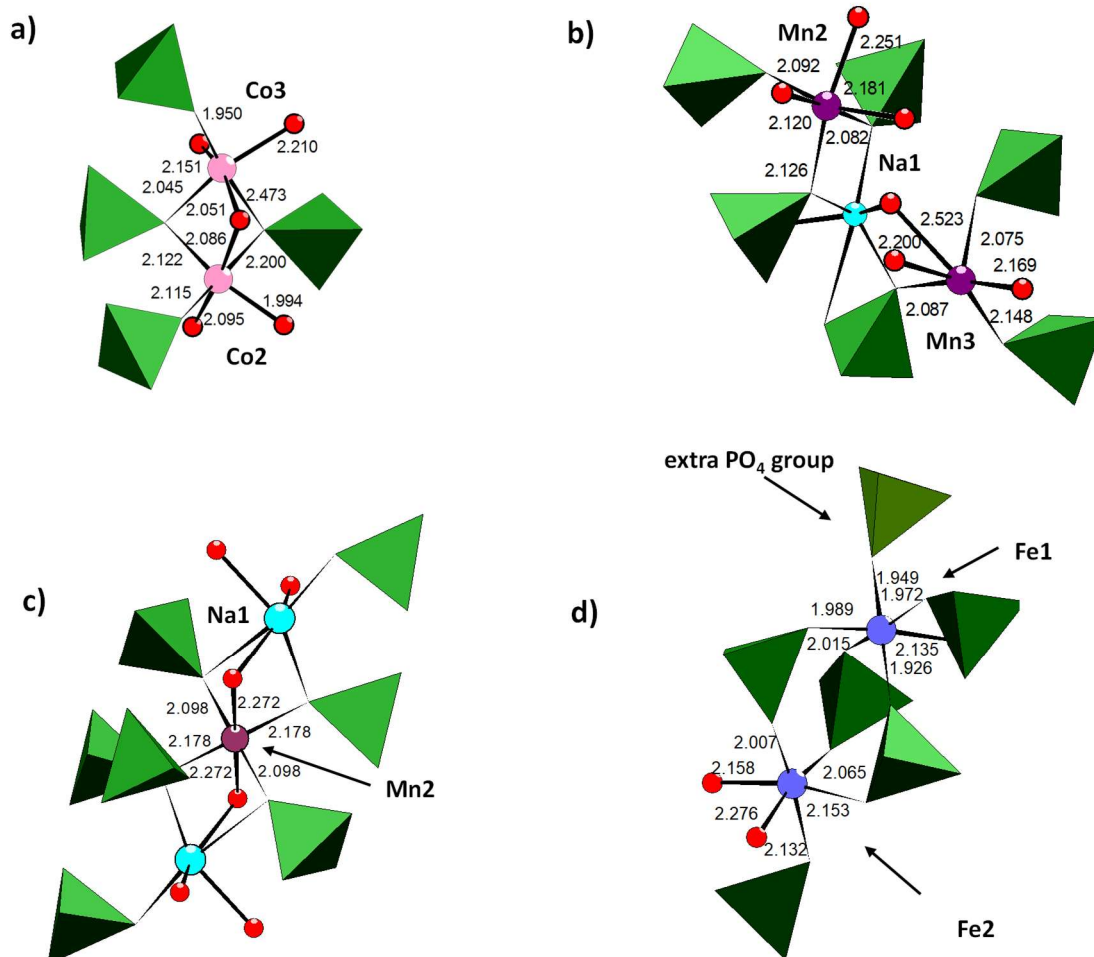
1. Lauinger, S. M., Yin, Q., Geletii, Y. V. & Hill, C. L. Polyoxometalate Multielectron Catalysts in Solar Fuel Production. in *Advances in Inorganic Chemistry* vol. 69 117–154 (Elsevier, 2017).
2. Lin, J., Han, Q. & Ding, Y. Catalysts Based on Earth-Abundant Metals for Visible Light-Driven Water Oxidation Reaction. *Chem. Rec.* **18**, 1531–1547 (2018).
3. Han, Q. & Ding, Y. Recent advances in the field of light-driven water oxidation catalyzed by transition-metal substituted polyoxometalates. *Dalton Trans.* **47**, 8180–8188 (2018).
4. Cao, Y., Chen, Q., Shen, C. & He, L. Polyoxometalate-Based Catalysts for CO₂ Conversion. **26** (2019).
5. Khenkin, A. M., Efremenko, I., Weiner, L., Martin, J. M. L. & Neumann, R. Photochemical Reduction of Carbon Dioxide Catalyzed by a Ruthenium-Substituted Polyoxometalate. *Chem. – Eur. J.* **16**, 1356–1364 (2010).
6. Girardi, M. *et al.* Electro-Assisted Reduction of CO₂ to CO and Formaldehyde by (TOA)₆[α -SiW₁₁O₃₉Co()] Polyoxometalate. *Eur. J. Inorg. Chem.* **2015**, 3642–3648 (2015).
7. Girardi, M. *et al.* Assessing the Electrocatalytic Properties of the Cp*RhIII²⁺-Polyoxometalate Derivative [H₂PW₁₁O₃₉RhIIICp*(OH₂)]³⁻ towards CO₂ Reduction. *Eur. J. Inorg. Chem.* **2019**, 387–393 (2019).
8. Barman, S., Sreejith, S. S., Garai, S., Pochamoni, R. & Roy, S. Selective Photocatalytic Carbon Dioxide Reduction by a Reduced Molybdenum-Based Polyoxometalate Catalyst. *ChemPhotoChem* **3**, 93–100 (2019).
9. Li, X.-X. *et al.* Hydrophobic Polyoxometalate-Based Metal-Organic Framework for Efficient CO₂ Photoconversion. *ACS Appl Mater Interfaces* **6** (2019).
10. Du, J. *et al.* Reduced polyoxometalates and bipyridine ruthenium complex forming a tunable photocatalytic system for high efficient CO₂ reduction. *Chem. Eng. J.* **398**, 125518 (2020).
11. Xie, S.-L. *et al.* Hetero-metallic active sites coupled with strongly reductive polyoxometalate for selective photocatalytic CO₂-to-CH₄ conversion in water. *Chem. Sci.* **10**, 185–190 (2019).
12. Du, Z.-Y. *et al.* Two 2D Layered P₄Mo₆ Clusters with Potential Bifunctional Properties: Proton Conduction and CO₂ Photoreduction. *Inorg. Chem.* (2020)
13. Haushalter, R. C. & Lai, F. W. Synthesis of a new one-dimensional sodium molybdenum phosphate polymer: structure of [(H₃O)₂NaMo₆P₄O₂₄(OH)₇]²⁻. *Inorg. Chem.* **28**, 2904–2905 (1989).
14. Mundi, L. A. & Haushalter, R. C. Hydrothermal synthesis of a layered zinc molybdenum phosphate with octahedral and tetrahedral zinc: structure of (TMA)₂(H₃O)₂[Zn₃Mo₁₂O₃₀(HPO₄)₂(H₂PO₄)₆].*cntdot*.11.5H₂O. *Inorg. Chem.* **31**, 3050–3053 (1992).
15. Meyer, L. A. & Haushalter, R. C. Hydrothermal synthesis, structure, and sorption properties of the new microporous ferric molybdenum phosphates [(CH₃)₄N]₂(NH₄)₂[Fe₂Mo₁₂O₃₀(H₂PO₄)₆(HPO₄)₂].*n*H₂O and [(CH₃)₄N]₂Na₄[Fe₃Mo₁₂O₃₀(H_xPO₄)₈].*n*H₂O. *Inorg. Chem.* **32**, 1579–1586 (1993).
16. Lightfoot, P. & Maason, D. A new 1-dimensional molybdenum phosphate: Synthesis and structure of [(CH₃)₄N][MN₂Mo₆O₁₂(OH)₄(PO₄)(HPO₄)(H₂PO₄)₂].*4H*₂O. *Mater. Res. Bull.* **30**, 1005–1013 (1995).
17. Lightfoot, P. & Masson, D. [N(CH₃)₄]₂[Co₂Mo₆O₁₂(OH)₄(PO₄)(HPO₄)₂(H₂PO₄)₂].*5H*₂O, a New One-Dimensional Molybdenum Phosphate. *Acta Crystallogr. C* **52**, 1077–1080 (1996).
18. du Peloux, C. *et al.* Three-dimensional Mn/Fe molybdenum(V) phosphates. *Solid-State Sci.* **6**, 719–724 (2004).

19. Akutagawa, T., Endo, D., Noro, S.-I., Cronin, L. & Nakamura, T. Directing organic–inorganic hybrid molecular-assemblies of polyoxometalate crown-ether complexes with supramolecular cations. *Coord. Chem. Rev.* **251**, 2547–2561 (2007).
20. Walsh, J. J., Bond, A. M., Forsert, R. J. & Keyes, T. E., Hybrid polyoxometalate materials for photo(electro-) chemical applications. *Coord. Chem. Rev.* **306**, 217–234 (2016).
21. Xu, H. *et al.* Highly Efficient Photoreduction of Low-Concentration CO₂ to Syngas by Using a Polyoxometalates/Ru^{II} Composite. *Chem. – Eur. J.* **26**, 2735–2740 (2020).
22. Hawecker, J., Lehn, J.-M. & Ziessel, R. Photochemical reduction of carbon dioxide to formate mediated by ruthenium bipyridine complexes as homogeneous catalysts. *J. Chem. Soc. Chem. Commun.* 56–58 (1985)
23. Salomon, W. *et al.* Effect of Cations on the Structure and Electrocatalytic Response of Polyoxometalate-Based Coordination Polymers. *Cryst. Growth Des.* **17**, 1600–1609 (2017).
24. Soriano-López, J., Song, F., Patzke, G. R. & Galan-Mascaros, J. R. Photoinduced Oxygen Evolution Catalysis Promoted by Polyoxometalate Salts of Cationic Photosensitizers. *Front. Chem.* **6**, 302 (2018).
25. Grant, J. L., Goswami, K., Otvos, J. W. & Calvin, M. Photochemical Reduction of Carbon Dioxide to Carbon Monoxide in Water using a Nickel(II) Tetra-azamacrocyclic Complex as Catalyst. *J CHEM SOC DALTON TRANS* 5 (1987).
26. Neri, G. *et al.* Photochemical CO₂ reduction in water using a co-immobilised nickel catalyst and a visible light sensitiser. *Chem. Commun.* **52**, 14200–14203 (2016).
27. du Peloux, C. *et al.* Three-dimensional Mn/Fe molybdenum(V) phosphates. *Solid-State Sci.* **6**, 719–724 (2004).
28. du Peloux, C. *et al.* Synthesis, crystal structure and magnetic properties of new molybdenum(V) phosphates containing Mn²⁺ or Co²⁺ with three-dimensional structures directed by the nature of the transition metal. *J. Mater. Chem.* **11**, 3392–3396 (2001).
29. Zhang, H. *et al.* The highest connected pure inorganic 3D framework assembled by {P₄Mo₆} cluster and alkali metal potassium. *RSC Adv.* **5**, 3552–3559 (2015).
30. Stanbury, M., Compain, J.-D. & Chardon-Noblat, S. Electro and photoreduction of CO₂ driven by manganese-carbonyl molecular catalysts. *Coord. Chem. Rev.* **361**, 120–137 (2018).
31. Davethu, P. A. & de Visser, S. P. CO₂ Reduction on an Iron-Porphyrin Center: A Computational Study. *J. Phys. Chem. A* **123**, 6527–6535 (2019).
32. Shakeri, J., Farrokhpour, H., Hadadzadeh, H. & Joshaghani, M. Photoreduction of CO₂ to CO by a mononuclear Re(I) complex and DFT evaluation of the photocatalytic mechanism. *RSC Adv.* **5**, 41125–41134 (2015).
33. Wang, F. *et al.* The effects of chelating N₄ ligand coordination on Co(II)-catalysed photochemical conversion of CO₂ to CO: reaction mechanism and DFT calculations. *Catal. Sci. Technol.* **6**, 7408–7420 (2016).
34. Wang, F., Neumann, R., de Graaf, C. & Poblet, J. M. Photoreduction Mechanism of CO₂ to CO Catalyzed by a Three-Component Hybrid Construct with a Bimetallic Rhenium Catalyst. *ACS Catal.* 1495–1504 (2021)
35. Yan, Z.-H. *et al.* Encapsulating a Ni(II) molecular catalyst in photoactive metal–organic framework for highly efficient photoreduction of CO₂. *Sci. Bull.* **64**, 976–985 (2019).
36. Zhu, C.-Y. *et al.* Photocatalytic reduction of CO₂ to CO and formate by a novel Co(II) catalyst containing a cis-oxygen atom: photocatalysis and DFT calculations. *Dalton Trans.* **47**, 13142–13150 (2018).
37. Shen, J., Kolb, M. J., Göttle, A. J. & Koper, M. T. M. DFT Study on the Mechanism of the Electrochemical Reduction of CO₂ Catalyzed by Cobalt Porphyrins. *J. Phys. Chem. C* **120**, 15714–15721 (2016).

38. Isegawa, M. & Sharma, A. K. CO₂ reduction by a Mn electrocatalyst in the presence of a Lewis acid: a DFT study on the reaction mechanism. *Sustain. Energy Fuels* **3**, 1730–1738 (2019).
39. Xie, S.-L. *et al.* Hetero-metallic active sites coupled with strongly reductive polyoxometalate for selective photocatalytic CO₂ -to-CH₄ conversion in water. *Chem. Sci.* **10**, 185–190 (2019).
40. Durham, B., Caspar, J. V., Nagle, J. K. & Meyer, T. J. Photochemistry of tris(2,2'-bipyridine)ruthenium(2⁺) ion. *J. Am. Chem. Soc.* **104**, 4803–4810 (1982).
41. Janik, I. & Tripathi, G. N. R. The nature of the CO₂^{•-} radical anion in water. *J. Chem. Phys.* **144**, 154307 (2016).
42. Liu, P., Zhao, J., Liu, J., Zhang, M. & Bu, Y. Ab initio molecular dynamics simulations reveal localization and time evolution dynamics of an excess electron in heterogeneous CO₂–H₂O systems. *J. Chem. Phys.* **140**, 044318 (2014).
43. Schneider, C. R., Lewis L. C. & Shafaat H. S. The good, the neutral, and the positive: buffer identity impacts CO₂ reduction activity by nickel(ii) cyclam. *Dalton Trans.* **48**, 15810-15821 (2019)
44. Broomhead, J. A., Young, C. G. & Hood, P. Tris(2,2''-Bipyridine)Ruthenium(II) Dichloride Hexahydrate. in *Inorganic Syntheses* 338–340 (John Wiley & Sons, Ltd, 1990).

8. Appendix

Figure A4.1: Co, Mn and Fe environments in the structures of a) **Ru(bpy)-Co**, b) **Ru(bpy)-Mn**, c) **Ni(cyclam)-Mn** and d) **Fe-Mn**



Inactivity of **Ru(bpy)-Co**.

We sought to understand why despite being structurally similar, the **Ru(bpy)-Mn** (active) and **Ru(bpy)-Co** (inactive) lead to remarkably distinct catalytic activities. Experimental UV-Vis spectra (**Figure 4.10**) already anticipated that the photochemical properties of both materials are rather alike. Thus, the nature of the POM-material should not alter the ability of the Ru complex to reduce CO₂ to CO₂^{•-}. This strongly support that the peripheral Mn(II) centers in the **Ru(bpy)-Mn** crystal participate explicitly in the reaction mechanism, in line with the mechanism proposed in Figure 4.17, playing a critical role that the Co(II) centers in **Ru(bpy)-Co** cannot. Indeed, analysis of the key coordination step of CO₂^{•-} to Co(II) centers **Ru(bpy)-Co** revealed that, unlike Mn(II) centers in **Ru(bpy)-Mn** and Fe(II) centers of the also catalytically active **Fe-Mn**, Co(II) ions *cannot* stabilize an M-COO^{•-} intermediate. Instead, {Co(II)}₂ dimers act as an electron sink taking the extra electron from the CO₂^{•-} fragment to form a Co-Co bond and regenerate CO₂. This can be explained by the fact that virtual Co-centered orbitals are deeper in energy than those of Mn (**Figure A4.2**), being more easily filled by a reducing agent, here the CO₂^{•-} anion. Importantly, the lack of CO/CH₄ products reported for **Ru(bpy)-Co** can be explained through its inability to coordinate and stabilize a reduced CO₂ molecule, further supporting our mechanistic proposal.

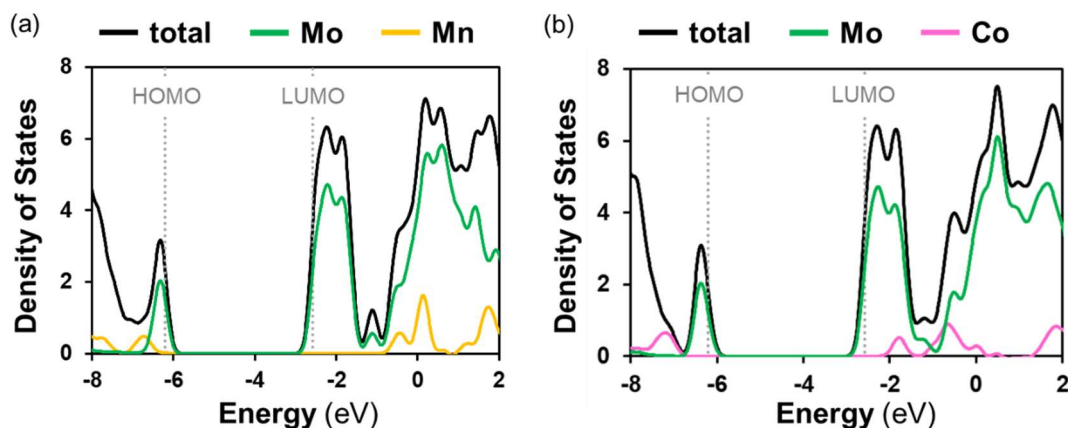


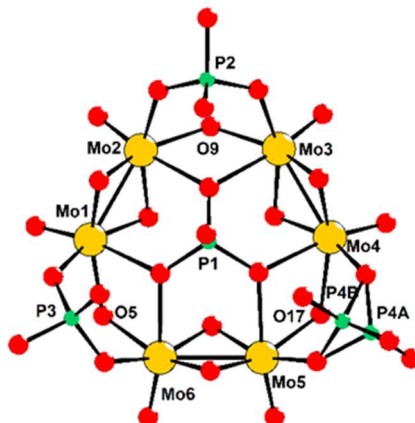
Figure A4.2: Comparison of the Density of States for **Ru(bpy)-Mn** (a) and **Ru(bpy)-Co** (b) models.

Table A4.2: Crystallographic data for **Ru(bpy)-Co**, **Ru(bpy)-Mn**, **Ni(cyclam)-Mn** and **Fe-Mn**.

	Ru(bpy)-Co	Ru(bpy)-Mn	Ni(cyclam)-Mn	Fe-Mn
Empirical formula	C ₆₀ H ₁₀₂ Co ₅ Mo ₁₂ N ₁₂ O ₈ 4P ₈ Ru ₂	C ₆₀ H ₈₀ Mn ₃ Mo ₁₂ N ₁₂ Na 2O ₇₂ P ₈ Ru ₂	C ₃₀ H ₁₁₂ Mn ₂ Mo ₁₂ N ₁₂ N a ₂ Ni ₃ O ₇₆ P ₈	Fe ₈ H ₈₂ Mn ₂ Mo ₂₄ Na ₇ O ₁ 59P ₁₇
Formula weight / g	4231.36	3933.34	3588.34	6173.31
Crystal system	Monoclinic	Triclinic	Triclinic	Tetragonal
Space group	<i>C2/c</i>	<i>P-1</i>	<i>P-1</i>	<i>I4₁/acd</i>
<i>a</i> / Å	25.734(3)	13.4831(10)	14.204(3)	27.4482(10)
<i>b</i> / Å	13.656(2)	19.2059(14)	14.319(2)	27.4482(10)
<i>c</i> / Å	35.406(4)	21.6348(15)	14.888(3)	37.9136(19)
<i>a</i> / °	90	95.036(3)	112.527(8)	90
<i>β</i> / °	106.329(5)	91.690(3)	108.688(9)	90
<i>γ</i> / °	90	98.550(3)	101.510(8)	90
<i>V</i> / Å ³	11941(2)	5513.6(7)	2463.4(8)	28564(3)
<i>Z</i>	4	2	1	8
ρ_{calc} / g cm ⁻³	2.354	2.369	2.419	2.871
μ / mm ⁻¹	2.356	2.146	2.532	3.332
Data / Parameters	17433 / 879	32042 / 1570	14439 / 548	10403 / 531
<i>R</i> _{int}	0.0276	0.0314	0.0410	0.0357
GOF	1.175	1.057	1.063	1.271
<i>R</i> (>2σ(<i>I</i>))	<i>R</i> _I ^a = 0.0516	0.0332	0.0424	0.0431
	<i>wR</i> ₂ ^b = 0.1368	0.0894	0.1111	0.1164

$$^a R_1 = \Sigma ||F_o| - |F_c|| / \Sigma |F_o|. \quad ^b wR_2 = [\Sigma w(F_o^2 - F_c^2)^2 / \Sigma w(F_o^2)^2]^{1/2}$$

Figure A4.3: Ball and stick representation with partial atomic labeling scheme and selected bond distances (Å) of the P₄Mo₆ unit in **Ru(bpy)-Co**. Bond Valence Sum (BVS) are given for Mo ions and for selected bridging atoms. Short Mo-Mo bonds around 2.6 Å also indicate the +V oxidation state of the Mo ions.



Mo(1)-O(1)	1.679(4)	BVS(Mo1) = 4.84
Mo(1)-O(2)	1.941(4)	
Mo(1)-O(3)	1.986(4)	
Mo(1)-O(4)	2.059(4)	
Mo(1)-O(5)	2.077(4)	
Mo(1)-O(6)	2.278(4)	
Mo(1)-Mo(2)	2.5976(7)	

Mo(4)-O(15)	1.682(4)	BVS(Mo4) = 4.79
Mo(4)-O(12)	1.940(4)	
Mo(4)-O(13)	1.976(3)	
Mo(4)-O(16)	2.076(4)	
Mo(4)-O(17)	2.099(4)	
Mo(4)-O(18)	2.276(4)	

Mo(2)-O(7)	1.684(4)	BVS(Mo2) = 4.88
Mo(2)-O(2)	1.932(4)	
Mo(2)-O(3)	1.978(4)	
Mo(2)-O(8)	2.038(4)	
Mo(2)-O(9)	2.089(4)	
Mo(2)-O(10)	2.272(4)	

Mo(5)-O(19)	1.682(4)	BVS(Mo5) = 4.82
Mo(5)-O(20)	1.934(4)	
Mo(5)-O(21)	1.976(3)	
Mo(5)-O(22)	2.060(4)	
Mo(5)-O(17)	2.087(4)	
Mo(5)-O(18)	2.303(4)	
Mo(5)-Mo(6)	2.5847(7)	

Mo(3)-O(11)	1.678(4)	BVS(Mo3) = 4.85
Mo(3)-O(12)	1.941(4)	
Mo(3)-O(13)	1.981(4)	
Mo(3)-O(14)	2.043(4)	
Mo(3)-O(9)	2.105(4)	
Mo(3)-O(10)	2.265(4)	
Mo(3)-Mo(4)	2.5896(6)	

Mo(6)-O(23)	1.681(4)	BVS(Mo6) = 4.84
Mo(6)-O(20)	1.932(4)	
Mo(6)-O(21)	1.980(4)	
Mo(6)-O(24)	2.073(4)	
Mo(6)-O(5)	2.085(4)	
Mo(6)-O(6)	2.267(4)	

BVS(O5) = 1.16, BVS(O9) = 1.11, BVS(O17) = 1.12 ⇒ OH

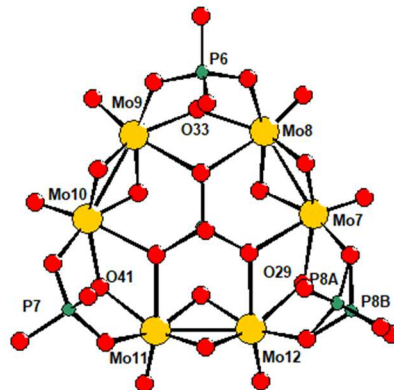
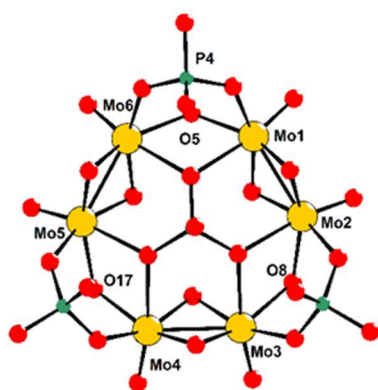
Co(1)-O(3)	2.141(3)	BVS(Co1) = 1.71
Co(1)-O(3)#1	2.142(3)	
Co(1)-O(13)#1	2.147(4)	
Co(1)-O(13)	2.147(4)	
Co(1)-O(21)	2.183(4)	
Co(1)-O(21)#1	2.183(4)	

Co(3A)-O(31)	1.939(7)	BVS(Co3A) = 2.15
Co(3A)-O(28)	2.053(5)	
Co(3A)-O(26)	2.064(4)	
Co(3A)-O(32)	2.128(13)	
Co(3A)-O(33)	2.135(11)	
Co(3A)-O(38)	2.15(5)	

Co(2)-O(25)	1.986(4)	BVS(Co2) = 1.66
Co(2)-O(26)	2.102(4)	
Co(2)-O(28)	2.118(5)	
Co(2)-O(29)	2.120(5)	
Co(2)-O(30)	2.208(5)	

Co(3B)-O(38)	1.85(4)	BVS(Co3B) = 1.92
Co(3B)-O(37)	1.97(2)	
Co(3B)-O(26)	2.047(9)	
Co(3B)-O(28)	2.198(9)	
Co(3B)-O(31)	2.367(9)	

Figure A4.4: Ball and stick representation with partial atomic labeling scheme and selected bond distances (Å) of the P₄Mo₆ unit in **Ru(bpy)-Mn**. Bond Valence Sum (BVS) are given for Mo ions and for selected bridging O atoms. Short Mo-Mo bonds around 2.6 Å also indicate the +V oxidation state of the Mo ions.



Mo(1)-O(1)	1.674(3)	BVS(Mo1) = 4.885
Mo(1)-O(2)	1.947(2)	
Mo(1)-O(3)	1.974(2)	
Mo(1)-O(4)	2.056(2)	
Mo(1)-O(5)	2.110(2)	
Mo(1)-O(6)	2.254(2)	
Mo(1)-Mo(2)	2.5864(4)	

Mo(2)-O(7)	1.681(2)	BVS(Mo2) = 4.77
Mo(2)-O(2)	1.942(2)	
Mo(2)-O(3)	1.967(2)	
Mo(2)-O(8)	2.092(2)	
Mo(2)-O(9)	2.108(2)	
Mo(2)-O(10)	2.272(2)	

Mo(3)-O(11)	1.678(2)	BVS(Mo3) = 4.83
Mo(3)-O(12)	1.932(2)	
Mo(3)-O(13)	1.970(2)	
Mo(3)-O(14)	2.070(2)	
Mo(3)-O(8)	2.099(2)	
Mo(3)-O(10)	2.294(2)	
Mo(3)-Mo(4)	2.5874(4)	

Mo(4)-O(15)	1.674(2)	BVS(Mo4) = 4.82
Mo(4)-O(12)	1.937(2)	
Mo(4)-O(13)	1.987(2)	
Mo(4)-O(16)	2.067(2)	
Mo(4)-O(17)	2.096(2)	
Mo(4)-O(18)	2.308(2)	

Mo(5)-O(19)	1.672(2)	BVS(Mo5) = 4.83
Mo(5)-O(20)	1.942(2)	
Mo(5)-O(21)	1.983(2)	
Mo(5)-O(22)	2.056(2)	
Mo(5)-O(17)	2.088(2)	
Mo(5)-O(18)	2.316(2)	
Mo(5)-Mo(6)	2.6062(4)	

Mo(6)-O(23)	1.674(2)	BVS(Mo6) = 4.84
Mo(6)-O(20)	1.933(2)	
Mo(6)-O(21)	1.979(2)	
Mo(6)-O(24)	2.046(2)	
Mo(6)-O(5)	2.111(2)	

Mo(6)-O(6)	2.306(2)
------------	----------

Mo(7)-O(25)	1.684(3)	BVS(Mo7) = 4.78
Mo(7)-O(26)	1.941(2)	
Mo(7)-O(27)	1.977(2)	
Mo(7)-O(28)	2.055(3)	
Mo(7)-O(29)	2.110(2)	
Mo(7)-O(30)	2.287(2)	
Mo(7)-Mo(8)	2.5891(4)	

Mo(8)-O(31)	1.684(3)	BVS(Mo8) = 4.80
Mo(8)-O(26)	1.943(2)	
Mo(8)-O(27)	1.964(2)	
Mo(8)-O(32)	2.058(2)	
Mo(8)-O(33)	2.086(2)	
Mo(8)-O(34)	2.326(2)	

Mo(9)-O(35)	1.679(3)	BVS(Mo9) = 4.80
Mo(9)-O(36)	1.937(3)	
Mo(9)-O(37)	1.969(2)	
Mo(9)-O(38)	2.071(3)	
Mo(9)-O(33)	2.098(2)	
Mo(9)-O(34)	2.294(2)	
Mo(9)-Mo(10)	2.5910(5)	

Mo(10)-O(39)	1.677(3)	BVS(Mo10) = 4.81
Mo(10)-O(36)	1.942(2)	
Mo(10)-O(37)	1.968(2)	
Mo(10)-O(40)	2.072(3)	
Mo(10)-O(41)	2.103(2)	
Mo(10)-O(42)	2.293(2)	

Mo(11)-O(43)	1.675(3)	BVS(Mo11) = 4.84
Mo(11)-O(44)	1.942(3)	
Mo(11)-O(45)	1.973(2)	
Mo(11)-O(46)	2.051(2)	
Mo(11)-O(41)	2.101(3)	
Mo(11)-O(42)	2.297(2)	
Mo(11)-Mo(12)	2.5851(4)	

Mo(12)-O(47)	1.676(2)	BVS(Mo12) = 4.84
Mo(12)-O(44)	1.938(2)	
Mo(12)-O(45)	1.979(2)	

Chapter 4: P₄Mo₆ based POM for CO₂ photoreduction

Mo(12)-O(48)	2.051(3)	Mo(12)-O(30)	2.305(2)
Mo(12)-O(29)	2.093(2)		

BVS(O5) = 1.07, BVS(O8) = 1.11, BVS(O17) = 1.12, BVS(O29) = 1.09, BVS(O33) = 1.12, BVS(O41) = 1.09 => OH

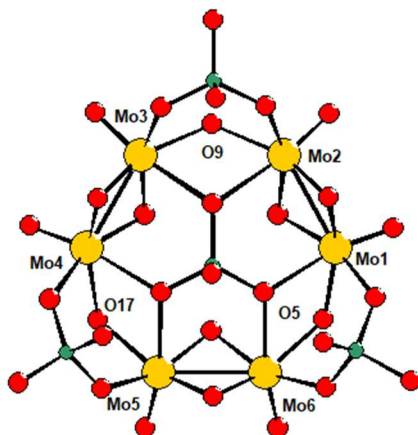
Mn(1)-O(21)#1	2.168(2)	BVS(Mn1) = 1.83
Mn(1)-O(21)	2.168(2)	
Mn(1)-O(13)#1	2.217(2)	
Mn(1)-O(13)	2.217(2)	
Mn(1)-O(3)	2.230(2)	
Mn(1)-O(3)#1	2.230(2)	

Mn(2)-O(49)	2.082(3)	BVS(Mn2) = 2.19
Mn(2)-O(50)	2.093(3)	
Mn(2)-O(52)	2.119(3)	
Mn(2)-O(51)	2.126(2)	
Mn(2)-O(53)	2.181(3)	
Mn(2)-O(54)	2.251(4)	

Mn(3)-O(55)	2.076(3)	BVS(Mn3) = 1.98
Mn(3)-O(56)	2.088(3)	
Mn(3)-O(57)	2.148(3)	
Mn(3)-O(58)	2.170(3)	
Mn(3)-O(59)	2.199(3)	
Mn(3)-O(1W)	2.525(7)	

Mn(4)-O(37)	2.176(2)	BVS(Mn4) = 1.90
Mn(4)-O(37)#2	2.176(2)	
Mn(4)-O(27)	2.189(2)	
Mn(4)-O(27)#2	2.189(2)	
Mn(4)-O(45)	2.208(2)	
Mn(4)-O(45)#2	2.208(2)	

Figure A4.5: Ball and stick representation with partial atomic labeling scheme and selected bond distances (Å) of the P₄Mo₆ unit in Ni(cyclam)-Mn. Bond Valence Sum (BVS) are given for Mo ions and for selected bridging O atoms. Short Mo-Mo bonds around 2.6 Å also indicate the +V oxidation state of the Mo ions.

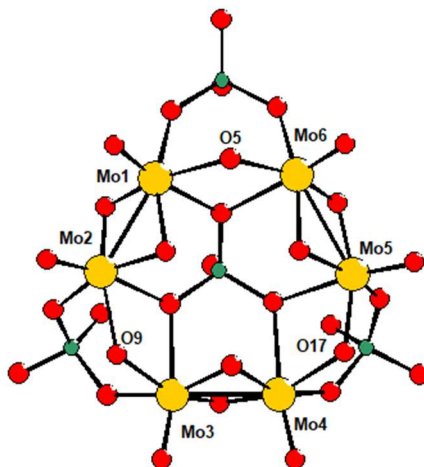


Mo(1)-O(1)	1.687(3)	BVS(Mo1) = 4.81	Mo(4)-O(15)	1.687(3)	BVS(Mo4) = 4.81
Mo(1)-O(2)	1.935(3)		Mo(4)-O(12)	1.940(3)	
Mo(1)-O(3)	1.977(3)		Mo(4)-O(13)	1.977(3)	
Mo(1)-O(4)	2.054(3)		Mo(4)-O(16)	2.040(3)	
Mo(1)-O(5)	2.118(3)		Mo(4)-O(17)	2.119(3)	
Mo(1)-O(6)	2.246(3)		Mo(4)-O(18)	2.263(3)	
Mo(1)-Mo(2)	2.5861(7)				
Mo(2)-O(7)	1.685(3)	BVS(Mo2) = 4.83	Mo(5)-O(19)	1.679(3)	BVS(Mo5) = 4.78
Mo(2)-O(2)	1.938(3)		Mo(5)-O(20)	1.942(3)	
Mo(2)-O(3)	1.970(3)		Mo(5)-O(21)	1.981(3)	
Mo(2)-O(8)	2.034(3)		Mo(5)-O(22)	2.058(3)	
Mo(2)-O(9)	2.106(3)		Mo(5)-O(17)	2.119(3)	
Mo(2)-O(10)	2.298(3)		Mo(5)-O(18)	2.285(3)	
			Mo(5)-Mo(6)	2.5936(7)	
Mo(3)-O(11)	1.685(3)	BVS(Mo3) = 4.80	Mo(6)-O(23)	1.685(3)	BVS(Mo6) = 4.80
Mo(3)-O(12)	1.944(3)		Mo(6)-O(20)	1.938(3)	
Mo(3)-O(13)	1.974(3)		Mo(6)-O(21)	1.973(3)	
Mo(3)-O(14)	2.041(3)		Mo(6)-O(24)	2.068(3)	
Mo(3)-O(9)	2.105(3)		Mo(6)-O(5)	2.091(3)	
Mo(3)-O(10)	2.293(3)		Mo(6)-O(6)	2.290(3)	
Mo(3)-Mo(4)	2.6006(6)				

BVS(O5) = 1.08, BVS(O9) = 1.08, BVS(O17) = 1.04 => OH

Mn(1)-O(3)#1	2.153(3)	BVS(Mn1) = 1.97
Mn(1)-O(3)	2.153(3)	
Mn(1)-O(13)	2.190(3)	
Mn(1)-O(13)#1	2.190(3)	
Mn(1)-O(21)#1	2.273(3)	
Mn(1)-O(21)	2.273(3)	
Mn(2)-O(25)#2	2.099(4)	BVS(Mn2) = 2.11
Mn(2)-O(25)	2.099(4)	
Mn(2)-O(26)#2	2.179(3)	
Mn(2)-O(26)	2.179(3)	
Mn(2)-O(27)#2	2.271(4)	
Mn(2)-O(27)	2.272(4)	

Figure A4.6: Ball and stick representation with partial atomic labeling scheme and selected bond distances (Å) of the P₄Mo₆ unit in **Fe-Mn**. Bond Valence Sum (BVS) are given for Mo ions and for selected bridging atoms. Short Mo-Mo bonds around 2.6 Å also indicate the +V oxidation state of the Mo ions.



Mo(1)-O(1)	1.684(4)	BVS(Mo1) = 4.83	Mo(4)-O(15)	1.679(4)	BVS(Mo4) = 4.84
Mo(1)-O(2)	1.951(4)		Mo(4)-O(12)	1.939(4)	
Mo(1)-O(3)	1.978(4)		Mo(4)-O(13)	1.973(4)	
Mo(1)-O(4)	2.056(4)		Mo(4)-O(16)	2.063(4)	
Mo(1)-O(5)	2.069(4)		Mo(4)-O(17)	2.085(4)	
Mo(1)-O(6)	2.275(4)		Mo(4)-O(18)	2.293(4)	
Mo(1)-Mo(2)	2.5991(6)				
Mo(2)-O(7)	1.677(4)	BVS(Mo2) = 4.86	Mo(5)-O(19)	1.677(4)	BVS(Mo5) = 5.23
Mo(2)-O(2)	1.949(4)		Mo(5)-O(17)	1.933(4)	
Mo(2)-O(3)	1.969(4)		Mo(5)-O(21)	1.950(5)	
Mo(2)-O(8)	2.065(4)		Mo(5)-O(20)	1.961(4)	
Mo(2)-O(9)	2.094(4)		Mo(5)-O(22)	2.018(4)	
Mo(2)-O(10)	2.247(4)		Mo(5)-O(18)	2.276(4)	
			Mo(5)-Mo(6)	2.8354(8)	
Mo(3)-O(11)	1.685(4)	BVS(Mo3) = 4.82	Mo(6)-O(23)	1.673(5)	BVS(Mo6) = 5.25
Mo(3)-O(12)	1.934(4)		Mo(6)-O(21)	1.920(5)	
Mo(3)-O(13)	1.970(4)		Mo(6)-O(5)	1.930(4)	
Mo(3)-O(14)	2.065(4)		Mo(6)-O(20)	1.948(4)	
Mo(3)-O(9)	2.118(4)		Mo(6)-O(24)	2.024(4)	
Mo(3)-O(10)	2.248(4)		Mo(6)-O(6)	2.401(4)	
Mo(3)-Mo(4)	2.5751(7)				
BVS(O5) = 1.47, BVS(O9) = 1.08, BVS(O17) = 1.43					
Mn(1)-O(20)	2.163(4)	BVS(Mn1) = 2.07	Fe(1)-O(28)	1.989(4)	Fe(1)-O(29)
Mn(1)-O(20)#2	2.163(4)		2.015(4)		
Mn(1)-O(3)#2	2.176(4)		Fe(1)-O(30)	2.135(4)	
Mn(1)-O(3)	2.176(4)				
Mn(1)-O(13)	2.214(4)				
Mn(1)-O(13)#2	2.214(4)		Fe(2)-O(31)	2.007(5)	BVS(Fe2) = 2.10
Fe(1)-O(25)	1.926(4)	BVS(Fe1) = 3.20	Fe(2)-O(32)	2.065(5)	
Fe(1)-O(26)	1.949(4)		Fe(2)-O(33)	2.132(4)	
Fe(1)-O(27)	1.972(4)		Fe(2)-O(33)#4	2.153(4)	
			Fe(2)-O(34)	2.157(6)	
			Fe(2)-O(35)	2.276(6)	

General Conclusion

The process of the photocatalytic reduction of CO₂ is known to be kinetically and thermodynamically challenging. Developing new catalysts is a necessary step to overcome this challenge. Many parameters have to be taken into consideration when developing new catalysts, precisely their efficiency, selectivity and stability. In the past decade, many efforts have been dedicated to the synthesis of new molecular catalysts for the photocatalytic reduction of CO₂. Nonetheless, due to their molecular nature they often lack stability and cannot be easily recycled. The objective of this PhD thesis was thus, thanks to the unique properties of Metal-Organic Frameworks and polyoxometalates, to develop new heterogeneous catalysts for CO₂ reduction.

In a first study, we synthesized three novel compounds containing P₄Mo₆ anionic building units connected by transition metals and studied a fourth structure already reported by our group, respectively Ru(bpy)-Mn, Ru(bpy)-Co, Ni(cyclam)-Mn and Fe-Mn. The P₄Mo₆ negative charges are compensated with coordination complexes, such as [Ru(bpy)₃]²⁺ and [Ni(cyclam)]²⁺. Both these complexes have been reported to be catalytically active in the reduction of CO₂, and were selected hoping to provide co-catalytic properties to the final POM-based composite. Under photocatalytic conditions, two of the four POM-based composites could reduce CO₂ to CO and CH₄ with methane as the major product (selectivity reaching 93% for Fe-Mn). DFT studies allowed shedding light on the mechanism involved, showing that CO₂ is reduced to CO₂^{•-} by a solvated electron released by [Ru(bpy)₃]²⁺ used as the external photosensitizer. This CO₂^{•-} may then be reduced by the POM-based materials. The Fe-Mn compound was shown to be the most effective one for CO₂ reduction out of the four compounds synthesized. Although the [Ru(bpy)₃]²⁺ species present in the novel compounds do not participate to the mechanism, they are required as structuring agent. Despite quite low efficiency, we can still point a number of assets, in particular for the Fe-Mn catalysts, which are its high selectivity towards CH₄ (which is hard to obtain as 8 electrons and 8 protons are needed for reducing CO₂), its stability with no decrease in the production rate after 8h and the absence of noble metal making it an affordable catalyst. Investigating other metals, such as copper, which has been reported to reduce CO₂ to C₂ products, could be considered in order to target compounds with increased efficiency. Another perspective would be to investigate CO or methanol reduction rather than CO₂, as the catalyst can actively reduce CO to CH₄. Lastly, CO₂ electroreduction experiments with Ni(cyclam)-Mn are worth of interest as Ni(cyclam) is way more active electrochemically.

General conclusion

In a second part, we worked on the photocatalytic properties of the (PW_{12} , Rh@MOF-UiO-67) composite. The immobilization of the Cp^*Rh complex, rhodium-based molecular catalyst, in the UiO-67 MOF was reported by a former postdoctoral researcher of our group. It was shown that upon immobilization in UiO-67, the Cp^*Rh complex could not only keep its activity toward CO_2 reduction but also increase the stability of the heterogenized catalyst, being recyclable up to five times without significant activity loss. Capitalizing on these results and knowing the properties of PW_{12} Keggin polyoxometalate as “electron reservoir”, one sub-project of my PhD consisted in studying the impact of the co-immobilization of the PW_{12} Keggin POM and the Cp^*Rh complex in the UiO-67 host. The first step of this project was to synthesize both $\text{Cp}^*\text{Rh@UiO-67}$ and $(\text{PW}_{12}, \text{Cp}^*\text{Rh})\text{@UiO-67}$ with a similar rhodium catalyst loading, in order to have the proper POM-free reference composite for further catalytic studies. Due to the POM presence in the MOF, we had to investigate different Cp^*Rh concentrations to find a matched loading with the POM-free composite. The second step was to compare the photocatalytic activity toward CO_2 reduction of $\text{Cp}^*\text{Rh@UiO-67}$ and $(\text{PW}_{12}, \text{Cp}^*\text{Rh})\text{@UiO-67}$ composites in the same conditions. This study showed interesting results: when co-immobilized with the Keggin POM, the Cp^*Rh catalyst was two to three times more effective, achieving higher TONs and TOFs. A mechanistic pathway based on DFT calculations was proposed by Dr. Albert Solé-Daura, pointing that the reduced form of the Keggin, $\text{POM}(2e^-)$ can act as an electron relay and is the reason for the catalytic increase in the $(\text{PW}_{12}, \text{Cp}^*\text{Rh})\text{@UiO-67}$ system. Concerning this project, we can point out two limits: first, the use of an external photosensitizer $[\text{Ru}(\text{bpy})_3]\text{Cl}_2$, and second, the presence of noble metal in the catalyst. We can thus propose few perspectives to enhance the attractiveness of this system:

- As seen in the state-of-the-art chapter, a wide range of transition metal pyridyl complexes can be immobilized in UiO-67 via post-synthetic exchange. We could then avoid the use of noble metal in the catalyst by using catalysts such as $\text{Mn}(\text{bpy})(\text{CO})_3\text{Br}$ or $\text{Cu}(\text{quaterpyridine})$ both reported to actively reduce CO_2 to CO.
- The mechanism suggests that the presence of a reduced PW_{12} , acting as an electron relay, is responsible for the enhancement of the catalytic properties of the $(\text{PW}_{12}, \text{Cp}^*\text{Rh})\text{@UiO-67}$ when compared to the POM-free one. Under photocatalytic conditions, the POM can be reduced with up to two electrons. However, it is still unclear which of the one or the two-electron reduced POM assists the catalysis via photo-induced or thermal/photoinduced electron transfer to the catalyst, respectively. In this

regard, photoelectrochemical experiments could be planned to clarify the nature of the mechanism.

- Finally, other types of POM could be investigated. As described in Chapter two perspectives section, varying the redox and acidic properties of the POM could indeed help us to experimentally support the proposed mechanism, and possibly enhance, furthermore, the catalytic activity of such composites. First POM to investigate would be $\text{PW}_{10}\text{Ti}_2$ as it has been described having better electron relay properties than PW_{12} , we could thus expect a greater increase in the catalytic CO_2 photoreduction.

The last sub-project I carried during my PhD thesis was the investigation of the effect of porphyrin metalation in MOF-545 on its CO_2RR photocatalytic activity. MOF-545 was selected as an interesting platform for performing CO_2 photocatalytic reduction in heterogeneous conditions: porphyrins are known to act as photosensitizers as well as catalysts for CO_2 reduction, and MOF-545 is highly porous and may thus be easily loaded with guest molecular (co)catalysts. MOF-545 can thus be considered as an interesting three-in-one platform combining its porosity, its ability to harvest light and to catalytically reduce CO_2 . We first investigated how the porphyrin metalated with a transition metal might modify the MOF catalytic activity towards CO_2RR . We found that MOF-545(Fe) was the one leading to the highest formate production with a 4-fold increase in activity when compared to that of the free-base MOF. A second strategy was investigated to further enhance MOF-545 catalytic efficiency, whereby the synthesis of nanoparticles was attempted. Indeed, as MOF are used in suspension, the smaller the particles, the higher the active surface area. We developed a microwave synthesis of NanoMOF-545(Fe), which to our knowledge had never been described so far. Working with those nanoparticles could increase by another two-fold the formate production, making an overall increase of 8-fold. Importantly, thanks to DFT calculations, the non-innocent role of TEOA in the CO_2 photoreduction mechanism was revealed: that the photo-oxidized form of TEOA is indeed responsible for the formation of the formate product with the assistance of a Zr(IV) site acting as a Lewis acid to release formate. This mechanistic proposal was further validated with additional photocatalytic experiments and allowed rationalizing the experimentally observed reactivity trends on the basis of the ability of the material to promote the initial photo-oxidation of TEOA.

In a second part, we immobilized different molecular catalysts in MOF-545 ($\text{Mn}(\text{bpy})$, $\text{Ni}(\text{cyclam})$, tetrakis(pentafluorophenyl)porphyrin) (noted F₂₀). For $\text{Mn}(\text{bpy})@\text{MOF-545}(\text{Zn})$ and $\text{Ni}(\text{cyclam})@\text{MOF-545}(\text{Zn})$, after only a few hours a high loading of 0.8 $\text{Mn}(\text{bpy})/\text{Zr}_6$ and

General conclusion

4 Ni(cyclam)/Zr₆ can be obtained, although three successive encapsulations were needed before reaching a 0.2 F₂₀/Zr₆ ratio, probably because of the bulkier nature of F₂₀. We then tested the three systems for CO₂ reduction. Unfortunately, we could not assess any activity. Nonetheless, we have shown that small molecular catalysts can be immobilized with high loadings. Lastly, in a preliminary study, we investigated the catalytic activity for CO₂ reduction of different POM@MOF-545 materials using four different POMs, Co₄, Ni₄, PW₁₂ and PW₁₀Ti₂ showing that SiW₁₂@MOF-545 was the most promising candidate among the POM@MOF series. We thus investigated five Keggin POMs, PW₁₂, BW₁₂, SiW₁₂, SiMo₁₂ and PMo₁₂. Due to their highly negative charge (from -3 to -5), aiming at moderate loading is mandatory to avoid damaging the resulting POM@MOF composite. Finally, photocatalytic tests on these materials have shown that the acidic encapsulation media is degrading the MOF activity for CO₂ reduction. To avoid this problem, we could work with PW₁₁M Keggin POM as they are stable in neutral pH.

Regarding the MOF-545 sub-project, the work reported here opens up numerous perspectives. Iron porphyrins and porphyrin-based MOFs have been widely reported for electrocatalytic CO₂ reduction. As we have shown here how efficient NanoMOF-545(Fe) is for CO₂ photocatalytic reduction, we may thus investigate its performance for CO₂ (photo)electroreduction by considering the deposition of NanoMOF on porous electrodes (gas diffusion electrodes). Another potentially interesting area of exploration is the use of MOF-545 for performing dual catalysis, *i.e.* both water oxidation and CO₂ reduction, using the ability of porphyrins to also oxidize water or the ability of the MOF to host a molecular water oxidation catalyst. For instance, the synthesis of Ti-doped homologues (Zr/Ti)MOF-545 could allow promoting charge separation upon illumination, while being able to oxidize water at the porphyrin linker and reduce CO₂ at the Zr/Ti centers. Another route for designing a MOF-545-based system working both for water oxidation and CO₂ reduction would be the immobilization of the sandwich cobalt-based POM, Co₄, in the NanoMOF-545(Zn) CO₂RR catalyst, taking advantage of the photocatalytic activity of Co₄@MOF-545 we previously reported for water oxidation, with the challenging issue of finding the appropriate photocatalytic conditions.

Overall, the experimental work reported herein, supported by theoretical calculations, has allowed highlighting mechanisms at work in the photocatalytic reduction of carbon dioxide by MOFs, extended POMs and related POM@MOF composites. I hope that in a near future this work will help to create new systems with largely improved performances in CO₂RR.